Alexandre H. M. Brigadeau

Modeling and numerical investigation of high pressure gas-liquid separation

Thesis for the degree of doktor ingeniør

Trondheim, September 2007

Norwegian University of
Science and Technology
Faculty of Engineering Science and Technology
Department of Energy and Process Engineering

NTNU
Innovation and Creativity

NTNU
Norwegian University of Science and Technology

Thesis for the degree of doktor ingeniør

Faculty of Engineering Science and Technology
Department of Energy and Process Engineering

ISBN 978-82-471-3652-2 (printed ver.)
ISBN 978-82-471-3666-9 (electronic ver.)
ISSN 1503-8181

Theses at NTNU, 2007:167

Printed by Tapir Uttrykk

Alexandre H. M. Brigadeau

Modeling and numerical investigation of high pressure gas-liquid separation

Department of Energy and Process Engineering
Norwegian University of Science and Technology
Trondheim, Norway, 2007

A mes parents

Abstract

In this Ph.D. thesis, a model for the study of the efficiency of high-pressure liquid/gas industrial separators has been developed. The model is a three fluid model (gas phase, droplet phase and film phase) and is entirely Eulerian. For the gas phase, a $k - \epsilon$ model extended to multiphase flows has been used. The turbulent kinetic energy of the dispersed phase, the turbulent dispersion coefficient and the momentum equation of the liquid film were closed algebraicly. The total deposition velocity was determined by turbulent dispersion and a near-wall deposition velocity. The latter was the sum of a non-diffusive term (due to the mean convection of the flow and gravity) and a diffusive term. This diffusive term accounted for the diffusion-impaction deposition regime and the inertia-moderated deposition regime. The gas/liquid film interfacial shear stress was calculated from the local value of the turbulent kinetic energy of the gas. The film acted on the gas as a steady rough wall. An experimental entrainment rate correlation was chosen. The model was implemented in a finite-volume commercial code (Fluent 6.2). The model is based on local closure relations so that it can be further developed for complex industrial geometries.
The results were first compared with experiments from the literature. Deposition rates and film heights were in agreement with the data of the literature. However, the calculated pressure drops were higher and the calculated entrainment rates were lower than the experimental values. The present work pinpoints the reasons of these inaccuracies and corrections to the original model are proposed. The model was finally applied to calculate the efficiency of a vane-pack demister. At atmospheric pressure with air and water the efficiency of the demister was 99.7%. This value agrees with the prediction of a former model from the literature. At high pressure with natural gas and condensate the efficiency of the separator was 0%. The deposition rate was lower, the entrainment rate very high and the liquid layer vanished.

Acknowledgments

I would like to thank my supervisor Stein Tore Johansen, first, for trusting in me by giving me the opportunity to start this Ph.D. and second, for sharing ideas and enthusiasm all along this work. Thanks also to my second supervisor Hugo Jakobsen who helped me during the first year. I have benefited from the help of numerous people over these Ph.D. years and I cannot name them all. I owe a lot to my the colleagues and friends from the department of energy and process engineering for fruitful discussions and their general support. I am also grateful to the people of the SINTEF Flow Technology research group, and all the people who participated in the HiPGaS project. I must mention as well the efficient help of the administrative staff and the crucial help of our data engineer.
Thanks are given to the industrial partners involved in the HiPGaS project and the research council of Norway for their financial support.
Finally I would like to thank my friends, my family and especially my fiancée for their help and patience. I must not forget the cat who always reminded me that as long as it is warm and there is food, partial differential equations do not really matter.

Contents

List of Figures

List of Tables

Nomenclature

Upper-case Roman

Symbol	Units	Description
A	m^2	Area
A	m^2	In equation (2.38), projection of the frontal area of the particle to the direction of the incoming flow
A	$m \cdot rad^{-1}$	Fourier transform coefficient of the velocity of the continuous phase
B	none	Additional constant of the log-law
B	$m \cdot rad^{-1}$	Fourier transform coefficient of the velocity of the continuous phase
C	$m \cdot rad^{-1}$	Fourier transform coefficient of the velocity of the particle phase
C	$m \cdot s^{-1}$	Velocity with which droplets are leaving the liquid film
C	$m \cdot s^{-1}$	Wave velocity in equation (3.140)
C_D	none	Drag coefficient
C_f	none	Interfacial friction coefficient defined by equation (3.59)
C_{fg}	none	Interfacial friction coefficient based on an average gas velocity
$C_{\epsilon 1}$, $C_{\epsilon 2}$	none	Constants in the model equation for ϵ
$C_{\epsilon 3}$	none	Constant in the model equation for ϵ for multiphase flows
C_μ	none	Turbulent viscosity constant in the $k - \epsilon$ model
D	m	Diameter of a pipe
D	$m \cdot rad^{-1}$	Fourier transform coefficient of the velocity of the continuous phase
D	$kg \cdot m^{-4} \cdot s^{-1}$	Deposition coefficient defined by relation (7.11)
D_{crit}	$kg \cdot m^{-3} \cdot s^{-1}$	Deposition coefficient threshold defined by relation (7.12)
D'	$kg \cdot m^{-3} \cdot s^{-1}$	Deposition coefficient defined by relation (7.20)
$\dot{D}$	$kg \cdot m^{-3} \cdot s^{-1}$	Rate of deposition
D	$m^2 \cdot s^{-1}$	Dispersion coefficient
E	none	Eastern neighboring grid point of a control volume
E	$kg \cdot m^{-3} \cdot s^{-1}$	Entrainment coefficient defined by relation (7.8)
E_{crit}	$kg \cdot m^{-2} \cdot s^{-1}$	Entrainment threshold coefficient defined by relation (7.9)
$\mathscr{E}$	$m^2 \cdot s^{-1}$	Energy spectrum function
$\dot{E}$	$kg \cdot m^{-3} \cdot s^{-1}$	Rate of re-entrainment
F^{int}	N	Force exerted by the gas on the film
F_D	$N \cdot m^{-3}$	Drag force density of the fluid on the particles of a control volume
F_P	N	Pressure forces exerted by the continuous phase on the particles
F_V	N	Viscous forces exerted by the continuous phase on the particles

Symbol	Units	Description
G	none	Fluid property group defined by equation (3.162)
G	$kg \cdot m^{-4} \cdot s^{-1}$	Gravity group defined by equation (6.23)
$\underline{H}$	m	Complex harmonic amplitude of the perturbation of the height of the liquid film
I	m	Equation of the gas/film interface
I	$kg \cdot m^{-3} \cdot s^{-1}$	Interfacial shear group defined by equation (6.24)
$\Im$	none	Imaginary part
$\mathscr{I}$	none	Intermittency
$\mathcal{I}_k$	$m^2 \cdot s^{-3}$	Interphase exchange of turbulent kinetic energy
$\mathcal{I}_\epsilon$	$m^2 \cdot s^{-4}$	Interphase exchange of dissipation
J_d	$kg \cdot m^{-2} s^{-1}$	Deposition flux of droplets
J_e	$kg \cdot m^{-2} s^{-1}$	Entrainment flux of droplets
J'_{e0}	$kg \cdot m^{-2} s^{-1}$	Constant entrainment flux of droplets defined by equation (7.17)
K_D	$m \cdot s^{-1}$	Near-wall deposition velocity
K_{disp}	$m \cdot s^{-1}$	Dispersion velocity
$K_{non\,diff}$	$m \cdot s^{-1}$	Near-wall non-diffusive deposition velocity
K_{set}	$m \cdot s^{-1}$	Settling deposition velocity
K_{total}	$m \cdot s^{-1}$	Total deposition velocity
K_{turb}	$m \cdot s^{-1}$	Turbulent deposition velocity
K_{wall}	$m \cdot s^{-1}$	Near-wall diffusive deposition velocity
L	m	Spacial period of the modeled interface (see Figure 6.5)
N	none	Number of particles in a control volume
P	Pa	Pressure
$\underline{P}$	Pa	Complex harmonic amplitude of the perturbation of the pressure
P	none	Grid point of a control volume
$\mathcal{P}$	$m^2 \cdot s^{-3}$	Rate of production of turbulent kinetic energy
$\dot{Q}_f$	$m^2 \cdot s^{-1}$	Film volume flow rate per unit length
R	m	Radius of curvature
R	m	Radius of the pipe (in equation 3.121)
$\mathscr{R}$	none	Normalized auto-correlation function
$\Re$	none	Real part
Re	none	Reynolds number
S	varies	General source term
S_1	varies	Part of the source term which is not a function of the dependent variable (in equation (4.9))
S_2	varies	Coefficient of the dependent variable in the linear form of the source term (in equation (4.9))
Sc	none	Schmidt number: Ratio of the kinematic viscosity of the gas to the Brownian diffusion coefficient
T	$N \cdot m^{-3}$	Total viscous force density
T	s	Integral quantity in equations (2.80) and (2.81)

Symbol	Units	Description
T_d	$kg \cdot m^{-3} \cdot s^{-1}$	Turbulence coefficient defined by relation (7.13)
$T_{d,crit}$	$kg \cdot m^{-2} \cdot s^{-1}$	Turbulence threshold coefficient defined by relation (7.14)
T'_d	$kg \cdot m^{-2} \cdot s^{-1}$	Turbulence coefficient defined by relation (7.21)
$\mathcal{T}_i$	$m^3 \cdot s^{-3}$	Flux of turbulent kinetic energy
U_i	$m \cdot s^{-1}$	Velocity
V	m^3	Volume
V_{drift}	$m \cdot s^{-1}$	Drift velocity of a particle in a turbulent flow
Vi	none	Viscosity group (defined by equation (3.143))
W	none	Western neighboring grid point of a control volume
We	none	Weber number
X_i	m	Space coordinates
Y	none	Parameter defined in equation (3.148)

Lower-case Roman

Symbol	Units	Description
a	varies	Coefficient of the dependent variable in the transport equations in their discrete form (equation (4.5))
b	varies	Additional term in the transport equations in their discrete form (equation (4.5))
c_i	$m \cdot s^{-1}$	Velocity with which droplets are leaving the liquid film in the reference frame defined by Figure 3.4
d	m	Diameter of a particle
d_{lig}	m	Diameter of a ligament generating droplets
f	s^{-1}	Frequency of a given turbulent fluctuation
f	none	Time scheme weighting coefficient
f_D	N	Drag force of the carrier phase on one particle
g	$m \cdot s^{-2}$	Gravitational acceleration
h	m	Height of the liquid film
h_1	m	Minimum height of the liquid film for the model for the shape of the interface (Figure 6.5)
h_2	m	Maximum height of the liquid film for the model for the shape of the interface (Figure 6.5)
$h^{'}$	m	Harmonic perturbation of the height of the liquid film
$\underline{h}^{'}$	m	Complex harmonic perturbation of the height of the liquid film
h^*	m	Typical film length scale
i	none	Imaginary unit
k	$m^2 \cdot s^{-2}$	Turbulent kinetic energy
k	m^{-1}	Wave number
l	m	Typical size of the large turbulent structures
$\dot{m}$	$kg \cdot s^{-1}$	Mass flow rate
n	none	Normal vector
$p^{'}$	Pa	Harmonic perturbation of the pressure

Symbol	Units	Description
$\underline{p}^{'}$	Pa	Complex harmonic perturbation of the pressure
$\underline{q}$	none	Particle
r	m	Radial position
s	m	Equivalent sand roughness
s^+	none	Non-dimensional sand roughness defined by equation (3.67)
t	s	Time
t^+	none	Non-dimensional particle relaxation time defined by equation (3.124)
u	$m \cdot s^{-1}$	Shorter notation for $\langle U_{ic} \rangle^{''}$ in Tchen's theory
u	$m \cdot s^{-1}$	Velocity in the x direction
u_τ	$m \cdot s^{-1}$	Friction velocity
u^+	none	Non-dimensional boundary layer velocity
v	$m \cdot s^{-1}$	Velocity in the y direction
v	$m \cdot s^{-1}$	Shorter notation for $\langle U_{id} \rangle^{''}$ in Tchen's theory
w	$m \cdot s^{-1}$	Velocity in the z direction
x	m	First space coordinate in the reference frame defined by Figure 3.4
y	m	Second space coordinate in the reference frame defined by Figure 3.4
y	m	In the non-diffusive deposition model: Distance from the centroid of the near-wall cell along an axis oriented by the outwardly directed normal to the wall
y^+	none	Non-dimensional boundary layer distance
z	m	Third space coordinate in the reference frame defined by Figure 3.4
z	none	Complex number defined by equation (8.4)
z	m	Vertical coordinate in equation (3.136)

Upper-case Greek

Symbol	Units	Description
Γ	none	Empirical coefficient defined by equation (3.66)
Δ_i	$m \cdot s{-}1$	Velocity defined by equation (3.9)
Λ	varies	General diffusion coefficient
Π	$N \cdot m^{-3}$	Total pressure force density
Σ	$N \cdot m^{-1}$	Surface tension
Ω	none	Ratio of the gravity forces against capillary forces

Lower-case Greek

Symbol	Units	Description
α	none	Volume fraction of a phase
β	$kg \cdot m^{-3} \cdot s^{-1}$	Momentum exchange coefficient defined by equation (2.55)
γ	none	Correction coefficient of the drag for non-creeping flows
δ_{ij}	none	Kronecker symbol
ϵ	$m^2 \cdot s^{-3}$	Rate of dissipation of turbulent kinetic energy
η	none	Ratio of the Lagrangian integral time scale of the continuous phase to the characteristic relaxation time of the particle
η'	none	Ratio of the Lagrangian integral time scale of the continuous phase, accounting for the crossing trajectory effect, to the characteristic relaxation time of the particle
θ	rad	Circumferential position
θ	rad	Angle between the droplet velocity vector and the gas velocity vector
κ	none	Von Kármán constant
λ	$kg \cdot m^{-1} \cdot s^{-1}$	Bulk viscosity coefficient
μ	$kg \cdot m^{-1} \cdot s^{-1}$	Dynamic molecular viscosity
μ_T	$kg \cdot m^{-1} \cdot s^{-1}$	Dynamic turbulent viscosity
$\mu_{Tf,d}$	$kg \cdot m^{-1} \cdot s^{-1}$	Dynamic turbulent viscosity of the film due to droplet deposition
$\mu_{Tf,i}$	$kg \cdot m^{-1} \cdot s^{-1}$	Dynamic turbulent viscosity of the film induced by the film flow
ν	$m^2 \cdot s^{-1}$	Kinematic viscosity
ν_T	$m^2 \cdot s^{-1}$	Kinematic turbulent viscosity
ρ	$kg \cdot m^{-3}$	Density
σ_{ij}	Pa	Stress tensor
σ^k	none	Turbulent Prandtl number related to the turbulent kinetic energy
σ^{α_c}	none	Turbulent Schmidt number related to turbulent dispersion
σ^ϵ	none	Turbulent Prandtl number related to the dissipation
τ	s	Characteristic relaxation time of a particle
τ_c	s	Lagrangian integral time scale of the continuous phase
τ_c'	s	Lagrangian integral time scale of the continuous phase accounting for the crossing trajectory effect
τ_c^*	s	Characteristic time defined by equation (2.69)
τ_i	Pa	Interfacial shear stress
τ_{ij}	Pa	Viscous stress tensor
υ	none	Under-relaxation factor
χ	none	Proportionality coefficient for the entrainment rate correlation (3.155)
χ'	none	Proportionality coefficient for the entrainment rate correlation (7.17)
ψ	varies	General field property
ω	$rad \cdot s^{-1}$	Pulsation (of a turbulent fluctuation, a wave or a particle)

Subscripts

Symbol	Description
$\underline{X}$	Complex quantity
0	Inlet value
0	Reference value
C	Related to the cell centroid
E	Eulerian
E	Value at/related to the eastern neighboring grid point of a control volume
L	Lagrangian
P	Value at/related to the grid point of a control volume
W	Value at/related to the western neighboring grid point of a control volume
avg	Space averaged value
c	Related to the continuous phase
$crit$	Critical
d	Related to the dispersed phase
e	Value at/related to the eastern boundary of a control volume
f	Related to the film
f	Related to a given face of a control volume
g	Related to the gas phase
i	Component i of a vector
ij	Component ij of a tensor
j	Component j of a vector
k	Component k of a vector
m	Relative to the fastest growing wave
min	Minimum
nb	Value at/related to the neighboring points of a control volume
p	Related to the particles
p	Projection of a vector on the wall
r	Related to the radial direction
rw	Relative to roll waves
tot	Total (sum of the turbulent and molecular components)
w	Value at/related to the western boundary of a control volume
$wall$	Related to the wall
x	Related to the x direction
y	Related to the y direction
z	Related to the z direction
κ	Related to phase κ

Superscripts

Symbol	Description
$+$	Non dimensional quantity
$*$	Guessed value
$\overline{X}$	Mean of X over an ensemble of samples
$X^{'}$	Fluctuating component $X^{'} \equiv X - \overline{X}$
$\widehat{X}$	Extensive average of X
$X^{\wedge}$	Fluctuating component $X^{\wedge} \equiv X - \widehat{X}$
$\widetilde{X}$	Favre average of X
$X^{''}$	Fluctuating component $X^{''} \equiv X - \widetilde{X}$
c	Correction term
$down$	Value in the downstream cell
i	Value at the iteration i
int	Related to the interface
n	Value at the time step n
up	Value in the upstream cell

Symbols

Symbol	Description
$\equiv$	Defined by
$\langle X \rangle$	Intrinsic average of X
$\times$	Vector product
Δ	Difference
$\|X\|$	Euclidean norm of the vector X

Abbreviations

Symbol	Description
1D	One Dimensional
2D	Two Dimensional
3D	Three Dimensional
AMG	Algebraic MultiGrid
BBO	Basset Boussinesq Oseen
CFD	Computational Fluid Dynamics
DNS	Direct Numerical Simulation
GCBA	Geometric Conservation Based Algorithm
HPE	High Pressure with Entrainment
HPNE	High Pressure with No Entrainment
LES	Large Eddy Simulation
LP	Low Pressure
MCBA	Mass Conservation Based Algorithm
NGL	Natural Gas Liquids

Symbol	Description
PDF	Probability Density Function
RANS	Reynolds Averaged Navier-Stokes
RMS	Root Mean Square
SAM	Simple Algebraic Model
SIMPLE	Simple Implicit Method for Pressure-Linked Equation
TKE	Turbulent Kinetic Energy
TETUSDIP	Transport Equations for the TUrbulent Stresses of the DIspersed Phase
UDF	User Defined Function
i.d.	Inner diameter
l.h.s	Left hand side
r.h.s	Right hand side

Chapter 1

Introduction

1.1 Natural gas

The use of natural gas. [1]Natural gas is an energy source that can be used both at home (cooking , heating) and in the industry. The production of certain liquid fuels uses natural gas as a raw material. Natural gas is also used for the production of electricity, pulp and paper, metals, chemicals, stone, clay, glass, and to process certain foods or treat waste materials.

What is natural gas? Natural gas is a combustible mixture of hydrocarbons. Its composition varies a lot depending on the gas deposit but it is mainly methane. A typical composition of natural gas is given in Table 1.1. The components can be either in a gas phase or in a liquid phase (condensate). Even methane can be substantially in a liquid form if the pressure is high.

[1]This paragraph is based on source:[199].

Methane CH_4	70-90%
Ethane C_2H_6	0-20%
Propane C_3H_8	
Butane C_4H_{10}	
Carbon Dioxide CO_2	0-8%
Oxygen O_2	0-0.2%
Nitrogen N_2	0-5%
Hydrogen sulphide H_2S	0-5%
Rare gases Ar, He, Ne, Xe	trace

Table 1.1: Typical composition of natural gas [215]

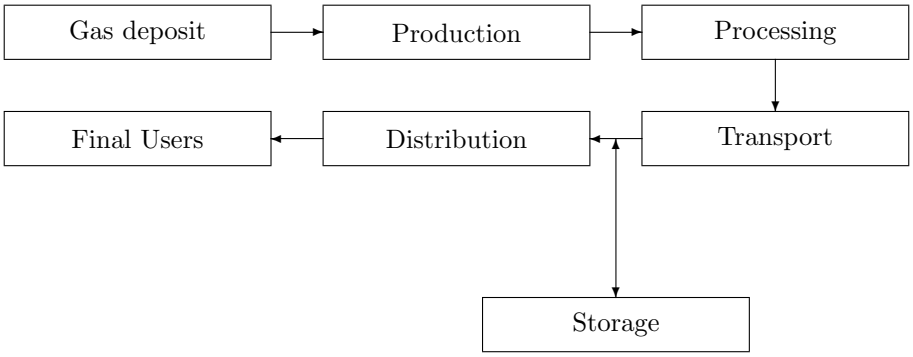

Figure 1.1: The natural gas chain

Natural gas chain. [2]Figure 1.1 shows a very simple diagram of the natural gas chain. During the production phase, the gas is extracted from the gas deposit and the flow ends up in a processing facility. Processing will be detailed further. Next is the transport that brings the gas to consumption regions, generally by pipelines. The gas may then be stored. Storage is necessary because the demand of natural gas varies during the year (higher in winter for heating). The distribution is similar to the transport step. However, smaller amounts of gas are carried and the distances are shorter.

1.2 Natural gas processing

[3]Processing is necessary because raw gas is very different from the gas sold to the market which is almost pure methane. Raw natural gas is found in two forms:

- Associated gas. It comes from oil wells, and can be either free gas or dissolved in the oil.
- Non-associated gas. It comes from pure gas wells or condensate wells. The latter produces, in addition to the gas, a semi-liquid hydrocarbon condensate.

The processing operation can be divided into four main steps:

- Oil and Condensate Removal.

[2]This paragraph is based on source:[199].
[3]This paragraph is based on source:[133].

- Water Removal.
- Separation of Natural Gas Liquids.
- Sulfur Removal.

Oil and Condensate Removal. Large amount of gas can be dissolved in the oil at high pressure. Generally, this gas separates from the liquid phase on its own when the pressure decreases. The gas and the oil can then be separated by gravity in a tank.

Water Removal. Liquid water is easy to remove by basic separation techniques. Nevertheless, separating water vapor is more difficult. Usually this type of dehydratation is achieved by using chemicals with hydrophilic properties, namely glycols. This process takes place in a contactor. The gas is afterward separated from the glycol solution.

Separation of Natural Gas Liquids (NGL). In general NGLs (that is ethane, propane, butane, iso-butane, and natural gasoline) are separated by an absorption technique which is similar to water removal by glycols. Nonetheless glycols are here replaced by an absorbing oil.

Sulfur Removal. Gas containing significant amounts of sulfur is lethal to breathe. Moreover it is very corrosive. Again an absorption technique is used. One uses an amine solution which has a good affinity for sulfur. After this last step the gas is clean and ready to use.

1.3 Context of the present work

1.3.1 Need for a technological step in separation processes

[4]Recently there has been an increased interest in remote and small off-shore gas fields. For such sources to be cost effective, it requires a major step forward in processing technologies. A requirement is to perform major parts of the separation sub-sea at high pressure. This would avoid building expensive facilities on the shore, enhance the efficiency of separation processes and decrease the amount of water to be transported. In addition, working at high pressure will avoid the expensive recompression at the inlet of transport pipelines.

1.3.2 Today's situation

[5]

[4]This paragraph is based on source:[185].
[5]This paragraph is based on source:[185].

Poor efficiency of separation techniques. Separation techniques are, at present, not efficient enough. It implies numerous problems:

- Gas treating equipment does not function properly.
- The gas does not fulfill quality standards.
- Chemicals are entrained.
- Compressors (designed for gas only), break down.

All these points contribute to a substantial increase in costs.

High pressure separation. Today, it is difficult to achieve high pressure gas/liquid separation because the quantity of entrained liquid is larger than for lower pressures. A first cause of this entrainment is the decrease of surface tension with the pressure. This decrease causes the break-up of liquid layers flowing along the walls, leading to a high droplet content. The decrease of the surface tension with pressure implies also a small average droplet size. Particularly striking pictures of this phenomenon are given in Havelka *et al.* (2004) who studied the disintegration of jets of n-decane up to 100 bars. While at low pressure the disintegration follows a regular Rayleigh break-up, at high pressure the jet becomes a spray. Small droplets lack of inertia and are difficult to separate from the gas flow. A second cause of entrainment is the decrease of the liquid/gas density ratio with the pressure. For a natural gas/condensate flow at 92 bars, the liquid/gas density ratio is less than 5 (Austrheim (2006)). This leads to a reduced inertia of the droplets relative to the gas and consequently to separation difficulties.

Designing rules. Design rules for separators have, up to now, been very empirical. These rules are deduced from tests at pressures of the order of 1 bar with air and water. Therefore, designs can be inefficient in scrubbers in operation at high pressure with real fluids.

1.3.3 Identified gaps in high pressure separation technology

Fluid properties. Physical properties of fluids encountered in gas production are not predicted correctly over a sufficiently wide range of temperature and pressures. Most of the time studies have focused on pure components and very few studies have been performed on densities, surface tensions, and viscosities of real NGLs mixture. The thermodynamic properties and viscosities of real NGLs mixtures at high pressures have been studied by Ahrabi *et al.* (1989), Ahrabi *et al.* (1987) and Schmidt *et al.* (2004).

Flow measurements at high pressure. The experimental study of the flow occurring in high pressure separation devices is difficult. Building a high pressure facility is expensive and requires very strict security norms. There are nonetheless some work-around to simulate real conditions. One can use low surface tension fluids such as Exxsol D60[6] (25 mN/m against air instead of 73 mN/m for water). The use of SF_6 (70 kg/m^3) instead of air provides high gas densities. This has been done by Verlaan (1991). Austrheim (2005) performed measurements on the flow of real fluids at high pressure in a separation equipment. Such data are rare.

Models. The efficiency of a separating device in operation can hardly be predicted quantitatively. Present models are almost entirely based on empirical correlations and usually fail when extrapolated to high-pressure situations.

1.3.4 The purpose of this study

This work aims to develop a new model for a quantitative prediction of the efficiency of separation devices especially for high-pressure conditions.

1.3.5 The strategy

Meso-scale phenomena. To obtain a good accuracy of the model, a part of empiricism must be removed. This can be done by integrating mesoscale phenomena such as:

- The dispersion of liquid droplets in a turbulent flow.
- The deposition of these droplets on walls (forming a liquid film).
- The flow of this liquid film.
- The entrainment of droplets from this film.

These are the key physical phenomena to understand and quantify if one wants to predict accurately the efficiency of a separator.

A local model. Given the complexity of the geometries of separation components, there is no typical macro-scale (such as a diameter). To be able to apply the present model to the widest possible range of designs, it has to be based on a purely local description of separation mechanisms. However one will only consider cases where:

1. Deposition occurs on surfaces (not applicable to wires).
2. The liquid loading is small (dispersed flow).

[6] A dearomatized aliphatic hydrocarbon.

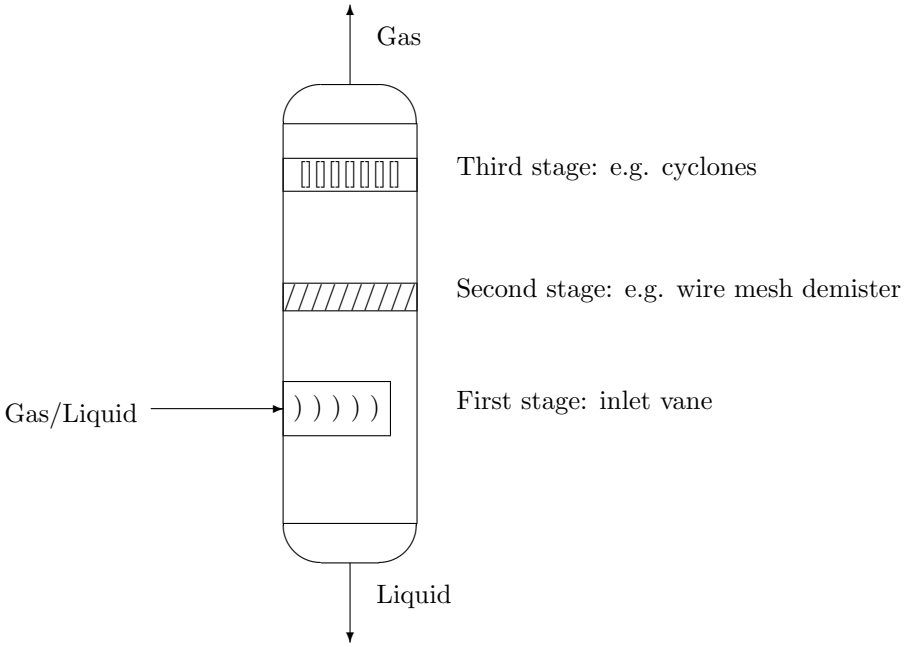

Figure 1.2: A typical scrubber configuration

3. Films are thin and wet perfectly the wall (no isolated drop on a wall, no rivulet or trickle).

Use of Computational Fluid Dynamics (CFD). CFD has been used and it is demonstrated to be a practical tool for the calculation of a fluid flow in a separator.

1.4 Scrubbers

General description. Scrubbers are tanks containing one or several demisting equipments. They are used to separate glycols or natural gas condensate from the gas. A simplified sketch of a scrubber is given in Figure 1.2.

The internals of a scrubber. The first stage of a scrubber (the inlet vane) has many possible designs. Some of them have been studied by Wehrli *et al.* (2003). Figure 1.3 shows a possible design for an inlet vane. The gas flow enters the internal by the square hole shown on the picture. As it flows forward into the device, the outer part of the gas stream is deviated by the curved plates into the scrubber core. The plates are placed closer and closer to the center plane of the inlet vane until eventually all the gas has been ejected out of the

Figure 1.3: An example of inlet vane design [32]

Figure 1.4: An industrial wire mesh demister [32]

device. Strictly speaking, this is not a separation equipment. Its function is to distribute the gas evenly over the whole section of the scrubber.
The most common second and third stages of separation are:

- Wire mesh demisters.
- Vane pack demister.
- Cyclones.

The mesh consists of knitted wires placed across the flow. It is a highly porous media (90% or more). Figures 1.4 and 1.5 show respectively an industrial wire mesh and its internal structure. The separation principle is that droplets are intercepted by wires, while the gas flows through the mesh.

A vane pack demister consists of parallel plates profiled with sharp bends as shown on Figure 1.6. The gas is diverted almost instantaneously after each

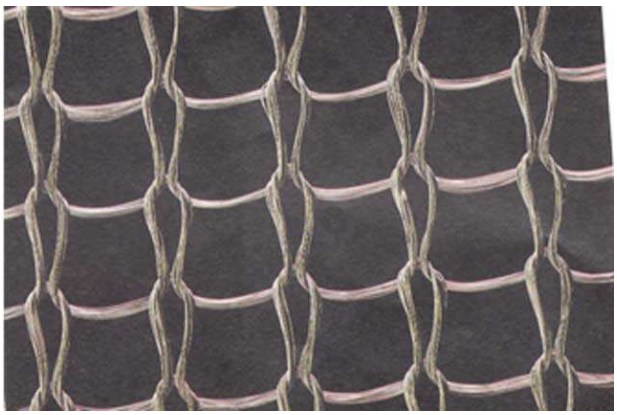

Figure 1.5: The structure of a wire mesh demister [74]

Figure 1.6: Details of a vane pack demister [158]

bend. By contrast, because of their inertia, the droplets impinge against the walls. Then, the liquid is collected through slits.

Finally, in cyclones, a tangential velocity is given to the gas. As a result of the centrifugal force, the droplets are deposited on the walls and collected. Figure 1.7 illustrates an example of an axial flow cyclone.

An in depth analysis of the previously cited internals can be found in Bürkholz (1989). It must be underlined that the above descriptions are how the internals should work and not how they really do work. That is why there are separation problems today. For example, recent studies of Austrheim (2005) showed that a significant amount of liquid can be re-entrained from the cyclone stage.

1.5 Selection of the flow solver

There are several ways to deal with the numerical solution of a given fluid flow. It is feasible to write a whole code from scratch, or we may use a multipurpose software, such as Matlab. Both options may be an interesting path for people focusing on discretization methods, algorithms for solving the Navier-Stokes equations or studying convergence acceleration. However, this is not the objective of this work. An other way is to use a software with an open code. Reference [105] usually presents an up to date list of links to such softwares. Nevertheless, the present flow challenges require the following from the software:

- ability to handle 3D geometries.
- ability to solve multiphase flows.
- ability to tackle complex geometries such as an inlet vane (unstructured grids).

When this study started we did not have an open-source code available that fulfilled these requirements. The last option is to use a standard commercial CFD code with a closed source. We chose this option, and the software Fluent was finally selected. Despite the drawbacks of not getting access to the source code, this software fulfilled the three previously cited demands. Moreover it was possible through User Defined Functions (UDF) to add subroutines to the main program. Recently, the former code FOAM was opened completely in a new release called Open Foam [138]. However it was then to late to make use of it for the present work.

1.6 Outline of the thesis

In part I we present a detailed analysis of the crucial physical phenomena occurring in a separation stage. Mathematical models and numerical representations are given. In part II we present the results of the simulations and discuss them.

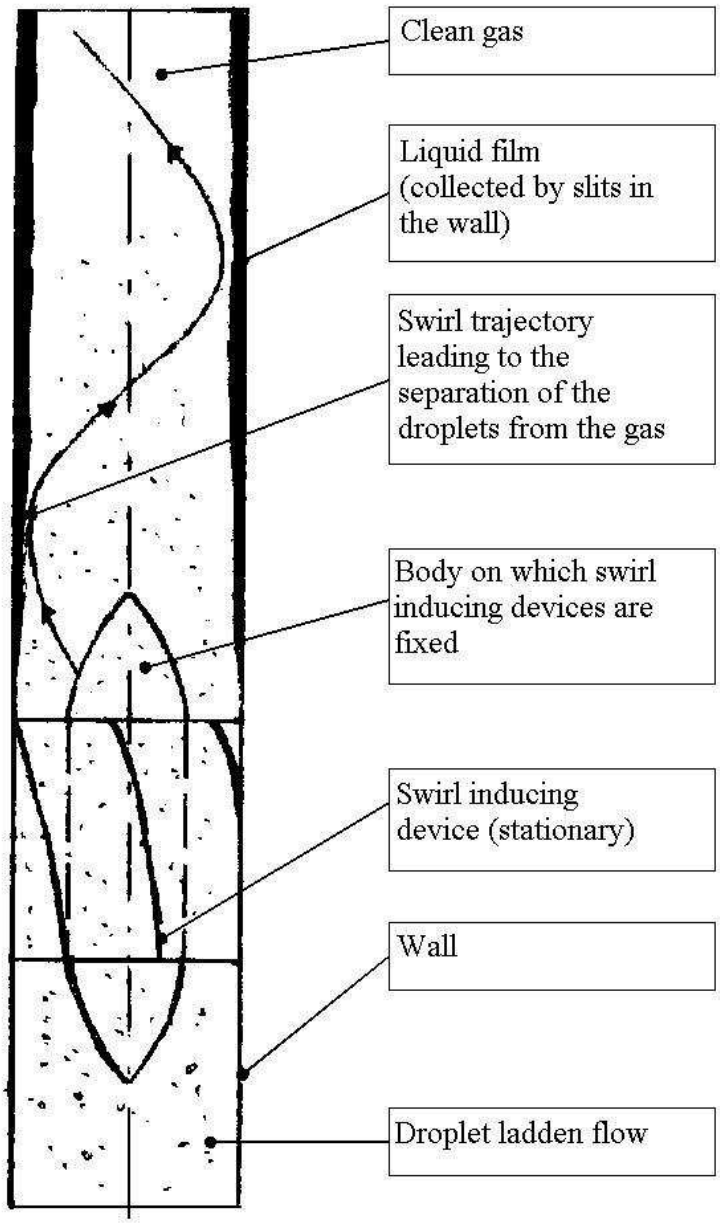

Figure 1.7: Inside view of an axial cyclone. After Verlaan (1991).

Part I

Theory

Outline of Part I

This part has three chapters. In the first we will describe the modeling of turbulent multiphase flows. The second chapter is more specifically about annular flows. Although this type of flow is not directly linked to separation equipments, some basic phenomena that are central to separation are occurring in annular flows. More precisely we have:

- The deposition of droplets on the walls
- The formation of a liquid film, due to the deposition of the droplets
- The flow of this film along the walls
- Re-entrainment of droplets from the film

The annular flow regime is also of general interest to the industry. In addition, this type of flow is likely to happen at the inlet of a scrubber, and it can thus be used as an inlet condition. Finally, experimental flow data are scarce for scrubbers, but there are numerous experiments on annular flows in pipes. Annular pipeflows are therefore good test cases for checking the validity of the model that is going to be presented. To close this theoretical part, the last chapter will present briefly the numerical methods that will be used for the calculations.

Chapter 2

Modeling of turbulent multiphase flows

2.1 Basic equations

We suppose that the fluid consists of continuous matter. It obeys the following equations:

- Conservation of mass
- Conservation of momentum

The mass conservation equation is:

$$\frac{\partial \rho}{\partial t} + \frac{\partial \left(\rho U_i\right)}{\partial X_i} = 0 \tag{2.1}$$

and the momentum conservation equation is:

$$\frac{\partial \left(\rho U_i\right)}{\partial t} + \frac{\partial \left(\rho U_i U_j\right)}{\partial X_j} = \frac{\partial \sigma_{ij}}{\partial X_j} + \rho g_i \tag{2.2}$$

where ρ, U_i, σ_{ij} and g_i are respectively the density, the velocity vector, the stress tensor and the gravity vector. Here and hereafter we will use Einstein's summation convention.
In addition only Newtonian fluids will be considered. Then the stress tensor is given by:

$$\sigma_{ij} = \left(-P + \lambda \frac{\partial U_k}{\partial X_k}\right) \delta_{ij} + \mu \left(\frac{\partial U_i}{\partial X_j} + \frac{\partial U_j}{\partial X_i}\right) \tag{2.3}$$

where P, λ, δ_{ij} and μ are the pressure, the bulk viscosity coefficient, the Kronecker symbol, and the viscosity of the fluid. As usually done we will assume the Stokes hypothesis to be valid:

$$\lambda + \frac{2}{3}\mu = 0 \tag{2.4}$$

and therefore:

$$\sigma_{ij} = -P\delta_{ij} + \mu\left(\frac{\partial U_i}{\partial X_j} + \frac{\partial U_j}{\partial X_i} - \frac{2}{3}\delta_{ij}\frac{\partial U_k}{\partial X_k}\right) \tag{2.5}$$

Finally the phases are considered incompressible. Doing so implies an important consequence for pressure. Indeed, in this case the pressure is totally decoupled from the density, and thereby loses its thermodynamical meaning.

2.2 Single phase turbulence

Pope (2000) made an up-to-date description of the different available turbulent modeling techniques (Direct Numerical Simulations (DNS), Large Eddy Simulations (LES), Reynolds Averaged Navier-Stokes models (RANS) and Probability Density Function models (PDF)). It is also worth to mention discrete vortex models. Crowe et al. (1996) described the possibilities of discrete vortex models for multiphase calculations. Because of their vast computational cost, DNS simulations are restricted to simple academic cases. LES and discrete vortex models are unsteady methods that still require too much computing power for a majority of industrial problems. PDF methods are currently not well developed in terms of algorithms and in terms of availability of codes. Hence, we will focus on the RANS models and more specifically on the k-ϵ model because of its widespread use in the industry.

2.2.1 k-ϵ model: the background

Jones and Launder (1972) developed the k-ϵ model. However, it is useful to review the essential assumptions and facts coming from earlier works on which the model is based. Reynolds was the first to derive (1894) the equations that govern the mean velocity field.

$$\frac{\partial \overline{U_i}}{\partial t} + \frac{\partial\left(\overline{U_i}\,\overline{U_j}\right)}{\partial X_j} = -\frac{1}{\rho}\frac{\partial \overline{P}}{\partial X_i} + \nu\frac{\partial^2}{\partial X_j \partial X_j}\overline{U_i} + g_i - \frac{\partial}{\partial X_j}\overline{U_i' U_j'} \tag{2.6}$$

where the overbar denotes the average of a quantity over an ensemble of samples, the prime denotes the fluctuation of this quantity and ν is the kinematic viscosity.
In equation (2.6) one can identify the crucial Reynolds stress term $-\frac{\partial}{\partial X_j}\overline{U_i' U_j'}$ that has to be modeled in the RANS approach. Boussinesq introduced the turbulent viscosity hypothesis. It is mathematically analogous to the stress-rate-of-strain relation for Newtonian fluids. He proposed the following relation:

$$-\overline{U_i' U_j'} + \frac{2}{3}k\delta_{ij} = \nu_T\left(\frac{\partial \overline{U_i}}{\partial X_j} + \frac{\partial \overline{U_j}}{\partial X_i} - \frac{2}{3}\delta_{ij}\frac{\partial \overline{U_k}}{\partial X_k}\right) \tag{2.7}$$

where k is the turbulent kinetic energy of the fluid and ν_T is the turbulent kinematic viscosity. The turbulent kinetic energy, is defined as:

$$k \equiv \frac{1}{2}\overline{U_i' U_i'} \tag{2.8}$$

In the k-ϵ model ν_T is specified as:

$$\nu_T = C_\mu \frac{k^2}{\epsilon} \tag{2.9}$$

where C_μ is one of the constant of the model. $C_\mu = 0.09$ is the usual value and comes from empirical observations. ϵ is the dissipation of turbulent kinetic energy and is defined as:

$$\epsilon \equiv 2\nu \overline{\left(\frac{1}{2}\left(\frac{\partial U_i'}{\partial X_j} + \frac{\partial U_j'}{\partial X_i} \right) \cdot \frac{1}{2}\left(\frac{\partial U_i'}{\partial X_j} + \frac{\partial U_j'}{\partial X_i} \right) \right)} \tag{2.10}$$

To have a complete model we now need relations for k and ϵ. Prandtl derived in 1945 the exact equation for the turbulent kinetic energy (see e.g. Tennekes and Lumley (1972)) :

$$\begin{aligned} & \frac{\partial k}{\partial t} + \frac{\partial \left(k\overline{U_i} \right)}{\partial X_i} \\ + \frac{\partial}{\partial X_i} & \left(\frac{1}{2}\overline{U_i' U_j' U_j'} + \frac{\overline{U_i' P'}}{\rho} - 2\nu \overline{\left(U_j' \cdot \frac{1}{2}\left(\frac{\partial U_i'}{\partial X_j} + \frac{\partial U_j'}{\partial X_i} \right) \right)} \right) \quad = \quad \mathcal{P} - \epsilon \end{aligned} \tag{2.11}$$

The third term on the l.h.s is a flux of turbulent kinetic energy. From now on, it will be noted $\mathcal{T}_i$. P' is the pressure fluctuation. $\mathcal{P}$ is the production of turbulent energy and is defined by:

$$\mathcal{P} \equiv -\overline{U_i' U_j'} \left(\frac{1}{2}\left(\frac{\partial \overline{U_i}}{\partial X_j} + \frac{\partial \overline{U_j}}{\partial X_i} \right) \right) \tag{2.12}$$

In a one equation model, Prandtl further proposed an algebraic relation for ϵ. He modeled the flux $\mathcal{T}_i$ with the gradient-diffusion hypothesis:

$$\mathcal{T}_i = -\frac{\nu_T}{\sigma^k} \frac{\partial k}{\partial X_i} \tag{2.13}$$

where σ^k is the turbulent Prandtl number. It is generally equal to 1.

2.2.2 The k-ϵ model

Prandtl suggested an algebraic relation for the dissipation requiring the specification of an unknown length-scale. To avoid specifying this length scale, the k-ϵ model uses a transport equation for ϵ.

$$\frac{\partial \epsilon}{\partial t} + \frac{\partial \left(\epsilon \overline{U_i} \right)}{\partial X_i} = \frac{\partial}{\partial X_i}\left(\frac{\nu_T}{\sigma^\epsilon} \frac{\partial \epsilon}{\partial X_i} \right) + C_{\epsilon 1} \frac{\mathcal{P}\epsilon}{k} - C_{\epsilon 2} \frac{\epsilon^2}{k} \tag{2.14}$$

Pope (2000) presents equation (2.14) as purely empirical. The standard values of the constants are based on simple flows, that is to say: decaying turbulence, homogeneous shear flow and the behavior of the log-law region in the boundary layer. Launder and Sharma (1974) proposed the following constants:

$$\sigma^{\epsilon} = 1.3 \quad C_{\epsilon 1} = 1.44 \quad C_{\epsilon 2} = 1.92 \tag{2.15}$$

Thus the k-ϵ model is a turbulence model that, in addition to the conservation equations of mass and momentum, solves two turbulent specific transport equations (2.11) and (2.14).

2.3 Multiphase modeling

2.3.1 What is a multiphase flow?

A phase is a state of macroscopic matter in which the chemical composition and physical properties are relatively uniform. A multiphase flow is the concurrent flow of two or more phases. Steam-water flows, air-water flows, gas-water-oil flows, or oil-water-hydrate flows are some examples of multiphase flows.

2.3.2 The three main classes of multiphase flow models

The flow regime is of importance when choosing a multiphase flow model. In a vertical evaporator for example, depending on the gas volume fraction, several flow patterns occur (Wallis (1969)): pure liquid, bubbly flow, slug flow, annular flow, droplet flow, and pure vapor (see Figure 2.1). In horizontal configurations, one can sometimes expect stratified flows.

Surface-tracking techniques. The conceptually simplest multiphase models are surface-tracking techniques, where the fluids are non-interpenetrating continua linked by interface conditions. Applications of these models can be stratified flows, free surface flows or motion of large bubbles. Frohn and Roth (2000) studied droplet-wall interactions with a surface-tracking technique. It is an interesting application for high pressure gas separation. They compared experimental results and simulations. Calculations were based either on the Navier-Stokes equations (volume of fluid) or on a Lattice-Boltzmann method.

Lagrange/Euler model. In case of a particle flow, one can consider the carrier fluid as a continuum while the dispersed phase is solved by tracking the particles, which can exchange mass, momentum and heat with the carrier phase. This is the so called Lagrange/Euler approach. The basics of this model can be found in Crowe et al. (1998).

Euler/Euler model. The Euler/Euler approach treats the different phases as interpenetrating continua. In this case the volume fractions are assumed to

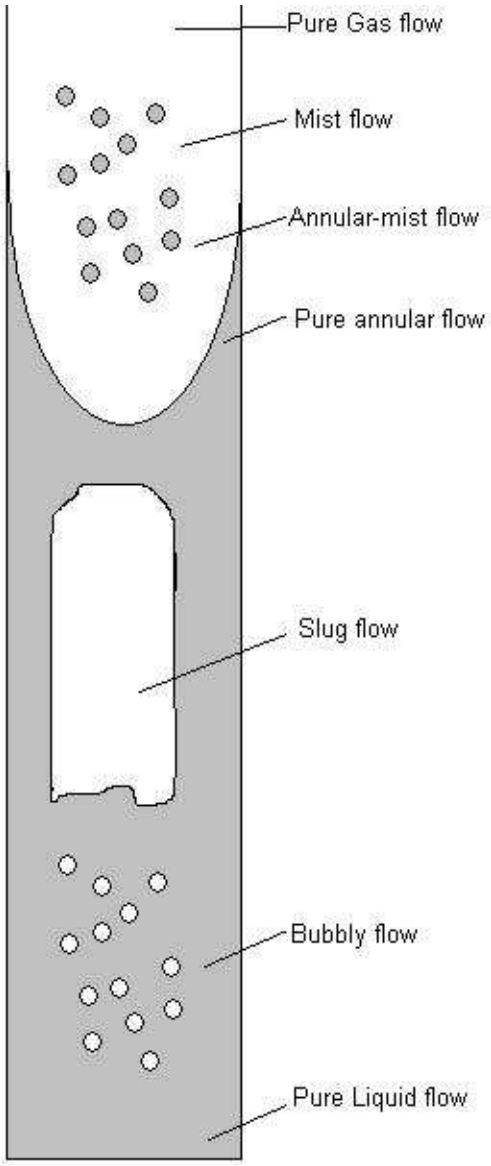

Figure 2.1: Different flow regimes in an evaporator

be continuous functions of space and time and their sum is equal to one. Ishii (1975) used this method to derive the two-fluid model.

Choice of a multiphase model. The interface-tracking techniques are out of question for our droplet laden flow. We further rejected Lagragian/Euler models, for two reasons:

1. In Lagrangian simulations, a very large number of trajectories must be calculated and then averaged to obtain quantities such as the particle velocities or their turbulent dispersion. Running a computation is therefore time-consuming.

2. It was difficult to handle quantitatively transfers between the dispersed droplets (Lagrangian) and the continuous film (Eulerian) with the flow solver that had been chosen (Fluent).

We chose an Euler/Euler model because it did not have these two drawbacks. However, even if Euler/Euler simulations are computed more rapidly, they require additional physical modeling efforts for their closure models. A recent description and comparison of the Lagrange/Euler and Euler/Euler approaches can be found in Mashayek and Pandya (2003) and in Gouesbet and Berlemont (1999).

2.3.3 The two-fluid model

To derive the two-fluid model, one can start from the local instantaneous conservation equations in each phase. Interface conditions are used as boundary conditions. These equations are then volume averaged giving averaged field equations. Here we will follow the method described by Soo (1989).

Volume averaging

Each phase κ is governed by its continuity equation (2.16) and its momentum equation (2.17)[1].

$$\frac{\partial \rho_\kappa}{\partial t} + \frac{\partial \left(\rho_\kappa U_{i\kappa}\right)}{\partial X_i} = 0 \tag{2.16}$$

$$\frac{\partial \left(\rho_\kappa U_{i\kappa}\right)}{\partial t} + \frac{\partial \left(\rho_\kappa U_{i\kappa} U_{j\kappa}\right)}{\partial X_j} = -\frac{\partial P_\kappa}{\partial X_i} + \frac{\partial \tau_{ij\kappa}}{\partial X_j} + \rho_\kappa g_i \tag{2.17}$$

where τ_{ij} is the viscous stress tensor.
Let us consider a control volume V bounded by a surface area A. V_κ is the volume of phase κ inside of V and A_κ is the area of the interface between phases κ and ϕ inside of V. At a given point belonging to A_κ, $n_{i\kappa}$ is the unit normal vector, outwardly directed. The displacement speed of the surface at

[1] The index κ means "related to the phase κ" and therefore the summation convention does not apply to it.

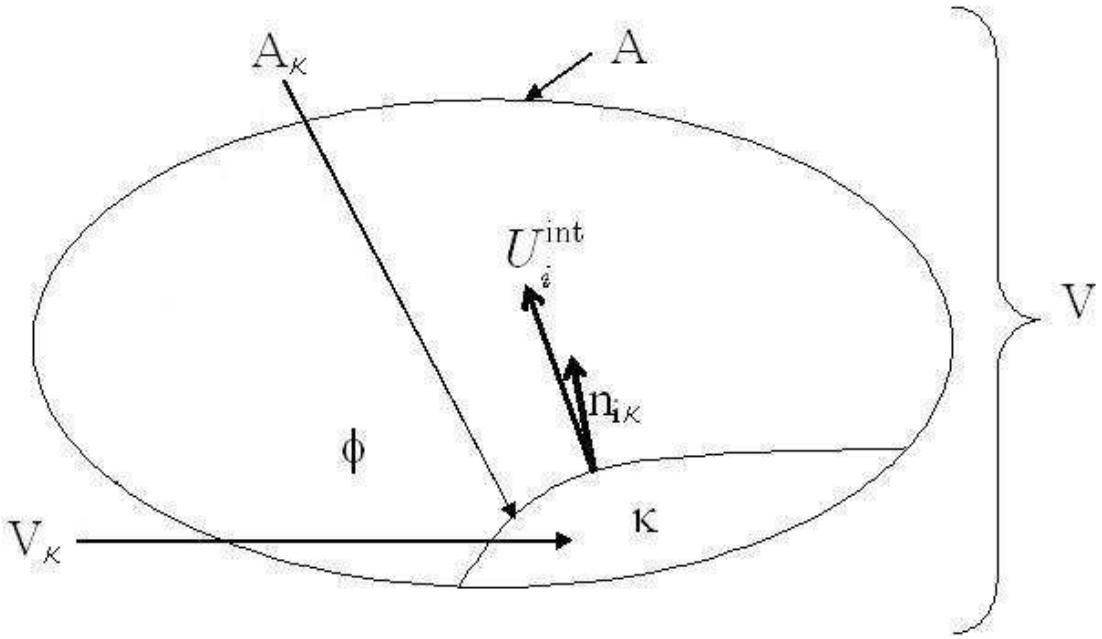

Figure 2.2: Considered control volume

that point is $U_i^{int} n_{i\kappa}$. The index *int* relates to the interface. See Figure 2.2. Let us now define the following operators:

- the extensive average operator:

$$\widehat{\ } = \frac{1}{V} \int_{V_\kappa} dV \tag{2.18}$$

- and the intrinsic average operator:

$$\langle\ \rangle = \frac{1}{V_\kappa} \int_{V_\kappa} dV \tag{2.19}$$

The volume fraction α_κ of the phase κ, is defined as:

$$\alpha_\kappa \equiv \frac{V_\kappa}{V} \tag{2.20}$$

As a result:

$$\widehat{\ } = \alpha_\kappa \langle\ \rangle \tag{2.21}$$

To perform the averaging of the continuity and Navier-Stokes equations we need the Reynolds transport theorem and the averaging theorems of Whitaker and

Slattery (Whitaker (1969)). Given ψ_κ, some property of the phase κ per unit volume, then:

$$\widehat{\frac{\partial \psi_\kappa}{\partial t}} = \frac{\partial \widehat{\psi_\kappa}}{\partial t} - \frac{1}{V}\int_{A_\kappa} \psi_\kappa U_i^{int} n_{i\kappa} dA \tag{2.22}$$

$$\widehat{\frac{\partial \psi_\kappa}{\partial X_i}} = \frac{\partial \widehat{\psi_\kappa}}{\partial X_i} + \frac{1}{V}\int_{A_\kappa} \psi_\kappa n_{i\kappa} dA \tag{2.23}$$

$$\widehat{\frac{\partial \psi_{i\kappa}}{\partial X_i}} = \frac{\partial \widehat{\psi_{i\kappa}}}{\partial X_i} + \frac{1}{V}\int_{A_\kappa} \psi_{i\kappa} n_{i\kappa} dA \tag{2.24}$$

If we apply the above theorems to equations (2.16) and (2.17) we obtain for the continuity:

$$\frac{\partial \widehat{\rho_\kappa}}{\partial t} + \frac{\partial \widehat{(\rho_\kappa U_{i\kappa})}}{\partial X_i} = \frac{1}{V}\int_{A_\kappa} \rho_\kappa \left(U_i^{int} - U_{i\kappa}\right) n_{i\kappa} dA \tag{2.25}$$

and for the Navier-Stokes equations:

$$\begin{aligned}\frac{\partial \widehat{(\rho_\kappa U_{i\kappa})}}{\partial t} + \frac{\partial \widehat{(\rho_\kappa U_{i\kappa} U_{j\kappa})}}{\partial X_j} &= -\frac{\partial \widehat{P_\kappa}}{\partial X_i} + \frac{\partial \widehat{\tau_{ij\kappa}}}{\partial X_j} + \widehat{\rho_\kappa} g_i \\ &+ \frac{1}{V}\int_{A_\kappa} \left(-P_\kappa \delta_{ij} + \tau_{ij\kappa}\right) n_{j\kappa} dA \\ &+ \frac{1}{V}\int_{A_\kappa} \rho_\kappa U_{i\kappa} \left(U_j^{int} - U_{j\kappa}\right) n_{j\kappa} dA \end{aligned} \tag{2.26}$$

The r.h.s term of equation (2.25) is the mass exchange rate for phase κ. If there is no mass transfer (i.e. no phase change), this term becomes zero and so does the last term of the r.h.s of the momentum equation (2.26).
As in the RANS models, a sub-averaging stress comes from the averaging of the convective term. Indeed:

$$\frac{\partial \widehat{(\rho_\kappa U_{i\kappa} U_{j\kappa})}}{\partial X_j} = \frac{\partial \left(\rho_\kappa \widehat{U_{i\kappa}} \widehat{U_{j\kappa}}\right)}{\partial X_j} + \frac{\partial \left(\rho_\kappa \widehat{U_{i\kappa}^\wedge U_{j\kappa}^\wedge}\right)}{\partial X_j} \tag{2.27}$$

where $U_{i\kappa}^\wedge \equiv U_{i\kappa} - \widehat{U_{i\kappa}}$. Crowe et al. (1996) pinpointed that no constitutive model is currently available and these extra stresses are neglected most of the time. Therefore we will assume them to be zero.
In the following, mass transfers between the two phases will not be considered. Then equation (2.25) can be written:

$$\frac{\partial\, \alpha_\kappa \langle \rho_\kappa \rangle}{\partial t} + \frac{\partial\, \alpha_\kappa \langle \rho_\kappa \rangle \langle U_{i\kappa} \rangle}{\partial X_i} = 0 \tag{2.28}$$

And equation (2.26) becomes:

$$\begin{aligned}\frac{\partial\,\alpha_\kappa\,\langle\rho_\kappa\rangle\,\langle U_{i\kappa}\rangle}{\partial t}+\frac{\partial\,\alpha_\kappa\,\langle\rho_\kappa\rangle\,\langle U_{i\kappa}\rangle\,\langle U_{j\kappa}\rangle}{\partial X_j} &= -\frac{\partial\,\alpha_\kappa\,\langle P_\kappa\rangle}{\partial X_i}+\frac{\partial\,\alpha_\kappa\,\langle\tau_{ij\kappa}\rangle}{\partial X_j}\\ &\quad+\alpha_\kappa\,\langle\rho_\kappa\rangle\,g_i\\ &\quad+\frac{1}{V}\int_{A_\kappa}\left(-P_\kappa\delta_{ij}+\tau_{ij\kappa}\right)n_{j\kappa}dA\end{aligned} \tag{2.29}$$

Here, the velocity is defined by $\langle\rho_\kappa U_{i\kappa}\rangle \equiv \langle\rho_\kappa\rangle\,\langle U_{i\kappa}\rangle$ (see Soo (1989)).

Pressure and viscous forces in a dispersed two phase flow

Prosperetti and Jones (1984) gave a derivation of the integral term in equation (2.29). They defined Π_κ and T_κ, the total pressure terms and the total viscous stress terms:

$$\Pi_\kappa \equiv -\frac{\partial\,\alpha_\kappa\,\langle P_\kappa\rangle}{\partial X_i}-\frac{1}{V}\int_{A_\kappa}P_\kappa n_{i\kappa}dA \tag{2.30}$$

$$T_\kappa \equiv \frac{\partial\,\alpha_\kappa\,\langle\tau_{ij\kappa}\rangle}{\partial X_j}+\frac{1}{V}\int_{A_\kappa}\tau_{ij\kappa}n_{j\kappa}dA \tag{2.31}$$

Let c be the index for the continuous phase and d the index for the dispersed phase. Prosperetti and Jones showed that

$$\Pi_c \approx -\alpha_c\frac{\partial\,\langle P_c\rangle}{\partial X_i}-\frac{1}{V}\sum_{part\,in\,V}F_P \tag{2.32}$$

$$\Pi_d \approx -\alpha_d\frac{\partial\,\langle P_c\rangle}{\partial X_i}+\frac{1}{V}\sum_{part\,in\,V}F_P \tag{2.33}$$

$$T_c \approx \alpha_c\frac{\partial\,\langle\tau_{ijc}\rangle}{\partial X_j}-\frac{1}{V}\sum_{part\,in\,V}F_V \tag{2.34}$$

$$T_d \approx \alpha_d\frac{\partial\,\langle\tau_{ijc}\rangle}{\partial X_j}+\frac{1}{V}\sum_{part\,in\,V}F_V \tag{2.35}$$

The limitations of these approximations are fully discussed in Prosperetti and Jones (1984). The first terms on the r.h.s of the above equations are due to buoyancy forces. The last terms represent the sum of the pressure forces (F_P) or viscous forces (F_V) exerted by the particles on the fluid, for instance drag or added mass forces. In equations (2.32) and (2.33) the pressure is the averaged continuous phase pressure. The same remark applies to the viscous stress tensor. As there is now no ambiguity, we will further drop the phase index for pressure, viscous stresses and consequently the viscosity.
The present model assumes:

$$\alpha_\kappa\frac{\partial\,\langle\tau_{ij}\rangle}{\partial X_j}\approx\frac{\partial}{\partial X_j}\left(\alpha_\kappa\mu\left(\frac{\partial\,\langle U_{ic}\rangle}{\partial X_j}+\frac{\partial\,\langle U_{jc}\rangle}{\partial X_i}-\frac{2}{3}\delta_{ij}\frac{\partial\,\langle U_{kc}\rangle}{\partial X_k}\right)\right) \tag{2.36}$$

The validity of equation (2.36) is studied in Ganesan and Poirier (1990) and Meland and Johansen (2002). To sum up, mass conservation is given by equation (2.28) and the momentum conservation is given by:

$$\begin{aligned} &\frac{\partial\, \alpha_\kappa \langle \rho_\kappa \rangle \langle U_{i\kappa} \rangle}{\partial t} \\ &+\frac{\partial\, \alpha_\kappa \langle \rho_\kappa \rangle \langle U_{i\kappa} \rangle \langle U_{j\kappa} \rangle}{\partial X_j} \quad = \quad -\alpha_\kappa \frac{\partial \langle P \rangle}{\partial X_i} \\ &\qquad \frac{\partial}{\partial X_j}\left(\alpha_\kappa \mu \left(\frac{\partial \langle U_{ic} \rangle}{\partial X_j} + \frac{\partial \langle U_{jc} \rangle}{\partial X_i} - \frac{2}{3}\delta_{ij}\frac{\partial \langle U_{kc} \rangle}{\partial X_k}\right)\right) \\ &\qquad +\alpha_\kappa \langle \rho_\kappa \rangle g_i \pm \frac{1}{V}\sum_{part\ in\ V}(F_P + F_V) \end{aligned} \tag{2.37}$$

The sign in front of the sum of the forces is positive if κ is the dispersed phase and negative otherwise. It remains to model the forces exerted by the fluid on the particles.

Forces on the dispersed phase

Particles are subjected to numerous forces. In the case of a large density of the particle phase relative to the carrier phase, it is reasonable to consider only the gravity force and the drag force[2]. In this case, the last term on the r.h.s of equation (2.37) is the drag force. The drag force exerted by the gas on one particle q is:

$$f_D(q) = \frac{1}{2}\rho_c C_D(q) A(q) \| \langle U_{ci} \rangle - U_i(q) \| \left(\langle U_{ci} \rangle - U_i(q)\right) \tag{2.38}$$

C_D is the drag coefficient and A the projection of the frontal area of the particle in the direction of the incoming flow. For N particles in the averaged volume, F_D, the total force per unit volume applied by the fluid on the particles, is:

$$F_D = \frac{1}{V}\sum_{q=1}^{N} f_D(q) \tag{2.39}$$

Stokes showed that for a steady creeping flow past a rigid sphere we have (see e.g. White (1991)):

$$C_D = \frac{24}{Re} \tag{2.40}$$

with the Reynolds number defined as:

$$Re \equiv \frac{\rho_c d(q)}{\mu} \| \langle U_{ci} \rangle - U_i(q) \| \tag{2.41}$$

[2]It may fail to assume a large ratio of the density of the particle phase to the density of the carrier phase. In a scrubber when the pressure increases, the densities of the gas and of the droplets converge toward the same value. Then the added mass force and the Basset force become important. In this case, one can use the Basset-Boussinesq-Oseen (B.B.O) equation (as described for example in Crowe *et al.* (1998)).

$d(q)$ being the diameter of the particle q. In case of a mono-dispersed flow, $d(q)$ is a constant d. It gives

$$F_D = \frac{18\,\mu\,\alpha_d}{d^2}\left(\langle U_{ci}\rangle - \langle U_{di}\rangle\right) \tag{2.42}$$

where $\langle U_{di}\rangle$ is by definition:

$$\langle U_{di}\rangle \equiv \frac{1}{N}\sum_{q=1}^{N} U_i(q) \tag{2.43}$$

Three problems remain:

- The flow is not a creeping flow.
- The particles are not spheres.
- The dispersed phase is not mono-dispersed.

One usually handles non-creeping flows by introducing a factor γ such as:

$$F_D = \gamma\frac{18\,\mu\,\alpha_d}{d^2}\left(\langle U_{ci}\rangle - \langle U_{di}\rangle\right) \tag{2.44}$$

and

$$\gamma = \frac{C_D(Re)}{24}Re \tag{2.45}$$

Equation (2.45) ensures the validity of relation (2.44) when $Re << 1$ ($\gamma \to 1$)[3]. The present model uses:

$$C_D = \begin{cases} 24(1 + 0.15\ Re^{0.687})/Re & Re \leq 1000 \\ 0.44 & Re > 1000 \end{cases} \tag{2.46}$$

This relation is inspired from Von Schiller and Naumann (1933). Another possible model is that of Morsi and Alexander (1972). Clift et al. (1978) discussed in details other sphere drag relations, their accuracies and ranges of validity.
If the particles are not spheres, one has to use a geometrical factor for the calculation of C_D and Re. Clift et al. (1978) presented a comparison of the drag of rigid spheres and that of water drops in air. As long as the Reynolds number was less than 1000, no significant difference in drag was noticed. However for a higher Re, due to the deformation of the droplets, the drag coefficient of the liquid particles was significantly higher than that of solid particles. In the present work the velocity differences between the droplet phase and the gas phase was small and $Re << 1000$. Consequently no significant deformation of the droplets

[3] In equations (2.45) and (2.46) the definition of the Reynolds number is:

$$Re \equiv \frac{\rho_c d}{\mu}\| \langle U_{ci}\rangle - \langle U_{di}\rangle \|$$

This definition is not identical to equation (2.41).

occurred and the particles were spheres.
Poly-dispersed flows are difficult to handle. Due to the averaging, the two-fluid model as such, is not able to deal with a particle size distribution. There are several methods available to solve this, such as:

- an additional transport equation for the interfacial area concentration ($m^2 \cdot m^{-3}$) (Kocamustafaogullari and Ishii (1995)).
- the use of a general multi-fluid model as proposed by Tomiyama and Shimada (2001) where droplets are divided into interacting classes, each class being a pseudo-phase.
- the quadrature method of moments that solves transport equations for the moments of the PDF of the size of the particles. Details on this technique can be found in Marchisio and Fox (2005).

The above cited methods are not tackled in this work but are a natural extension of it.
We now completely explained the two-fluid model in its general lines. The next section will deal with the combination of this multiphase-flow model with the k-ϵ model.

2.4 Multiphase turbulence

2.4.1 Preliminaries

To obtain the governing equations of a turbulent two-phase dispersed flow, the most straightforward approach would be to decompose the volume averaged velocities into a ensemble averaged part and a fluctuation as in the conventional Reynolds averaging (see Elghobashi and Abou-Arab (1983)).

$$\langle U_{\kappa i} \rangle = \overline{\langle U_{\kappa i} \rangle} + \langle U_{\kappa i} \rangle^{'} \tag{2.47}$$

If the continuity equation (2.28) and equation (2.47) are combined, it gives:

$$\frac{\partial\, \overline{\alpha_\kappa}}{\partial t} + \frac{\partial\, \overline{\alpha_\kappa} \overline{\langle U_{i\kappa} \rangle}}{\partial X_i} = -\frac{\partial\, \overline{\alpha_\kappa^{'} \langle U_{i\kappa} \rangle^{'}}}{\partial X_i} \tag{2.48}$$

The r.h.s term represents turbulent dispersion and requires modeling. Another type of averaging has been proposed, inspired by the work of Favre (1969). It uses a phase weighted average. For any arbitrary physical quantity ψ one defines:

$$\widetilde{\psi} \equiv \frac{\overline{\alpha\psi}}{\overline{\alpha}} \tag{2.49}$$

and

$$\psi^{''} \equiv \psi - \widetilde{\psi} \tag{2.50}$$

Then equation (2.28) becomes:

$$\frac{\partial\,\overline{\alpha_\kappa}}{\partial t}+\frac{\partial\,\overline{\alpha_\kappa}\widetilde{\langle U_{i\kappa}\rangle}}{\partial X_i}=0 \tag{2.51}$$

Conventional Reynolds decomposition leads to a large number of unknown fluctuation terms. Favre averaging, in contrast, considerably reduces the modeling work. However, Favre averaging complicates the comparisons with experimental data. If we use a momentum probe together with concentration measurements we can record the phase weighted velocity directly. With Particle Image Velocimetry all the relevant quantities can be extracted. Abou-Arab (1986) underlined that it is not simple to extract the phase weighted velocity when Laser Doppler Anemometry was used. In practice, it is common to compare directly the Favre averaged velocity with experimental values.

2.4.2 Momentum equation

If we now introduce the Favre averaging in the momentum equation (2.37), and take its ensemble average, it gives:

$$\begin{aligned}
&\frac{\partial\,\overline{\alpha_\kappa}\widetilde{\langle U_{i\kappa}\rangle}}{\partial t}\\
&+\frac{\partial\,\overline{\alpha_\kappa}\widetilde{\langle U_{i\kappa}\rangle}\widetilde{\langle U_{j\kappa}\rangle}}{\partial X_j}\\
&+\frac{\partial\,\overline{\alpha_\kappa}\widetilde{\langle U_{i\kappa}\rangle''\langle U_{j\kappa}\rangle''}}{\partial X_j} \;=\; -\frac{\overline{\alpha_\kappa}}{\rho_\kappa}\frac{\partial\overline{\langle P\rangle}}{\partial X_i}-\overline{\frac{\alpha'_\kappa}{\rho_\kappa}\frac{\partial\langle P\rangle'}{\partial X_i}}\\
&\qquad +\frac{\partial}{\partial X_j}\frac{\overline{\alpha_\kappa}}{\rho_\kappa}\mu\left(\widetilde{\frac{\partial\langle U_{ic}\rangle}{\partial X_j}}+\widetilde{\frac{\partial\langle U_{jc}\rangle}{\partial X_i}}-\frac{2}{3}\delta_{ij}\widetilde{\frac{\partial\langle U_{kc}\rangle}{\partial X_k}}\right)\\
&\qquad +\overline{\alpha_\kappa}g_i\pm\frac{1}{\rho_\kappa}\left(\widetilde{F_{Di}}+\overline{F''_{Di}}\right)
\end{aligned} \tag{2.52}$$

Let us study the unknown terms of this equation.

Reynolds stresses. As in equation (2.6), Reynolds stresses appear. Following the Boussinesq approximation it is natural to model the stresses of the continuous phase as:

$$-\widetilde{\langle U_{ic}\rangle''\langle U_{jc}\rangle''}+\frac{2}{3}k_c\delta_{ij} \;=\; \nu_{Tc}\left(\frac{\partial\widetilde{\langle U_{ic}\rangle}}{\partial X_j}+\frac{\partial\widetilde{\langle U_{jc}\rangle}}{\partial X_i}-\frac{2}{3}\delta_{ij}\frac{\partial\widetilde{\langle U_{kc}\rangle}}{\partial X_k}\right) \tag{2.53}$$

k_c is the turbulent kinetic energy of continuous phase. The modeling of ν_{Tc}, k_c and of the Reynolds stresses of the dispersed phase are discussed afterward.

Pressure-volume fraction correlation. The second term on the r.h.s of equation (2.52) is the pressure-volume fraction correlation. It is sometimes modeled, and sometimes neglected. Elghobashi and Abou-Arab (1983) and Johansen (1990) proposed expressions for it. As shown by Jakobsen (1993), its modeling remains difficult and relies on somewhat arbitrary assumptions. In addition there is no experimental data to validate the models currently available. Qualitatively, this term has a diffusion like effect. As its modeling still remains uncertain, it will be neglected, although in reality it is not necessarily negligible with respect to the other diffusion terms.

Viscous stress tensor. The third term on the r.h.s of equation (2.52) is the viscous stress term. Fluent evaluates it by:

$$\frac{\partial}{\partial X_j}\frac{\overline{\alpha_\kappa}}{\rho_\kappa}\mu\left(\frac{\partial\widetilde{\langle U_{ic}\rangle}}{\partial X_j}+\frac{\partial\widetilde{\langle U_{jc}\rangle}}{\partial X_i}-\frac{2}{3}\delta_{ij}\frac{\partial\widetilde{\langle U_{kc}\rangle}}{\partial X_k}\right)$$

(see Fluent (2005)). It is an approximation because the Favre average of the derivative of the velocity is not the derivative of the Favre averaged velocity.

Interaction terms. The last term on the r.h.s of equation (2.52) represents interactions between phases. It has two parts:

1. The mean drag force density:

$$\widetilde{F_{Di}}=\overline{\alpha_d}\beta\left(\widetilde{\langle U_{ic}\rangle}-\widetilde{\langle U_{id}\rangle}\right) \tag{2.54}$$

   where β is a momentum exchange coefficient defined according to equation (2.44) as:

$$\beta\equiv\gamma\frac{18\,\mu}{d^2} \tag{2.55}$$

2. The turbulent dispersion:

$$\overline{F''_{Di}}=\beta\overline{\langle U_{ic}\rangle''} \tag{2.56}$$

$\overline{F''_{Di}}$ represents the dispersion of the particles by the turbulent eddies of the continuous phase. Its modeling will be discussed later, together with the modeling of the Reynolds stresses of the dispersed phase.

The unknowns now remaining to model are:

- The turbulent viscosity of the gas phase
- The turbulent kinetic energy of the gas phase
- The turbulent dispersion
- The turbulent stresses of the dispersed phase

We will first tackle the problem of the turbulent quantities of the continuous phase. We saw Prandtl derived equation (2.11) for k for a single-phase flow. The derivation of a similar transport equation in a two-phase flow is particularly complex and gives rise to numerous extra unknown terms.

2.4.3 The extended k-ϵ model

The phenomenological point of view

The first attempts to extend the k-ϵ model to multiphase flows were based on modifications of the single-phase flow equations. It introduced a dispersed phase induced turbulence in addition to the continuous phase turbulence (see Kataoka and Serizawa (1989) and references therein). This type of modeling became quickly limited. First it had a narrow range of applicability because of relations relaying on experimental results. Second, two phase flow turbulence is not a simple sum of dispersed phase induced turbulence and continuous-phase turbulence. As a general rule, large particles tend to increase the turbulence level in the continuous phase while small particles tend to reduce the turbulence level in the continuous phase. This phenomenon is known as turbulence modulation.

Conservation equation of the turbulent energy

Deriving a conservation equation for TKE is a tedious work. Elghobashi and Abou-Arab (1983) did it from the volume-averaged equations presented by Soo (1967). As they did not use Favre averaging they ended up with an equation that had numerous terms requiring modeling. Kataoka and Serizawa (1989) used phase-weighted averaging and derived a TKE transport equation. It is worth noticing their starting point, based on a local formulation of a two phase flow based on the article of Kataoka (1986). Because of this starting point, the momentum equations slightly differed from equation (2.52) and Kataoka and Serizawa did not need volume averaging. However, their k transport equation was remarkably similar to equation (2.11):

$$\frac{\partial \overline{\alpha_\kappa} k_\kappa}{\partial t} + \frac{\partial \left(\overline{\alpha_\kappa} k_\kappa \widetilde{U_{j\kappa}} \right)}{\partial X_j} + \frac{\partial \mathcal{T}_{\kappa j}}{\partial X_j} = \overline{\alpha_\kappa} \left(\mathcal{P}_\kappa - \epsilon_\kappa \right) + \mathcal{I}_{k\kappa} \tag{2.57}$$

Equation (2.57) requires some comments:

- The definition of the turbulent energy is not the same in the paper of Elghobashi and Abou-Arab (1983) and in relation (2.57). In the former:

$$k_\kappa \equiv \frac{1}{2} \overline{\langle U_{i\kappa} \rangle' \langle U_{i\kappa} \rangle'} \tag{2.58}$$

  while in the latter:

$$k_\kappa \equiv \frac{1}{2} \widetilde{U''_{i\kappa} U''_{i\kappa}} \tag{2.59}$$

- $\mathcal{T}_{\kappa j}$ is a flux of k_κ. Its analytical expression is not tractable and will be modeled.
- $\mathcal{P}_\kappa$ transfers kinetic energy from the mean flow to the fluctuating velocity field.

$$\mathcal{P}_\kappa \equiv \widetilde{U''_{i\kappa} U''_{j\kappa}} \frac{\partial \widetilde{U_{i\kappa}}}{\partial X_j} \tag{2.60}$$

- As for the dissipation ϵ_κ its expression is:

$$\epsilon_\kappa \equiv \frac{1}{\rho_\kappa} \widetilde{\tau''_{ij\kappa} \frac{\partial U''_{i\kappa}}{\partial X_j}} \tag{2.61}$$

The very difference between (2.57) and (2.11) is the interaction term $\mathcal{I}_k$. It is mainly due to the interfacial drag force work. Other sources of exchange of TKE between the phases are detailed in Kataoka and Serizawa (1989). Several authors have derived an equation for the turbulent kinetic energy similar to relation (2.57). Hwang and Shen (1993) derived the TKE equation for a fluid-solid flow. Gillandt and Crowe (1998) proposed an equation for the TKE for a particle-fluid mixture from the volume averaged mechanical energy equation. They gave the following expression of $\mathcal{I}_{k\kappa}$ for a dilute flow:

$$\mathcal{I}_{kc} = -\mathcal{I}_{kd} = \frac{\overline{\alpha_d}\beta}{\rho_d} \| \langle U_{ic} \rangle - \langle U_{id} \rangle \|^2 \tag{2.62}$$

Since $\mathcal{I}_{kc} \geq 0$, according to equation (2.62), the interaction term can only result in an increase of the turbulent kinetic energy k_c. Nevertheless, as earlier mentioned, there is experimental evidence that the TKE of the continuous phase increases if large particles are carried and decreases if small particles are carried (Crowe (2000) and references therein). This was theoretically confirmed by Pourahmadi (1982). He showed that in a fluid-particle flow there was an extra dissipation term due to the interphase covariance $\widetilde{U''_{id} U''_{ic}}$. Crowe (2000) also suggested that the presence of particles in a turbulent flow modifies the turbulent dissipation length scale. If particles are small enough, this modification can lead to an increased dissipation rate of the TKE. The multiphase turbulent model presented here and used in this work is the model implemented in Fluent. This model does not account either for an extra dissipation term in the transport equation for k_c or for a modification of the turbulent dissipation length scale.
Like for single-phase flow turbulence, both Kataoka and Serizawa (1989) and Gillandt and Crowe (1998) proposed:

$$\mathcal{T}_{j\kappa} = -\frac{\nu_{T\kappa}}{\sigma_\kappa^k} \frac{\partial k_\kappa}{\partial X_j} \tag{2.63}$$

The turbulent viscosity is given by equation (2.9). The present model uses equations (2.62) and (2.63).
Note that equation (2.57) does not use volume averaged velocities whereas (2.51) and (2.52) do. As a result, mathematically speaking, we have a consistency problem. We chose to present the momentum equation using:

- Volume averaging for the multiphase model
- Ensemble averaging for the turbulence with a Favre averaging on certain quantities.

This approach is heuristic. Nevertheless, a consistent $k-\epsilon$ model using this method has not been derived. Drew and Passman (1998) presented a set of equations (continuity, momentum, energy and entropy inequality) using ensemble averaging for a multifluid model and gave a comprehensive mathematical discussion about the different possible averaging procedures. Their work may be a starting point to get a consistent model. However their closure relations for the turbulent Reynolds stresses are presented as a good guess. As the equations of Kataoka (1986) are similar to equations (2.51) and (2.52), using these latter relations together with (2.57) does not present practical problems.

Turbulent dissipation in a dispersed two-phase flow

The exact equation for ϵ_κ can also be derived and is formidable. This equation is related to processes at the Kolmogorov scale. Nevertheless Pope (2000) argued that, for a model equation, the dissipation is best viewed as the energy flow-rate in the energy-cascade and is hence determined by large scale motions. Hence, the exact equation cannot be a starting point. Usually by analogy with equation (2.14), and inspired by theory, one writes the dissipation equation as:

$$\frac{\partial \overline{\alpha_\kappa}\epsilon_\kappa}{\partial t}+\frac{\partial\left(\overline{\alpha_\kappa}\epsilon_\kappa\widetilde{U_{i\kappa}}\right)}{\partial X_i}=\frac{\partial}{\partial X_i}\left(\frac{\nu_{T\kappa}}{\sigma_\kappa^\epsilon}\frac{\partial\epsilon_\kappa}{\partial X_j}\right)+\overline{\alpha_\kappa}\frac{\epsilon_\kappa}{k_\kappa}\left(C_{\epsilon 1}\mathcal{P}_\kappa-C_{\epsilon 2}\epsilon_\kappa\right)+\mathcal{I}_{\epsilon\kappa} \quad (2.64)$$

$\mathcal{I}_\epsilon$ is the interchange of turbulent dissipation between the two phases. Elghobashi and Abou-Arab (1983) proposed:

$$\mathcal{I}_{\epsilon\kappa}=C_{\epsilon 3}\frac{\epsilon_\kappa}{k_\kappa}\mathcal{I}_{k\kappa} \quad (2.65)$$

They advised $C_{\epsilon 3}=1.2$. The present model uses equations (2.64) and (2.65) with $C_{\epsilon 3}=1.2$. We now have a complete set of equations describing a turbulent dispersed flow, by means of an extended k-ϵ model. Even if the turbulent equations (2.57) and (2.64) are meant to be valid for both the continuous and the dispersed phase, we will use it only for the continuous phase and perform a simpler closure for the dispersed phase that does not require the introduction of a turbulent dissipation and introduces an algebraic closure for the TKE.

2.4.4 Reynolds stresses and turbulent dispersion in the dispersed phase

In the momentum equation (2.52), two terms still ought to be modeled:

1. The Reynolds stresses in the dispersed phase: $\widetilde{\langle U_{id}\rangle''\langle U_{jd}\rangle''}$

2. The turbulent dispersion: $\beta\overline{\langle U_{ic}\rangle''}$

The latter is an extremely important term because it controls how the dispersed phase spreads out by turbulent agitation in the continuous phase. For example, in the case of a liquid film from which droplets are created, the turbulent dispersion will help the particles moving away from the vicinity of the wall and has thus an important impact on the entrained fraction. In the case of a jet breaking up at the center line of a pipe, the turbulent dispersion will transport particles toward the wall where they can possibly deposit. Thus the turbulent dispersion has a strong impact on the final deposited liquid fraction and is a key parameter in the simulation of a gas-liquid separator.

a) Modeling of the Reynolds stresses of the dispersed phase

In this section we will first give some experimental results that will lead us to discuss Tchen's theory of particle diffusion and the crossing trajectory effect. We will then discuss the modeling of the Reynolds stresses of the dispersed phase.

Experimental data. Lee (1987) measured the eddy diffusivity, and the turbulent intensities of droplets in a air/water vertical downward flow in a 2 inches i.d. pipe. He obtained the relation:

$$\sqrt{\overline{\langle U_{rd}\rangle''^2}} = \sqrt{\overline{\langle U_{rc}\rangle''^2}}\sqrt{\frac{\eta}{0.7+\eta}} \tag{2.66}$$

with

$$\eta = \frac{\tau_c}{\tau} \tag{2.67}$$

The index r relates to the radial component. η is the ratio of the Lagrangian integral time scale of the continuous phase τ_c to the characteristic relaxation time of the particles τ. τ_c is defined by

$$\tau_c(t) \equiv \int_0^{+\infty} \mathscr{R}_{Lc}(t,t')dt' \tag{2.68}$$

$\mathscr{R}_{Lc}$ is the normalized Lagrangian auto-correlation function of the continuous phase. $\mathscr{R}_{Lc}$ is independent of t if statistical stationarity is assumed. Let us define the turbulent time scale τ_c^*:

$$\tau_c^* \equiv \frac{\nu_{Tc}}{\frac{2}{3}k_c} = \frac{3}{2}C_\mu\frac{k_c}{\epsilon_c} \tag{2.69}$$

As a first guess one can model τ_c as:

$$\tau_c = \tau_c^* \tag{2.70}$$

As we will see later, τ_c can be dramatically reduced if there is a significant drift of the particles.
For the sake of simplicity, τ will be the Stokesian relaxation time:

$$\tau = \frac{\rho_d d^2}{18\mu} \tag{2.71}$$

When necessary, it can be corrected if the drag coefficient is outside the Stokes regime with:

$$\tau = \frac{\rho_d}{\beta} \tag{2.72}$$

β is the momentum exchange coefficient defined by equation (2.55).
Equation (2.66) has been used by Binder and Hanratty (1991) and Guha (1997) to correlate directly the Reynolds stresses in the dispersed phase to that of the continuous phase. The so called "Tchen's theory" about the diffusion of particles in homogeneous, isotropic, stationary turbulence, predicts an identical expression but with a value of 1 instead of 0.7.

Tchen's Theory. This theory will not be discussed in details here. Further pieces of information can be found in Hinze (1959). Starting from a particle undergoing a Stokes drag it is possible to give a relation between the fluctuating velocities of the dispersed phase v (in our case $\langle U_{id} \rangle''$), and that of the continuous phase u ($\langle U_{ic} \rangle''$):

$$\frac{dv}{dt} + \frac{v}{\tau} = \frac{u}{\tau} \tag{2.73}$$

One can express u and v by their Fourier integrals:

$$u = \int_0^{+\infty} (A\, cos(\omega t) + B\, sin(\omega t))\, d\omega \tag{2.74}$$

$$v = \int_0^{+\infty} (C\, cos(\omega t) + D\, sin(\omega t))\, d\omega \tag{2.75}$$

where $\omega = 2\pi f$ and f is the frequency of a given turbulent fluctuation. Replacing u and v in (2.73) by their Fourier integrals, leads to the following relations:

$$C = \left(1 - \frac{\tau^2\omega^2}{1+\tau^2\omega^2}\right) A - \frac{\tau\omega}{1+\tau^2\omega^2} B \tag{2.76}$$

$$D = \left(\frac{\tau\omega}{1+\tau^2\omega^2}\right) A + \left(1 - \frac{\tau^2\omega^2}{1+\tau^2\omega^2}\right) B \tag{2.77}$$

Tchen expressed then $\overline{u^2}$ and $\overline{v^2}$ two ways: first with the Lagrangian energy spectrum function $\mathscr{E}_L$:

$$\overline{u^2} = \int_0^{\infty} \mathscr{E}_{Lc}(f) df \tag{2.78}$$

$$\overline{v^2} = \int_0^{\infty} \mathscr{E}_{Ld}(f) df \tag{2.79}$$

and second as:

$$\overline{u^2} = \pi^2 \int_0^\infty \frac{A^2 + B^2}{T} df \tag{2.80}$$

$$\overline{v^2} = \pi^2 \int_0^\infty \frac{C^2 + D^2}{T} df \tag{2.81}$$

where T is an integral quantity with dimension time (Hinze (1959)). From equations (2.76), (2.77), (2.78), (2.79), (2.80), and (2.81) one deduces:

$$\frac{\mathscr{E}_{Ld}}{\mathscr{E}_{Lc}} = \frac{1}{1 + \tau^2\omega^2} \tag{2.82}$$

If we now express the Lagrangian energy spectrum function as a function of its Fourier transform $\mathscr{R}_{Lc}$ (the normalized Lagrangian auto-correlation function), we have the following relation between $\overline{v^2}$ and $\overline{u^2}$:

$$\overline{v^2} = \int_0^\infty \frac{\mathscr{E}_{Lc}(\omega)}{1 + \tau^2\omega^2} d\omega = \frac{2}{\pi} \overline{u^2} \int_0^\infty \int_0^\infty \frac{\mathscr{R}_{Lc}(t)\, cos(\omega t)}{1 + \tau^2\omega^2}\, dt d\omega \tag{2.83}$$

It remains now to find a proper representation of the Lagrangian normalized auto-correlation function. The Lagrangian nature of the function is a difficult point to handle. Indeed it is the velocity fluctuations encountered along the particle path that matters here and it can not be identified with the turbulent fluctuations along a fluid particle trajectory. One of the hypothesis of Tchen's theory is that during the motion of the particle the neighborhood of the particle is formed by the same fluid particles. If it is verified, the Eulerian and Lagrangian fluctuations are similar. However Hinze (1959) underlined that it is highly improbable given the great distortions underwent by a fluid particle in a turbulent flow. Reeks (1977) studied theoretically the motion of particles in isotropic turbulence under the action of a Stokesian drag force and gravity. In the absence of gravity, he plotted the particle mean square velocity as a function of τ. First he used the Lagrangian auto-correlation function. Second he replaced $\mathscr{R}_{Lc}$ by the Eulerian autocorrelation function $\mathscr{R}_{Ec}$. The results of Reeks show that, as a first approximation one can use:

$$\mathscr{R}_{Lc}(t) \approx \mathscr{R}_{Ec}(t) \tag{2.84}$$

If this approximation is made, $\mathscr{R}_{Ec}(t)$ needs to be modeled. A classical representation would be:

$$\mathscr{R}_{Ec}(t) = e^{-\frac{|t|}{\tau_c}} \tag{2.85}$$

It has the advantage of representing correctly the function $\mathscr{E}_{Ec}(\omega)$ in the inertial subrange (the Kolmogorov -5/3 spectrum)[4]. Putting back this relation in (2.83)

[4]Considerations on the derivative of $\mathscr{R}_{Ec}(t)$ at $t = 0$ and on the acceleration integral time scale implies that relation (2.85) must be rejected for theoretical reasons (Gouesbet and Berlemont (1999)). Gouesbet *et al.* (1984) studied the dispersion of particles with a more complex representation of the fluid auto-correlation function (two-parameter Frenkiel correlation functions). However for our purpose we will consider relation (2.85) as accurate enough.

gives:

$$\begin{aligned}\overline{v^2} &= \frac{2}{\pi}\overline{u^2}\int_0^\infty \frac{\tau_c}{(1+\tau^2\omega^2)(1+\tau_c^2\omega^2)}d\omega \\ &= \overline{u^2}\frac{\tau_c}{\tau_c+\tau} = \overline{u^2}\frac{\eta}{1+\eta}\end{aligned} \tag{2.86}$$

We thus obtained by theory a relation that is close to that found experimentally by Lee (1987) (equation (2.66)). Nevertheless in this theory an important effect called the "crossing trajectory effect" has not been included.

The crossing trajectory effect. This effect is important when particles have a significant drift (under the action of gravity for example). In this case, the velocity correlation drops more rapidly for the dispersed phase, than for the continuous one. As the residence time of a particle in an eddy becomes shorter, one can expect a drop of the dispersion coefficient. Csanady (1963) studied the diffusion of heavy particles in the atmosphere. These particles had a free falling speed due to gravitation that was normal to the main flow. They were also dispersed by the gas turbulence. Csanady proposed a new form of the normalized auto-correlation function of the particle phase, namely:

$$\mathscr{R}_p(t) = e^{-\frac{t}{l_c}\sqrt{V_{drift}^2+\left(\frac{l_c}{\tau_c^*}\right)^2}} \tag{2.87}$$

where V_{drift} is the drift velocity of the particles. l_c is a typical length scale of turbulence. As in Picart *et al.* (1986) and Simonin (1990) we can use the modeling:

$$l_c = \tau_c^*\sqrt{\frac{2}{3}k_c} \tag{2.88}$$

Taking into account the crossing trajectory effect implies that the relation (2.86) between $\overline{v^2}$ and $\overline{u^2}$ becomes:

$$\overline{v^2} = \overline{u^2}\frac{\eta'}{1+\eta'} \tag{2.89}$$

with

$$\eta' = \frac{\tau_c'}{\tau} \tag{2.90}$$

and

$$\tau_c' = \frac{\tau_c^*}{\sqrt{1+\frac{3V_{drift}^2}{2k_c}}} \tag{2.91}$$

Picart *et al.* (1986) showed that the crossing trajectory effect was important in order to reproduce experimental values of dispersion coefficients. A proof that the crossing trajectory effect may have an impact on the results of simulations is a comparison between the results of Young and Leeming (1997) and

Johansen (1991). Both described by similar methods the deposition of particles on vertical walls. Young and Leeming did not find any change on the deposition coefficient of the particles when changing from an upward to a downward configuration. In contrast, Johansen found an important impact of the gravity on the deposition rate. The difference between the two models was that Johansen took into account the crossing trajectory effect. Therefore it may have a direct impact on the deposition rate of droplets in a separator.

The turbulent viscosity hypothesis. To make the following clearer we will now drop the intrinsic average operator. The simplest way of modeling the Reynolds stresses of the dispersed phase $\widetilde{U''_{id}U''_{jd}}$ is to apply directly the Boussinesq approximation to the dispersed phase:

$$-\widetilde{U''_{id}U''_{jd}} = \nu_{Td}\left(\frac{\partial\widetilde{U_{id}}}{\partial X_j} + \frac{\partial\widetilde{U_{jd}}}{\partial X_i}\right) - \frac{2}{3}\left(k_d + \nu_{Td}\frac{\partial\widetilde{U_{kd}}}{\partial X_k}\right)\delta_{ij} \tag{2.92}$$

According to Tchen's theory and integrating in addition the crossing trajectory effect, the modeling of k_d is:

$$k_d = \frac{\eta'}{1+\eta'}k_c \tag{2.93}$$

It now remains to model the eddy viscosity of the particle phase ν_{Td}. Let us consider the eddy dispersion coefficient of the particles D_p:

$$D_p(t) = \widetilde{U''^{\,2}_{id}}\int_0^t \mathscr{R}_p(t')dt' \tag{2.94}$$

One can relate the eddy viscosity ν_{Td} to $D_p(+\infty)$. Then equations (2.87) and (2.88) lead to:

$$\nu_{Td} \approx D_p(+\infty) = \frac{\eta'}{1+\eta'}\nu_{Tc}\frac{1}{\sqrt{1+\frac{3V^2_{drift}}{2k_c}}} \tag{2.95}$$

Simonin and Viollet (1990) gave the eddy turbulent viscosity ν_{Td} has a function of the interphase covariance $\widetilde{U''_{id}U''_{ic}}$. This covariance was itself a function of the TKE k_c. If we neglect the added mass force and the correlation of the fluid-pressure fluctuation with the dispersed phase volume fraction, this model reduces to equation (2.95). Rizk and Elghobashi (1989) presented experimental evidences that the kinematic eddy viscosity of the dispersed phase is not equal to but proportional to the dispersion coefficient of the particles. They proposed:

$$\nu_{Td} \approx \frac{D_p(+\infty)}{0.67} \tag{2.96}$$

Pourahmadi and Humphrey (1983), Chung *et al.* (1986) presented other various correlations to express ν_{Td}. Crowe *et al.* (1996) underlined however that further comparisons with experimental data are necessary to validate present correlations.

Advanced models: transport equations of the turbulent stresses of the dispersed phase. Some authors used second order closure models to model the Reynolds stresses of the dispersed phase. Derevich and Zaichik (1988) presented a transport equation for the distribution function $p(X_d, U_d, t)$ of the particles in the phase space. Reeks (1991) also developed a transport equation for the particle phase space distribution. The integration of such an equation on the velocity space leads to the mass balance, the momentum equation and the Transport Equations of the TUrbulent Stresses of the DIspersed Phase (TETUSDIP). It is important to note that a full picture of the physical system is not obtained if one does not have a transport equation for the interphase covariance. This equation has been derived by Simonin *et al.* (1993). Presently all the TETUSDIP have been reported in a non-conservative form.
One can use the TETUSDIP directly or simplify them to get a model of the Reynolds stresses of the dispersed phase. Derevich and Zaichik (1988) and Slater *et al.* (2003) chose the latter option and provided a model for the Reynolds stresses of the dispersed phase by assuming an homogeneous stationary velocity field. It is a strong assumption. A weaker assumption would be to assume an homogeneous stationary fluctuating velocity field. Zaichik *et al.* (1997), Wang *et al.* (1998), Derevich (2000a, 2000b) and Yu *et al.* (2003) used the TETUSDIP directly. This approach is computationally very demanding. In addition, there is little evidence at present that a high closure level does increase accuracy. Slater *et al.* (2003) highlighted indeed that present particle turbulence modeling is too coarse and that it is unlikely that a significant improvement will be obtained by solving the particle stresses transport equations.

b) Modeling of the turbulent dispersion

We will now focus on the modeling of the turbulent dispersion:

$$\beta\overline{U_{ic}''}$$

It is a matter of algebra to show that:

$$\overline{U_{ic}''} = -\frac{\overline{\alpha_c' U_{ic}'}}{\overline{\alpha_c}} \tag{2.97}$$

Using the gradient diffusion hypothesis one can model the velocity-volume fraction correlation as:

$$\overline{\alpha_c' U_{ic}'} = -D_p(+\infty)\frac{\partial\overline{\alpha_c}}{\partial X_i} \tag{2.98}$$

Using equation (2.95), the turbulent dispersion can then be modeled by:

$$\beta\overline{U_{id}''} = \frac{\beta}{\overline{\alpha_c}}\frac{\eta'}{1+\eta'}\frac{\nu_{Tc}}{\sqrt{1+\frac{3V_{drift}^2}{2k_c}}}\frac{\partial\overline{\alpha_c}}{\partial X_i} \tag{2.99}$$

An adjustable parameter σ^{α_c} of the order of 1 is sometimes added and the model of the turbulent dispersion becomes:

$$\beta\overline{U''_{id}} = \frac{\beta}{\sigma^{\alpha_c}\overline{\alpha_c}}\frac{\eta'}{1+\eta'}\frac{\nu_{Tc}}{\sqrt{1+\frac{3V^2_{drift}}{2k_c}}}\frac{\partial\overline{\alpha_c}}{\partial X_i} \tag{2.100}$$

Johansen (1991), Young and Leeming (1997) and Slater *et al.* (2003) did not use this additional parameter ($\sigma^{\alpha_c} = 1$). Simonin (1990) and Rizk and Elghobashi (1989) chose $\sigma^{\alpha_c} = 0.67$. Fluent uses a value of 0.67. This value is not modifiable.

2.5 Summary

The modeling of turbulence in multi-phase systems is complex. The present model uses volume-averaged equations that are then ensemble averaged. The modeling of the turbulent dispersion, and of the turbulent stresses in the dispersed phase are two key points.
The transport equations of the model are:

- The continuity equations (2.51)
- The momentum equations (2.52)
- The TKE equation for the continuous phase (2.57)
- The dissipation equation of the continuous phase (2.64)

The key closure equations are:

- The Boussinesq equations (2.53) and (2.92)
- The modeling of the turbulent viscosities (2.9) and (2.95)
- The modeling of the TKE of the dispersed phase (2.93)
- The modeling of the turbulent dispersion (2.100)

Clearly the overall model should be able to provide an industrially applicable solution, but it is at the price of tremendous simplifications. In a nutshell, the presented set of equations is valuable but its limitations must be born in mind. Mass transfer and additional forces on particles such as added mass or lift forces require additional sophistications that are not straightforward.

Chapter 3

Annular flows

In this chapter we will first give a description of the physical phenomena occurring in annular flows. Then we will detail the equations of a "three fluid" model that can locally describe annular flows. Boundary conditions will be especially emphasized. Finally we will examine closure relations for:

- The interfacial gas/film shear stress
- The deposition rate
- The entrainment rate

3.1 Description of an annular flow

Definition

An annular flow is a special stable gas/liquid flow configuration. The gas is located in the center of the duct ("core"). The liquid flows in the form of a liquid film along the wall. Pure annular flows are rare in practice. The gas core often contains droplets, and the liquid film may contain bubbles. The liquid film is wavy as a general rule. Figure 3.1 shows a picture of an annular flow. One can see, the gas core, the wavy film and bubbles in the liquid film.

Key parameters

In the case of a separation device, there are two fundamental parameters:

- The volume fraction of droplets, which should be as small as possible after the separation.
- The pressure loss, which should be as small as possible to minimize recompression work downstream.

Figure 3.1: An annular flow [204]

The quantity of dispersed liquid depends on the balance of two processes. On the one hand, the droplets are impinging against the wall and form a liquid film. This process is the deposition. It decreases the volume fraction of droplets. On the other hand, under certain conditions, the film is highly deformed and can generate droplets. This process is the re-entrainment. Deposition and re-entrainment also increase the pressure drop. Lopes and Dukler (1986) and Fore and Dukler (1995a) presented theoretical and experimental evidences of the significant impact of droplet deposition and re-entrainment on the pressure drop. As a result sensible modeling of deposition and re-entrainment is a key to good prediction of liquid hold-up and pressure drop in a separator.

The liquid film

Re-entrainment is a very complex phenomena. It is local and highly non-linear. Figure 3.2 is a drawing after a real photography (Azzopardi and Gibbons (1983)) that shows the complex nature of re-entrainment. At present, there is no analytical models that can describe it. Re-entrainment is then calculated by means of empirical or semi-empirical correlations. All of these correlations are using the average liquid film thickness as a parameter. Consequently we will need a model for the film. The model should provide a good estimation of the height and of the velocity of the liquid layer. The so called "three-field " or "three-fluid" models are able to describe deposition, re-entrainment and the liquid film. It is this type of model that has been chosen in the present work.

Figure 3.2: Re-entrainment in an annular flow

3.2 Local three-fluid model of an annular flow

3.2.1 Literature study

The three-fluid model is a development of the two-fluid model. Instead of having a dispersed phase d and a continuous phase c, there are two continuous phases: the gas (indexed g) and the film (indexed f) and a dispersed phase (indexed d). Saito *et al.* (1978) are the first to use a three-fluid model to simulate an annular flow. The model was 1D. It could handle both adiabatic and diabatic flows. They also applied the concept to different geometries (annuli and rod arrays). Sugawara (1990) developed a similar model with different closure relations for the deposition, and the re-entrainment. Sugarawa and Miyamato (1990) presented a non-adiabatic axisymmetric code. Stevanovic and Studovic (1995) developed a 1D code with a new entrainment correlation. Fossa (1995) proposed a 1D model for flows with heat transfer outside thermal equilibrium that was able to handle smooth variation of pipe sections (diffusers and nozzles). Antal *et al.* (1998) were the first to adapt a three-fluid model on a local scale in 3D. It relied on experimental correlations originally developed for 1D flows. It is also interesting to pinpoint the attempt of Schmehl *et al.* (1999) who solved the gas and liquid phases in an Eulerian frame of reference and solved the dispersed phase with a Lagrangian tracking. The same approach was used recently by Adechy and Issa (2004) to calculate an annular flow through a T-junction. Ho Kee King and Piar (1999) studied the applicability of a three-field model in a converging nozzle. They compared their results with measured pressures and liquid film heights. They computed three cases:

- Pure annular flow (film and gas)
- Pure mist flow (droplets and gas)
- A model including the 3 phases

The latter gave the best results both for pressure gradients and film thicknesses. Kumar and Trabold (2000) compared the results of their three-fluid model with high-pressure (14 and 24 bars) experimental data of a refrigerant fluid. They had low surface tensions and high gas densities as in a scrubber. They observed a tendency for the droplets to have a velocity close to the overall mixture velocity. Their model was similar to the model of Antal *et al.* (1998). Yano *et al.* (2001) used a three-field model to calculate the flow around a fuel spacer in a boiling water reactor. Their geometry was axisymmetric but more complex than a pipe or an annulus. Alipchenkov *et al.* (2002a), Alipchenkov *et al.* (2002b), Antipin *et al.*(2003) and Alipchenkov *et al.* (2004) developed one of the most advanced three-fluid model. This model takes into account complex boundary conditions for the droplet phase (reflexion on the film or not) and calculates an average droplet size by means of break-up and coalescence models. Nevertheless it is a 1D model. Finally Jayanti and Valette (2004) presented a 1D model for high-pressure steam-water systems (up to 200 bars). They mainly focused on dryout, post-dryout and heat transfers.
This literature study showed that three-fluid models are well established for calculating annular flows. Only the models of Antal *et al.* (1998) and Kumar and Trabold (2000) dealt with 3D flows. However both works used a hydraulic diameter. As a result, these models are strictly limited to relatively simple geometries. An inlet-vane has no well defined hydraulic diameter. Consequently, there is a need for a model that can describe relevant processes without presupposing any type of geometry. This model must be purely local. Such a local model is presented in the next sections.

3.2.2 Governing equations

a) Continuity equations

Mass transfers because of phase changes are not considered. The only exchange of matter is a consequence of deposition and re-entrainment. According to equation (2.51) we have for the gas:

$$\frac{\partial\ \rho_g\overline{\alpha_g}}{\partial t} + \frac{\partial\ \rho_g\overline{\alpha_g}\widetilde{U_{ig}}}{\partial X_i} = 0 \tag{3.1}$$

For the sake of clarity, the intrinsic averaging symbol is no longer reported. For the droplet phase and the liquid film:

$$\frac{\partial\ \rho_d\overline{\alpha_d}}{\partial t} + \frac{\partial\ \rho_d\overline{\alpha_d}\widetilde{U_{id}}}{\partial X_i} = -\widetilde{\dot{D}} + \widetilde{\dot{E}} \tag{3.2}$$

$$\frac{\partial\ \rho_d\overline{\alpha_f}}{\partial t} + \frac{\partial\ \rho_d\overline{\alpha_f}\widetilde{U_{if}}}{\partial X_i} = \widetilde{\dot{D}} - \widetilde{\dot{E}} \tag{3.3}$$

where $\widetilde{\dot{D}}$ and $\widetilde{\dot{E}}$ are respectively the average rate of deposition and of entrainment in $kg \cdot m^{-3} \cdot s^{-1}$.

b) Gas and droplets momentum equations

Equations. For the gas, from equation (2.52) and neglecting the pressure-volume fraction correlation, we can write:

$$\begin{aligned}\frac{\partial\ \rho_g\overline{\alpha_g}\widetilde{U_{ig}}}{\partial t}+\frac{\partial\ \rho_g\overline{\alpha_g}\widetilde{U_{ig}}\widetilde{U_{jg}}}{\partial X_j}&\\ +\frac{\partial\ \rho_g\overline{\alpha_g}\widetilde{U''_{ig}U''_{jg}}}{\partial X_j} &= -\overline{\alpha_g}\frac{\partial\overline{P}}{\partial X_i}+\frac{\partial}{\partial X_j}\overline{\alpha_g}\widetilde{\tau_{ij}}+\rho_g\overline{\alpha_g}g_i\\ &\quad -\widetilde{F_D}-\overline{F''_D}\end{aligned} \tag{3.4}$$

The main differences between single phase and multiphase turbulent flows are the mean drag and the turbulent dispersion term. The flow of the gas will also be changed by the presence of the liquid film but this will be integrated into the boundary conditions and not into the field equations.
For the droplets, the momentum equations are:

$$\begin{aligned}\frac{\partial\ \rho_d\overline{\alpha_d}\widetilde{U_{id}}}{\partial t}+\frac{\partial\ \rho_d\overline{\alpha_d}\widetilde{U_{id}}\widetilde{U_{jd}}}{\partial X_j}&\\ +\frac{\partial\ \rho_d\overline{\alpha_d}\widetilde{U''_{id}U''_{jd}}}{\partial X_j} &= -\overline{\alpha_d}\frac{\partial\overline{P}}{\partial X_i}+\frac{\partial}{\partial X_j}\overline{\alpha_d}\widetilde{\tau_{ij}}+\rho_d\overline{\alpha_d}g_i\\ &\quad +\widetilde{F_D}+\overline{F''_D}\\ &\quad -\widetilde{U_{id}\dot{D}}+\widetilde{C_i\dot{E}}\end{aligned} \tag{3.5}$$

The two last terms represent the sink of momentum due to deposition and the source of momentum due to re-entrainment. C_i is the velocity with which the droplets are leaving the liquid film.

Consequences of deposition and entrainment on the momentum balance. For long pipes, an equilibrium takes place between the rate of atomization and the rate of deposition.

$$\widetilde{\dot{D}}=-\widetilde{\dot{E}} \tag{3.6}$$

The last two terms of equation (3.5) can then be simplified as follows

$$-\widetilde{U_{id}\dot{D}}+\widetilde{C_i\dot{E}}=-\widetilde{(U_{id}-C_i)\,\dot{D}} \tag{3.7}$$

Usually $U_{id}-C_i >> 0$ which means that, in a developed flow, the net contribution of the entrainment and deposition terms is a strong sink of momentum. It has two important implications:

1. This loss of momentum increases the pressure gradient.
2. The droplets leaving the film are undergoing an acceleration.

There are experimental evidences that droplets are, as an average, impinging on the wall before they reach their terminal velocity. Indeed, Azzopardi and Teixeira (1994a), and Fore and Dukler (1995b) measured a difference of 20% between the local droplet velocity and the local gas velocity. In gas/solid flows, the particles reach their terminal velocity and the particle/gas velocity ratio is much closer to one (Tsuji *et al.* (1984)).
A priori, one could think that the momentum loss of the droplet phase is mainly transfered to the film. The liquid layer should then be accelerated. However, Fore and Dukler (1995a) showed that this is not the case. A possible explanation, is that, as a drop deposits, the film becomes turbulent (or increases its turbulent intensity) close to the impact point. Energy is then dissipated in heat or by wall friction. The overall results is that the momentum transfered by the droplet phase to the film phase does not accelerate the liquid layer substantially.

c) Equations for the film

The present model does not describe the velocity of the film by the mean of a transport equation. It uses assumptions that are simplifying the momentum equation of the film into a simple algebraic relation.

Effect of high pressure and high gas density on the liquid film. The equations of the liquid film can be simplified by using some experimental facts. Especially interesting is the question of whether the film is turbulent or laminar. Note that in this paragraph we will not consider the turbulence generated by the droplet impaction but only by the convection inside the film.
As a rule, in annular flows, the film should be considered as turbulent. Indeed Hewitt and Hall Taylor (1970) underlined the inability of a laminar model to predict the mass throughput of the film from its thickness and from pressure drop data. In contrast, assuming the universal turbulent velocity profile, leads to the correct mass throughput. More recently Vassalo (1999) used hot film anemometry to measure the velocity profile in the film of an annular flow in a rectangular channel. He found that for clear annular configurations (far from a churn flow) the velocity profile inside the film was similar to the law-of-the-wall. Consequently the film can be considered as laminar only if it is thin enough to be included in the viscous sub-layer. In addition, according to Hewitt and Hall Taylor (1970), good predictions depend on the non-disturbance by the interfacial waves of the region where gradients of velocities are strong (in the viscous zone). As a result for supposing a laminar film we must have:

1. A thin film, being characterized as fully inside the viscous sub-layer.
2. A relatively smooth film so that ripples do not disturb the film velocity profile.

In an industrial scrubber, the gas has got high densities. Jepson *et al.* (1989) studied the effect of gas properties on drops in annular flows. They performed air/water and helium/water tests. A reduction in gas density caused a lower

shear on the film and a reduced entrainment. On the contrary, at high pressures, one expects a higher droplet content and a thinner liquid film. High pressures also decrease the surface tension. Dallman *et al.* (1979) reported experiments made by Whalley and coworkers on 1,1,1-trichloroethane. 1,1,1-trichloroethane has got a surface tension of 0.029 N/m compare to 0.073 N/m for water (both against air at 20℃). They showed that atomization was easier for the 1,1,1-trichloroethane than for water. Therefore, if the surface tension is low, the droplet content is high and the film is thin. Finally Trabold *et al.* (1999) took high speed videos of an annular flow at high pressure (24 bars) in a rectangular channel. They watched the combined effect of low liquid/gas density ratio and low surface tension. The images showed a very thin film. Summing-up the above pieces of information, it seems that in a high pressure gas separator the film is likely to be thin.
Trabold *et al.* (1999) also noted small-amplitude waves on the liquid layer. Paras and Karabelas (1991) studied film properties in horizontal annular flows. They recorded smaller amplitudes of the waves on thin films than on large ones. Besides, they measured the *intensity* of the film thickness fluctuations. The intensity is the root-mean-square (RMS) of the film thickness fluctuations divided by the time-averaged film thickness and shows how strongly the film is disturbed by interfacial waves relatively to its height. The intensity was lowest when the film was thin (at high gas flow rates). Thus thin films seems to be smoother than thick films, even relative to their heights. Consequently experimental works show that the film in a scrubber is probably thin and rather smooth. Therefore, the film is likely to be well calculated with a laminar model.

Continuity equation for the film. If the film is thin, it is computed only in the first row of cells by the wall. Its height h, the deposition rate $\widetilde{\dot{D}}$ and the entrainment rate $\widetilde{\dot{E}}$ are non zero in these near wall cells. Let us consider a cell which has got a wall-boundary face of area A (see Figure 3.3). For a thin film the interface area can be approximate by A on the condition that:

- The film is thin compare to the size of the computational cell.

- The gradients of the interface equation are not too important in the directions parallel to the wall.

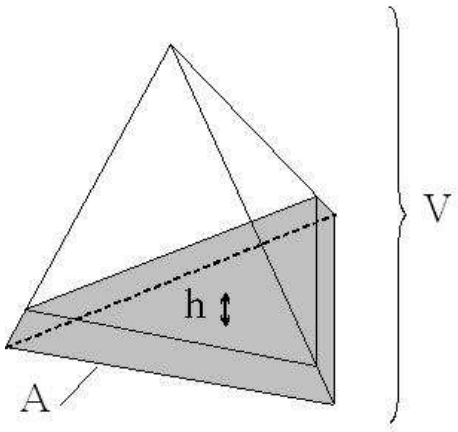

Figure 3.3: Thin film approximation

If these two conditions are verified[1], a mass balance on a film element gives in a local form :

$$\frac{\partial h}{\partial t} + \frac{\partial}{\partial X_i} h\, U_{if} = \frac{V}{\rho_f A}\left(\widetilde{\dot{D}} - \widetilde{\dot{E}}\right) \tag{3.8}$$

The velocity of the film will now be modeled.

Momentum equations for the film. The aim here is to get an approximate algebraic expression for the velocity of the film. First, one considers a new frame of reference. Let (x, y, z) be the position of a film particle. x is the coordinate along a vector Δ_i. Δ_i is defined by:

$$\Delta_i \equiv U_{g\,i,p} - U_{i,p}^{int} \tag{3.9}$$

$U_{gi,p}$ is the projection on the wall of the gas velocity of the near-wall cell. $U_{i,p}^{int}$ is the projection on the wall of the interface velocity. y is the coordinate normal to the wall. z is the position on a third axis such as (x, y, z) forms a right handed coordinate system. This coordinate system is pictured on Figure 3.4. To get a good estimation of the film velocity, the best is to start from the momentum equation of the film. To obtain a simple analytical solution we will do three assumptions.

[1]These conditions are necessary in order to derive the relation

$$\alpha_f \equiv \frac{V_f}{V} = \frac{h \cdot A}{V}$$

If these conditions are not verified, V_f, the volume of the film in the computational cell is depending on the geometry of the cell and on the geometry of the interface. In this case, there is no simple relation between the height of the film h, the area of the wall-boundary A and V_f and

$$V_f \neq h \cdot A.$$

It is then necessary to express the continuity equation of the film in terms of the volume fraction α_f and not in terms of h.

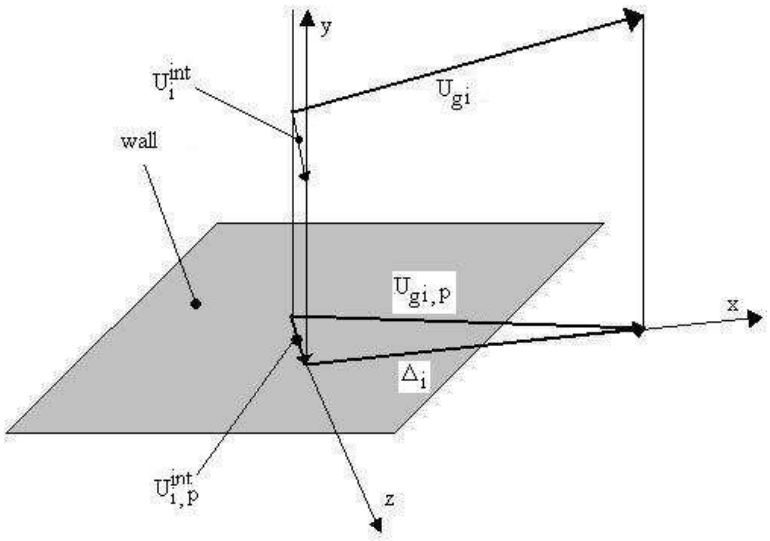

Figure 3.4: Coordinate system for the film

1. The film is steady.
2. Gradients in the x and z directions are zero.
3. The wall normal velocity is zero.

If the film is 2D, gradients in the y direction are infinite compare to gradients in the other directions. It justifies assumption 2 (Therefore the gradients of the interface equation are negligible in the directions parallel to the wall and the area of deposition can be identified with the wall area). Hypothesis 3 comes from the 2D assumption as well. The velocity of the liquid layer depends only on y. In the new coordinate system, the velocity vector of the film can then be written:

$$\begin{pmatrix} u(y) \\ v(y) = 0 \\ w(y) \end{pmatrix} \tag{3.10}$$

In addition we know that:

- The liquid layer gains momentum through deposition, the resulting acceleration is:

$$\widetilde{\dot{D}} \frac{V}{hA} \frac{u_d}{\rho_f} \tag{3.11}$$

u_d is the velocity of the droplet in the new coordinate system. $\widetilde{\dot{D}}$ is given per volume of computational cell. However here we consider the volume of film in a computational cell (hA). This is why the ratio $V/(hA)$ is necessary. The above formula is for the x direction. In the z direction, u_d

is replaced by w_d. It is worth noticing that the transfer of momentum from the droplet phase to the liquid layer happens first at the interface of the film. Then, the transfered momentum diffuses inside the liquid layer due to molecular and turbulent diffusion. The acceleration given by equation (3.11) assumes that the momentum transfered from the droplet phase to the film phase diffuses instantaneously through the whole thickness of the liquid film.

- There is a sink of momentum due to entrainment. One can write for the x direction a sink of the form:

$$\widetilde{\dot{E}}\frac{V}{hA}\frac{c_x}{\rho_f} \tag{3.12}$$

where c_x is the velocity at which the droplets leave the film in the x direction. Here as well, equation (3.12) assumes an instantaneous redistribution of the momentum inside the liquid layer.

Besides, as we previously discussed, there are indications that the film is turbulent although the turbulence is not generated by convective terms but by the impact of the droplets. With the above assumptions and pieces of information, the momentum conservation equation in the x direction can be written:

$$0 = -\frac{1}{\rho_f}\frac{\partial P}{\partial x} + \nu\frac{\partial^2 \overline{u}}{\partial y^2} + g_x + \frac{V}{\rho_f hA}\left(\widetilde{\dot{D}}u_d - \widetilde{\dot{E}}c_x\right) - \frac{\partial \overline{u'v'}}{\partial y} \tag{3.13}$$

If we consider a purely hydrostatic case, along the axis x, in the gas phase we have:

$$\frac{\partial P}{\partial x} = \rho_g g_x \tag{3.14}$$

As a result $\frac{1}{\rho_f}\frac{\partial P}{\partial x}$ scales as $\frac{\rho_g}{\rho_f}g_x$. If $\rho_g << \rho_f$ the pressure term becomes negligible against the gravity term and the momentum equation along the x axis becomes:

$$0 = \nu\frac{\partial^2 \overline{u}}{\partial y^2} + g_x + \frac{V}{\rho_f hA}\left(\widetilde{\dot{D}}u_d - \widetilde{\dot{E}}c_x\right) - \frac{\partial \overline{u'v'}}{\partial y} \tag{3.15}$$

Similarly along z:

$$0 = \nu\frac{\partial^2 \overline{w}}{\partial y^2} + g_z + \frac{V}{\rho_f hA}\left(\widetilde{\dot{D}}w_d - \widetilde{\dot{E}}c_z\right) - \frac{\partial \overline{v'w'}}{\partial y} \tag{3.16}$$

The equation along y does not give any velocity information (only pressure).

Turbulence modeling. We will use the standard turbulent viscosity hypothesis. It is the simplest choice but it is probably extremely rough. Indeed one can expect that an impinging droplet does not give raise to a shear flow but rather to a compression of the film. This is actually the exact case where the

turbulent viscosity hypothesis fails. Pope (2000) illustrated that in the case of the axisymmetric contraction of a turbulent flow, the turbulent fluid reacts more as an elastic solid than a viscous liquid. Nevertheless, for the sake of simplicity we will use the turbulent viscosity hypothesis, being aware that it is very crude. The turbulent viscosity due to deposition must be somehow related to the deposition flux $\widetilde{\dot{D}}V/A$ and a penetration length scale. If the film is very thin, the penetration length is likely to be the height of the film. As a result we will model the turbulent viscosity as:

$$\mu_{Tf} = \widetilde{\dot{D}}\frac{V}{A}h \tag{3.17}$$

One can notice that in this case the turbulent viscosity is a constant throughout the liquid layer. Therefore we get simply:

$$0 = \nu_{tot}\frac{\partial^2 \overline{u}}{\partial y^2} + g_x + \frac{V}{\rho_f h A}\left(\widetilde{\dot{D}}u_d - \widetilde{\dot{E}}c_x\right) \tag{3.18}$$

and

$$0 = \nu_{tot}\frac{\partial^2 \overline{w}}{\partial y^2} + g_z + \frac{V}{\rho_f h A}\left(\widetilde{\dot{D}}w_d - \widetilde{\dot{E}}c_z\right) \tag{3.19}$$

with

$$\nu_{tot} \equiv \nu + \nu_{Tf} \tag{3.20}$$

It is important to note that ν_{Tf} is not depending on y in the present model. The validity of this model will be discussed in chapters 6 and 7.

Boundary conditions at the film/gas interface. Delhaye (1974) derived all the jump conditions (mass, momentum, energy and entropy) across an interface. For momentum, it is:

$$n_{fj}\ \sigma_{fij}|_{y=h} + n_{gj}\ \sigma_{gij}|_{y=h} + \frac{\Sigma}{R}n_{fi} = 0 \tag{3.21}$$

There is no summation on the f index (film) and on the g index (gas). Σ is the surface tension and R the radius of curvature of the interface. Let us notice that momentum transfers due to entrainment and deposition through the interface are not taken into account because they are already included in the momentum equations. Moreover, since the gradients in the x and z direction are neglected, there is no Marangoni effect. Given $h = I(x,z)$ the equation of the interface, the expression of the radius of curvature is:

$$\frac{1}{R} = \frac{\frac{\partial^2 I}{\partial x^2}\left(1+\left(\frac{\partial I}{\partial z}\right)^2\right) - 2\frac{\partial I}{\partial x}\frac{\partial I}{\partial z}\frac{\partial^2 I}{\partial x \partial z} + \frac{\partial^2 I}{\partial z^2}\left(1+\left(\frac{\partial I}{\partial x}\right)^2\right)}{\left(1+\left(\frac{\partial I}{\partial x}\right)^2+\left(\frac{\partial I}{\partial z}\right)^2\right)^{\frac{3}{2}}} \tag{3.22}$$

It leads to $1/R = 0$ when the x and z gradients are zero. As a result, surface tension effects are negligible. The normal vectors are given by:

$$n_{fj} = -n_{gj} = \frac{1}{\left(1 + \left(\frac{\partial I}{\partial x}\right)^2 + \left(\frac{\partial I}{\partial z}\right)^2\right)} \begin{pmatrix} -\frac{\partial I}{\partial x} \\ 1 \\ -\frac{\partial I}{\partial z} \end{pmatrix} \tag{3.23}$$

and neglecting the x, and z gradients, it reduces to:

$$n_{fj} = -n_{gj} = \begin{pmatrix} 0 \\ 1 \\ 0 \end{pmatrix} \tag{3.24}$$

That is to say, we have a flat film parallel to the wall. Thus the interface velocity is parallel to the wall and $U_{i,p}^{int} = U_i^{int}$ (Figure 3.4). As for the stress tensor, our film behaves exactly as a laminar fluid of viscosity μ_{tot}. Using the Newtonian fluid hypothesis (2.3), we have on the liquid side:

$$\sigma_{fxy}|_{y=h} = \sigma_{fyx}|_{y=h} = \mu_{tot} \left.\frac{\partial \overline{u}}{\partial y}\right|_{y=h} \tag{3.25}$$

$$\sigma_{fyz}|_{y=h} = \sigma_{fzy}|_{y=h} = \mu_{tot} \left.\frac{\partial \overline{w}}{\partial y}\right|_{y=h} \tag{3.26}$$

And on the gas side, because of the way that the reference frame (x, y, z) has been built:

$$\sigma_{gxy}|_{y=h} = \sigma_{gyx}|_{y=h} = \tau_i \tag{3.27}$$

$$\sigma_{gyz}|_{y=h} = \sigma_{gzy}|_{y=h} = 0 \tag{3.28}$$

where τ_i is the interfacial shear stress exerted by the gas on the film. Consequently the jump condition (3.21) leads to the following boundary conditions at the interface:

$$\mu_f \left.\frac{\partial \overline{u}}{\partial y}\right|_{y=h} = \tau_i \tag{3.29}$$

$$\left.\frac{\partial \overline{w}}{\partial y}\right|_{y=h} = 0 \tag{3.30}$$

Algebraic model for the velocity in the film. From (3.18), (3.19), (3.29) and (3.30), it is straightforward to show that:

$$\overline{u} = \frac{\rho_f g_x + \frac{V}{hA}\left(\widetilde{\dot{D}} u_d - \widetilde{\dot{E}} c_x\right)}{\mu_{tot}} \left(hy - \frac{y^2}{2}\right) + \frac{\tau_i}{\mu_{tot}} y \tag{3.31}$$

and

$$\overline{w} = \frac{\rho_f g_z + \frac{V}{hA}\left(\widetilde{\dot{D}} w_d - \widetilde{\dot{E}} c_z\right)}{\mu_{tot}} \left(hy - \frac{y^2}{2}\right) \tag{3.32}$$

We can note that we obtain a type of Poiseuille/Couette flow. Without the shear due to the gas, and the deposition/entrainment processes, we would have had the well-known solution of Nusselt (1916) for a gravity-driven film. Ruyer-Quil and Manneville (1998) showed that Nusselt's solution is a zeroth order approximation of the velocity. They developed first and second order models, for a film falling down an inclined plane. Four points remain in order to find the mean velocity of the film in the global reference frame (U_{if} in equation (3.8)):

- Averaging the velocity over the film thickness
- Finding a model for the velocity at which the droplets leave the film
- Expressing the film velocity and the velocity at which the droplets leave the film in the global coordinate system
- Expressing the droplet velocity in the local coordinate system

Averaging. Let us denote $\overline{u}_{avg}$ and $\overline{w}_{avg}$ the averaged values of the components of the film velocity over the film thickness.

$$\overline{u}_{avg} \equiv \frac{1}{h}\int_0^h \overline{u}dy = \frac{\rho_f g_x + \frac{V}{hA}\left(\widetilde{\dot{D}}u_d - \widetilde{\dot{E}}c_x\right)}{\mu_{tot}}\frac{h^2}{3} + \frac{\tau_i}{\mu_{tot}}\frac{h}{2} \tag{3.33}$$

and

$$\overline{w}_{avg} \equiv \frac{1}{h}\int_0^h \overline{w}dy = \frac{\rho_f g_z + \frac{V}{hA}\left(\widetilde{\dot{D}}w_d - \widetilde{\dot{E}}c_z\right)}{\mu_{tot}}\frac{h^2}{3} \tag{3.34}$$

Velocity at which the droplets leave the film. The velocity at which the droplets leave the film is denoted c_i. c_i will only take part in the loss of momentum by the film due to entrainment. Hence, its modeling does not need to be very advanced. A first guess is that c_i is the velocity of the film at the interface:

$$\begin{pmatrix} c_x \\ c_z \end{pmatrix} = \begin{pmatrix} \overline{u}(h) \\ \overline{w}(h) \end{pmatrix} \tag{3.35}$$

Together with equations (3.31) and (3.32) we get:

$$c_x = h\left(\frac{2\tau_i + \rho_f g_x h + \frac{V}{A}\widetilde{\dot{D}}u_d}{2\mu_{tot} + \frac{V}{A}\widetilde{\dot{E}}h}\right) \tag{3.36}$$

and

$$c_z = h\left(\frac{\rho_f g_z h + \frac{V}{A}\widetilde{\dot{D}}w_d}{2\mu_{tot} + \frac{V}{A}\widetilde{\dot{E}}h}\right) \tag{3.37}$$

Hewitt and Hall Taylor (1970) indicated that the velocity of the interface likely tends toward $2\overline{u}_{avg}$ at high gas flow rate. If all phenomena are neglected but

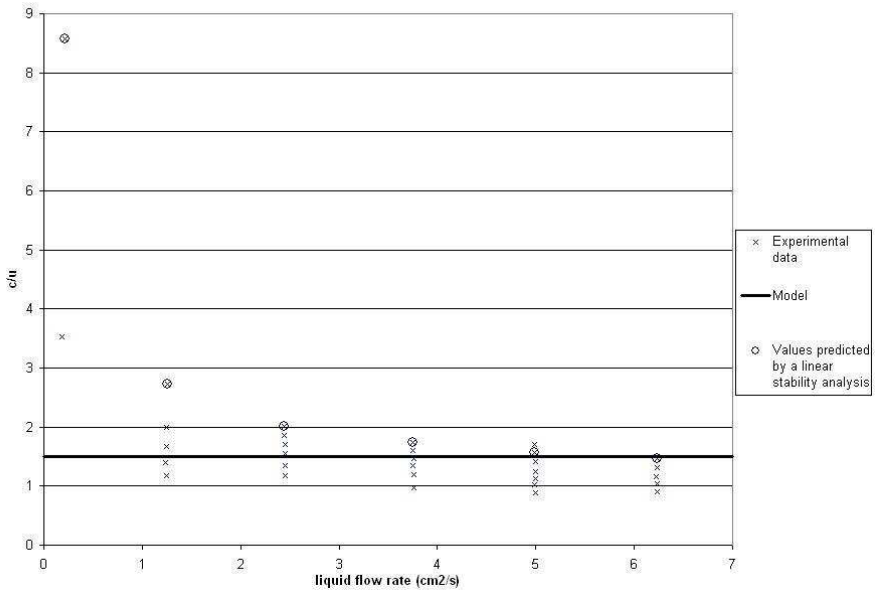

Figure 3.5: Celerity of the interface of a film falling in vacuum.

the gas shear stress on the liquid interface, one gets this results. Deposition and entrainment do not have a simple effect if taken into account. It is also interesting to consider the case of a film falling in vacuum. Figure 3.5 shows the ratio of the velocity of the interface to the average film velocity in such a case. On the graph there are the experimental data of Hewitt and Hall-Taylor (1970), the theoretical values of a model based on a linear stability analysis (see Hewitt and Hall Taylor), and the constant value of 3/2 predicted by the present model. 3/2 is a good estimation except at low liquid flow rates. The model for c_i is expected to be accurate except when the liquid flow rate is small and the interfacial shear stress is small. However in this case the entrainment rate is small and the loss of momentum of the film is negligible. Thus the accuracy of the model for calculating c_i is sufficient.

Change of coordinate system. Let us denote (n_{xi}, n_{yi}, n_{zi}) the coordinates of the orthonormal base of the coordinate system (x, y, z) expressed in the reference frame (X_i). n_{yi} is the normal to the wall and is known. n_{xi} is given by:

$$n_{xi} \equiv \frac{\Delta_i}{\|\Delta_i\|} = \frac{U_{gi} - (U_{gj} n_{yj})\, n_{yi} - C_i}{\|U_{gi} - (U_{gj} n_{yj})\, n_{yi} - C_i\|} \tag{3.38}$$

Lastly n_{zi} is given by:

$$n_{zi} \equiv n_{xi} \times n_{yi} \tag{3.39}$$

We can write U_{if} by means of a transformation matrix:

$$U_{if} = \begin{pmatrix} n_{x1} & n_{y1} & n_{z1} \\ n_{x2} & n_{y2} & n_{z2} \\ n_{x3} & n_{y3} & n_{z3} \end{pmatrix} \begin{pmatrix} \overline{u}_{avg} \\ 0 \\ \overline{w}_{avg} \end{pmatrix} \tag{3.40}$$

Or:

$$U_{if} = n_{xi}\overline{u}_{avg} + n_{zi}\overline{w}_{avg} \tag{3.41}$$

Similarly:

$$C_i = n_{xi}c_x + n_{zi}c_z \tag{3.42}$$

Let us note that n_{xi} is needed for the calculation of C_i and that C_i is needed for the calculation of n_{xi}. To solve this, n_{xi} can be calculated with the velocity of the interface at the previous iteration. For the droplet phase we have:

$$u_d = n_{xi}\widetilde{U_{id}} \tag{3.43}$$

$$w_d = n_{zi}\widetilde{U_{id}} \tag{3.44}$$

The model for the film is now complete.

Volume fraction in the cells by the wall. When the film is modeled by a transport equation for a scalar h, the relation:

$$\alpha_g + \alpha_d = 1 \tag{3.45}$$

is used by Fluent in the whole domain. This is not strictly true for cells having a wall boundary. In these cells the volume fraction of film is not zero. The relation between the volume fraction becomes:

$$\alpha_g + \alpha_d + \alpha_f = 1 \tag{3.46}$$

Nevertheless, in Fluent, it is the volume fraction of gas that is calculated by help of relation (3.45). Thus α_d is correct. In a scrubber, the liquid loading is small. In this case assuming $\alpha_f \approx 0$ does not generate a significant error.
The field equations have now been detailed. The next section discusses the boundary conditions associated with each phase.

3.2.3 Boundary conditions

a) Film height boundary condition

At the wall we will have to specify a boundary condition for the height of the film. It is a no flux condition. This is automatically verified because in the algebraic model for the velocity of the film $v = 0$.

b) Volume fraction boundary condition.

At the wall the volume fraction boundary condition for droplet phase and for the gas phase is a no flux boundary condition:

$$\left.\frac{\partial \alpha_\kappa}{\partial y}\right|_{y=0} = 0 \tag{3.47}$$

It must be born in mind that this boundary condition is not at the film interface but at the wall because the film is modeled by a scalar h transported by the flow. Mass/momentum transfers are modeled in the fields equations with sources and sinks due to deposition and re-entrainment. In contrast, no transfer occurs between the gas and the wall or between the droplet field and the wall. This justifies the boundary condition (3.47).

c) Velocity boundary condition for the gas phase

c1) The log law. Let u^+ be the mean velocity normalized by a friction velocity u_τ:

$$u^+ \equiv \frac{\widetilde{U_{gx}}}{u_\tau} \tag{3.48}$$

u_τ will be modeled later. ν_g/u_τ is a viscous length scale and the distance from the wall normalized by this length scale is:

$$y^+ \equiv \frac{y\, u_\tau}{\nu_g} \tag{3.49}$$

Then if $y^+ > 30$ and if y is sufficiently small for the mean velocity profile to be determined by the viscous scale only, we can write the log law (see e.g. White (1991)):

$$u^+ = \frac{1}{\kappa} ln\left(y^+\right) + B \tag{3.50}$$

where $\kappa \approx 0.4$ is the Von Kármán constant and $B \approx 5.2$[2].

c2) Wall functions. Pope (2000) showed that a good approximation of u_τ in a single phase flow is:

$$u_\tau \approx \sqrt{\left|\overline{u'v'}\right|} \approx C_\mu^{\frac{1}{4}} k^{\frac{1}{2}} \tag{3.51}$$

This relation assumes the equilibrium between the production and the dissipation rate of the turbulent kinetic energy. By analogy with single phase flows,

[2]Let us notice that this is not valid if there are strong mean pressure gradients. If the pressure gradient is very favorable a relaminarization can occur. If the pressure gradient is adverse a separation can occur. In addition inlet vanes or cyclones have got curved walls. Convex curvatures have a stabilizing effect. Concave walls destabilize the flow. Mean pressure gradients and curvature effects are neglected in this work. Curvature is considered in the work of Schmehl *et al.* (1999) on spray/liquid film interactions.

u_τ is here modeled as:

$$u_\tau \approx \sqrt{\left|\widetilde{U''_{gx}U''_{gy}}\right|} \approx C_\mu^{\frac{1}{4}} k_g^{\frac{1}{2}} \tag{3.52}$$

If equations (3.52) and (3.50) are used at the centroid C of the boundary cell we get:

$$u^+\Big|_{y=y_C} = \frac{1}{\kappa} ln \left(\frac{y_C C_\mu^{\frac{1}{4}} \; k_g^{\frac{1}{2}}\Big|_{y=y_C}}{\nu_g} \right) + B \tag{3.53}$$

Then a boundary condition for the gas which is linear in $\widetilde{U_{gx}}$ is:

$$\tau_i = \rho_g u_\tau \frac{\widetilde{U_{gx}}\Big|_{y=y_C}}{u^+\left(y^+\right)} \tag{3.54}$$

τ_i is the stress exerted by the film on the gas phase. If the interface is moving with a velocity C the log-law is written:

$$\frac{U_g - C}{u_\tau} = \frac{1}{\kappa} ln\left(y^+\right) + B \tag{3.55}$$

where C is the velocity of the interface. In the following it will be assumed that the velocity of the interface is small compare to the velocity of the gas at the centroid of the near-wall cell. Therefore equation (3.50) will be used instead of (3.55). This approximation has an important consequence for the film. The force F^{int} exerted by the gas on the film, arising from the interfacial shear stress, is parallel to the vector Δ_i (see Figure 3.4). Using equation (3.50) instead of (3.55) implies that the force F^{int} is also parallel to $U_{gi,p}$. Thus, given λ a real number:

$$\begin{aligned}
& \Delta_i && = \lambda U_{gi,p} \\
\Leftrightarrow \quad & U_{gi,p} - C_i && = \lambda U_{gi,p} \\
\Leftrightarrow \quad & C_i && = (1-\lambda)\, U_{gi,p} \\
\Leftrightarrow \quad & \begin{pmatrix} c_x \\ c_z \end{pmatrix} && = (1-\lambda) \begin{pmatrix} U_{g,p} \\ 0 \end{pmatrix} \\
\Rightarrow \quad & c_z && = 0
\end{aligned} \tag{3.56}$$

Combining equation (3.37) and equation (3.56) implies that:

$$\rho_f g_z h + \frac{V}{A} \widetilde{\dot{D}} w_d = 0 \tag{3.57}$$

If the above relation is fulfilled and if $c_z = 0$ then, according to equation (3.32):

$$\overline{w}(y) = 0 \tag{3.58}$$

The consistency of the model demands that if the velocity of the interface is neglected compare to the velocity of the gas then the film can only move along a line which is parallel to the gas velocity.
So far, there is no difference between the gas boundary condition in our case and in a standard single phase flow simulation. Nevertheless the liquid film has got a strong influence on the gas phase. To study how the film influences the gas phase, we will first find a correlation that links the height of the film to the friction coefficient. Then we will find a relation between the friction coefficient and a sand roughness. Equating the two expressions of the friction coefficient will give an expression for the equivalent sand roughness of the film as a function of the height of the film. This will provide a boundary condition for the gas.

c3) Friction coefficient as a function of the film height. A lot of research has been going on about this subject over the last 50 years. Most of the papers related the interfacial friction to macroscopic quantities such as the average gas velocity, the average liquid velocity or the diameter of the pipe . The friction coefficient C_f is defined as:

$$C_f \equiv \frac{2\tau_i}{\rho U^2} \tag{3.59}$$

Depending on the author, C_f is based on an average gas velocity (C_{fg}) or a mixture velocity (and its corresponding mixture density). It can also be based on superficial velocities.

Wallis' correlation. Wallis (1969) proposed the following correlation based on experimental results:

$$C_{fg} = 0.005\left(1 + 300\frac{h}{D}\right) \tag{3.60}$$

D is the diameter of the pipe. As underlined by Hewitt and Hall-Taylor(1970) equation (3.60) agreed with older studies. Wallis further suggested that the coefficient 0.005 could be replaced by $0.079Re_g^{-\frac{1}{4}}$. Relation (3.60) was successfully used by numerous authors either with a 0.005 coefficient (Antal *et al.* (1998), Kumar and Trabold (2000)) or with $0.079Re_g^{-\frac{1}{4}}$ (Saito *et al.* (1978), Sugawara and Miyamoto (1990), Sugarawa (1990), Stevanovic and Studovic (1995) and Fossa *et al.* (1998)). Yano *et al.* (2001) used this correlation adding an adjustment to fit additional experiments performed by Ueda[3]. Alipchenkov *et al.* (2004), Antipin *et al.* (2003) and Alipchenkov *et al.* (2002a) also used a correlation inspired of Wallis'. Moeck and Stachiewicz (1972), Fukano and Furukawa (1998), Fore *et al.* (2000) and Wongwises and Kongkiatwanitch (2001) did a direct testing of Wallis' correlation and plotted C_{fg} as a function of h/D. Their results are summarized in Table 3.1. The category "large" means roughly $h/D \geq 0.03$. "Small" corresponds approximately to $h/D \leq 0.005$ or 0.01. Accurate pieces of information can be found in the original articles. We included

[3]Ueda, T. (1981). *Two-phase flow-Flow and Heat transfer.* Yokendo: Japan (in Japanese)

h/D	Authors	Result	Remarks
Large	Fuk. and Fur. (1998)	$C_{fg,W} < C_{fg,exp}$	Various visc.
	Fore *et al.* (2000)	$C_{fg,W} < C_{fg,exp}$	
	Fore *et al.* (2000)	$C_{fg,W} \approx C_{fg,exp}$	17 bars
	Wong. and Kong. (2001)	$C_{fg,W} > C_{fg,exp}$	
	Moeck and Stach. (1972)	$C_{fg,W} < C_{fg,exp}$	
Medium	Fuk. and Fur. (1998)	$C_{fg,W} \approx C_{fg,exp}$	Various visc.
	Fore *et al.* (2000)	$C_{fg,W} \approx C_{fg,exp}$	
	Fore *et al.* (2000)	$C_{fg,W} \approx C_{fg,exp}$	17 bars
	Moeck and Stach. (1972)	$C_{fg,W} \approx C_{fg,exp}$	
Small	Fore *et al.* (2000)	$C_{fg,W} > C_{fg,exp}$	
	Fore *et al.* (2000)	$C_{fg,W} > C_{fg,exp}$	17 bars
	Jay. and Val. (2004)	$C_{fg,W} >> C_{fg,exp}$	30-90 bars
	Moeck and Stach. (1972)	$C_{fg,W} > C_{fg,exp}$	

Table 3.1: Validity of the Wallis correlation:
$C_{fg,W}$: Friction factor predicted by relation (3.60).
$C_{fg,exp}$: Experimental friction factor.

as well in Table 3.1 the results of Jayanti and Valette (2004) that compared the data of Würtz[4] with the results given by relation (3.60). They did not provide values of the ratio between the height of the film and the diameter. However they used high pressure data so that it is probable that h/D was small. Wallis' correlation is able to reproduce data reasonably for at least low pressures. Discrepancies for thick films need further investigation as experimental results are contradictory. It seems that the relation overpredicts friction factors for thin films. It is inconvenient as thin films occur in scrubbers. This effect was predicted by Wallis. He indeed emphasized that when the regime is not fully rough but more in a ripple or smooth film region, as in the case of thin films, the correlation (3.60) was not accurate. More fundamentally, for very thin films, it is not obvious that the diameter of the pipe is an appropriate dimension to scale the height of the film with.

Other correlations.

- Moeck and Stachiewicz (1972) developed an equation similar to Wallis':

$$C_{fg} = 0.005 \left(1 + 1458 \left(\frac{h}{D} \right)^{1.42} \right) \tag{3.61}$$

  This correlation has been used by Fukano and Furukawa (1998) and underpredicted their data. Wongwises and Kongkiatwanitch (2001) also tested relation (3.61) and obtained good results. It is an interesting correlation because it predicts a lower friction coefficient for thin films than (3.60).

[4]Würtz, J. (1978). An experimental and theoretical investigation of annular steam water in tubes and annuli at 30 and 90 bars. *RISO Report No. 372.*

- Henstock and Hanratty (1976) proposed a complicated correlation. It has been tested by Fore *et al.* (2000) and gave poor results for thick films and similar results to Wallis' relation for thin films.

- Asali and Hanratty (1985) also proposed a relation to relate Cf_g and h. It was developed further by Ambrosini *et al.* (1991) to include surface tension effects. Fossa *et al.* (1998) found Wallis' correlation to be better (with or without surface tension effect). Hurlburt and Newell (2000) noted that Asali's correlation had a limited range of application. Fore *et al.* (2000) obtained good predictions for low h/D (range where the correlation was developed). Finally Jayanti and Valette (2004) obtained very bad results at high pressure condition with over-predictions of over 100% of the interfacial friction factor. Therefore it is believed that the correlation of Asali and Hanratty is not suitable to our case.

- Fossa *et al.* (1998) tested a correlation given by Oliemans *et al.* (1986) which gave poorer results than relation (3.60).

- Fukano and Ousaka (1989) proposed a correlation that was shown to be unable to represent the results of Fukano and Furukawa (1998).

- Tso and Sugarawa (1990) used an expression proposed by Ueda which has many adjustable parameters and should probably not be used outside the range it was designed for.

- Nigmatulin (1991) emphasized the importance of splashes or secondary re-entrainment on the interfacial friction factor. When this phenomena is not negligible he proposed the following:

$$C_{fg} = 0.005 + 1.2\frac{h}{D} + 1.49 \cdot 10^6 \left(\frac{h}{D}\right)^{5.5} \tag{3.62}$$

  It is nevertheless based on a single set of experiments. Provided that $h << 0.044D$, equation (3.62) can be written:

$$C_{fg} = 0.005 \left(1 + 240\frac{h}{D}\right) \tag{3.63}$$

  Equation (3.63) is remarkably similar to equation (3.60).

- Fukano and Furukawa (1998) studied the effect of liquid viscosity with aqueous glycerol solutions. They proposed a correlation depending on the ratio of the kinematic viscosities of the fluids that overpredicted strongly the interfacial friction factor measured by Wongwises and Kongkiatwanitch (2001).

- Ho Kee King and Piar (1999) used successfully a correlation presented by Dobran (1987) which integrates the effect of the density ratio. It can be

approximated by:

$$C_{fg} = 0.005 \left(1 + 24 \frac{h}{D} \left(\frac{\rho_f}{\rho_g} \right)^{\frac{1}{3}} \right) \tag{3.64}$$

In high pressure scrubbers, ρ_f/ρ_g is smaller and the film is thinner than for low pressure conditions. In the case of thin film, Wallis correlation overpredicts the interfacial friction coefficient. Correlation (3.64) considerably reduces the friction coefficient C_{fg} when ρ_f/ρ_g becomes small. As a result this is a valuable correlation for high pressure applications. For air/water system at 1 bar it gives:

$$C_{fg} = 0.005 \left(1 + 240 \frac{h}{D} \right) \tag{3.65}$$

which is very close to relation (3.60) and identical to (3.63). Even at low pressures, this relation gives smaller coefficients than Wallis' correlation. Predictions for small films may then be more accurate.

- Fore *et al.* (2000) modified the correlation of Wallis with an offset, so it could better predict data for small h/D ratios. The effect of this offset was almost negligible on the data of Wongwises and Kongkiatwanitch (2001).

- Wongwises and Kongkiatwanitch (2001) proposed a pure empirical fit with three adjustable constants. It has not been yet tested by other authors.

We can conclude from the above study that few of the literature correlations are of any use outside the range where they have been developed. The most promising ones are that proposed by Moeck and Stachiewicz (1972) and correlations that looks like:

$$C_{fg} = 0.005 \left(1 + \Gamma \frac{h}{D} \right) \tag{3.66}$$

Γ is an empirical coefficient comprised between 240 (equations (3.63) and (3.65)) and 300 (equation (3.60)). A dependence of Γ with the density ratio can be useful at high pressure (equation (3.64)).

c4) Friction coefficient as a function of the sand roughness. Nigmatulin (1991) reported the work of Kapitsa[5] who showed that a flow of a gas over a wavy liquid film is similar to a flow past a rough surface. Therefore one could think of specifying the presence of a liquid film by having a rough boundary condition for the gas.

Law of the wall for a rough wall. As described for example in Schlichting (1958), the protrusions of the boundary surface generate a downward shift

[5]Kapitsa, P. L. (1948). Wave flow of thin layers of liquid. ZhETF 18(1), in Russian.

in the $u^+(y^+)$ profile. Given a sand roughness of height s, and defining the non-dimensional quantity

$$s^+ \equiv \frac{su_\tau}{\nu_g} \tag{3.67}$$

the log-low becomes:

$$u^+ = \frac{1}{\kappa} ln\left(y^+\right) + B \;\; ; \; s^+ < 2.25 \tag{3.68}$$

$$u^+ = \frac{1}{\kappa} ln\left(y^+\right) + B - sin\left(\frac{\pi}{2}\frac{ln\left(\frac{s^+}{2.25}\right)}{ln\left(\frac{90}{2.25}\right)}\right)\left(\frac{1}{\kappa} ln\left(s^+\right) - 3\right) \;\; ; \; 2.25 < s^+ < 90 \tag{3.69}$$

$$u^+ = \frac{1}{\kappa} ln\left(y^+\right) + B - \left(\frac{1}{\kappa} ln\left(s^+\right) - 3\right) \;\; ; \; 90 < s^+ \tag{3.70}$$

The above relations have been given by Ligrani and Moffat (1986) who fitted the data of Nikuradse[6]. Equation (3.68) represents the smooth regime. Equation (3.69) represents the transitional regime. Equation (3.70) represents the fully rough regime.

Friction coefficient and sand roughness. In the case of a fully rough regime, Pope (2000) proposed a theoretically justified approximation of C_{fg}:

$$C_{fg} = \frac{1}{4}\frac{1}{\left(1.99\, log\left(\frac{D}{2s}\right) + 1.71\right)^2} \tag{3.71}$$

Schlichting (1958) found 2 instead of 1.99 and 1.74 instead of 1.71, by fitting Nikuradse's experimental results.

c5)Relation between film height and sand roughness.

Simple relations. By means of (3.71) and (3.66) one gets an explicit function s/D dependent on h/D:

$$\frac{s}{D} = \frac{1}{2} 10^{-3.536\left(1+\Gamma\frac{h}{D}\right)^{-\frac{1}{2}}+0.8593} \tag{3.72}$$

Unfortunately in a full 3D geometry, D is not properly defined. To avoid this, we have to approximate relation (3.72) by a proportionality relation:

$$\frac{s}{D} \propto \frac{h}{D} \Rightarrow s \propto h \tag{3.73}$$

Wallis (1969) cleverly noticed that the relation (3.71) could be approximated by :

$$C_{fg} \approx 0.005\left(1 + 75\frac{s}{D}\right) \tag{3.74}$$

[6]Nikuradse, J. (1933). Laws of flow in rough pipes. *VDI Forschungsheft 361*, in German.

when $0.001 < \frac{s}{D} < 0.03$. Combined with (3.66), it leads to:

$$\frac{s}{h} = \frac{\Gamma}{75} \tag{3.75}$$

That is to say:

$$3.2 \leq \frac{s}{h} \leq 4 \tag{3.76}$$

depending on the value of Γ.
A diameter independent relation between s and h can not be obtained with the expression (3.61) developed by Moeck and Stachiewicz (1972). The correction given by Nigmatulin (1991) for secondary re-entrainment in equation (3.62) has got the same drawback. Himmelsbach *et al.* (1994) gave s as a function of the wall shear stress. Their relation was used by Schmehl *et al.* (1999). Adechy and Issa (2004) proposed a relation where the sand roughness was both a function of the liquid height and of D. Last, Jayanti and Valette (2004), to compensate high pressure effects, used a correlation that gave the sand roughness as a function of the diameter and the height of the film.

Possible improvements. Oliemans *et al.* (1986) proposed a dependency of s/h on a Weber number:

$$\frac{s}{h} = \frac{30}{We} \tag{3.77}$$

The Weber number was based on the mean height of the liquid film, the relative velocity of the core and the interface, and the core density. This relation correlated accurately a large number of experimental data. It performed significantly better than $s/h = 4$ with high pressure data. The Weber number is based on the mean velocity of the gas which is not local. The mean gas velocity U_{avg} and u_τ are linked by the relation:

$$U_{avg} = u_\tau \sqrt{\frac{2}{C_{fg}}} \tag{3.78}$$

Oliemans *et al.* (1986) also mentioned the work of Whalley and Hewitt who advised:

$$\frac{s}{h} = 0.3 \left(\frac{\rho_f}{\rho_g}\right)^{0.33} \tag{3.79}$$

Given the approximation (3.74) true, it is very close to relation (3.64) as it gives:

$$C_{fg} = 0.005 \left(1 + 22.5 \frac{h}{D} \left(\frac{\rho_f}{\rho_g}\right)^{0.33}\right) \tag{3.80}$$

Oliemans *et al.* (1986) who worked with high-pressure data, emphasized a better pressure drop prediction with equation (3.80) than with Wallis' correlation. However the scatter was large.

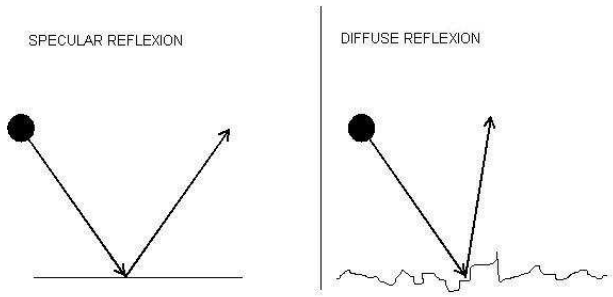

Figure 3.6: Boundary condition for a solid particle on a wall

Transitional and smooth regimes. To obtain equation (3.75), two expressions of the interfacial friction coefficient were used, namely (3.66) and (3.74). However Wallis' correlation which is a special case of (3.66) is valid only for the fully rough regime. Similarly (3.74) is an approximation of (3.71) which is the expression of C_{fg} in the fully rough regime. Thus it can not be expected that $s/h = \Gamma/75$ works outside a fully rough regime. Thin films are smoother than thick films. As a result for high pressure separation devices, we expect relation (3.75) to overestimate the equivalent sand roughness of the film. Oliemans *et al.* (1986) already pointed out that the sand roughness must be zero when the interface irregularities are within the viscous sublayer. They proposed the following modification of the sand roughness:

$$s = Max\left(\frac{\Gamma}{75}\left(h - 5\frac{\nu_g}{u_\tau}\right);\ 0\right) \tag{3.81}$$

c6) Summary. The velocity of the gas by the wall will follow the law of the wall for a rough wall. The sand roughness of the film will be:

$$s = 4\,h \tag{3.82}$$

This may overestimate the sand roughness of thin films.

d) Velocity boundary condition for the droplet phase

Given a solid particle which size is much larger than the roughness of the wall; when impinging against the wall, if the shock is elastic, the solid particle is reflected and conserves its tangential momentum. As a result it does not exert any shear force on the wall. This type of boundary condition is a *specular* reflexion. If now, in contrast, the solid particles are noticeably scattered due to the wall roughness, the lack of tangential reflected momentum is balanced by a shear force on the wall. This type of boundary condition is a *diffuse* reflexion. The two situations are illustrated on Figure 3.6. Specifying a slip velocity for the droplet phase (be it zero or not), is in fact a consequence of the loss of

tangential velocity of the droplets. This loss is already taken into account in the field equation (3.5) by the deposition term. Therefore the only consistent boundary condition for the droplet field is a no-shear condition.

$$\left.\frac{\partial \widetilde{U_{di}}}{\partial y}\right|_{y=0} = 0 \tag{3.83}$$

e) Boundary condition for the turbulent kinetic energy of the gas.

The boundary condition for the turbulent kinetic energy (TKE) by a smooth wall is:

$$\left.\frac{\partial k_\kappa}{\partial y}\right|_{y=0} = 0 \tag{3.84}$$

Let us notice that, whereas the condition (3.84) is correct strictly speaking, applying it at a point located in the log-law region leads to an inaccurate flat profile in the near wall region for $0 < y < y_C$ (C is the centroid of the near wall cell). This is a known and accepted drawback of wall functions.
The roughness changes dramatically the non-dimensional TKE $k^+ = k/u_\tau^2$ in the vicinity of the wall. Nevertheless, as shown by Ashrafian *et al.* (2004), one can expect little change in the non-dimensioanl Reynolds stresses and in k^+ if y is much larger than s. In the present case it requires $y_C >> 4h$. Equation (3.84) is used in the present model for the gas phase.
There is no boundary condition for k_d because the TKE of the droplet phase is computed by relation (2.93).

f) Boundary condition for the rate of dissipation.

The balance between production and dissipation (see e.g. Pope (2000)) quickly leads to:

$$\epsilon_{Cg} = \frac{u_{\tau g}^3}{\kappa y_C} \tag{3.85}$$

We will use this boundary condition. However the balance between $\mathcal{P}$ and ϵ (also used in equation (3.51)) is not obvious at all if roughness is present. Ashrafian (2004) performed a DNS in a rough channel with square rods. The top of the rods were at $y^+ = 13.6$. His results showed that $\mathcal{P}/\epsilon \approx 1$ is not valid for $y^+ < 75$ and can be over 3 for $y^+ \approx 20$. To take into account more accurately the dissipation transfers between the film and the gas phase, another boundary condition should be found based on the roughness height.

3.3 Closure relations

We now have a complete set of differential equations with boundary conditions and some algebraic relations to close the system. Some unknowns remain. For the continuity and momentum equations of the droplet phase and of the film,

the average deposition rate $\widetilde{\dot{D}}$ and entrainment rate $\widetilde{\dot{E}}$ are needed. For the film velocity we need the interfacial shear stress τ_i. We will first handle the closure of τ_i, then we will discuss the closure for the deposition rate and finally the closure for the entrainment rate.

3.3.1 The interfacial shear stress

As a rule, when one uses a correlation for the interfacial friction factor C_f the interfacial shear is deduced automatically by the definition of C_f itself (equation (3.59)). However in our case Wallis' correlation was used to find a plausible way to describe locally the roughness of the film and not to find the interfacial shear directly.
The shear on both sides of the interface must be the same. The shear exerted on a fluid by a rough wall in a single phase flow is approximated by:

$$\tau_{wall} \equiv \rho\, u_\tau^2 \approx \rho\sqrt{C_\mu} k_C \tag{3.86}$$

This assumes an equilibrium between production and dissipation. From the previous relation, a consistent way of modeling the interfacial shear in the film momentum equation is:

$$\tau_i = \rho_g \sqrt{C_\mu} k_{gC} \tag{3.87}$$

3.3.2 Deposition rate

To built a correlation for the deposition rate we will go through the following points:

1. How can the experimentally observed deposition rate be reduced to a model for the deposition velocity?
2. How can this deposition velocity be split into two components, diffusive and non diffusive?
3. How to model the non diffusive deposition velocity?
4. How to model the diffusive velocity?

a) Deposition velocity

Mass sink and deposition velocity. The deposition sink $\widetilde{\dot{D}}$ from the droplet phase is given in equation (3.2) per unit volume and per second. If we multiply $\widetilde{\dot{D}}$ by the volume of the cell and divide by the area of a plane in the vicinity of the interface, we obtain the flux of droplet J_d leaving the dispersed phase. As the liquid film is supposed 2D and parallel to the wall, the considered plane has the area of the wall of the computational cell.

$$J_d = \frac{\widetilde{\dot{D}} \cdot V}{A} \tag{3.88}$$

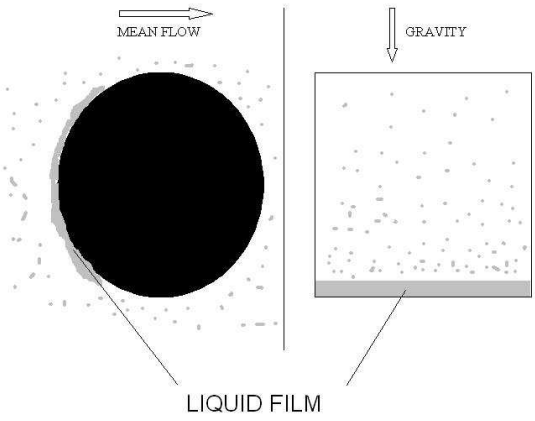

Figure 3.7: Deposition due to non-stochastic processes

It is now natural to express this flux as a product of a concentration and a velocity. The concentration of the droplets in the near wall cell is:

$$\overline{\alpha_{dC}}\rho_d$$

As a result we can write:

$$J_d = \overline{\alpha_{dC}}\rho_d \cdot K_D \tag{3.89}$$

where K_D is the deposition velocity. Finally the sink of droplets becomes:

$$\widetilde{\dot{D}} = \overline{\alpha_{dC}}\rho_d \frac{A}{V} \cdot K_D \tag{3.90}$$

One now needs a correlation for the deposition velocity.

The two types of deposition processes. K_D takes into account the deposition due to non stochastic and stochastic movements. Figure 3.7 illustrates the former. On the left hand, deposition is due to the mean convection toward a bluff body. On the right hand, deposition is due to the settling of the particles because of gravity. Typical example of stochastic processes leading to deposition will be Brownian diffusion or dispersion of droplets in a turbulent gas stream. This type of dispersion leads to a velocity toward the wall that is different from zero. Figure 3.8 illustrates the case of particle depositing on the wall of a vertical tube because of their movement induced by the turbulence in the gas.

Interaction of deposition processes. Handling the two types of deposition at the same time is not easy. Nevertheless a common and instructive case is that of horizontal pipe flows where deposition occurs both by turbulent dispersion

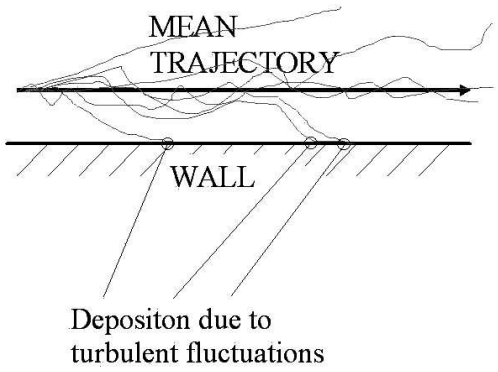

Figure 3.8: Deposition due to turbulent fluctuations

and gravitational settling. McCoy and Hanratty (1977) already noticed that the total deposition velocity K_{total} was depending on a settling deposition K_{set} and a turbulent deposition K_{turb}. They noted the following:

- if $K_{set} << K_{turb} \Rightarrow K_{total} \approx K_{turb}$
- if $K_{set} >> K_{turb}$ then at the bottom of the tube $K_{total} \approx K_{set}$ and $K_D \approx 0$ at the top.

Binder and Hanratty (1992), Williams *et al.* (1996), Mols and Oliemans (1998), and Mols *et al.* (2002) proposed then that the total deposition velocity was the sum of the settling and the turbulent velocity. Given the circumferential position θ (θ being 0 at the bottom and π at the top of the pipe), all the above cited papers give relations similar to:

$$K_{total} = K_{turb} + K_{set} \cdot cos(\theta) \tag{3.91}$$

Pan and Hanratty (2002b) derived a deposition velocity by considering that the velocities of the particles were normally distributed and had a mean $K_{set}\ cos(\theta)$. Mito and Hanratty (2004) performed Lagrangian tracking of particles with various relaxation times in a turbulent gas stream which was described by the mean of a Langevin equation. The particles were generated from the top and bottom wall of a channel. Mito and Hanratty noticed that at the bottom of the channel, the deposition velocity was not a linear function of the settling velocity. In particular they pointed out a regime called "saltation" regime. In this regime, the particles do not have the time to reach their settling velocity before depositing. In addition, when the settling velocity was less than the turbulent deposition velocity, as the settling velocity increased, the deposition velocity on the bottom wall decreased. The study of Mito and Hanratty (2004) shows that the deposition velocity is not a simple sum of the deposition due to stochastic and non

stochastic movements. The mechanisms influences each others. Nevertheless, one can not deny that a formula such as (3.91) provides a good first guess (see *e.g.* Binder and Hanratty (1992)).
A striking example that the total deposition velocity is not a straightforward sum of the deposition velocities of the various mechanisms taken separately, is described by Slater *et al.* (2003). They studied the deposition of particles on the blades of a turbine cascade with an Euler/Euler model. Here the two important mechanisms contributing to the deposition were the diffusion (Brownian and turbulent) , and the inertia provided by the mean flow. First they calculated the deposition due to diffusion. Then they performed a simulation were inertia was the only deposition mechanism. Finally they calculated the deposition with the two effects together. The sum of the deposition of the two effects taken separately was different from the total deposition when both effects were included. Therefore as a rule one can not assume that the total deposition is the sum of the deposition due to stochastic processes on the one hand and non-stochastic processes on the other hand. In fact, these deposition mechanisms are strongly interacting.
Nevertheless, we are confronted with an important practical problem. The interactions between the different deposition mechanisms is difficult to model by *ad hoc* assumptions. Both Slater *et al.* (2003) and Mito and Hanratty (2004) made a fine mesh in the boundary layer. It is however computationally too demanding to resolve the boundary layer in a separation equipment. A single large cell by the wall, the centroid of which is in the log law zone, bounds us to model the interaction of the deposition processes instead of computing them directly. Such a model does not exist presently. Therefore, the deposition velocity is modeled as the sum of two velocities, the first is due to inertia and gravitation (non diffusive), the second due to turbulent diffusion. Even if this is not theoretically justifiable it is a pragmatical choice as:

1. A fine grid by the film is not needed.

2. This approach has been tested and gave fair results in the case of horizontal annular flows.

Therefore we will model K_D as:

$$K_D = K_{non\,diff} + K_{wall} \tag{3.92}$$

It is important to note that K_D which is defined by equation (3.89) is a deposition velocity based on a local flux of droplets near the wall. K_D is not identical to the total deposition rate which includes the effect of turbulent dispersion in the core. Measured deposition velocities refer usually to the total deposition velocity K_{total}. $K_{non\,diff}$ is the deposition velocity due to non diffusive phenomena (mean convection of the flow toward the wall, gravity). K_{wall} is a deposition velocity due to near-wall diffusive phenomena and does not include the turbulent dispersion in the core.

b) The non diffusive velocity

Basic momentum equation. Some assumptions are needed to find the non diffusive deposition velocity of the particles by the wall:

- Assumption 1: At $t = 0$ the particles are at the cell centroid.
- Assumption 2: The particles are submitted to a drag force, buoyancy and the gravitation force.

The model will require the velocity of the particle phase at $t = 0$ in the wall normal direction. As the velocity of the particle is available only at the cell centroid, assumption 1 is the only possible choice. The drag, the gravity and buoyancy must be taken into account to be consistent with the momentum equation (3.5). However other forces could have a significant impact, especially lift forces. Lift forces will be neglected here. In the direction normal to the wall, Newton's second law is:

$$\frac{dU_d}{dt} = \frac{U_g - U_d}{\tau} + g\frac{\rho_d - \rho_c}{\rho_d} \tag{3.93}$$

In this section about the non diffusive deposition velocity, all the vectors are projected on the wall normal direction. This will not be reported on the notation. Austrheim (2006) made experiments in a high pressure scrubber (92 bars) with natural gas and condensate. He reported for $\frac{\rho_d - \rho_c}{\rho_d}$ a value of 0.8. In the following we will assume that:

$$\frac{\rho_d - \rho_c}{\rho_d} \approx 1 \tag{3.94}$$

One now needs to assume a velocity profile for the gas. A simple choice is to suppose a linear profile between the centroid and the wall. Hence:

$$U_g = U_{gC} - U_{gC}\frac{y}{y_{wall}} \tag{3.95}$$

The index C represents the values at the centroid of the cell. The index $wall$ represents the value at the wall. Here $y_C = 0$. The velocities are positive when they point toward the wall. Equation (3.93) together with equation (3.95) gives the following ordinary differential equation for the position y of the particle:

$$\ddot{y} + \frac{\dot{y}}{\tau} + \frac{U_{gC}}{y_{wall}\tau}y = g + \frac{U_{gC}}{\tau} \tag{3.96}$$

This is a typical equation for a damped oscillator driven by an external force.

Solution of the equation. Deposition takes place when $y = y_{wall}$ for the first time. The velocity at this instant is the velocity of deposition. The solution of equation (3.96) is straightforward and the results are given without details.

- Underdamped oscillator ($\frac{1}{\tau^2} - \frac{4U_{gC}}{y_{wall}\tau} < 0$)

$$
\begin{aligned}
y &= e^{-\frac{t}{2\tau}}\left(A\,cos(\omega t) + B\,sin(\omega t)\right) + y_s && (3.97)\\
\dot{y} &= e^{-\frac{t}{2\tau}}\left(-A\omega sin(\omega t) + B\omega cos(\omega t)\right) \\
&\quad -\frac{e^{-\frac{t}{2\tau}}}{2\tau}\left(A\,cos(\omega t) + B\,sin(\omega t)\right) && (3.98)\\
A &= -y_s && (3.99)\\
B &= \frac{U_{dC} - \frac{y_s}{2\tau}}{\omega} && (3.100)\\
\omega &= \sqrt{\frac{4U_{gC}}{y_{wall}\tau} - \frac{1}{\tau^2}} && (3.101)\\
y_s &= \frac{y_{wall}\tau g}{U_{gC}} + y_{wall} && (3.102)
\end{aligned}
$$

- Overdamped oscillator ($\frac{1}{\tau^2} - \frac{4U_{gC}}{y_{wall}\tau} > 0$)

$$
\begin{aligned}
y &= A\,e^{\lambda_1 t} + B\,e^{\lambda_2 t} + y_s && (3.103)\\
\dot{y} &= A\lambda_1 e^{\lambda_1 t} + B\lambda_2 e^{\lambda_2 t} && (3.104)\\
A &= \frac{U_{dC} + \lambda_2 y_s}{\lambda_1 - \lambda_2} && (3.105)\\
B &= -y_s - \frac{U_{dC} + \lambda_2 y_s}{\lambda_1 - \lambda_2} && (3.106)\\
\lambda_1 &= \frac{-\frac{1}{\tau} + \sqrt{\frac{1}{\tau^2} - \frac{4U_{gC}}{y_{wall}\tau}}}{2} && (3.107)\\
\lambda_2 &= \frac{-\frac{1}{\tau} - \sqrt{\frac{1}{\tau^2} - \frac{4U_{gC}}{y_{wall}\tau}}}{2} && (3.108)\\
y_s &= \frac{y_{wall}\tau g}{U_{gC}} + y_{wall} && (3.109)
\end{aligned}
$$

- Critical oscillator ($\frac{1}{\tau^2} - \frac{4U_{gC}}{y_{wall}\tau} = 0$)

$$
\begin{aligned}
y &= (A + B\,t)\,e^{-\frac{t}{2\tau}} + y_s && (3.110)\\
\dot{y} &= e^{-\frac{t}{2\tau}}\left(B - \frac{A + B\,t}{2\tau}\right) && (3.111)\\
A &= -y_s && (3.112)\\
B &= U_{dC} - \frac{y_s}{2\tau} && (3.113)\\
y_s &= \frac{y_{wall}\tau g}{U_{gC}} + y_{wall} && (3.114)
\end{aligned}
$$

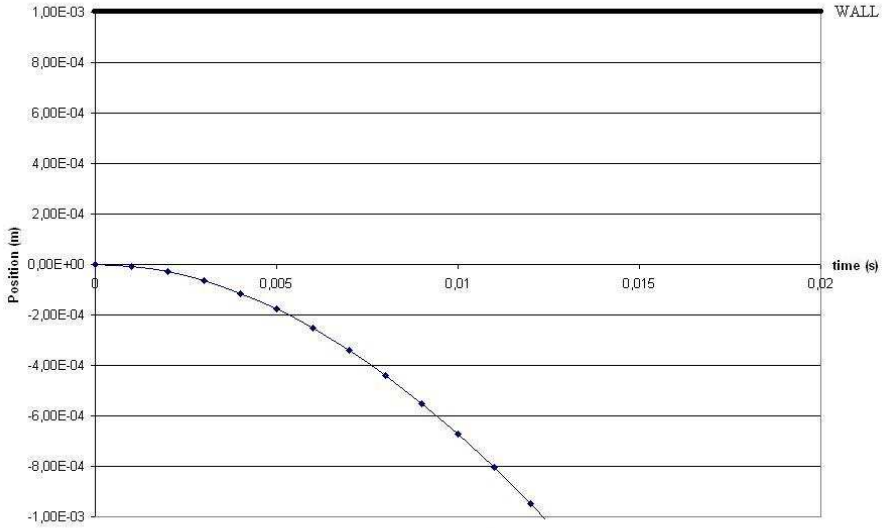

Figure 3.9: Particle moving away from the wall.

There is also an important case where the velocity of the gas normal to the wall is zero (annular vertical flow for example). Then equation (3.96) becomes:

$$\ddot{y} + \frac{\dot{y}}{\tau} = g \tag{3.115}$$

- if $U_{gC} = 0$

$$\begin{aligned} y &= -A\tau e^{-\frac{t}{\tau}} + g\tau t + B && (3.116)\\ \dot{y} &= A\, e^{-\frac{t}{\tau}} + g\tau && (3.117)\\ A &= U_{dC} - g\tau && (3.118)\\ B &= \tau\,(U_{dC} - g\tau) && (3.119) \end{aligned}$$

Deposition velocity. To get the deposition velocity, we will find the time t_{wall} such as $y(t_{wall}) = y_{wall}$ and assume that the non diffusive deposition velocity is $\dot{y}(t_{wall})$. This assumption requires, to compute the correct deposition flux, that the concentration of the particles is independent of y in the cell by the wall. Now t_{wall} does not necessarily exist. For example in the case of an horizontal annular flow, at the top of the pipe, the gravity will accelerate the droplets away from the wall as shown on Figure 3.9. In the cases where there are several t_{wall} as in Figure 3.10 it is the smallest that is the relevant time to calculate $\dot{y}(t_{wall})$. It is also important, in order to find the correct t_{wall}, to look closely at the time scales involved. There are three time scales:

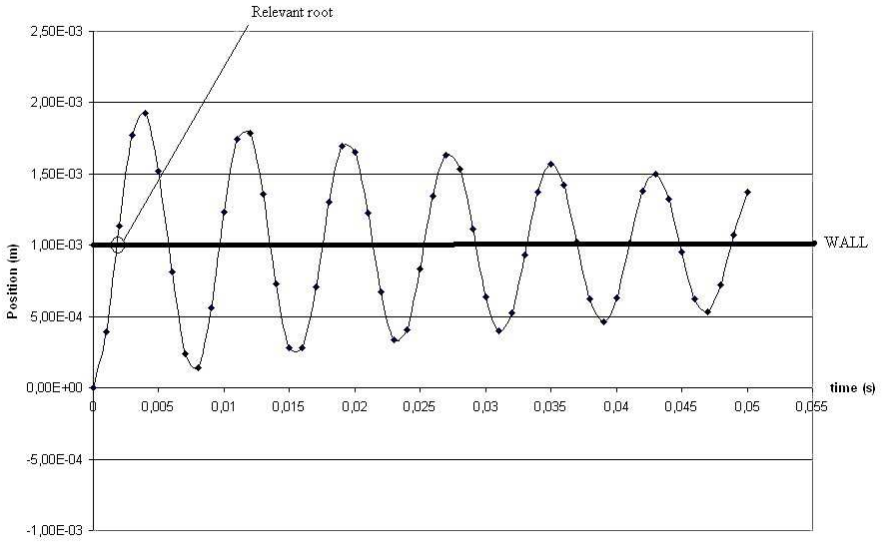

Figure 3.10: Multiple roots of the equation $y(t_{wall}) = y_{wall}$.

- One based on the pulsation $1/\omega$
- One based on the initial velocity of the particle y_{wall}/U_{dC}. This is the time for a rectilinear uniform motion from the centroid to the wall.
- One based on gravity $\sqrt{\frac{2y_{wall}}{g}}$. This is the time of a free fall toward the wall.

If the time scale is not properly taken into account one could eventually have problem with aliasing, as shown on Figure 3.11. On this figure the typical time scales are:

- $2.78 \cdot 10^{-4}$ s for the pulsation.
- 10^{-3} s for the rectilinear uniform movement.
- $+\infty$ for the gravity ($g = 0$).

While the non-aliased curve is sampled with a time scale of 10^{-4} s, the aliased one is sampled with a time step of $1.5 \cdot 10^{-3}$ s. It is larger than the smallest time scale. If the time sampling is too large, the calculated deposition velocities are meaningless.

Conclusion on the non diffusive deposition. The non diffusive deposition velocity is calculated as follows:

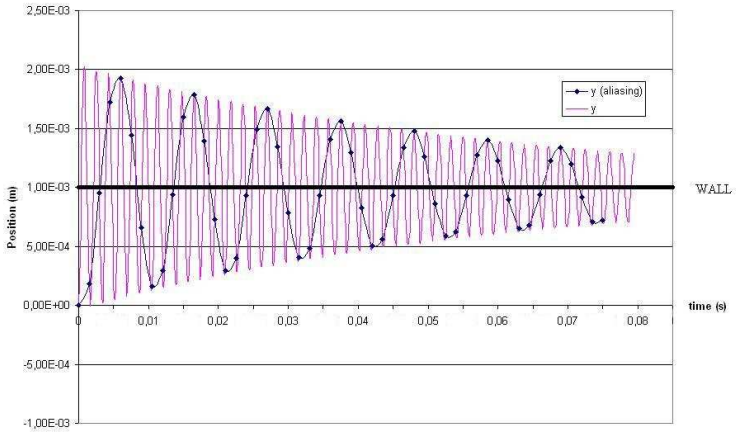

Figure 3.11: Aliasing of the position.

1. One calculates t_{wall} such as $y(t_{wall}) = y_{wall}$ taking care of the relevant time scales to avoid aliasing. $y(t_{wall})$ is calculated by the mean of the equation (3.97) or (3.103) or (3.110) or (3.116). If t_{wall} does not exist then $K_{nondiff} = 0$. If t_{wall} is not unique, one takes the smallest value of t_{wall}.

2. One calculates $K_{nondiff} = \dot{y}(t_{wall})$ where $\dot{y}(t_{wall})$ is given by the equation (3.98) or (3.104) or (3.111) or (3.117).

c) The diffusive deposition velocity

c1) Core diffusion and wall layer. Alexander and Coldren (1951) measured the rate of deposition of droplets in a turbulent air stream in a horizontal tube. They found that in the fully developed region of the flow, the mass transfer was controlled by a region close to the wall. For a developed flow, the droplet concentration profiles in the core were flat. In contrast, in the inlet region, the profiles were bell-shaped, indicating a limitation of deposition in the core of the duct itself. Friedlander and Johnstone (1957) also found similar results for a vertical flow of solid particles. They interpreted their results as follows:

1. The particles in the bulk diffuse toward the boundary. Their diffusion coefficient is equal to the one of the gas.

2. At a certain distance from the wall called by Friedlander and Johnstone "stopping distance", the particle stops diffusing and the only force acting on the particle is a Stokesian drag force.

3. The velocity of the particle at the stopping distance is provided by the turbulent fluctuations of the gas. It gives the particle the necessary impulse to travel through the boundary layer and finally deposit.

This is known as the "free-flight" theory. The very problem of the free-flight model, was rather rapidly pinpointed by Davis (1966). He noticed that the velocity specified by Friedlander and Johnstone to start the free-flight was unreasonably high. By introducing the real diffusivity of the fluid in the vicinity of the wall, he predicted deposition rate that were two order of magnitudes lower than Friedlander and Johnstone. Nevertheless as underlined first by Huntchinson *et al.* (1971), whereas the theory seems correct, the predictions of Davis are not representing correctly experimental data. However, numerous authors separate the flow in two zones: a diffusive region (the core) and a free-flight region (Hutchinson *et al.* (1971), Reeks and Skyrme (1976), Ganić and Mastanaiah (1981), Trela (1982), Trela *et al.* (1982) and Papavergos and Hedley (1984)). A significant improvement of the "free-flight" theory has been made by Owen (1969) and Cleaver and Yates (1975). They considered the effect of near wall structures that are not taken into account into the free-flight models. In their work, the particles penetrate the boundary layer through the action of down sweeps. The flow is modeled as a 2D stagnation point flow which was later justified by Fichman *et al.* (1988). Then Cleaver and Yates (1975) added an *ad hoc* contribution to model the axial convection. The deposition rate was a function of the position of the particle when entering the sweep and of its inertia. When a particle entered an ejection region it was carried away from the wall. Papavergos and Hedley (1984) combined this model of boundary penetration with the random diffusion model in the core presented by Hutchinson *et al.* (1971). Lee *at al.* (1989) measured the deposition of particles in a downward vertical pipe turbulent flow. The authors gave a particularly interesting interpretation of their results. The deposition was seen as the results of two processes in series:

1. A dispersion process characterized by a velocity K^+_{disp}.

2. An inner boundary mechanism characterized by a velocity K^+_{wall}.

The dispersion is already modeled with the turbulent dispersion equation (2.100). Therefore the only deposition velocity we are looking for here, is K^+_{wall}. The $+$ signs means the deposition velocities have been non-dimensionalized by the friction velocity u_τ. If the concentration profiles are very flat, then $K^+_{disp} >> K^+_{wall}$. In this case, the bottle neck is the inner boundary deposition mechanism and we have:

$$K^+_{total} = \frac{1}{\frac{1}{K^+_{disp}} + \frac{1}{K^+_{wall}}} \approx K^+_{wall} \tag{3.120}$$

Relation (3.120) is useful because, virtually all measurements correlate the flux of droplets toward the wall with the concentration of droplet averaged over the pipe cross-section. This average concentration comes into the definition of

K_{total}:

$$K_{total} \equiv \frac{J_d}{\rho_d} \frac{\pi R^2}{\int_0^R \int_0^{2\pi} \overline{\alpha_d(r,\theta)}\, r\, dr\, d\theta} \tag{3.121}$$

The bar on the volume fraction is the turbulent ensemble average. If, in some experiments, the turbulent dispersion had been a substantial brake to the deposition, the empirical value proposed for K_{total} would have been smaller than K_{wall}. But in the case of flat concentration profile, with $K_{disp} \to +\infty$, the experimental value K_{total} is equal to K_{wall}. Lee *et al.* (1989) proposed:

$$K_{wall} = \frac{u_\tau}{\sqrt{2\pi}} \frac{\sqrt{\widetilde{U''^2_{rd}}}}{\sqrt{\widetilde{U''^2_{rg}}}} \tag{3.122}$$

or according to (2.86):

$$K_{wall} = \frac{u_\tau}{\sqrt{2\pi}} \sqrt{\frac{\eta}{1+\eta}} \tag{3.123}$$

As we will see later, it is correct in certain circumstances but the general picture is somewhat more complex. Binder and Hanratty (1991, 1992), Mols and Oliemans (1998) and Mols *et al.* (2000) calculated the diffusion and deposition of droplets in annular flows. They used a diffusion equation for the concentration of particles together with a non zero concentration on the wall. Their modeling of the deposition velocity was close to (3.123). In the following, a model for K^+_{wall} will be presented. It is based on experimental data. This experimental data have been confirmed and explained theoretically in a series of articles (Derevich and Zaichik (1988), Kallio and Reeks (1989), Johansen (1991)). This authors brought a new insight in the understanding of the turbulent deposition velocity by introducing the momentum equation of the droplet phase.

c2) Particle deposition in fully developed turbulent vertical pipe flow

The aim of this section is to find a model for K_{wall}, the deposition velocity due to near-wall diffusive phenomena. Here we will find a value for K_{total}, the total deposition velocity, and then use relation (3.120) to find K_{wall}.

Dimensional analysis. The non-dimensional deposition velocity K^+_{total} is a function of several parameters. Liu and Agarwal (1974) presented a graph were K^+_{total} was plotted as a function of a non-dimensional particle relaxation time

$$t^+ \equiv \frac{\tau u_\tau^2}{\nu_g} \tag{3.124}$$

where τ is the particle relaxation time. It has often been seen as the only important parameter influencing the deposition velocity. However for very small particles, the Brownian diffusion coefficient is important as well. Other parameters can be taken into account, such as the Reynolds number of the gas, or the

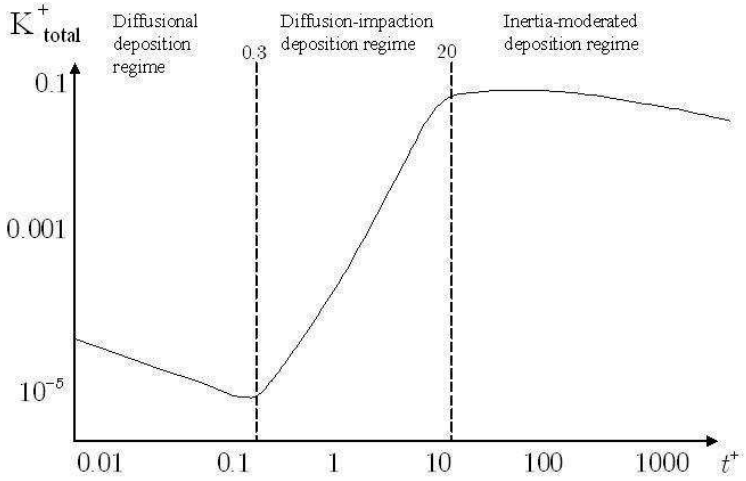

Figure 3.12: Turbulent deposition velocity vs. particle relaxation time

density ratio between the phases. McCoy and Hanratty (1977) proposed that the non-dimensional deposition velocity was dependent of 4 non-dimensional numbers:

$$K^+_{total} = f(t^+, Sc, Re_g, \frac{\rho_d}{\rho_g}) \tag{3.125}$$

where Sc is the ratio of the kinematic viscosity of the gas to the Brownian diffusivity. It is interesting to point out that if we use a Reynolds number based on the friction velocity (that is roughly proportional to the bulk velocity) and on a typical large eddy size (that scales roughly as the diameter of the tube) we can write Re as:

$$Re = \frac{u_\tau^2 \tau_c}{\nu_g} \tag{3.126}$$

where τ_c is the eddy time scale. The ratio of this Reynolds number with t^+ is $\eta = \tau_c/\tau$ so that we can also write:

$$K^+_{total} = f(t^+, Sc, \eta, \frac{\rho_d}{\rho_g}) \tag{3.127}$$

Study of $K^+_{total}(t^+)$. The most important parameter when studying the turbulent deposition velocity remains the relaxation time of the particles. Figure 3.12 represents K^+_{total} as a function of t^+. The curve of Figure 3.12 was first deduced from experimental results. The collapse of the experimental data is generally good except for times over 20. This curve and experimental data can been found in McCoy and Hanratty (1977) or Young and Leeming (1997) among others. Figure 3.12 shows three deposition regimes: the diffusional depo-

sition regime, the diffusion-impaction regime and the inertia-moderated regime[7].

The diffusional deposition regime. For very small particles ($t^+ < 0.3$), Brownian diffusion dominates very close to the wall and determines totally the deposition flux. The deposition velocity is a function of the Schmidt number only. Young and Leeming (1997) derived the relation:

$$K^+_{total} = 0.073\, Sc^{-2/3} \tag{3.128}$$

which is confirmed first experimentally and second analytically (Slater *et al.* (2003) and references therein). With Einstein's relation[8] , it is possible to show that, in this regime, $K^+_{total} \propto {t^+}^{-1/3}$. Diffusional deposition is most relevant for particles having a diameter of 1 μm or less.
Havelka *et al.* (2004) studied the diameter of the droplets generated by a jet of hydrocarbons. At high pressure (around 100 bars) droplets were considerably smaller than at atmospheric pressure. Besides, secondary droplets (generated from droplet splash on the film) can also be very small. As a result, during high pressure gas/liquid separation there are probably numerous small droplets. However, the total mass of tiny droplets is probably negligible compare to the mass of large drops. That is why Brownian diffusion is neglected in the present model.

The diffusion-impaction regime. In the diffusion-impaction regime, the inertia of the dispersed phase becomes significant. This region is characterized by a tremendous increase in deposition rates with the diameter of the particles. Three recent papers (Narayan *et al.* (2003), Marchioli *et al.* (2003) and Mito and Hanratty (2004)) separated the deposition process in the diffusion impaction regime in two categories:

- The turbulent diffusion: particles are transported toward the wall and then diffuse to the wall under the effect of the residual turbulent fluctuations of the gas in the boundary layer.

- An inner boundary layer phenomenon where particles disengage from turbulent structures at a certain distance from the wall and deposit.

All, noted that the percentage of deposited particles because of the second mechanism increased with the relaxation time. McCoy and Hanratty (1977)

[7]To keep the presentation clear and concise the description of the phenomena involved in each regime has been voluntarily simplified. Effects due to lift forces, the so called "direct impaction" mechanism, thermo-, electro- or diffusiophoresis, low speed streaks and droplet concentration are not discussed.

[8]Given B the Brownian diffusion coefficient, m_p the mass of the particle, τ its relaxation time, k_B Boltzmann's constant and T the temperature, according to Einstein's relation:

$$B = \frac{k_B T \tau}{m_p}$$

proposed for the diffusion-impaction region:

$$K^+_{total} = 3.25 \cdot 10^{-4} {t^+}^2 \tag{3.129}$$

Liu and Agarwal (1974) proposed:

$$K^+_{total} = 6 \cdot 10^{-4} {t^+}^2 \tag{3.130}$$

Equation (3.130) is based on a smaller range of t^+, so equation (3.129) will be preferred. The increase of several orders of magnitude of the deposition velocity, is due to a phenomenon called "turbophoresis". It has been mentioned first by Reeks (1983). Qualitatively Slater *et al.* (2003) described turbophoresis as follows:"*Particles impelled toward the wall by eddies in the buffer layer coast into the sub-layer from where they are unable to return because the turbulent fluctuations are on average too small.*"
In the diffusion-impaction regime, the particles are sufficiently small to be very reactive to turbulence in the core. Consequently the turbulent dispersion is very effective and the related deposition velocity K^+_{disp} is very large. As a result, in this regime $K_{total} \approx K_{wall}$. Then, in the present model, according to equation (3.129), K_{wall} will be computed in the diffusion-impaction regime by:

$$K^+_{wall} = 3.25 \cdot 10^{-4} {t^+}^2 \tag{3.131}$$

The Inertia moderated regime. In this regime, the size of the particles is so large that they respond only partially to the gas turbulence. Consequently, the deposition becomes smaller as the relaxation time increases. For this regime McCoy and Hanratty (1977) reported the experimental data of Farmer that could be correlated by:

$$K^+_{total} = \frac{20.7}{\sqrt{t^+}} \tag{3.132}$$

where t^+ was between 1 000 and 100 000[9]. However, in this regime, there was a significant scatter of the data, between:

1. The data of Liu and Agarwal (1974), where the non-dimensional deposition velocity decreases slightly with the relaxation time. This velocity had a maximum value of about 0.15. [10]

[9]The literature mentions sometimes the work of Sehmel (1970) who correlated data as

$$K^+_{total} \approx \frac{1.49}{\sqrt{t^+}}$$

Nevertheless it was not only for large t^+ but also included times as small as 0.2. This is in contradiction with theory and experimental data.

[10]They used mono-dispersed particles of olive oil between 1.4 and 21 μm, injected in an air stream. The particles deposited on the wall of a 1.27 cm i.d tube which was about 80 diameters long. The particles were electrically neutralized. The flow was downward. They took special care to ensure a perfect adherence of the particles on the wall so that no bouncing or re-entrainment could occur.

2. The data of Cousins and Hewitt[11], where the non-dimensional deposition velocity was around 0.095 for a pipe of 0.00953 m i.d and 0.068 for a pipe of 0.0318m i.d. [12]

3. Various other data collected by McCoy and Hanratty (1977) which average is $K^+_{total} = 0.17$.

The decrease of the deposition velocity seemed to appear at larger t^+ for Farmer than for Liu and Agarwal. Uijttewaal and Oliemans (1996) brought a new insight in the understanding of the inertia moderated regime. They were the first to use LES to compute the deposition of particles in a pipe at high Reynolds numbers. They also performed a DNS to compute the flow of the gas. They did a Lagrangian tracking of 10 000 particles per relaxation time, and used 12 different relaxation t^+ between 5 and 10 240. Depending on the Reynold number of the gas, the values of $K^+_{total}(t^+)$ were spread out from 0.03 to 0.08 for a relaxation time of 10 000. On the contrary, the collapse of the data was quasi perfect when K^+_{total} was plotted as a function of $1/\eta$. In Figure 3.13 the simulation results of Uijttewaal and Oliemans (1996) have been plotted together with relation (3.123) and with the best possible fit:

$$K_{total} = 1.72 \frac{u_\tau}{\sqrt{2\pi}} \sqrt{\frac{\eta}{1+\eta}} \tag{3.133}$$

It is crucial however to consider that, for very large particle diameters, the dispersion coefficient of the droplets in the core drops dramatically so that $K^+_{total} < K^+_{wall}$. As a matter of fact, Uijttewaal and Oliemans (1996) underlined that for large particles the deposition velocity was first determined by the turbulent dispersion. Hence, it is not possible to find the value of K^+_{wall} for $t^+ > 20$ from Figure 3.12. Here we will tentatively suppose that $K^+_{wall} = 0.17$ for $t^+ > 20$. The validity of this assumption will be studied in chapter 5.

To sum up:

- The diffusional deposition regime is not considered in our case.
- For $t^+ < 22.871$, it is the diffusion-impaction regime.

$$K^+_{total} = K^+_{wall} = 3.25 \cdot 10^{-4} {t^+}^2 \tag{3.134}$$

- For $22.871 < t^+$, it is the inertia-moderated regime.

$$K^+_{wall} \approx 0.17 \tag{3.135}$$

The value of 22.871 ensures the continuity of the function $K^+_{wall}(t^+)$ at the transition between the diffusion-impaction regime and the inertia moderated regime.

[11] Cousins, L. B. and G. F. Hewitt (1968). Liquid phase transfer mass transfer in annular two-phase flow: droplet deposition and liquid entrainment. *AERE-R 5657.*

[12] The experiments were done in an air/water upward annular flow not far from equilibrium. The film was totally removed a first time, through a porous media. The droplets then redeposited on the wall and were extracted again at various downstream locations. The amount of liquid extracted lead to the deposition coefficient.

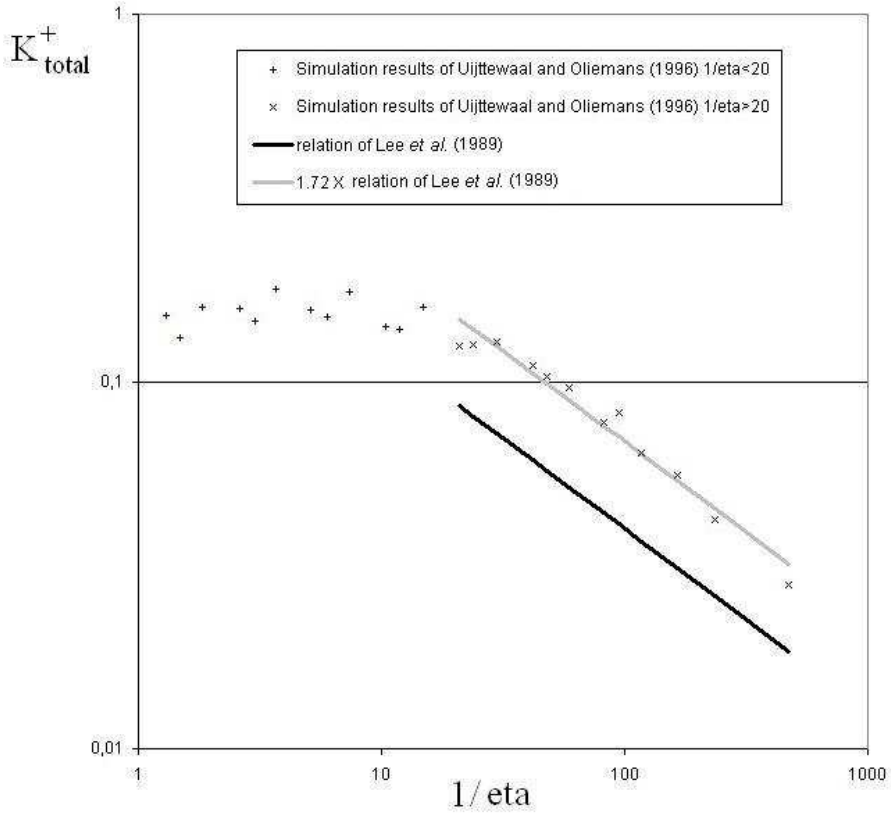

Figure 3.13: Results of Uijttewaal and Oliemans (1996) compared to the relation of Lee *et al.* (1989).

Additional remarks. Andreussi (1983) pointed out that as far as droplet flows were concerned, the diameter of the particles were still relaying on correlations that were far from certain so that the experimental points on a graph such as Figure 3.12 should be taken with caution. Another interesting point for annular flows was underlined by Lopes and Dukler (1986). They noted that a non negligible part of the pressure gradient was due to droplet deposition and re-entrainment. Thus the friction velocity calculated from this gradient was overestimated. This could explain the low values of deposition obtained by Cousins and coworkers.

3.3.3 Entrainment rate

a) Qualitative description of entrainment

One of the first studies on entrainment was performed by Hanratty and Engen (1957). They studied the effect of the velocity of an air stream on the interface of a film. The experiment was performed in a rectangular channel for a stratified flow. They observed as the gas flow rate increased:

1. A smooth interface
2. 2D waves
3. 3D waves (squalls)
4. roll waves (or disturbance waves)
5. Atomization

In the last regime, liquid is torn out of the film and dispersed as droplets. Woodmansee and Hanratty (1969) pinpointed that the entrainment of droplets from roll waves was the main source of droplets. They described it rather precisely. First wavelets on top of the roll wave are accelerated toward the front of the large wave. The small ripples are then detached from the wave and form a liquid rim, which can surround a liquid membrane (Dykhno *et al.* (1996)). The rim, attached to the wave, disintegrates into droplets. The potential membrane contributes very little to the mass entrained. These steps are illustrated on Figures 3.14, 3.15, and 3.16. Azzopardi (1997) reported an interesting experiment that showed that droplets can be generated from roll waves. A single roll wave was generated in a tube. As the wave approached, a high speed camera detected more and more droplets. Their number decreased as the wave passed away. Another result comes from the work of Paras and Karabelas (1991). They studied the properties of the liquid film in a horizontal air-water annular flow at atmospheric pressure in a tube of 50.8 mm i.d. They measured the reduction of the correlation coefficient of the roll waves (film height) with the axial position. They could then deduce the life time of the wave. The coefficient showed a very rapid decay (exponential). It indicated that the waves were quickly distorted

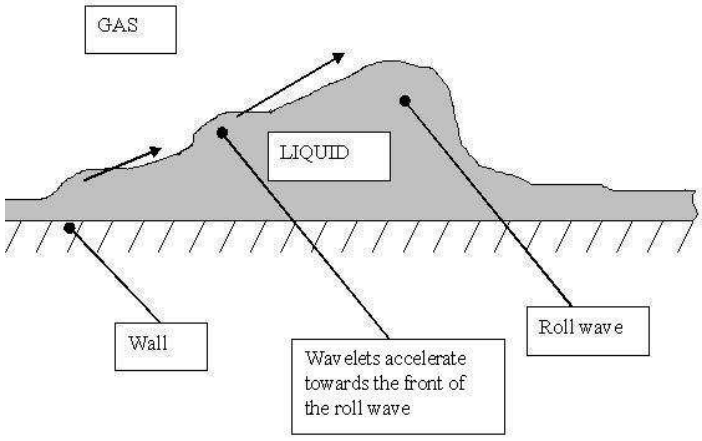

Figure 3.14: Side view of a roll wave with its accelerated wavelets.

after their creation (less than a second). The reason of the quick wave disappearance can be a strong entrainment of droplets. At least at low-pressure, entrainment from roll waves is seen today as the main source of entrainment (see among others: Van Rossum (1959), Hewitt and Hall Taylor (1970), Ishii and Grolmes (1975), Nigmatulin (1991)). We will now give two additional pieces of information relevant to the case of scrubbers and gas production, namely the effect of large diameter and the effect of high pressure. Azzopardi and Gibbons (1983) studied annular flows in large diameter tube (125 mm i.d.). They showed that the disturbance waves had different geometrical characteristics, in particular they were:

- localized circumferentially
- not perpendicular to the main flow but curved

However, Azzopardi and Gibbons could, to reproduce their entrained fraction data, use the model of Ishii and Mishima (1989) which is not developed for large diameter pipes. It may be an indication, that, whereas the waves are geometrically different, the overall impact of this difference is small.
Trabold and Kumar (2000a) presented experiments with a refrigerant fluid (R-134a) at high pressure (14 and 24 bars). They also observed disturbance waves. Thus at high pressure, entrainment mechanisms are likely to be similar.
Roll waves are necessary for entrainment, but not sufficient. The onset of entrainment does not necessarily coincide with the onset of roll waves (Van Rossum (1959)). However, Hewitt and Hall Taylor (1970) pointed out that at high gas flow rate the creation of droplets and the appearance of disturbance waves are simultaneous. To conclude about the entrainment from roll waves we can say that:

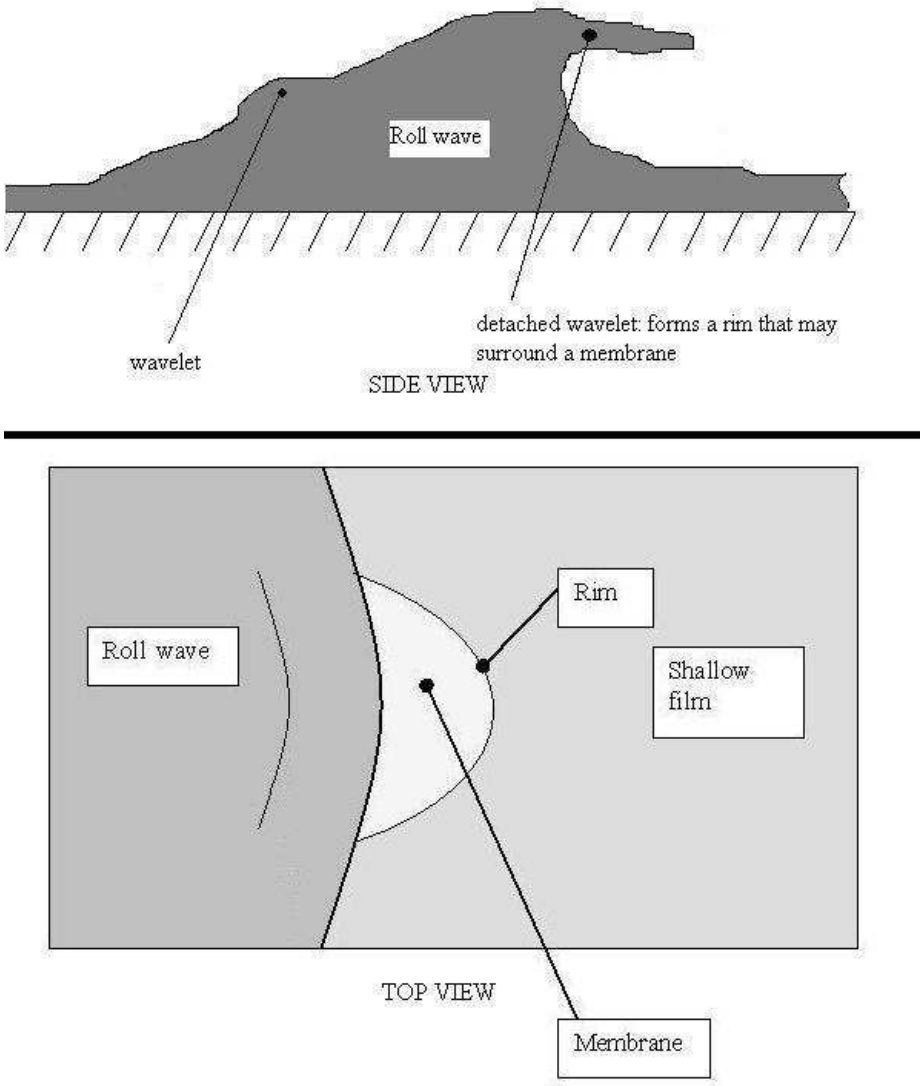

Figure 3.15: Forming of an arch from a ripple.

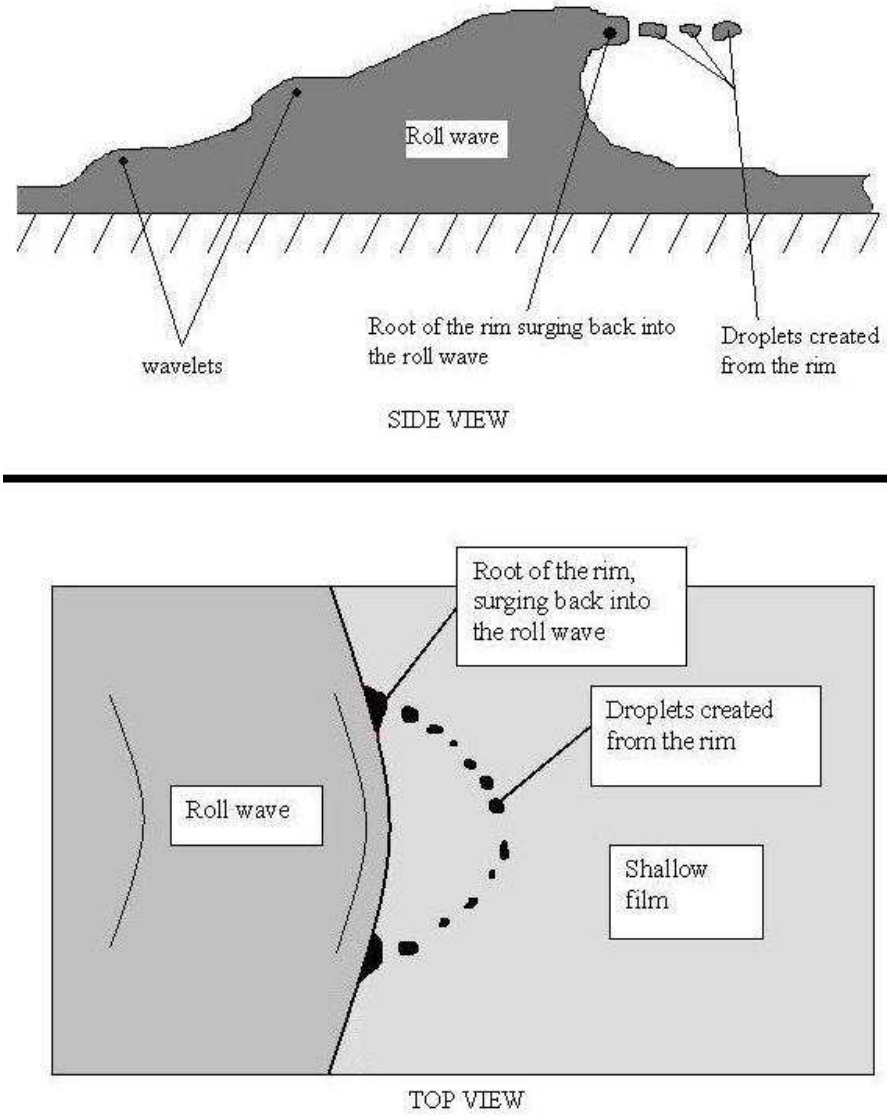

Figure 3.16: Forming of droplets from an arch.

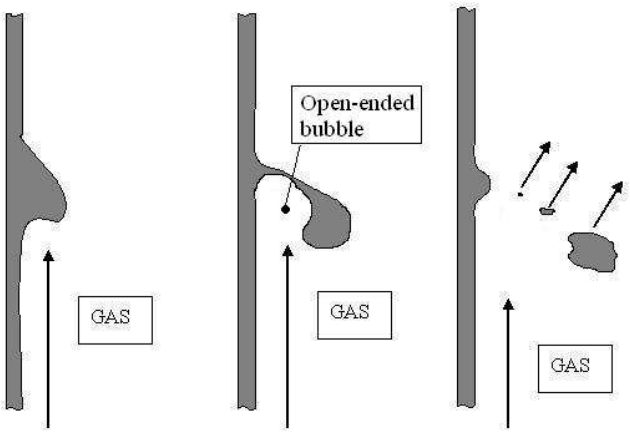

Figure 3.17: The wave undercut mechanism.

- The shearing of roll waves is, according to experimental observations and measurements, an important mechanism for droplet generation in an annular flow.
- According to the study of Azzopardi and Gibbons (1983), roll waves in large diameter pipes are geometrically different from roll waves in small diameter pipes. The entrained liquid fraction may however not change.
- Roll waves occur in high pressure systems.
- Roll waves do not necessarily generate droplets especially at low gas flow rate.

There are other entrainment mechanisms than the shearing of droplets from disturbance waves:

1. The wave undercut mechanism[13]: This is probably the most important mechanism after the generation of droplets from disturbance waves. This entrainment type occurs at moderate gas velocities. According to Hewitt and Hall-Taylor (1970), this entrainment process comes from the formation of an open-ended bubble that undercuts the wave. The dynamic pressure increases in this bubble until the wave bursts. Figure 3.17 illustrates this mechanism. Ishii and Grolmes (1975) showed, based on experimental evidences, that the wave undercut mechanism enhances significantly entrainment at low film fluxes. Azzopardi (1997) and Ishii and Grolmes (1975) proposed a criterion to draw the line between the wave

[13]Azzopardi (1997) mentioned a similarity between this type of break up and the bag break-up of droplets. He also noted a similarity between the shearing of roll waves and the ligament break up of droplets. These droplet break-up mechanisms were photographed by Hinze (1955).

undercut mechanism and the shearing of roll wave mechanism. Jepson *et al.* (1989) pointed out that the wave undercut mechanism might generate larger droplets than the shearing of roll waves.

2. Bursting of bubbles: It has been described extensively by Hewitt and Hall Taylor (1970). Bubbles come from gas trapped in the film. They can also be generated by a boiling film. This last point has been studied by Nigamatulin (1991). Meng *et al.* (2001) performed experiments with air and oil[14]. They pinpointed that bubble bursting was an important source of entrainment.

3. Splashes of droplets: This mode of entrainment has been studied by Nigmatulin (1991). He proposed an entrainment rate proportional to the deposition rate. Schmehl *et al.* (1999) also did a detailed study of the splashing and rebound condition of droplets on the liquid interface. Ishii and Grolmes (1975) mentioned a similar mechanism involving the tip of a disturbance wave splashing on the interface.

4. Liquid bulge disintegration: This mechanism has been mentioned by Ishii and Grolmes (1975). It can be encountered in annular counter-current flows near the flooding point where waves located at different circumferential positions join and form a liquid bridge across the tube section. The disintegration of this bridge generates droplets.

b) Measuring entrainment rates

Measuring the entrainment rate from a liquid film is difficult. The first reliable technique consisted in considering the mass balance on the film. Given a vertical annular flow oriented along the z axis, the liquid mass flow rate $\dot{m}_f$, the deposition rate J_d and the entrainment rate J_e, the mass conservation equation is:

$$\frac{d\dot{m}_f}{dz} = \pi D \left(J_d - J_e \right) \tag{3.136}$$

The first measurements reported were at equilibrium when $\frac{d\dot{m}_f}{dz} = 0$. In this case, the measurement of J_d leads to the entrainment rate J_e. This has been done by Hutchinson and Whalley (1973). Ueda (1979) measured in addition the gradient of the film mass flow rate and thereby got rid of the equilibrium assumption. Quandt (1965), Jagota *et al.* (1973) and Andreussi (1983) developed a technique which is based on the injection of a tracer in the liquid film. The tracer is usually a solution of sodium chloride so that the measurement of the electrical conductivity of the dispersed phase along the flow provides the entrainment rate. Leman *et al.* (1985) and Schadel (1988) used this technique.

[14]Experiments were performed in a 50.1 mm pipe that could be inclined by $\pm 2^{\circ}$. The liquid properties of the oil at 24℃ were a viscosity of 5.66 cP and a surface tension of 30 dyne/cm.

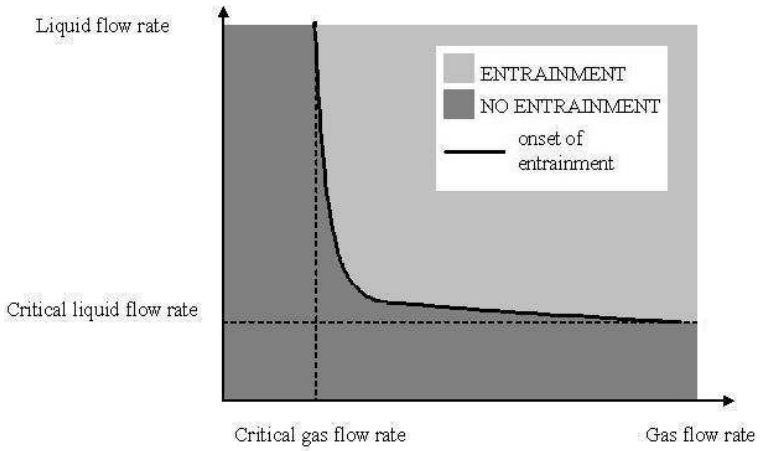

Figure 3.18: Onset of re-entrainment

c) Critical liquid flow rate and critical gas flow rate

Cousins and coworkers[15] measured the entrained fraction[16] and entrainment rates in upward annular air-water flow. Graph 3.18 illustrates their results.

1. There is a region were the gas flow rate is too low to lead to any entrainment irrespective of the liquid flow rate. This zone is bounded by a critical gas flow rate.

2. There is a region were the liquid flux is too low to lead to any entrainment irrespective of the gas flow rate. This zone is bounded by a critical liquid flow rate.

3. In between those two regions there is a zone were the onset of re-entrainment is dependent both on the gas and on the liquid flow rate.

Wallis (1969) performed a series of experiments in an air-water downward annular flow that confirmed these results. As the air flow rate increased he classified the results in 4 zones:

1. No entrainment.

2. A small entrained fraction increasing very slowly with the gas flux.

[15]Cousins, L. B. and G. F. Hewitt (1968). Liquid phase transfer mass transfer in annular two-phase flow: droplet deposition and liquid entrainment. *AERE-R 5657.*
Cousins, L. B., W. H. Denton and G. F. Hewitt (1965). Liquid phase transfer mass transfer in annular two-phase flow. In *Proc. of the Symp. on Two Phase Flow. Paper C4.* Exeter.
Cousins, L. B., W. H. Denton and G. F. Hewitt (1965). Liquid phase transfer mass transfer in annular two-phase flow. *R6426.* Harwell.

[16]Unless specified otherwise the entrained fraction is defined in the present work as the ratio of the entrained mass flux to the total liquid mass flux.

3. A zone where the entrained fraction increased linearly with the air flux.

4. A saturation zone where the entrained fraction becomes constant.

The last zone is characterized by a critical film flow rate under which no entrainment occurs. The value of the gas velocity for the onset of entrainment was a decreasing function of the liquid flow rate. This gas velocity tended toward a constant at high liquid flow rates. Thus at high liquid flow rate, the onset of entrainment depends only on the gas flux. It confirms perfectly the experiments conducted by Cousins and coworkers. The existence of a critical gas velocity and of a critical liquid flow rate has been confirmed theoretically by the study of Andreussi *et al.* (1985) though they did not take surface tension effects into account and had one adjustable parameter.
In the case of a gas pipe the gas flux is very high, it is likely that the film flow rate is the critical one. This special flow regime is called *fully entrained atomization region*. In this regime:

- The entrained fraction (defined in terms of mass flow rate or volume fractions) is maximal and less than 1.
- The film mass flow rate is the critical one.
- An increase of gas velocity has little impact on the entrained fraction.

One should note that the previously described experimental results were obtained in a developed regime. Leman *et al.* (1985) pointed out that at the inlet of a pipe there is no entrainment because a certain length is necessary for the development of roll waves.
It is important to take into account the effect of the critical film flow rate. An example to the contrary is the entrainment correlation of Ishii and Mishima (1989). Assad *et al.* (1998) tested this correlation against air/water, Freon and steam/water data. The steam data were taken from 34 to 69 bars and the Freon data from 2.5 to 56 bars. Both data sets were characterized by low surface tensions (roughly 0.01 $N \cdot m^{-1}$). Assad *et al.* (1998) noticed an extremely good collapse of the data in spite of the wide spread in fluid properties. Nonetheless the relation of Ishii and Mishima (1989) overpredicted the entrained fraction when the entrained fraction was above 40%. The very same result has been obtained by Meng *et al.* (2001) for oil/air flows. Pan and Hanratty (2002a) and Su *et al.* (2003) emphasized the same drawback. When the entrained fraction is over 40%, the film flow rate is small and tends toward its critical value. At the critical value the entrainmed fraction is less than one. The relation of Ishii and Mishima (1989) that does not take the critical film flow rate into account, predicts an entrained fraction of 1 at large gas flow rates. Therefore it overpredicts the real entrained fraction. It is thus necesseray to include the critical film flow rate.
The characterization of the critical gas velocity is less obvious. Wallis (1968) published data that indicated that it decreases with the pressure of the system. Pan and Hanratty (2002a) correlated the critical gas velocity based on air-water

P (bars)	Σ (N/m)	ρ_f/ρ_g	μ_f/μ_g
5	0.01085	41	24
10	0.00705	19	16
20	0.00355	7	11

Table 3.2: Physical properties for the Freon experiments as reported by Lopez de Bertodano *et al.* (2001)

experiments at different pressures and one Helium-water experiment. Nevertheless the Freon data of Lopez de Bertodano *et al.* (2001) did not collapse with the relation proposed by Pan and Hanratty (2002a). The fluid properties of the experiment of Lopez de Bertodano *et al.* (2001) are given in Table 3.2. These experiments are interesting because they were performed at high pressures with low surface tension fluids as in an operating scrubber. The data obtained with freon showed that the critical gas velocity was very small for low surface tension/high pressure tests. It is therefore not strictly necessary to include a critical gas flow rate in the case of high pressure gas-liquid separation. More research is needed to characterize precisely the critical gas flow rate.

d) Elements of theory

The Kelvin Helmholtz instability. There is at present no analytical means to calculate an entrainment rate. However, theory can give a good understanding of the mechanisms taking place when a drop is torn away from a liquid film. Woodmansee and Hanratty (1969) explained entrainment as a result of the Kelvin-Helmholtz instability. This instability is illustrated on Figure 3.19. A small harmonic perturbation generates an increased pressure above troughs and a suction over the crests (Bernoulli). If the stabilizing effect of the surface tension is overcome, the interface becomes unstable. The theory of the Kelvin-Helmholtz instability considers inviscid fluids and an infinitely thick film. Given some height and pressure perturbations $h^{'}$ and $p^{'}$, such as:

$$h^{'} = \Re\left(\underline{h}^{'}\right) = \Re\left(\underline{H}\, e^{i(k\,x-\omega\,t)}\right) \tag{3.137}$$

$$p^{'} = \Re\left(\underline{p}^{'}\right) = \Re\left(\underline{P}\, e^{i(k\,x-\omega\,t)}\right) \tag{3.138}$$

$\Re(z)$ is the real part of the complex number z. The stability condition is (supposing $\rho_d >> \rho_g$):

$$\Sigma k^2 - \rho_d g_y + \frac{\Re\left(\underline{P}\right)}{\Re\left(\underline{H}\right)} \geq 0 \tag{3.139}$$

The value of $\Re\left(\underline{P}\right)/\Re\left(\underline{H}\right)$ is originally found by supposing two uniform velocity profiles. However Woodmansee and Hanratty (1969) found this hypothesis to be inaccurate. Instead they assumed a gas profile depending on the gas eddy viscosity. They obtained a semi-empirical expression for $\Re\left(\underline{P}\right)/\Re\left(\underline{H}\right)$ that was

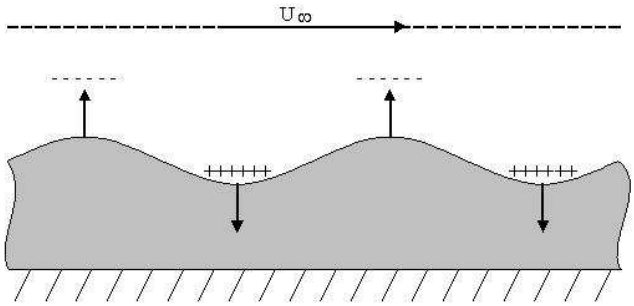

Figure 3.19: Kelvin-Helmholtz instability.

proportional to the solution assuming uniform profiles [17]. As Woodmansee and Hanratty identified the type of instability generating entrainment, they could provide a sensible dimensional analysis of the problem. Neglecting the gravity, they proposed the Weber number to be the most important parameter:

$$We = \frac{\rho_g \left(U_g - C\right)^2 h^*}{\Sigma} \tag{3.140}$$

where U_g is the gas velocity, C the wave velocity and h^* some characteristic length of the film (mean height of the film or height of the wave or height of the crest from the wall). From experimental results, they suggested $We \geq 5.5$ as a criteria for re-entrainment; h^* being the height of the roll waves.

Work of Tatterson and Taylor. Tatterson (1975) tried to get a quantitative expression for the rate of entrainment from theory. He used the theory developed by Taylor (1963) that studied the growth rate of a harmonic wave perturbation on a viscous fluid of infinite depth on top of which flowed an inviscid fluid of small density compared to the first fluid.

$$\rho_g << \rho_f$$

[17] This solution being:

$$\frac{\Re\left(\underline{P}\right)}{\Re\left(\underline{H}\right)} = -\rho_g U_g^2 k$$

Let us consider a perturbation:

$$\underline{h}^{'} = \underline{H}\, e^{i(k\,x - \underline{\omega}\,t)} \tag{3.141}$$

where $\underline{h}^{'}$, $\underline{H}$ and $\underline{\omega}$ are complex numbers. The real part of $\underline{\omega}$ is an angular frequency. The imaginary part of $\underline{\omega}$ describes the growth rate of the waves. As long as the amplitude is small Taylor derived:

$$\Im(\underline{\omega}) = 2\,We\,k\,U_g\sqrt{\frac{\rho_g}{\rho_g}}f\left(We, \frac{1}{We\,Vi^2}\right) \tag{3.142}$$

$\Im(\underline{\omega})$ is the imaginary part of the complex number $\underline{\omega}$. We is a Weber number. Its definition is flexible, not only concerning the length scale but also concerning the velocity and the density. One can use the friction velocity, the interfacial shear stress or the superficial gas velocity to define We. This point will be discussed later. f is a function. Taylor (1963) tabulated the value of this function for the fastest growing wave. The number Vi is the viscosity group. Hinze (1955) showed that it was an important factor for the break-up of a drop in a turbulent stream. For a drop of diameter d, its definition is:

$$Vi \equiv \frac{\mu_d}{\sqrt{\rho_d \Sigma d}} \tag{3.143}$$

The viscosity number Vi was presented by Sleicher (1962) as the viscosity forces arising from the natural vibration of the droplet in its first mode. In relation (3.142), the Weber and the viscosity number are based on the length scale $1/k$. Taylor argued that the characteristic time for a wave to grow to the stage where droplet creation is imminent, is proportional to $1/\Im(\underline{\omega})$:

$$t \propto \frac{1}{\Im(\underline{\omega})} \tag{3.144}$$

Taylor proposed that the area of the wave generating the droplets scales like $1/k^2$. Tatterson (1975) postulated that the volume entrained from this wave is equal to the volume of a fluid ligament detaching from the wave. Based on former works Tatterson proposed an expression for the diameter of the ligament d_{lig}:

$$d_{lig} = \frac{1}{k\sqrt{We}} \tag{3.145}$$

And if the length of the ligament is $1/k$, the entrained volume scales as:

$$\frac{d_{lig}^2}{k}$$

As a result, combining equations (3.144) and (3.145) and the different volume and surface scalings we obtain:

$$\begin{aligned} J_e &\propto \rho_f \frac{\frac{d_{lig}^2}{k}\Im(\underline{\omega})}{\frac{1}{k^2}} \\ &\propto \sqrt{\rho_f \rho_g} U_g f\left(We, \frac{1}{We\,Vi^2}\right) \end{aligned} \tag{3.146}$$

It is then natural to define:

$$\dot{E}^{+} \equiv \frac{J_e}{\sqrt{\rho_f \rho_g} U_g} \tag{3.147}$$

The second variable of the function f in relation (3.146) corresponds to a viscous damping of the wave. For moderate viscosities, $1/(We \cdot Vi^2)$ tends toward infinity and f becomes a function of We only. Lopez de Bertonado *et al.* (2001) gave the following quantitative criteria:

$$if\ \frac{1}{We\,Vi^2} > 100\ \ then\ f\left(We, \frac{1}{We\,Vi^2}\right) \approx f\left(We\right)$$

Taylor (1963) found it convenient to replace We by the variable:

$$Y = \frac{We - 1}{We_m - 1} \tag{3.148}$$

where the index m is associated with the wave number k_m of the fastest growing wave. $f(Y)$ becomes the constant $f(1)$ for this wave. Taylor argued that k_m was the wave number to be used in equation (3.146). In this case $\dot{E}^{+}$ is a constant. Thus the theory developed by Taylor shows that the entrainment flux is proportional to $\sqrt{\rho_f \rho_g} U_g$. This theory also shows that, for a liquid film of infinite depth, small viscosity and large density compared to the density of the gas, the non-dimensional entrainment flux is a constant.

Finite depth of fluid, viscosity of the gas phase and intermittency. Tatterson pinpointed that in annular flows the liquid film is far from being of infinite depth as in the study of Taylor. Tatterson proposed that the height of the film imposed a lower limit on the wave number such as:

$$k_{min} = \frac{1}{h} \tag{3.149}$$

This condition changes equation (3.148) into:

$$Y = \frac{We(h) - We_{crit}}{We_m - We_{crit}} \tag{3.150}$$

where We is now based on the height of the film. In (3.150) a critical Weber number appears. Under We_{crit} no entrainment occurs.
Tatterson pointed out another important weakness of the analysis of Taylor. The shear stress of the gas on the liquid is a very important factor for the study of atomization. However Taylor supposed an inviscid flow of the gas. When the viscosity is taken into account it leads to the well-known Orr-Sommerfeld equation. By supposing a universal turbulent profile over the surface Tatterson concluded that one should use the equation:

$$\dot{E}^{+} \propto f\left(We(h)\sqrt{\frac{h}{D}}\right) \tag{3.151}$$

instead of $f(We(h))$. Nevertheless Dallman *et al.* (1979) underlined that equation (3.151) could not really be used with confidence without further verification. In addition Tatterson introduced a quantity he called the intermittency. The surface of a film in an annular flow is not entirely covered with roll waves. The intermittency $\mathscr{I}$ represents the fraction of the film covered with these waves. Taking the intermittency into account, equation (3.151) becomes:

$$\dot{E}^+ \propto \mathscr{I} \cdot f\left(We(h)\sqrt{\frac{h}{D}}\right) \tag{3.152}$$

Schadel (1988) and Paras *et al.* (1994) provided intermittency data for respectively vertical up-flow and horizontal flow. Schadel claimed the intermittency to be independent of the gas velocity. But her data presented by Azzopardi (1997) showed a decrease of $\mathscr{I}$ with the gas velocity. In contrast, Paras *et al.* (1994) presented intermittency data where, at least at low gas velocity (stratified flow), the intermittency increased roughly linearly with the gas velocity. At high gas velocities (annular flow), the intermittency became independent of the gas velocity. Hence, at present experimental data are contradictory. It is then difficult, to say anything general about intermittency today. There is no correlation that relates it to flow variables. It must be experimentally determined. It seems however that a value of 0.4 can be a fair estimation (Paras and Karabellas (1991), Schadel (1988)).

e) Dimensional analysis

There are numerous different correlations for the rate of entrainment in the literature. These correlations are, as a rule, difficult to compare, because the entrainment flux is not non-dimensionalized the same way or because the correlations are dimensional. The aim of this paragraph is to collect some key correlations and to translate them into the same language. Then the physical meaning of each correlation will appear clearly through the dimensional group involved.

According to the theory developed by Taylor (1963), a natural scaling for the rate of entrainment is the one defined by equation (3.147). The correlations of Dallman *et al.* (1979) and Lopez de Bertodano *et al.* (2001) can easily be expressed with $\dot{E}^+$. Schadel (1988) presented her result with this non-dimensional entrainment rate. Alipchenkov *et al.* (2002b) presented a correlation similar but where $\sqrt{\rho_f \rho_g} U_g$ was replaced by $\sqrt{\rho_f \tau_i}$ where τ_i was the interfacial shear stress. Pan and Hanratty (2002a) introduced the critical gas velocity $U_{g,crit}$ and replaced (3.147) by:

$$\dot{E}^+ = \frac{J_e}{\sqrt{\rho_f \rho_g}\,(U_g - U_{g,crit})} \tag{3.153}$$

As discussed previously, the introduction of a critical gas velocity for high pressure applications is not necessarily pertinent. Other non-dimensionalization factors are possible. Hewitt and Govan (1990) chose to scale the entrainment rate with the mass flux of gas. Nigmatulin (1991) chose the liquid film flow

Exponents (Corresponding group)	a_1 $(\frac{\mu_f}{\mu_g})$	a_2 $(\frac{\rho_f}{\rho_g})$	a_3 $(\frac{h}{D})$	a_4 (Re_f)	a_5 (We)	a_6 (Vi)	a_7 (Ω)
Hewitt and Govan (1990)	0	0.132	0.316	0.632	0	0.632	0
Nigmatulin (1991)	0	0.5	1	0	0.35	1	-0.7[18]
Lopez de Bertodano *et al.* (1997)	-0.26	0.4625	0.075	0.925	0.425	1	0
Lopez de Bertodano *et al.* (2001) and Pan and Hanratty (2002a)	0	0.5	0	1	0.5	1	0
Alipchenkov *et al.* (2002b)	0	0	0	0	1	0	0

Table 3.3: Some correlations of the literature expressed as a function of the basic non-dimensional numbers.

rate. Lopez de Bertodano *et al.* (1997) and Kataoka *et al.* (2000) chose the quantity μ_f/D. However it is possible to express most of these correlations with the scaling used in (3.147). All the correlations depend on the 10 following parameters:

$$\mu_g; \mu_f; \rho_g; \rho_f; \Sigma; h; D; U_f; U_g; g$$

It gives 7 non-dimensional parameters:

$$\frac{\mu_f}{\mu_g}; \frac{\rho_f}{\rho_g}; \frac{h}{D}; Re_f = \frac{\rho_f U_f h}{\mu_f}; We = \frac{\rho_g U_g^2 h}{\Sigma}; Vi = \frac{\mu_f}{\sqrt{\Sigma \rho_f h}}; \Omega = \mu_f \sqrt[4]{\frac{g}{\rho_f \Sigma^3}}$$

The last group is the ratio of the gravity forces against capillary forces. It is then possible to express the non-dimensional entrainment flux $\dot{E}^+$ as a function of the above non-dimensional parameters. For example:

$$\dot{E}^+ = \left(\frac{\mu_f}{\mu_g}\right)^{a1} \left(\frac{\rho_f}{\rho_g}\right)^{a2} \left(\frac{h}{D}\right)^{a3} Re_f^{a4} We^{a5} Vi^{a6} \Omega^{a7} \tag{3.154}$$

Table 3.3 shows the values of the exponents of each group for different correlations of the literature, far from the onset of entrainment. We can see that there is no general agreement.

f) Choice of a correlation

A pertinent correlation for the rate of entrainment is hard to find. Theory can give some clues but is not sufficient. The correlation must be tested against

[18] There is a misprint in Nigmatulin (1991) where Ω is at the power 1 instead of -0.7 (see Nigmatulin *et al.* (1996)).

a large number of experiments. In our case it must also be tested with high pressure data where surface tensions are significantly low. If possible it should be confirmed by independent results. The correlation must also have a local nature. Indeed, in a scrubber or in a complex geometry it is not easy to get or even to define such a thing as a superficial velocity or a diameter. Finally we believe that the correlation must represent simple physics. Basically, so little is known about entrainment that a correlation having a great complexity is a priori not trustworthy outside the range it has been designed for.
One correlation in the literature does have all these criteria fulfilled. It is a relation presented by Alipchenkov *et al.* (2002b) (see also Alipchenkov *et al.* (2004)). The correlation is the following:

$$J_e = 0.023 \sqrt{\rho_f \tau_i} \, (We - We_{crit}) \tag{3.155}$$

The Weber number is defined as:

$$We = \frac{\tau_i h}{\Sigma} \tag{3.156}$$

Relation (3.155), as the theory of Tatterson (1975), includes both a Weber number and a critical Weber number. It has been tested on air/water and steam/water data with pressures up to 100 bars. Antipin *et al.* (2003) tested the correlations of Alipchenkov *et al.* (2002b) against their own experimental data. They performed tests in a pipe of 15 mm i.d. with air-water and air-glycerin flows. The flows were both upward and downward, the surface tensions between 0.065 N/m and 0.072 and the viscosity of the liquid between 0.001 and 0.0022 $kg \cdot m^{-1} \cdot s^{-1}$. The predictions in terms of pressure gradients and film thickness were rather correct. There was no systematic under or over prediction of the experimental results although a scatter was noticed. The work of Schadel and Hanratty (1989) brings an independent confirmation of relation (3.155) at least for the coefficient 0.023. They performed air/water experiments at 1 bar in a downward annular flow. They plotted the quantity:

$$\dot{E}^+ = \frac{J_e}{u_\tau \sqrt{\rho_g \rho_f}}$$

as a function of

$$\mathscr{J} \frac{h_{rw} \rho_g u_\tau^2}{\Sigma}$$

where h_{rw} is the height of the roll waves. The collapse of the data was good even if the data came from two different pipes (42 and 25.4 mm i.d.). To compare with correlation (3.155), one needs to find an expression for $\mathscr{J}$ and h_{rw}. We mentioned previously that the intermittency in a developed annular flow has roughly a constant value of 40%. Wallis' correlation (relation (3.60)) tends to indicate that a liquid film of thickness h is similar to having a wall of $4h$ equivalent sand roughness. As a first guess, we could think that the actual height of the roll wave is generating this roughness. Therefore it may be sensible to suppose that:

$$h_{rw} \approx 4h \tag{3.157}$$

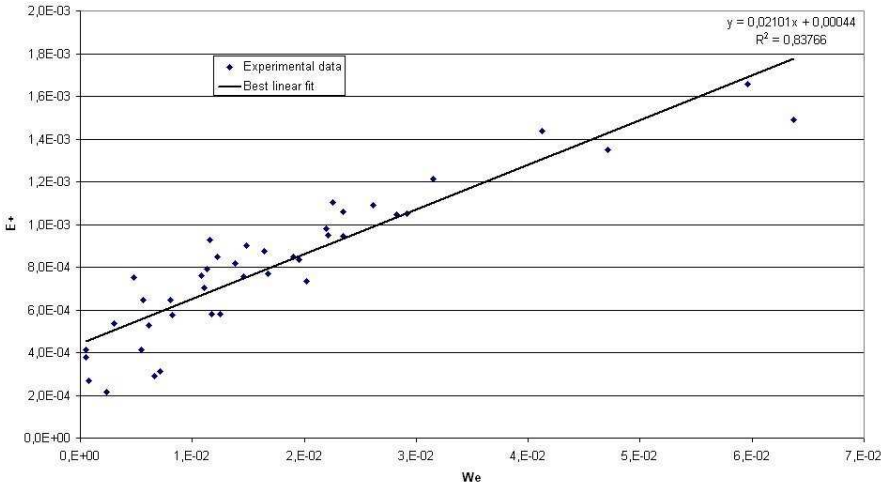

Figure 3.20: Experimental points reported by Schadel and Hanratty (1989)

We now will plot the data of Schadel as $\dot{E}^+$ as a function of $We = \tau_i h/\Sigma$ with the above assumptions for the intermittency and the height of the disturbance waves and supposing that the interfacial shear can be approximated by $\rho_g u_\tau^2$. One can see on Figure 3.20 that the derivative of $\dot{E}^+$ with respect to the Weber number is 0.02101 which is remarkably close to the value of 0.023 determined by Alipchenkov *et al.* (2002b).
The correlation (3.155) also expresses a very simple physics. Indeed far above the onset of entrainment it reduces to:

$$\dot{E}^+ \propto We \tag{3.158}$$

which means that the entrainment rate is inversely proportional to the surface tension and proportional to the shear exerted by the gas on the liquid film. Finally this correlation is quite unique because it is local.
It now remains to find a proper relation for the critical Weber number. There are not many correlations available because it is more usual to use a critical Reynolds number (Leman *et al.* (1985), Lopez de Bertodano *et al.* (1997,2001)) or dimensionally a critical liquid flow rate (Dallman *et al.* (1979), Schadel *et al.* (1990), Hewitt and Govan (1990), Williams *et al.* (1996), Dykhno and Hanratty (1996), Pan and Hanratty (2002a, 2002b), Su *et al.* (2003)). However using a Weber number is more in agreement with theory. We tested two correlations. First the one of Nigmatulin *et al.* (1996):

- if $Re_f \leq 300$

$$We_{crit} = 0.0025\, Re_f^{0.2} G \tag{3.159}$$

- if $Re_f > 300$

$$We_{crit} = 2.8\,10^{-5}\,Re_f G \tag{3.160}$$

where Re_f is the Reynolds number of the liquid film[19]:

$$Re_f \equiv \frac{\rho_f U_f h}{\mu_f} \tag{3.161}$$

G is a fluid property group defined as:

$$G \equiv \left(\frac{\rho_g}{\rho_f}\right)^{1/2} \left(\frac{\mu_f}{\mu_g}\right) \tag{3.162}$$

The second correlation is from of Alipchenkov *et al.* (2002b):

$$We_{crit} = \left(2.8 \cdot 10^{-5} + \frac{5.28 \cdot 10^{-4}}{\left(Re_f - Re_{f,crit}\right)^{0.8}}\right) Re_f \tag{3.163}$$

where the critical value of the Reynolds number was 40. The correlations (3.159),(3.160) and (3.163) have been tested against the experimental data of Van Rossum (1959) which included a great variety of fluids. The fluids used by Van Rossum and their properties are given in Table 3.4. The operating temperatures were between 14 and 20 ℃. The data of Van Rossum were not directly usable. He gave the critical Weber number as a function of a parameter S, and a critical Reynolds number as a function of S as well. It was then possible to have the critical Weber number as a function of the critical Reynolds number. The non-dimensional numbers of Van Rossum are based on the superficial gas velocity while the correlations of Nigmatulin *et al.* (1996) and Alipchenkov *et al.* (2002b) are based on the interfacial shear stress. To compare the correlations with the experimental values two assumptions were necessary:

1. $\tau_i \approx \rho_g u_\tau^2$
2. The ratio of u_τ to the superficial velocity is approximated by 1/20. Pope (2000) showed that for a large range of Reynolds numbers, the ratio of the friction velocity to the core velocity is between 15 and 25.

[19] One should notice that there are different ways of defining the Reynolds number of the liquid film. Some authors define Re_f based on the velocity of the film and its height:

$$Re_f \equiv \frac{\rho_f U_f h}{\mu_f}$$

Others prefer to define it with the mass flux of film , and the diameter of the tube:

$$Re_f \equiv \frac{\frac{\dot{m}_f}{\frac{\pi D^2}{4}} D}{\mu_f} = \frac{4\dot{m}_f}{\pi D \mu_f}$$

For a thin film:

$$\dot{m}_f = \rho_f U_f h \pi D$$

There is therefore a factor 4 between the two Reynolds numbers. The first definition is the one we will choose unless specified otherwise.

Liquid	ρ_f $(kg \cdot m^{-3})$	Σ (N/m)	μ_f $(kg \cdot m^{-1} \cdot s^{-1})$
Water	1000	0.073	0.0011
Water+1.5% butanol	1000	0.050	0.0013
Water+3.7% butanol	1000	0.040	0.0014
Water+7% butanol	990	0.031	0.0014
Kerosene	800	0.032	0.0015
Gas oil	830	0.031	0.0038
Mineral oil 3	850	0.030	0.016
Mineral oil 1	860	0.030	0.051

Table 3.4: Physical properties of the fluids used by Van Rossum (1959)

The second assumption is rather rough but we will see at least if the trends of the experimental points are correctly reproduced. The data of Van Rossum and correlation (3.163) are plotted on Figure 3.21. Except for the water/air data the correlation is not satisfactory. There is an obvious effect of liquid properties. That is why we next will investigate the effect of a dependency of the critical Reynolds number on G.
Azzopardi (1997) presented experimental values of the critical Reynolds number for the inception of roll waves. It was seen previously that it can be a good indication for the onset of entrainment. Azzopardi tested 4 correlations. In addition we tested a modified version of the correlation of Ishii and Grolmes (1975) advised by Azzopardi (1997). The correlation of Pan and Hanratty (2002b) was tested as well. Numerous authors also proposed various constant values for $Re_{f,crit}$ but Figure 3.21 shows that it is not correct. The best results were obtained with the correlation of Ishii and Grolmes modified by Azzopardi and the correlation of Pan and Hanratty. We chose to use the former which is:

$$Re_{f,crit} = 804\, G^{-3/2} \tag{3.164}$$

The effect of this modification is plotted on Figure 3.22. The results are clearly better than on Figure 3.21. Nevertheless, the order of magnitude is not correct especially for gas oil, and mineral oils.
Figure 3.23 shows the results of the correlation of Nigmatulin *et al.* (1996). It gives an acceptable trend and the right order of magnitude. One should bear in mind that discrepancies also come from the estimation of the friction velocity so that one does not expected more than the correct order of magnitude. In the present model the critical Weber number will thus be given by (3.159) and (3.160).
We now have a complete model where entrainment rate, deposition rate and interfacial shear stress can be calculated.

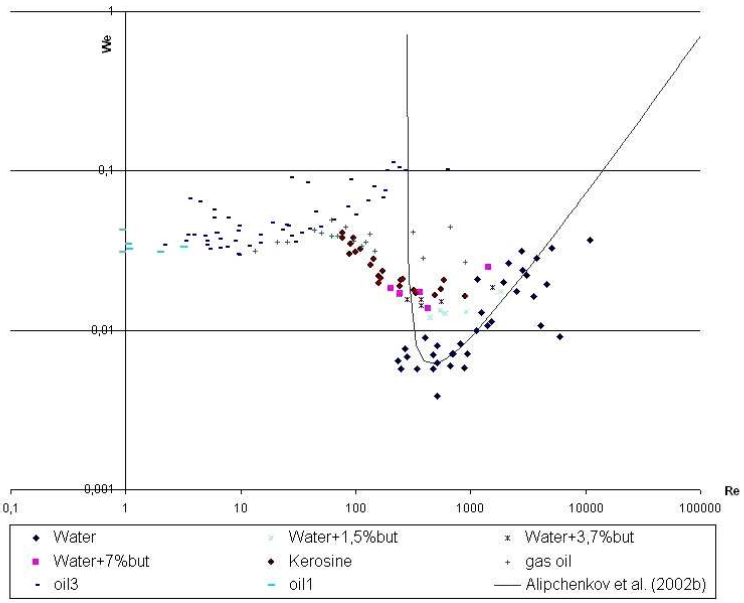

Figure 3.21: Correlation (3.163) against the data collected by Van Rossum (1959)

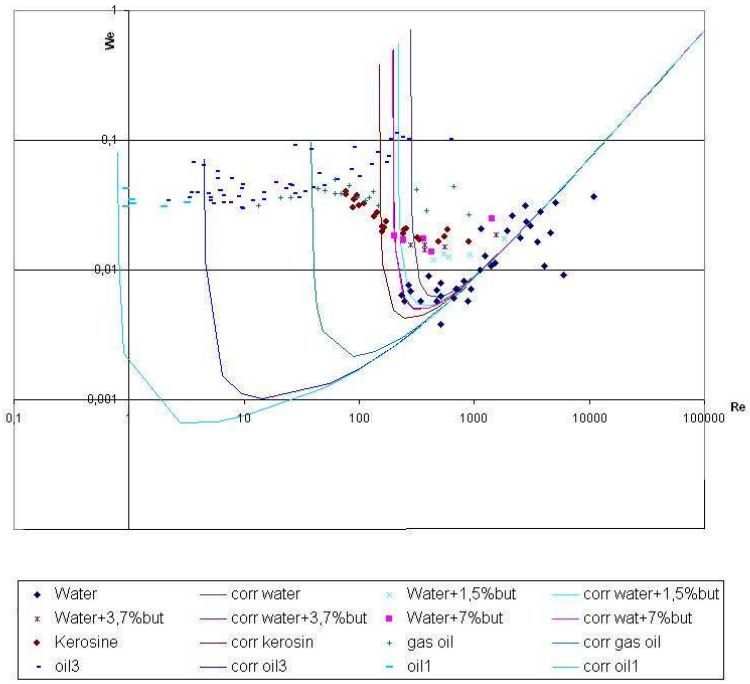

Figure 3.22: Modified correlation (3.163) against the data collected by Van Rossum (1959)

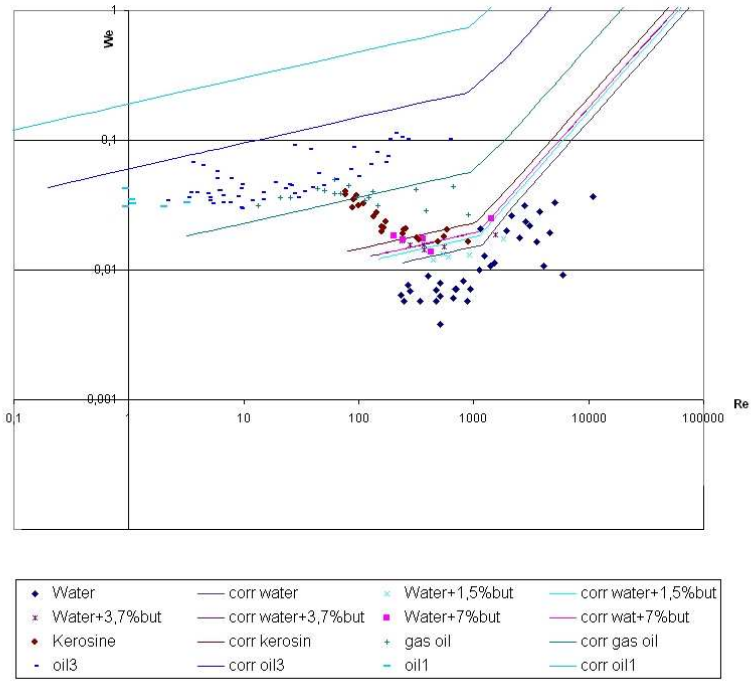

Figure 3.23: Correlations (3.159) and (3.160) against the data collected by Van Rossum (1959)

Chapter 4

Numerical issues

This chapter is divided in four. First a general description of the computer and of the different softwares is given. Then we discuss briefly the numerical methods that were used. Numerical methods were not a key part of the present work. They were handled automatically by Fluent. Next is a description of the subroutines necessary to implement the models developed in the previous chapters. Finally we examine issues related to complex geometries and unstructured grids.

4.1 Hardware and software

Hardware and operative system

The majority of the calculations have been computed on a Hewlett-Packard workstation xw9300. It was equipped with 2 processors Opteron 246 (2 GHz). The machine had 4 GB of Random Access Memory. The operative system was Microsoft Windows XP 64-bit. Unfortunately, the 64-bit version of Fluent for Windows has not been released yet so a standard 32-bit version has been used.

Gambit

Gambit is a software package designed to build up a geometry, mesh it and specify boundary conditions. The geometry is generated from points (or vertexes) which coordinates are specified by the user. Those points are linked and form edges. A set of closed edges forms a face, and a set of closed surfaces forms a volume. The whole computational domain is formed of all the volumes.
There are several types of mesh available. One can mesh the edges, the faces, or the volumes.

Edges. Edges can be meshed regularly but it is also common to use a grading ratio were the length of an element equals the length of the previous element multiplied by a constant. More complex edge meshing techniques are possible.

Faces. Surfaces can be meshed by two types of elements: quadrilaterals and triangles. One can measure the quality of the mesh by checking the equi-angle skew of its elements. It is a quantity between 0 and 1. 0 corresponds to an equilateral element (in 2D: equilateral triangle, square or rectangle). 1 corresponds to a degenerated element (for example a triangle made of three aligned points). More details on the equi-angle skew and on other variables to check the quality of a mesh can be found in Fluent Inc. (2004a). Each node can be adjusted manually if the automatically generated mesh is not satisfactory.

Volumes. The possible types of cells are:

- Hexahedrons
- Wedges
- Tetrahedrons
- Pyramids

All of these cells were used. Volumes have been usually meshed by a Cooper method which is fully described in Fluent Inc (2004b). Hexahedrons were systematically preferred when the geometry allowed it. In the case of a volume with a particularly complex topology, meshes made of tetrahedrons were used. It is difficult to control the skewness of tetrahedrons and pyramids but it was kept as low as possible. It was paid special attention to avoid cell types that could generate numerical difficulties, in particular:

- Tetrahedron and pyramid zones
- Deformed cells
- Poor resolution (low number of cells in narrow areas)
- Large aspect ratios when the cell is not aligned with the stream
- Cells oriented obliquely with respect to the stream

Gambit also allows to use non-conformal meshes, that is, faces which sides are meshed independently from each other.

When the grid is finished, it remains to specify the boundary conditions:

- for faces: wall, interior, velocity inlet, pressure outlet, or axis (among others)
- and for volumes: fluid or solid

Fluent

Fluent is a program for computing fluid flows. It can solve problems using unstructured meshes and is therefore interesting for industrial applications with complex geometries. It is written in the C computer language. Some functionalities, especially concerning the graphical user interface and the text user interface, use the Scheme language. An important aspect of the software is that the user can integrate its own sub-routines, called UDFs (User Defined Functions). The possibility of writing UDFs provides a certain flexibility. However, it has to be made in the frame of macros provided by the software and the main source code still remains unaccessible.

4.2 Numerical methods

4.2.1 Discretization method

An approximation of the solution of the partial differential equations governing a fluid flow can be obtained by focusing on the field values at specific locations called grid points. In the finite-volume formulation, used by Fluent, each grid point is associated with a small region called control volume. The discretization equations, which are algebraic, are obtained by integration of the governing differential equations over the control volumes. In this section we will focus on the discrete equations but not on the algorithm to solve them. We will consider the case of a general transport equation:

$$\frac{\partial \rho\psi}{\partial t} + \frac{\partial \rho U_j \psi}{\partial X_j} = \frac{\partial}{\partial X_j}\left(\Lambda \frac{\partial \psi}{\partial X_j}\right) + S \tag{4.1}$$

where ψ is some field property, Λ a diffusion coefficient and S a source. In the following, we will focus on the discrete form of this equation, studying briefly each term. We follow closely the development made by Patankar (1980). The explanations are brief. More details are provided in Patankar (1980).

Purely diffusive equation

For the sake of simplicity we will first consider a 1D problem. Let us consider the grid points of Figure 4.1. w and e represent the boundary of the control volume. ΔX_w (resp. ΔX_e) is the distance between the center of the control volume P and its neighbor W (resp. E). ΔX is the width of the control volume. A purely diffusive 1D equation is:

$$0 = \frac{\partial}{\partial X}\left(\Lambda \frac{\partial \psi}{\partial X}\right) \tag{4.2}$$

An integration from w to e leads to:

$$0 = \left(\Lambda \frac{\partial \psi}{\partial X}\right)_e - \left(\Lambda \frac{\partial \psi}{\partial X}\right)_w \tag{4.3}$$

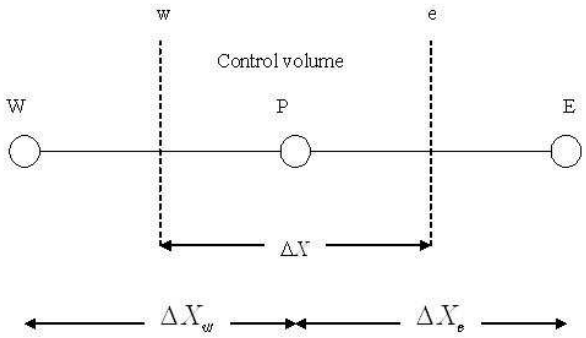

Figure 4.1: Grid points

If one approximates the variation of ψ between to grid points by a linear function we obtain:

$$\psi_P \left(\frac{\Lambda_e}{\Delta X_e} + \frac{\Lambda_w}{\Delta X_w} \right) = \frac{\Lambda_e}{\Delta X_e} \psi_E + \frac{\Lambda_w}{\Delta X_w} \psi_W \tag{4.4}$$

A general form of this discrete equation is:

$$a_P \psi_P = \sum_{nb} a_{nb} \psi_{nb} + b \tag{4.5}$$

where the nb index relates to the neighboring points. In the case of a purely diffusive equation b is zero. It is essential that the a coefficients are positive, because the variation of the field quantity can not have a different trend in P and in its vicinity. For example, if ψ is a temperature and $a_w < 0$, a decrease in the temperature at W would induce an increase of the temperature at P. This is not physically realistic.

Source term

Adding a source term leads to the equation:

$$0 = \left(\Lambda \frac{\partial \psi}{\partial X} \right)_e - \left(\Lambda \frac{\partial \psi}{\partial X} \right)_w + \int_w^e S dX \tag{4.6}$$

If we define:

$$S_{avg} \equiv \frac{1}{\Delta X} \int_w^e S dX \tag{4.7}$$

We obtain the coefficients:

$$\begin{aligned} a_E &= \frac{\Lambda_e}{\Delta X_e} \\ a_W &= \frac{\Lambda_w}{\Delta X_w} \\ a_P &= a_E + a_P \\ b &= S_{avg}\Delta X \end{aligned} \tag{4.8}$$

The discrete equations are solved by linearization techniques, consequently S is put in the form of:

$$S_{avg} = S_1 + S_2\psi_P \tag{4.9}$$

Then a_P becomes:

$$a_P = a_E + a_W - S_2\Delta X \tag{4.10}$$

and b becomes:

$$b = S_1\Delta X \tag{4.11}$$

To ensure that $a_P > 0$, it is best to have $S_2 \leq 0$. If $S_2 > 0$, the grid size ΔX should be sufficiently small for a_P to be positive.

Unsteady term

Let us now consider an unsteady diffusion equation:

$$\frac{\partial \rho\psi}{\partial t} = \frac{\partial}{\partial X_j}\left(\Lambda\frac{\partial \psi}{\partial X_j}\right) \tag{4.12}$$

This equation is integrated on space and on time from a time t to a time $t+\Delta t$. Quantities at t will be indexed n, and quantities at $t+\Delta t$ will be indexed $n+1$. The unsteady term can be written:

$$\int_w^e \int_t^{t+\Delta t} \rho\frac{\partial \psi}{\partial t} dt\, dX = \rho\Delta X\left(\psi_P^{n+1} - \psi_P^n\right) \tag{4.13}$$

Here the value of ψ at P is assumed to prevail over the whole control volume. Following the usual discretization practice for the diffusive term we obtain:

$$\rho\Delta X\left(\psi_P^{n+1} - \psi_P^n\right) = \int_t^{t+\Delta t}\left(\frac{\Lambda_e\left(\psi_E - \psi_P\right)}{\Delta X_e} - \frac{\Lambda_w\left(\psi_W - \psi_P\right)}{\Delta X_w}\right) dt \tag{4.14}$$

We now need an additional assumption concerning the integration of ψ with respect to time. A simple one is:

$$\int_t^{t+\Delta t} \psi\, dt = \left(f\psi^{n+1} + (1-f)\,\psi^n\right)\Delta t \tag{4.15}$$

where f is a weighting parameter between 0 and 1. After some algebra one gets:

$$\begin{aligned} a_P\psi_P^{n+1} &= a_E\left(f\,\psi_E^{n+1} + (1-f)\,\psi_E^n\right) + a_W\left(f\,\psi_W^{n+1} + (1-f)\,\psi_W^n\right) \\ &\quad \left(\rho\frac{\Delta X}{\Delta t} - (1-f)\,a_E - (1-f)\,a_W\right)\psi_P^n \end{aligned} \tag{4.16}$$

with:

$$\begin{aligned} a_E &= \frac{\Lambda_e}{\Delta X_e} \\ a_W &= \frac{\Lambda_w}{\Delta X_w} \\ a_P &= f\, a_E + f\, a_W + \rho\frac{\Delta X}{\Delta t} \end{aligned} \tag{4.17}$$

If $f = 0$ the time scheme is explicit because ψ_P^{n+1} is dependent of quantities at the time t only. Since the coefficient of ψ_P^n in equation (4.16) must be positive it implies:

$$\Delta t \leq \rho\frac{\Delta X}{a_E + a_W} \tag{4.18}$$

If equation (4.18) imposes a very small time step, the explicit scheme is unsuitable. The other extreme is the fully implicit scheme where $f = 1$. When $f = 1$ the stability is always ensured. We chose to work with an implicit scheme.

The convective term

Let us now consider the equation:

$$\frac{\partial \rho U\psi}{\partial X} = \frac{\partial}{\partial X}\left(\Lambda\frac{\partial \psi}{\partial X}\right) \tag{4.19}$$

where U is a known velocity field. Integrating equation (4.19) in space gives:

$$(\rho U\psi)_e - (\rho U\psi)_w = \left(\Lambda\frac{\partial \psi}{\partial X}\right)_e - \left(\Lambda\frac{\partial \psi}{\partial X}\right)_w \tag{4.20}$$

One could choose a linear profile for ψ as we did with $\partial\psi/\partial X$. For a regular grid, this would lead to:

$$\psi_e = \frac{\psi_E + \psi_P}{2} \tag{4.21}$$

and

$$\psi_w = \frac{\psi_W + \psi_P}{2} \tag{4.22}$$

However, this convection scheme, known as the central-difference scheme, does not necessarily imply the positivity of the discretization coefficients. In general the present computations were performed with an upwind scheme. For this scheme the value of ψ at the boundary of the control volume equals that of the grid point on the upwind side of the boundary. With this scheme the convection flux depends on the sign of ρU. It gives:

$$\begin{aligned} (\rho U\psi)_e &= \psi_P\, max\{(\rho\, U)_e, 0\} - \psi_E\, max\{-(\rho\, U)_e, 0\} \\ (\rho U\psi)_w &= \psi_W\, max\{(\rho\, U)_w, 0\} - \psi_P\, max\{-(\rho\, U)_w, 0\} \end{aligned} \tag{4.23}$$

The upwind scheme ensures the stability of the calculation but has a tendency to smear out sharp gradients.

Calculation of the flow field

The calculation of the velocity field is related to the pressure gradient term which is not known a priori. Assuming that the control volumes are equal in size, integrating the pressure gradient term gives:

$$-\int_w^e \frac{\partial P}{\partial X} dX = P_w - P_e = \frac{P_W + P_P}{2} - \frac{P_P + P_E}{2} = \frac{P_W - P_E}{2} \tag{4.24}$$

Then, we can see that the momentum equation contains a pressure difference between alternate grid points and not adjacent ones. The very problem is that any alternate highly non-uniform pressure field ("checker-board" field) will act as a uniform field in the discretized momentum equation. Furthermore checker-board pressure field are not suppressed during the iteration process. Finally any checker-board pressure field can be added to a realistic pressure field without any consequences for the discretized momentum equation.
There are two main ways to avoid such unrealistic alternate pressure fields. The oldest is the so called "staggered grid method" which consist in locating the velocity nodes at the edges of the control volume while the pressure nodes are at its center. Nevertheless, for 3D problems and with the emergence of new unstructured meshing techniques, this method became cumbersome. Fluent uses a "collocated" method that stores all the variables at the center of the control volume. To avoid unrealistic alternate pressure fields special interpolation techniques are used to evaluate the velocity at the faces of the control volume. A robust and widespread method is the one presented by Rhie and Chow (1983). Mathur and Murthy (1997) extended this method to unstructured grid.
Let us now consider a guessed pressure field P^*. In the context of a 1D collocated grid, the discrete form of the momentum equation is written:

$$a_P U_P^* = \sum_{nb} a_{nb} U_{nb}^* + b + (P_w^* - P_e^*) \tag{4.25}$$

U^* is a guessed velocity field that satisfies the momentum equation. However if the pressure field is not correct, U^* does not satisfy the mass conservation equation. We now have to find a pressure-velocity coupling method so that the velocity field fulfills the continuity equation. We used the SIMPLE (Simple Implicit Method for Pressure-Linked Equation) algorithm which is an iterative procedure based on a correction of the pressure and velocity fields. Let us now define the corrections:

$$P^c \equiv P - P^* \tag{4.26}$$

$$U^c \equiv U - U^* \tag{4.27}$$

P and U being the correct pressure and velocity fields. These two fields fulfill the momentum equation so that:

$$a_P U_P = \sum_{nb} a_{nb} U_{nb} + b + (P_w - P_e) \tag{4.28}$$

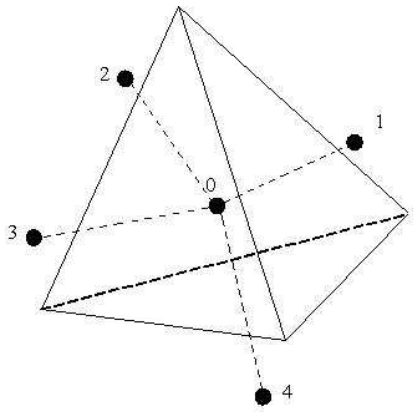

Figure 4.2: A control volume in an unstructured grid

Subtracting equation 4.25 from 4.28 leads to:

$$a_P U_P^c = \sum_{nb} a_{nb} U_{nb}^c + (P_w^c - P_e^c) \tag{4.29}$$

We will now neglect the term $\sum_{nb} a_{nb} U_{nb}^c$. It is possible because the way to build the pressure correction does not influence the correctness of the converged solution. We then have:

$$U_P = U_P^* + \frac{P_w^c - P_e^c}{a_P} \tag{4.30}$$

If this equation is now introduced into the discrete form of the continuity equation one gets a pressure correction equation that can be solved. When P^c is known, one gets the values of P and U.
This process is more complex for Euler/Euler multiphase flow models where there are several continuity equations. There are two types of algorithms to handle pressure-velocity coupling in this case (Moukalled and Darwish (2002)). First there are algorithms based on the geometric conservation equation (GCBA). Second there are Mass Conservation Based Algorithms (MCBA). Moukalled and Darwish (2002) studied the performance of MCBA algorithms (among which the SIMPLE algorithm) in collocated structured grids. Vasquez and Ivanov (2000) presented a similar study for unstructured grids.

Unstructured grids

Let us now consider an unstructured grid made of e.g tetrahedrons. In this case a cell with centroid 0 will have four neighbors with centroids $1, 2, 3$ and 4 as pictured on Figure 4.2. If we now integrate over the control volume a steady convection-diffusion transport equation with a source term, we have:

$$\iiint \frac{\partial \rho U_j \psi}{\partial X_j} dV = \iiint \frac{\partial}{\partial X_j} \left(\Lambda \frac{\partial \psi}{\partial X_j} \right) dV + \iiint S dV \tag{4.31}$$

Applying the divergence theorem one gets in the case of a tetrahedron:

$$\sum_{f=1}^{4} \rho_f \psi_f U_{fj} n_{fj} A_f = \sum_{f=1}^{4} \Lambda_f \left. \frac{\partial \psi}{\partial X_j} \right|_f n_{fj} A_f + S_{avg} V \tag{4.32}$$

f represents the face between the cell of centroid f and the cell of centroid 0. One can see from equation (4.32) that there is no fundamental difference with a structured grid. All the terms can be discretized according to the methods previously detailed for a 1D case.

Under-relaxation factor

Under-relaxation factors helps to have a more stable calculation. The corrected value of a field quantity ψ should have been:

$$\psi = \psi^* + \psi^c \tag{4.33}$$

Instead one uses:

$$\psi = \psi^* + \upsilon \psi^c \tag{4.34}$$

where υ is an under-relaxation factor between 0 and 1. Under relaxation factors avoid divergence but slow down convergence.
The next section deals with the resolution of the discrete equations of the flow. It is a system of linear algebraic equations.

4.2.2 Solver

The following section details first some common algorithms to solve a system of linear algebraic equations. Second it describes shortly the principles of multigrid methods. We used an algebraic multigrid (AMG) method to perform the calculations. A short paragraph explains the basic idea of this technique.

Direct and iterative methods

Conceptually speaking the simplest linear equation solver is certainly the standard Gaussian elimination method. This method, as any other direct method, is not very adapted for our purpose. Indeed, the system is represented by a sparse matrix, that is, a matrix containing many zeros. This particular configuration is not kept during the elimination process and zero elements can be replaced by non-zero elements (Dahlquist and Björk (1974)). Consequently direct methods require as a rule a large amount of computer storage (except in the 1D case where one can use the tridiagonal matrix algorithm (Patankar (1980)). An other family of methods are the iterative methods. They start from an initial guess which is improved gradually until an acceptable solution is obtained. Let us now consider the following linear system of n equations:

$$\sum_{\beta=1}^{n} a_{\alpha\beta} \psi_\beta = b_\alpha \tag{4.35}$$

There are two usual types of iterative methods. With Jacobi's method, the values are kept to the present iteration until the whole iteration is completed. In this case we have:

$$\psi_\alpha^{i+1} = \frac{1}{a_{\alpha\alpha}} \left(- \sum_{\beta=1;\beta\neq\alpha}^{n} a_{\alpha\beta}\psi_\beta^i + b_\alpha \right) \tag{4.36}$$

i being the number of the iteration. In the Gauss-Seidel method, the values of the field are updated as soon as they are computed:

$$\psi_\alpha^{i+1} = \frac{1}{a_{\alpha\alpha}} \left(- \sum_{\beta=1}^{\alpha-1} a_{\alpha\beta}\psi_\beta^{i+1} - \sum_{\beta=\alpha+1}^{n} a_{\alpha\beta}\psi_\beta^i + b_\alpha \right) \tag{4.37}$$

In general the Gauss-Seidel method (used by Fluent) converges faster than Jacobi's. Scarborough (1962) derived a sufficient criteria for the convergence of an iteration method. This condition is that for all α:

$$\frac{1}{|a_{\alpha\alpha}|} \left(\sum_{\beta=1;\beta\neq\alpha}^{n} |a_{\alpha\beta}| \right) < 1 \tag{4.38}$$

Multi-grid methods

Multi-grid methods are used to accelerate convergence. These methods have been described formally by Brandt (1977). Briggs (1987) wrote an introduction to multi-grid techniques which is easier to access for the non-mathematicians. Conventional iterative methods (Jacobi, Gauss-Seidel) remove efficiently high frequency errors but poorly eliminate low frequency errors. On coarser grids low frequency errors are better damped. The idea of the multigrid method is:

1. Apply as usual the iterative technique on the original grid. This eliminates the high frequencies.

2. Solve the problem on a coarser grid, obtain a correction and transfer it to the fine grid level. This removes low frequencies.

The speed of convergence is then much higher.

Algebraic multigrid (AMG)

Conventional multigrid methods are based on the geometrical information of the grid. However, building a coarser grid can be difficult especially if a fully unstructured grid is used. The AMG methods are independent of the mesh because they work directly on the coefficients of the matrix of the system (Stüben (1999)). An AMG method provided by Fluent was used in the present work.

4.3 Subroutines related to the model

4.3.1 Film flow

The convective term of the film transport equation presents an non-linearity. Indeed, the velocity of the film is a function of the film height itself. If one wants to calculate the height of the film at the iteration $i+1$, it is necessary that the coefficients of the matrix are independent of h^{i+1}. Therefore the convective flux has been programmed as:

$$\frac{\partial}{\partial X_j} h^{i+1} U_{jf}^{i}$$

After a number of iterations which is large enough, $U_{jf}^{i} \approx U_{jf}^{i+1}$ and the true convective term is practically recovered. In practice, the values of h and U_{jf} for a given time step converged after 10 iterations at the most.
The flux of film between two cells was calculated with an upwind scheme.

4.3.2 Memory management

In the present model, a significant amount of calculations must be done in the near wall cells: deposition, flux of film, entrainment. This requires the storage of values in the memory. These stored values can be:

- Geometrical: volume of the cell, area of deposition, wall normal vector, the distance between the centroid and the wall.
- Related to the flow: height of the film, deposition flux, entrainment flux, velocity of the droplet phase, velocity and turbulent kinetic energy of the gas phase .

Finally the gravity vector, the iteration number and some flow data at the previous iteration must be stored. In total the programs stores permanently 28 scalar values per wall-cell.
In Fluent it is possible to allocate memory for 500 scalars. However, this memory is allocated for each cell in the calculation domain. Most of the above cited quantities are irrelevant for cells that are not in contact with the wall. Consequently, if the Fluent's standard procedure of memory allocation for scalars was used, most of the memory would store zeros. To avoid this waste another allocation technique has been developed.
At the initialization phase a pointer is allocated for each cell of the domain. If the cell is not located at the wall its pointer points to the NULL pointer. If the cell is located at the wall, the pointer points to a structure that contains all the relevant quantities. Thus there is no waste of memory.
Allocating a pointer in each cell is also flexible for further developments of the code. It allows any number of parameters to be stored for wall cells. For example, it can be useful for corner-cells where one can have to store two or three areas of deposition, normal vectors and distances between the centroid and the wall. With this technique, data may also be stored for cells inside the domain.

The present NULL pointer would just have to be pointing to an other type of structure than the wall-cell structure.
There are at present two drawbacks with this technique of memory allocation. First, data only stored in the structure can not be plotted. For example, if one wants to plot the entrainment flux one needs to allocate a scalar for each cell of the domain. Second, if Fluent is used only for checking the data of a previous simulation, one needs to initialize the solution. This can take a significant amount of time for large grids. The most consuming task in the initialization process is the localization of cells at the wall that share just one point (or one line in 3D) with it. This process is at present far from being optimized.

4.4 Issues related to complex geometries

4.4.1 Unstructured grids

a) Mass transfers between the droplet phase and the film

The continuity equation for the droplet phase (3.2) together with the modeling of J_d (equation (3.89)) and J_e (equation (3.155)), gives:

$$\frac{\partial\ \rho_d\overline{\alpha_d}}{\partial t} + \frac{\partial\ \rho_d\overline{\alpha_d}\widetilde{U_{id}}}{\partial X_i} = \frac{A_{wall}}{V}\left(-\overline{\alpha_d}\rho_d \cdot K_D + 0.023\sqrt{\rho_d\tau_i}\,(We - We_{crit})\right) \tag{4.39}$$

This equation depends on A_{wall} the area that the cell shares with the wall and V the volume of the cell. The continuity equation for the film (3.8) is:

$$\frac{\partial h}{\partial t} + \frac{\partial}{\partial X_i} h\, U_{if} = \overline{\alpha_d} \cdot K_D - 0.023\sqrt{\frac{\tau_i}{\rho_d}}\,(We - We_{crit}) \tag{4.40}$$

Equation (4.40) shows that the height of the film is not depending on the geometry of the cell. To have a perfect mass conservation the area of deposition should be well defined. However, even if the interface of the film is perfectly parallel to the wall, the area of deposition is dependent of the geometry of the cell. Figure 4.3 illustrates the case of a cell which is an equilateral triangle. Its height is normal to the wall. On the left side of Figure 4.3, the base of the triangle is the wall. The exact area of deposition is:

$$A(h) = A_{wall} - \frac{2h\sqrt{3}}{3} \tag{4.41}$$

In this case the model considers that the area of deposition is A_{wall}. On the right of Figure 4.3, the cell has only a point on the wall. The exact area of deposition is:

$$A(h) = \frac{2h\sqrt{3}}{3} \tag{4.42}$$

In this case the model considers that the area of deposition is 0. If the mesh is 3D, the calculation of $A(h)$ is extremely complicated (Son (2003)). Calculating

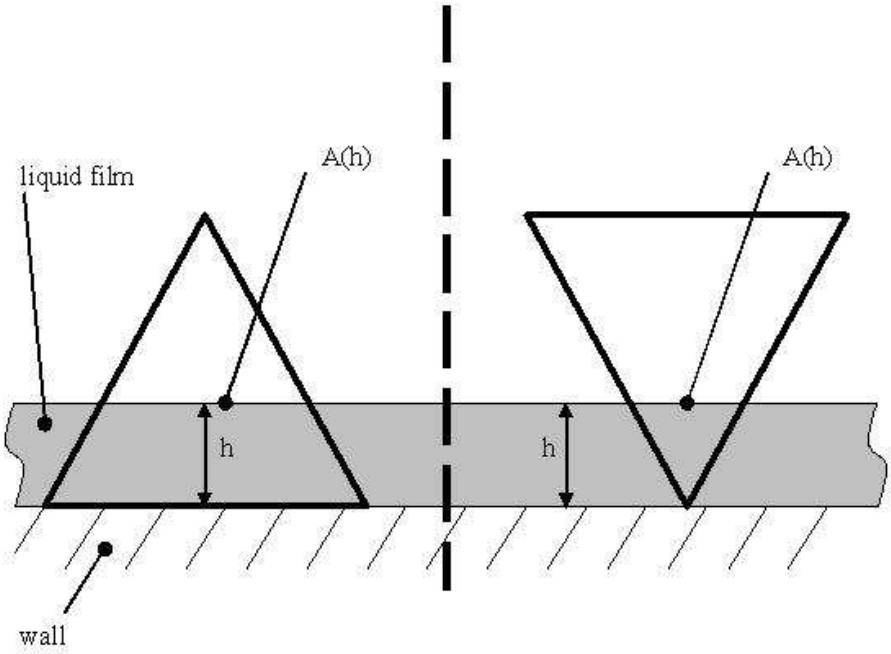

Figure 4.3: Area of deposition for an example of unstructured grid.

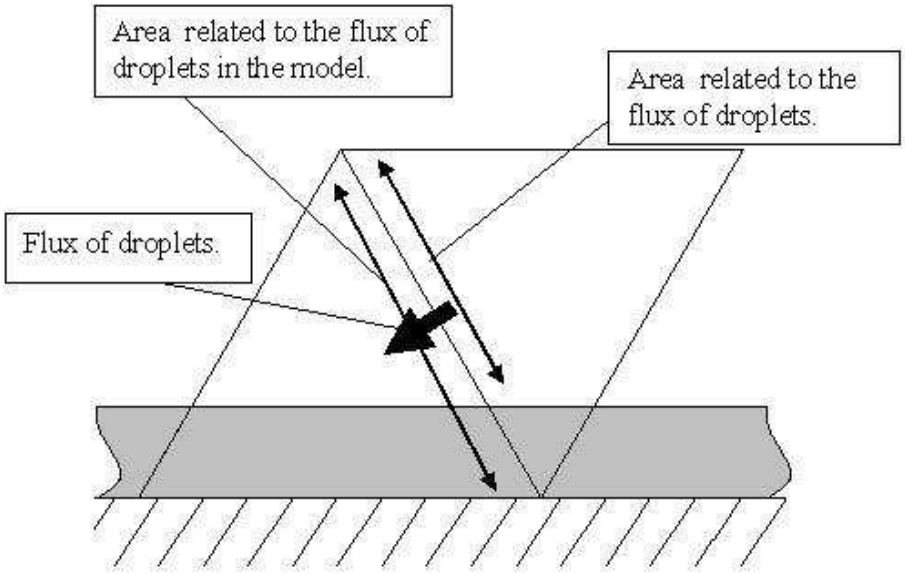

Figure 4.4: Flux of droplet by the wall.

the exact interface area becomes computationally too demanding. That is why, in the present model, there is no correction of the mass imbalance generated by the grid.

b) Droplet flux in the near wall cells

Figure 4.4 illustrates the flux of droplet near the wall for an unstructured grid. Because of the film thickness, the actual area with which the flux must be calculated is reduced[1]. If one takes again the example of equilateral triangles, the surface available for the flux of droplets between the two cells has been reduced from A_{wall} to $A_{wall} - 2h\sqrt{3}/3$. The model does not take this reduction into account. If the film is thin, this reduction is negligible.

c) Flux of film in unstructured grids

In the present model, the film is parallel to the wall. This assumes that the normal to the wall is defined. It can happen in unstructured grids that the film is located in a cell with no defined normal. In 2D grids, these are cells that have only one point on the wall. In 3D, these cells have either one point or one line on the wall. To compute the orientation of the film in such cells, a normal must be specified.

[1]This effect occurs in structured grid as well.

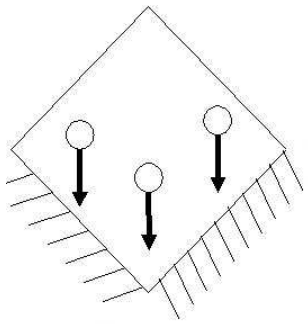

Figure 4.5: A concave corner cell.

Specification for cells having one point on the wall (2D or 3D). Let us call P the only contact point of the cell with the wall. C is the centroid of the cell. Then the normal to the wall (inwardly oriented) is defined by:

$$\vec{n} \equiv \frac{\vec{PC}}{\left\|\vec{PC}\right\|} \tag{4.43}$$

Specification for cells having one line on the wall (3D). Let us call P_1 and P_2 the ends of the segment that the cell shares with the wall. C is the centroid of the cell. Then the normal to the wall (inwardly oriented) is defined by:

$$\vec{n} \equiv \frac{\vec{P_1C} - \left(\vec{P_1C} \cdot \frac{\vec{P_1P_2}}{\left\|\vec{P_1P_2}\right\|}\right) \frac{\vec{P_1P_2}}{\left\|\vec{P_1P_2}\right\|}}{\left\|\vec{P_1C} - \left(\vec{P_1C} \cdot \frac{\vec{P_1P_2}}{\left\|\vec{P_1P_2}\right\|}\right) \frac{\vec{P_1P_2}}{\left\|\vec{P_1P_2}\right\|}\right\|} \tag{4.44}$$

This is a vector normal to $\vec{P_1P_2}$ in the plane (P_1P_2C).

4.4.2 Corners

The present model does not have a special treatment for the cells located in corners. It was not considered as a crucial issue scientifically speaking. However the code may be used by professionals of separation equipment. These users should be aware of the inaccuracies arising in corner cells. This subsection pinpoints the consequences of the incorrect treatment of corner cells.

Deposition in concave corners

Cells located in concave corners have 2 or 3 deposition wall areas. Figure 4.5 shows a corner cell in a 2D structured grid. The arrows represent the deposition velocity of the droplets. In the model only one deposition-wall is considered. Walls are detected by the software at the initialization of the solution. The

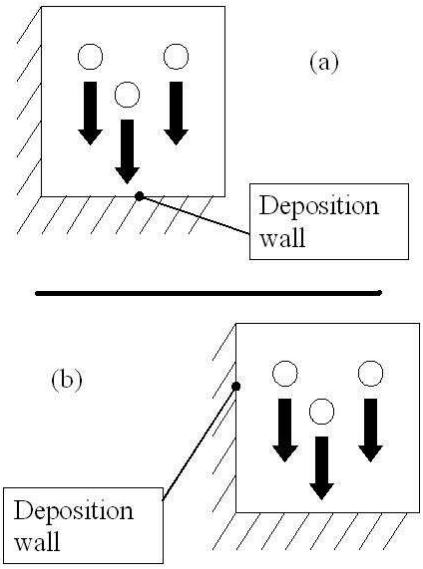

Figure 4.6: Deposition in a concave corner cell.

program loops over all the faces of each cell to see if it has a wall-face. If it has a wall-face, the geometric characteristics of this face are stored in the memory. In case of a cell with several walls, the memory stores the geometry of the first wall-face detected by the program. The selection of the one wall on which deposition occurs in corner cells is thus arbitrary.
In reality the deposition flux depends on the scalar product of the deposition velocity with the normal vector to the gas/liquid interface. In the model, the deposition flux depends on the projection of the deposition velocity with the normal to the deposition-wall. Two extreme cases can happen:

1. The velocity of deposition is normal to the deposition-wall. Then there is no error on the deposition flux. This situation is illustrated on Figure 4.6 (a).

2. The velocity of deposition is parallel to the deposition-wall. This situation is illustrated on Figure 4.6 (b). In this case the model predicts no deposition. This generates a large error because in reality, the deposition occurs on the wall that was not selected as the deposition-wall.

Liquid film flux in concave corners

Figure 4.7 shows a liquid film flowing along a concave corner. In the corner cell, the film flows along two walls. In the model, the film is not simulated as a real film. Instead its height h is a scalar which is transported with a velocity U_f and

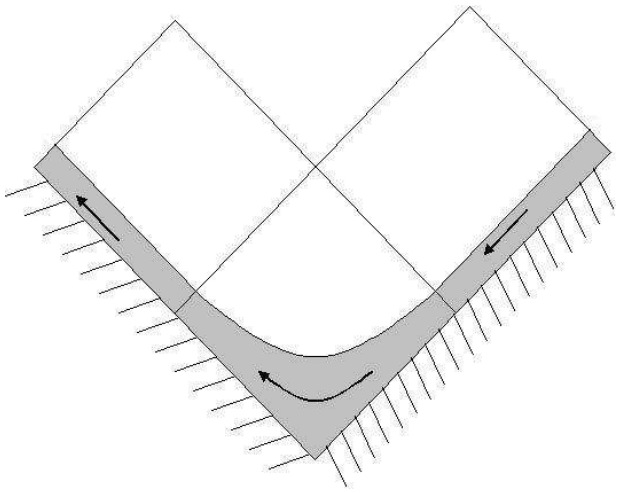

Figure 4.7: Liquid film flowing in a concave corner.

the velocity of the film is parallel to the deposition-wall. In the case illustrated by Figure 4.7 two situations can occur.

1. The deposition-wall of the corner cell is on the left. Figure 4.8 illustrates this case. The film flows from the upstream cell to the corner cell. Then the film flows from the corner cell to the downstream cell.

2. The deposition wall of the corner cell is on the right. Figure 4.9 illustrates this situation. The film flows from the upstream cell to the corner cell. However, the velocity of the liquid layer is oriented in such a way that the flux in the downstream cell is zero. The boundary condition for the scalar h at the wall is a zero flux. As a result the film is trapped in the corner cell. The liquid layer will then grow until entrainment occurs.

Entrainment in convex corners

Figure 4.10 illustrates a situation of entrainment at a convex corner. No special treatment is given for this type of disintegration. However the mechanism leading to entrainment in this case is very different from the mechanism studied previously. The correlation used in the model is based on a force balance between the shear exerted by the gas on the interface and the surface tension forces. In a convex corner, the centrifugal acceleration of the film plays an important role. Maroteaux *et al.* (2002) showed that the balance between the centrifugal force (destabilizing) and the surface tension forces (stabilizing) is responsible for the disintegration of a film on wall edges. Consequently, the calculation of the entrainment flux at sharp edges is based on an irrelevant physical phenomenon. Therefore, one cannot expect a correct quantitative prediction of the entrainment flux in this situation.

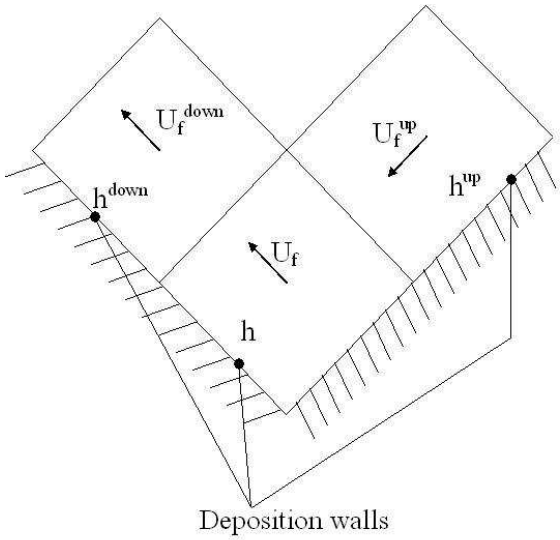

Figure 4.8: Modeled film flowing in a concave corner with the deposition-wall on the left.

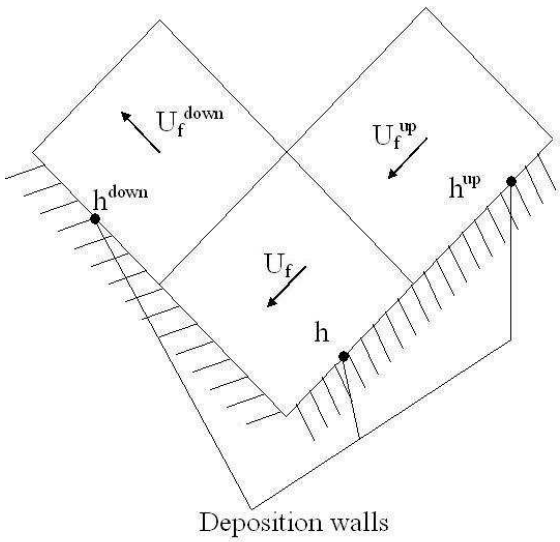

Figure 4.9: Modeled film flowing in a concave corner with the deposition-wall on the right.

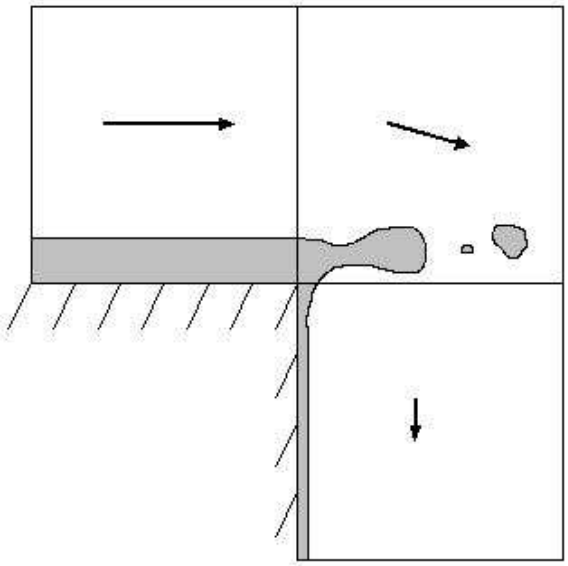

Figure 4.10: Entrainment at convex corners

Part II

Results

Outline of Part II

This part has four chapters. In chapter 5, the deposition model is analyzed. In chapter 6, the film model is studied. Chapter 7 deals with a full annular flow with re-entrainment. Finally chapter 8 studies high pressure liquid/gas separation in a vane-pack demister. In the chapters 5, 6 and 7 the model is compared to experimental results. In chapter 8 the model is compared to another type of model for an air/water flow at atmospheric pressure.

Chapter 5

Pure deposition

In this chapter we will compare the results obtained by Liu and Agarwal (1974) and the predictions of the present model. It is a case of pure deposition.

5.1 Experimental set-up

Liu and Agarwal (1974) studied the deposition of uniform spherical droplets of olive oil in a tube. The droplets contained a tracer (uranine) to determine quantitatively the fractional deposition along the pipe. The deposition pipe was 1.27 cm i.d. and 102 cm long. The flow was downward. We chose to simulate the run where the particle diameter was 16.8 μm and the gas flow rate was 1510 cm^3/s.

5.2 Set-up of the numerical case

5.2.1 Grid

The present case is axisymmetric. All the cells were rectangles. They were 0.635 mm wide and 1.27 mm long.

5.2.2 Simplification for the study of pure deposition

The concentration of droplets was not specified by Liu and Agarwal. It was probably very small. As a result, it was assumed that the quantity of liquid deposited on the wall was too small to form a continuous moving film. Thus we did not consider the formation of a liquid film. When droplets impacted on the wall they were removed from the simulation domain.
At first, the crossing trajectory effect was not included in the calculation to keep the analysis of the results simple. Results showed that the deposited fraction of the droplets was underpredicted by 20-25% without including the crossing

trajectory effect. In this chapter we try to explain and correct this underprediction. It seemed to us that these corrections had to be made before including the crossing trajectory effect which adds a greater complexity to the model. That is why the crossing trajectory effect has not been accounted for in the results presented in the following.
For the calculation of the relaxation time of the particle (equation (2.72)), the correction of the drag coefficient for flows beyond the Stokes regime has been neglected. This was justified because the results showed that the Reynolds number of the flow around the particles was less than 1 in the whole computational domain (maximum 0.88).

5.2.3 Inlet condition

At the inlet, the velocity profile of the gas phase was assumed to be flat (11.92 m/s). The droplet phase had the same inlet velocity as the gas. The turbulent kinetic energy (TKE) of the gas was set to 1 m^2/s^2 and the rate of dissipation of the TKE of the gas was 1 m^2/s^3. Since Liu and Agarwal did not specify the volume fraction of olive oil, four values have been tested in the simulation: 1%, 0.1%, 0.01% and 0.001%.

5.3 Results

5.3.1 Expected results

We will first look at the prediction of a simple 1D model. Let α_{d0} be the concentration of the droplets at the inlet of the test section. U_d is the average velocity of the droplets that is supposed to be the average velocity of the gas U_g. Then, the continuity equation for the droplet phase leads to:

$$\frac{d\alpha_d}{d\frac{X}{D}} = -4K^+_{total}\frac{u_\tau}{U_g}\alpha_d \tag{5.1}$$

Here the velocity of the gas was assumed to be independent of X. Averaging symbols have been dropped for the sake of clarity. K^+_{total} is the total deposition velocity defined by equation (3.121). We have then:

$$ln\left(\frac{\alpha_d}{\alpha_{d0}}\right) = -4K^+_{total}\frac{u_\tau}{U_g}\frac{X}{D} \tag{5.2}$$

Supposing that the particles are in the inertia moderated deposition regime, according to McCoy and Hanratty (1977) $K^+_{total} \approx 0.17$. According to equation (3.78), u_τ/U_g can be calculated from the friction coefficient C_{fg}. C_{fg} is here calculated with the Blasius formula for a turbulent flow in a smooth pipe:

$$C_{fg} = \frac{0.3164}{4}\left(\frac{U_g D}{\nu}\right)^{1/4} \tag{5.3}$$

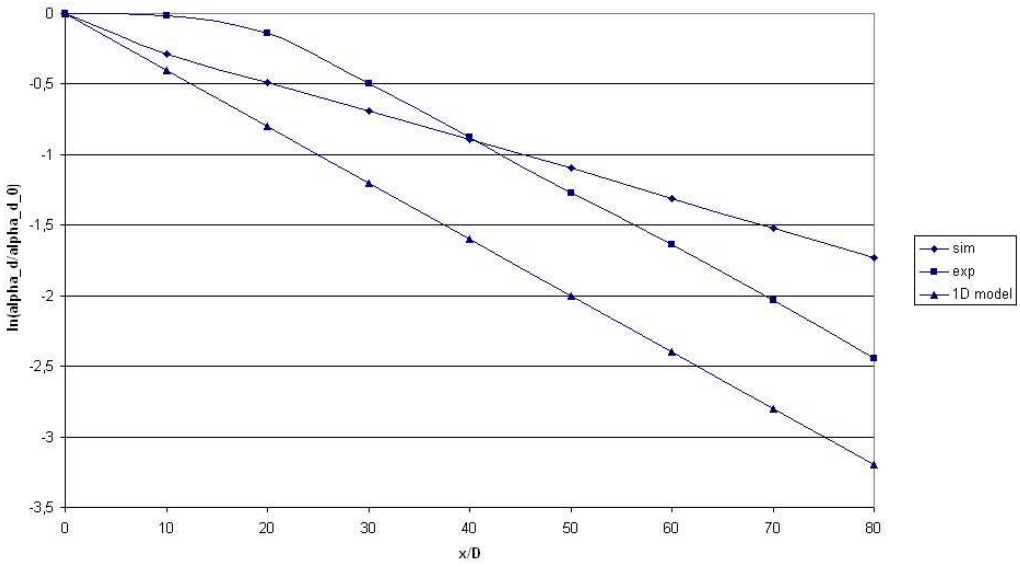

Figure 5.1: Evolution of the volume fraction of the droplet phase along the test section.

The calculation gives $u_\tau/U_g \approx 1/17$ and equation (5.2) becomes:

$$ln\left(\frac{\alpha_d}{\alpha_{d0}}\right) = -0.04\frac{X}{D} \tag{5.4}$$

5.3.2 Raw data

Figure 5.1 shows $ln\,(\alpha_d/\alpha_{d0})$ as a function of X/D. The three curves represent:

- The data of the simulation for a volume fraction of 0.01% (diamond symbols)
- The results of Liu and Agarwal (square symbols)
- Equation (5.4) (triangle symbols)

The experimental curve presents a different shape than the two other curves. It is flat at the beginning of the test section and then decreases linearly. The other two curves decrease linearly from the beginning of the pipe.
The experimental data show that a very small fraction of the droplets deposited before 10 diameters (only 1.5%). The deposition flux is depending on the turbulent dispersion of the droplets. This dispersion is depending on the turbulent kinetic energy of the gas. Thus one may assume that, at the inlet of the pipe,

the turbulent kinetic energy is much smaller in the experiment than in the simulation. First, it is important to check if the inlet values of the turbulent kinetic energy of the gas and of the dissipation are correct. In the simulation $k_g = 1\ m^2/s^2$ and $\epsilon = 1\ m^2/s^3$ at the inlet of the pipe. For k_g we can expect in the experiment a value such as:

$$k_g \approx \frac{3}{2} u_\tau^2 = 0.76 \approx 1 \tag{5.5}$$

Therefore, the inlet value of the TKE of the gas is correct. If now we consider l a typical length scale for large eddies we can write;

$$\nu_{T,g} = C_\mu \frac{k_g^2}{\epsilon} \approx l\sqrt{\frac{2k_g}{3}} \tag{5.6}$$

If ϵ has a value of $1\ m^2/s^3$, it leads to $l = 0.07$ m. This is impossible since the diameter of the pipe is 1.27 cm. If one approximates l by $D/5$, then $\epsilon = 29 >> 1$. This underestimation of the inlet value of ϵ may explain the gap on Figure 5.1 between the measured droplet concentrations and the droplet concentrations calculated by the simulation.
However, according to Figure 5.1, the comparison of the measured droplet concentrations with the droplet concentrations calculated with the simple 1D model shows that there is a strong inlet effect in the experiment. The reduced value of the deposition rate at the inlet of the pipe may indicate a relaminarization of the flow at the inlet of the test section.

5.3.3 Possible relaminarization of the flow

In the experiment of Liu and Agarwal, there was a pipe of 3.2 cm i.d upstream of the 1.27 cm i.d. test section . This upstream pipe was connected to the test section by a reducer which exact geometry has not been detailed by the authors. The average gas speed in the test section was 11.92 m/s while in the upstream pipe it was only 1.88 m/s. Thus if the reducer was relatively short, the flow was undergoing a significant acceleration at the beginning of the test section. This acceleration can be responsible for a relaminarization of the flow (Narasimha and Sreenivasan (1979)). Despite the lack of information about the reducer we supposed that the flow became fully turbulent only after a certain distance. To calculate this distance we tentatively correlated the experimental points except the one closest to the inlet. According to equation (5.4), a good choice is a function of the type:

$$ln\left(\frac{\alpha_d}{\alpha_{d0}}\right) = -m\left(\frac{X}{D} - \frac{X_0}{D}\right) \tag{5.7}$$

where m is a coefficient related to the total deposition velocity and X_0 the distance after which the flow becomes turbulent. The best fit was given by:

$$ln\left(\frac{\alpha_d}{\alpha_{d0}}\right) = -0.0385\left(\frac{X}{D} - 16.92\right) \tag{5.8}$$

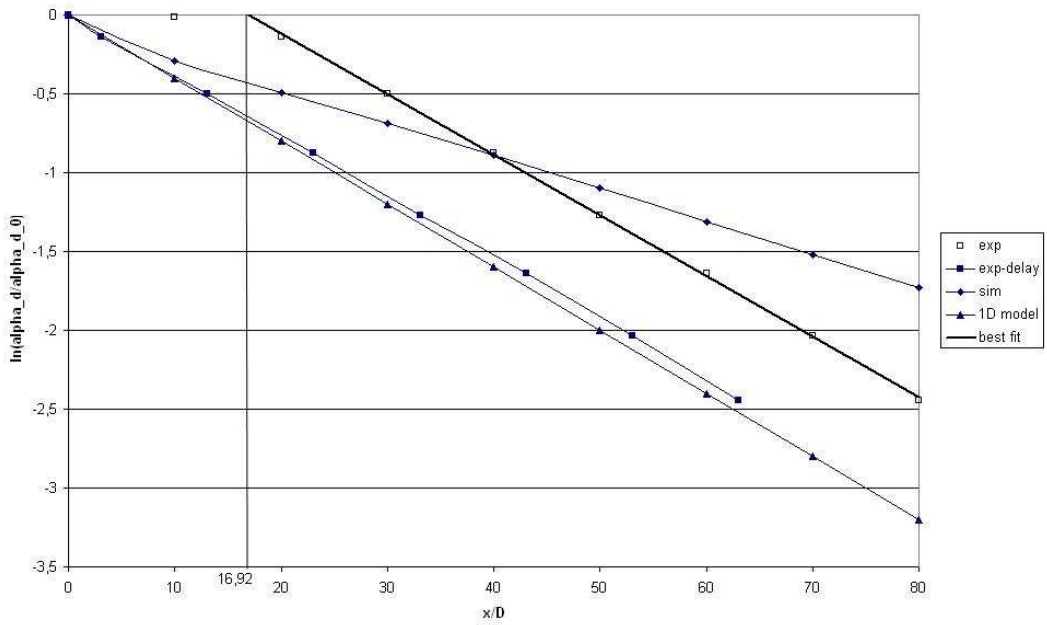

Figure 5.2: Estimation of a possible relaminarization effect.

series	exp-delay	simulation	1D model
slope	0.0385	0.0223	0.04

Table 5.1: Comparison of the slopes of the different series.

This means that we can estimate the laminar region to be roughly 17 diameters long. We can then translate the experimental points 16.92 diameters upstream. This is done on Figure 5.2, where the "exp-delay" curve is the translated experimental curve. The curve labeled "best fit" is equation (5.8).

5.3.4 Critical analysis of the model assuming a relaminarization of the flow

On Figure 5.1, the simulation did not show a clear tendency of under or overestimation of the droplet concentration. In contrast, if a relaminarization is assumed, Figure 5.2 shows that the simulation overestimates systematically this concentration. Table 5.1 shows the slopes of the different series pictured on Figure 5.2. These slopes are proportional to the deposition velocity (equation (5.2)). Therefore Table 5.1 shows that the simulation calculates a total deposition velocity which is significantly below the experimental value. In contrast, the agreement between the 1D model and the measurements is excellent.
The value of the deposited fraction $(1 - \frac{\alpha_d}{\alpha_{d0}})$ predicted by the simulation is in

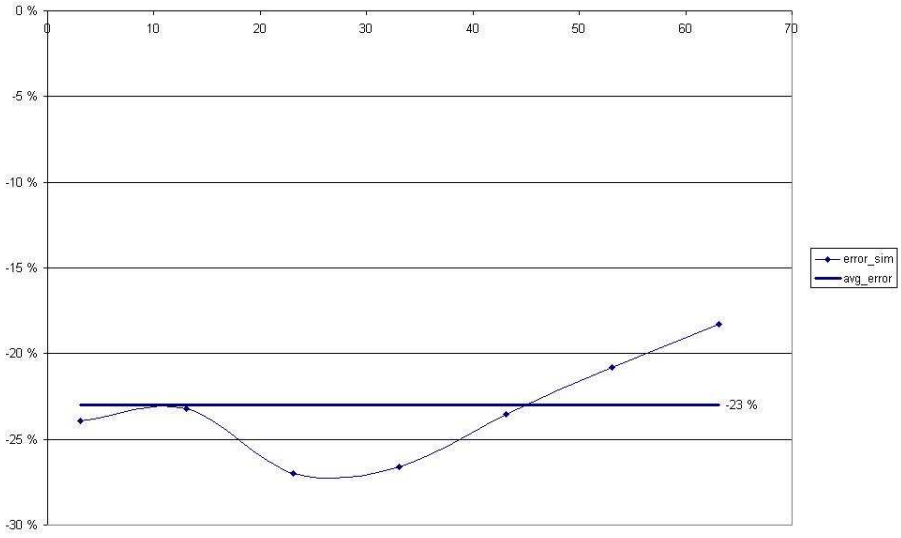

Figure 5.3: Error on the deposited fraction (assuming a relaminarization of the flow).

rather good agreement with the experiment. Figure 5.3, shows the error on the deposited fraction assuming a relaminarization at the inlet of the test section. In average, the simulation underpredicts the deposited fraction by 23%.
The good results of the 1D model show that $K^+_{total} \approx 0.17$ is a very good estimation of the total deposition velocity. The value of the total deposition K^+_{total} is controlled by two resistances in series: the resistance due to turbulent dispersion K^+_{disp} and a boundary layer resistance due to what we will call the "near-wall" deposition K^+_{wall}. This is readily expressed in equation (3.120). Let us come back to Figure 3.12. The curve of Figure 3.12 was considered to represent the variation of the near wall deposition velocity K^+_{wall} with the non-dimensional time t^+ in the diffusion-impaction regime. In this regime, it was assumed that:

$$K^+_{wall} \approx K^+_{total} \tag{5.9}$$

That is to say:

$$K^+_{disp} >> K^+_{wall} \tag{5.10}$$

It has been emphasized that the decrease of the total deposition velocity in the inertia-moderated regime was due to a decrease of the turbulent dispersion but not to a decrease of the near wall deposition velocity. That is why, in the model, the near-wall deposition velocity was kept constant (0.17) for relaxation times larger than 20. For relaxation times much larger than 20, the actual value of the near-wall deposition velocity is not important because the turbulent dispersion controls entirely the deposition rate. For particles with relaxation times much

smaller than 20, the turbulent dispersion is large and equations (5.9) and (5.10) are verified. For relaxation times that are at the limit of the inertia moderated regime and of the diffusion impaction regime the situation is more complex. Let us assume that the dispersion resistance and the near wall resistance are identical at the edge of these two regimes. Then

$$\frac{1}{K^+_{total}} = \frac{1}{K^+_{wall}} + \frac{1}{K^+_{disp}} = \frac{2}{K^+_{wall}} \tag{5.11}$$

It implies that:

$$K^+_{wall} = 2\,K^+_{total} \approx 0.34 \tag{5.12}$$

It means that, at the edge of the inertia-moderated regime and of the diffusion-impaction regime, the model uses a near-wall deposition velocity which is half of its likely value. In the experiment of Liu and Agarwal (1974) that has been simulated, the relaxation time of the particles was $t^+ = 29.6$. The deposition regime is therefore very close to the hybrid regime where both the turbulent dispersion and the near wall deposition velocity have an influence. It is then possible that the underprediction of the total deposition velocity comes from an underestimation of the near-wall deposition velocity.
Equation (3.123) developed by Lee *et al.* (1989) is supposed, according to the authors, to give the value of K^+_{wall} and not K^+_{total}. However this relation follows remarkably the values of K^+_{total} at high relaxation times (see Figure 3.13) where the decrease of the deposition rate is controlled by the turbulent dispersion. Relation (3.123) is actually an empirical fit of Lee (1987) over an entire pipe cross section and has not been sufficiently tested to be used with confidence. At present the variation with t^+ of the near-wall deposition velocity for $t^+ > 20$ is not known. It seems that $K^+_{wall} = 0.17$ is too small. There are indications that $K^+_{wall} = 0.34$ is a better guess but further studies have too be conducted to confirm this value.

5.3.5 Influence of the volume fraction

Figure 5.4 shows the results of the simulation for volume fractions of 1%, 0.1%, 0.01% and 0.001%. The deposited fraction is much lower in the case of large concentrations. The curve for the two lowest concentrations are identical except at the end of the test section. In the following, we will first study the cause of the low deposited fraction at high concentrations. Then we will discuss the reason of the slight difference between the simulation with a volume fraction of 0.01% and that with a volume fraction of 0.001%.

Deposition at large droplet concentration

The droplet concentration has an influence on the deposition flux. It is a well established experimental fact. Namie and Udea (1972) were the first to show that the deposition velocity was a decreasing function of the concentration. This

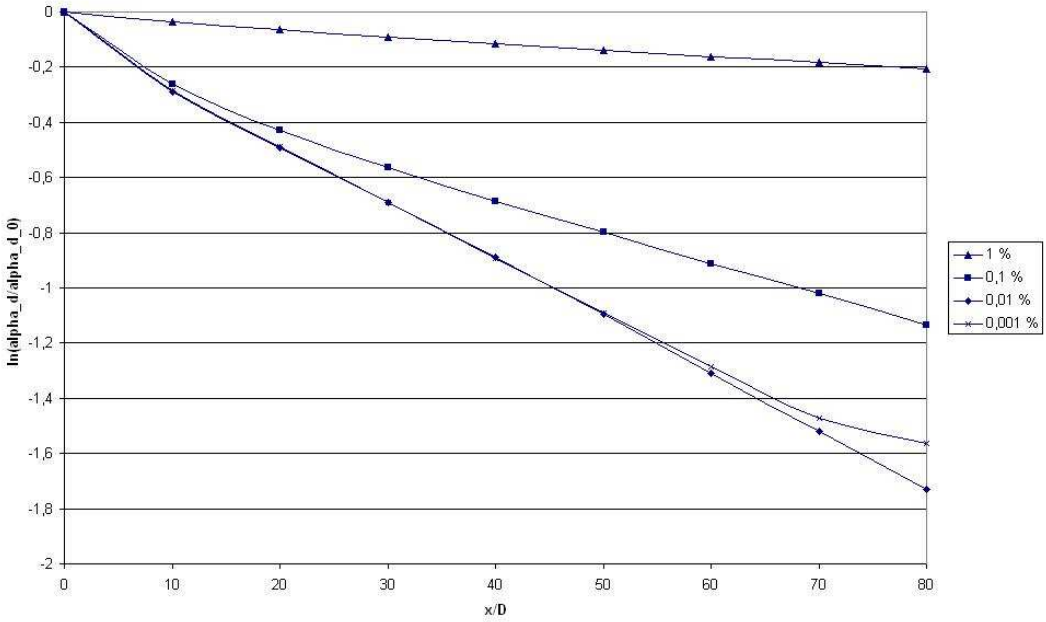

Figure 5.4: Effect of the droplet concentration on the deposited fraction.

has been confirmed by Andreussi (1983) and Leman et al. (1985). Schadel *et al.* (1990) proposed two possible explanations:

- High concentrations lead to more frequent droplet-droplet collisions. It promotes coalescence. As the droplets increase in size they become less reactive to turbulence. Then, the deposition rate decreases.
- Droplets damp turbulence in the gas phase.

Hay et al. (1996) proposed a third mechanism:

- Droplets are experiencing inelastic collisions that are not leading to coalescence. These collisions damp the turbulent movements of the droplets and lead to a reduction of the deposition flux.

Soldati and Andreussi (1996) showed that the decrease of the deposition rate because of coalescence in annular dispersed flows can be significant. According to their model, in a vertical annular flow, if each droplet/droplet collision leads to coalescence, the total deposition velocity can drop by roughly 80%. Zaichik and Alipchenkov (2001) integrated both coalescence and inelastic collisions. They showed that the latter is unlikely to have a large impact on the deposition rate. In our model there is no modeling of droplet-droplet interactions. Thus the decrease of the deposited fraction with droplet concentration is due to the damping

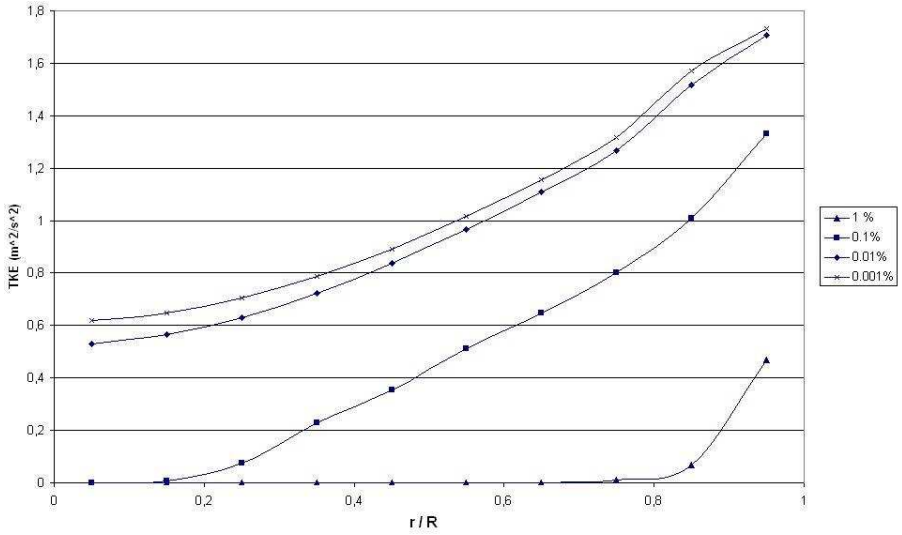

Figure 5.5: Effect of droplet concentration on the turbulent kinetic energy of the gas. X/D=80.

of the turbulence intensity of the gas phase by the droplet phase. Figure 5.5 shows the turbulent kinetic energy profiles at $X/D = 80$. Each curve is labeled with the inlet volume fraction of the droplet phase. One can see that the TKE decreases with the droplet concentration. The modification of the turbulence intensity by the presence of a dispersed phase is called "turbulence modulation". When particles are large, there is an increase of the TKE because of the wake of the droplets. In contrast, when particles are small, the droplets generate a greater dissipation[1]. Pourahmadi (1982) showed that this was the consequence of an additional dissipation term due to the interphase covariance $\widetilde{U''_{id}U''_{ic}}$. Crowe (2000) also suggested that small particles generate a larger dissipation because they modify the turbulent dissipation length scale of the continuous phase. Crowe (2000) discussed the criteria to find whether the dispersed phase increases or decreases the turbulent intensity of the gas. He presented a synthesis of different measurements of the change in turbulent in-

[1]The picture is however different in an annular flow. In this type of flow, there are experimental evidences that the turbulent intensity is enhanced whatever the size of the particles (Azzopardi (1999) and Trabold and Kumar (2000b)). Azzopardi (1999) suggested that it came from:

1. The rough film/gas interface
2. The newly created droplets moving slowly close to the interface

Both effects will be accounted for in our complete model: the first with a rough wall boundary condition for the gas phase and the second effect by the loss of momentum of the droplet phase during deposition.

tensity versus the ratio of the diameter of the droplet d to l the size of the largest eddies in the flow. The graph showed that the turbulent intensity decreases if:

$$\frac{d}{l} < 0.1 \tag{5.13}$$

This is only a rough estimation based on purely experimental results. In our case, if one considers that the typical turbulent length scale is a tenth of the diameter of the pipe, we have:

$$\frac{d}{l} = \frac{16.8\ 10^{-6}}{1.27\ 10^{-3}} \approx 1.3\ 10^{-2} < 0.1 \tag{5.14}$$

Thus, one indeed expects a decrease of the turbulent kinetic energy with the droplet concentration.
However, there is nothing in the equations of the present model that may decrease the turbulent kinetic energy of the gas with the concentration. This is shown by equation (2.62) where the interaction term is positive. There is however an explanation to this peculiarity. In the present work, it was decided to switch off certain phase-interaction terms of Fluent's default transport equation for the turbulent kinetic energy. The reason for doing so, was that Fluent user's guide (Fluent Inc. (2005)) did not provide references for these additional terms which expressions were somewhat postulated. It appeared that some of these additional terms that according to the user's guide could be switched off, were always switched on (Laux (2006)). These terms can explain the decrease of the kinetic turbulent energy with the concentration of the droplets. However the values of the turbulent kinetic energy of the gas phase on Figure 5.5 should be taken with care.

Deposition for the case of a volume fraction of 0.001%

At a downstream distance of 80 D, Figure 5.4 showed that the value of $ln\,(\alpha/\alpha_0)$ was slightly higher for $\alpha_0 = 0.001\%$ than for $\alpha_0 = 0.01\%$. Figure 5.6 shows a close up of this curve with a sampling of the values every diameter for $70 \leq X/D \leq 80$. It shows oscillating values for $\alpha_0 = 0.001\%$. These values were also changing with the number of iterations. At this stage of the iteration process, the residuals were not decreasing anymore and indicated that the convergence was reached. It is believed that, at very small concentrations, the value of α/α_0 was influenced by the residual numerical oscillations occurring after the convergence of the solution. The use of a double precision solver may help working out this defect.

5.4 Summary: Performance of the model for pure deposition

Compared to the results obtained by Liu and Agarwal (1974), the model predicts the right order of magnitude of the deposited fraction but underestimates

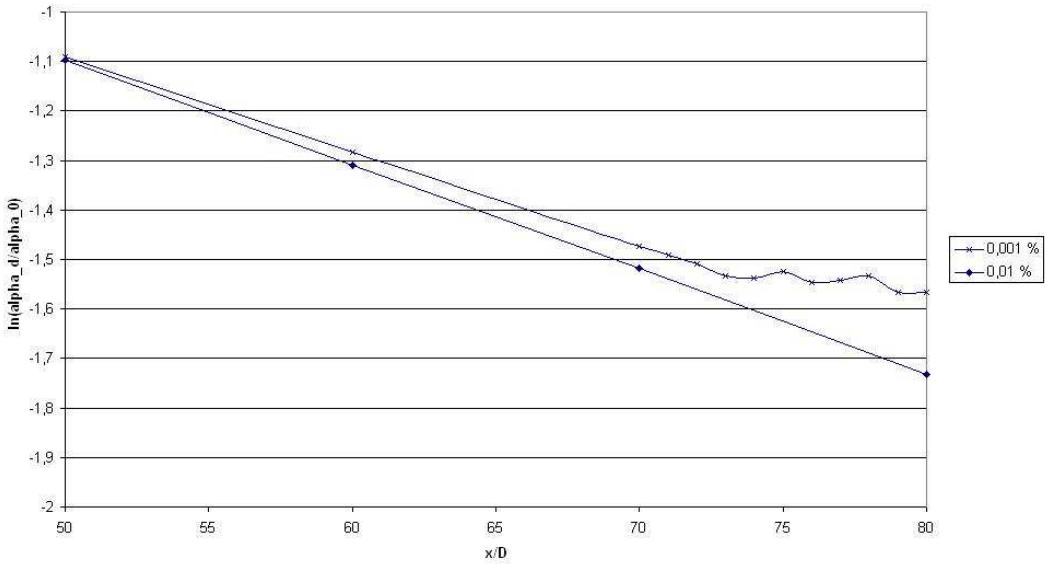

Figure 5.6: Comparison of $ln\,(\alpha/\alpha_0)$ for $\alpha_0 = 10^{-4}$ and $\alpha_0 = 10^{-5}$.

this deposited fraction by $20 - 25\%$. This underestimation is probably mainly due to an inaccurate value of the near-wall deposition velocity when the particle relaxation time t^+ is greater than 20. In the present model, when $t^+ \geq 20$, $K^+_{wall} \approx 0.17$. $K^+_{wall} \approx 0.34$ is believed to be a better estimate. When t^+ is significatly larger than 20, the modelling of K^+_{wall} is not important since the turbulent dispersion in the core controls the deposition flux.
The model predicts a correct qualitative behavior at large droplet concentration. This is due to Fluent's additional terms in the turbulent kinetic energy transport equation. However the justification of the mathematical expressions of these terms is not provided by Fluent and as a result the simulation data at high droplet concentration should be considered with care. At very low concentrations, one may need a double precision solver.

Chapter 6

Annular flow without dispersed phase

In this chapter we will compare the prediction of the model with an experimental study of an annular flow without droplets. The experimental work was carried by Asali (1984). The purpose of this chapter is to validate the film model.

6.1 Description of the experiments

Asali (1984) did measurements of liquid film heights and pressure drops in vertical annular flows. The inner diameters of the pipes were 4.2 and 2.29 cm. The fluids were either air and water or air and glycerin. Here the case chosen is that of an air/water flow with no entrainment in a 4.2 cm i.d. pipe. The water had a density of 990 kg/m^3 and a viscosity of 0.0011 $kg/(ms)$. Liquid and gas mass flow rates were varied. In the experiment, the liquid was introduced along the wall by an annular slot. Asali measured the pressure gradients with two water-filled manometers. They were located 4.57 m, 4.65 m and 4.77 m from the annular slot. The total length of the pipe was 9 m. The film thickness was determined by the measurement of the conductance between two electrodes. These electrodes were mounted flush in the wall.

6.2 Set-up of the numerical case

6.2.1 Grid

The grid was axisymmetric. Four grids were tested for a single phase flow. The radial spacing of the cells was always a twentieth of a diameter. The length of the cells were varied between 1/5 and 2 diameters. The single phase solution was grid-independent. Multiphase simulations were performed with the coarser grid ($D/20$ X $2D$).

6.2.2 Inlet condition

In this experiment the flux of film must be specified at the inlet. This type of boundary condition is slightly more delicate to handle than the inlet of a liquid phase which is dispersed. As presently programmed, our model requires an inlet film height h_0 and an inlet turbulent kinetic energy of the gas k_{g0}. However, as will be detailed below, the film mass flow rate at the inlet is entirely defined from h_0 and k_{g0}. As a result for a given inlet film mass flow rate, h_0 and k_{g0} can not be chosen independently. The inlet liquid flow rate is:

$$\dot{m}_{f0} = \rho_f \, \pi \, D \overline{u}_{avg} \, h_0 \tag{6.1}$$

If one introduces relation (3.33) for $\overline{u}_{avg}$ and the modeling of τ_i (3.87), it gives:

$$\dot{m}_{f0} = \rho_f \, \pi \, D \left(\frac{\rho_f g_x h_0^3}{3\mu_f} + \frac{\rho_g \sqrt{C_\mu} k_{g0} h_0^2}{2\mu_f} \right) \tag{6.2}$$

Equation (6.2) is the relation that links $\dot{m}_{f0}$, h_0 and k_{g0}. Note that in equation (6.2) g_x is negative. To fulfill equation (6.2), the easiest way is to impose a film height at the inlet of the pipe. This will give the turbulent kinetic energy at the inlet. If one wants to impose a TKE at the inlet, this requires the resolution of a third order algebraic equation to find h_0. The turbulent kinetic energy at the inlet is given by:

$$k_{g0} = \frac{2\mu_f}{\rho_g \sqrt{C_\mu} h_0^2} \left(\frac{\dot{m}_{f0}}{\rho_f \, \pi \, D} - \frac{\rho_f g_x h_0^3}{3\mu_f} \right) \tag{6.3}$$

The inlet value of the turbulent kinetic energy should be in agreement with the average gas velocity. The function $k_{g0}(h_0)$ given by equation (6.3) has a minimum. Often the values of the heights that give a TKE in agreement with the average gas velocity, are not far from the height that gives a minimum turbulent kinetic energy. In one series of experiments of Asali (1984), the liquid mass flow rate was 3.18 g/s. In this case, according to equation (6.3), the minimum turbulent kinetic energy is about 7.1 m^2/s^2 for a height of 250 μm. This roughly corresponds to a turbulent intensity of:

$$\sqrt{\frac{2}{3} k_{g0}} = 2.2 \ m/s$$

Asali made the gas flow rates vary between 32.61 g/s and 104.9 g/s. This corresponded to average gas velocities between 20.3 and 57.4 m/s. It means that, at the inlet of the computational domain, the ratio of the turbulent intensity to the mean gas velocity is between 4 and 11%. It seems correct. On the contrary, if one chooses a height of 1 cm, it gives ratios between 19 and 55 %. If one chooses a height of 10 μm, it gives ratios between 56 and 158 %. Both estimations are clearly incorrect. It is interesting to see that equation (6.3) gives an estimation of the equilibrium thickness of the film. In all the simulations, we chose an inlet height of $h_0 = 400 \mu m$. This value was chosen significantly higher than the experimental equilibrium value, to see if the model could predict the experimental values with a rather incorrect inlet height.

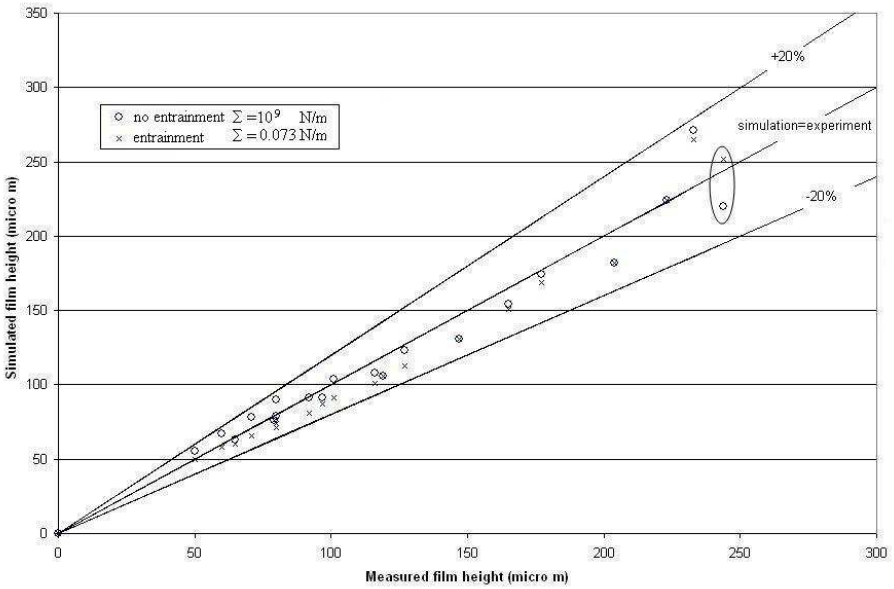

Figure 6.1: Simulated vs. measured film height. (Measurements made by Asali (1984))

6.2.3 Test cases

The simulations were performed for 5 liquid flow rates: 0, 3.18, 5.17, 7.45 and 9.94 g/s. Each of this flow rates have been tested with five possible gas flow rates: 32.61, 49.10, 71.81, 87.93, and 104.9 g/s.

6.3 Results

6.3.1 Film heights

The results for the film height obtained in the simulation are plotted versus the experimental values on Figure 6.1. Circle symbols represents the data obtained without entrainment. In the present model, the only use of the surface tension is to calculate the entrainment flux. It was then possible to impede entrainment by specifying a surface tension of 10^9 N/m. Under each circle of Figure 6.1 is a cross that represents the value of the height of the film when entrainment was allowed. The measured values and the simulated values are in very good agreement within $\pm 20\%$. As a rule the entrainment was either zero or very small. It agrees with the observations made by Asali (no entrainment at all). One simulation gave a height of the film which was lower without entrainment than with entrainment. These data have been circled on Figure 6.1. It corresponds to the lowest gas flow rate (32.61 g/s) and the highest liquid flow rate (9.94 g/s).

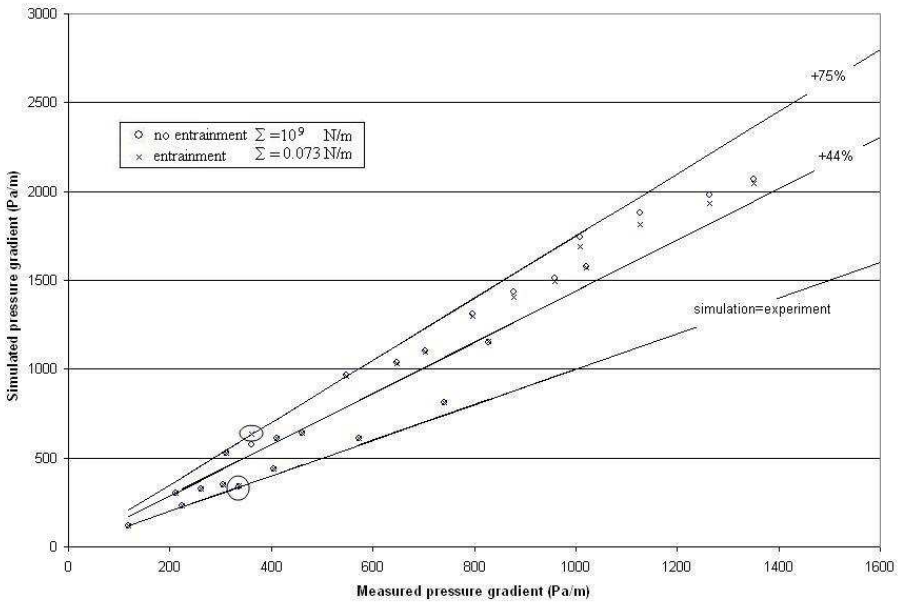

Figure 6.2: Simulated vs. measured pressure drop. (Measurements made by Asali (1984))

The calculation indicated that, in this case, the gas barely sustained the film flow in the upward direction. As a result, the computed film height was very unstable with time and had doubtful values when the velocity of the film was close to zero. The predictions represented by these points are untrustworthy.

6.3.2 Pressure drops

The results for the pressure drops obtained in the simulation are plotted versus the experimental values on Figure 6.2. The predicted pressure gradient is significantly above the measured value. Pressure gradients are systematically overpredicted with an overprediction of +44% in average and +75% at the most. A tentative explanation of this overprediction will be given in the next section. Looking into the literature, it seems that good predictions of the pressure drop remain difficult to perform. The recent three fluid model of Alipchenkov *et al.* (2004) could predict pressure gradients with an average precision ±30%. Ho Kee King and Piar (1999) needed to adjust their modelling of the wall-friction of the film to get a correct prediction of pressure gradients. Experimental correlations are not particularly reliable. Owen *et al.* (1985) tested 9 different relations. When they compared them to their experimental results, they noted 50% of overprediction at best and sometimes up to 150%.
Figure 6.2 shows that the pressure gradient with entrainment is lower than with-

out entrainment. A possible explanation is that the height of the film is lower when entrainment occurs. As a result the equivalent sand roughness $s = 4h$ (equation (3.82)) is lower. Then the pressure drop decreases. The entrained fraction of droplets is very small[1]. Therefore the pressure loss due to deposition and re-entrainment is not big enough to compensate the gain due to the deacrease of the roughness height.
Two data points are circled on the graph. The circle that contains both the entrainment and the no-entrainment points corresponds to the simulation where the force exerted by the gas on the film and the gravity force were practically equal. The film was very unstable and barely flowing upward. The circle containing only the entrainment data was exactly at the onset of entrainment. The volume fraction of the droplet phase at the outlet was $7 \cdot 10^{-7}$. Although the height of the film was perfectly stable, the pressure gradient was oscillating significantly in time because of the continuous shift between the entrainment regime and the no-entrainment regime. Hence, the prediction represented by this point is not particularly reliable.

6.3.3 Critical analysis

In this section we will try to explain the discrepancies between the computed and the experimental results. First we will study the consequences of assuming that the velocity of the gas/film interface is zero for the wall boundary condition of the gas. Second we will study closely the relation between the equivalent sand roughness of the film and its height. The assumption that the film is laminar will also be studied.

a) Overestimation of the pressure drop

a1) Velocity of the gas/film interface. The overprediction of the pressure drop may be due to a non-negligible velocity of the interface compared to the velocity of the gas. Indeed, if the velocity of the interface is non-negligible, the wall boundary condition for the gas phase in the present model is inaccurate. This inaccuracy leads to an overprediction of the interfacial shear stress and consequently to an overprediction of the pressure drop. According to equation (3.36), without deposition and entrainment and assuming a laminar film, the velocity of the interface can be estimated by:

$$c_x = h\left(\frac{2\tau_i + \rho_f g_x h}{2\mu_f}\right) \tag{6.4}$$

A force balance on an infinitesimal length of pipe leads to:

$$\tau_i = -\frac{D}{4}\frac{\partial P}{\partial X} \tag{6.5}$$

[1]For the largest liquid and gas mass flow rate, when the entrainment is largest, the volume fraction was 0.0042 % at the tube outlet.

According to Figure 6.2, we can evaluate the interfacial shear stress by:

$$\tau_i \approx \frac{0.04}{4} \cdot 800 = 8\ Pa \tag{6.6}$$

If we now estimate the height of the film to be $200\mu m$ (Figure 6.1), according to equation (6.4), the velocity of the interface is 1.3 m/s. In the experiments conducted by Asali (1984), the average value of the gas velocity was comprised between 20.3 and 57.4 m/s. The ratio of the interface velocity to the average gas velocity is then approximately 4 or 5 %. The ratio of the interface velocity to the gas velocity at the centroid of the near wall cell is larger. The velocity of the interface c_x is thus much lower than the velocity of the gas, but assuming $c_x = 0$ leads to a significantly inacurate wall boundary condition for the gas phase. This inaccuracy contributes to an overestimation of the pressure drop.

a2) Equivalent sand roughness and turbulent viscosity of the film. The equivalent sand roughness of the liquid layer is also a key parameter for a correct computation of the pressure drop. This roughness is given by $s/h = 4$. In the following we will study closely the ratio s/h and its influence on the pressure drop.
In the present simulation the turbulent viscosity of the film is very small or zero because the only turbulence possible in the liquid layer comes from deposition. As previously emphasized in chapter 3, neglecting the turbulence induced by the flow of the film requires two conditions:

1. The film is very thin.
2. The interface of the film is rather smooth.

These conditions are fulfilled in a high pressure scrubber. In contrast, we simulate here an annular flow with air and water at atmospheric pressure. Hewitt and Hall Taylor (1970) showed that a laminar model of the liquid layer was not satisfactory in this case. Moreover specifying $s/h = 4$ is likely to be in contradiction with the assumption of a smooth interface. Therefore the effect of the turbulent viscosity of the film must be studied.
In the following we will study the influence of a lower value of s/h and of a higher value of the turbulent viscosity of the film. To study s/h another series of simulation has been performed with $s/h = 3.2$ which is the lowest possible value according to equation (3.76). These calculations gave encouraging results but showed that $s/h = 3.2$ may still be to high a value. Next we will give some pieces of information that confirms s/h to be much lower than first expected. Finally, a simplified analysis of the flow is given to see what is the influence of s/h on the pressure drop. This last analysis also quantifies the effect of an increased turbulent viscosity of the film.

b) Influence of s/h: additional simulations

The ratio $s/h = 3.2$ was compared to the ratio $s/h = 4$. Three gas mass flow rates have been tested (32.61, 71.81 and 104.9 g/s) against three liquid mass

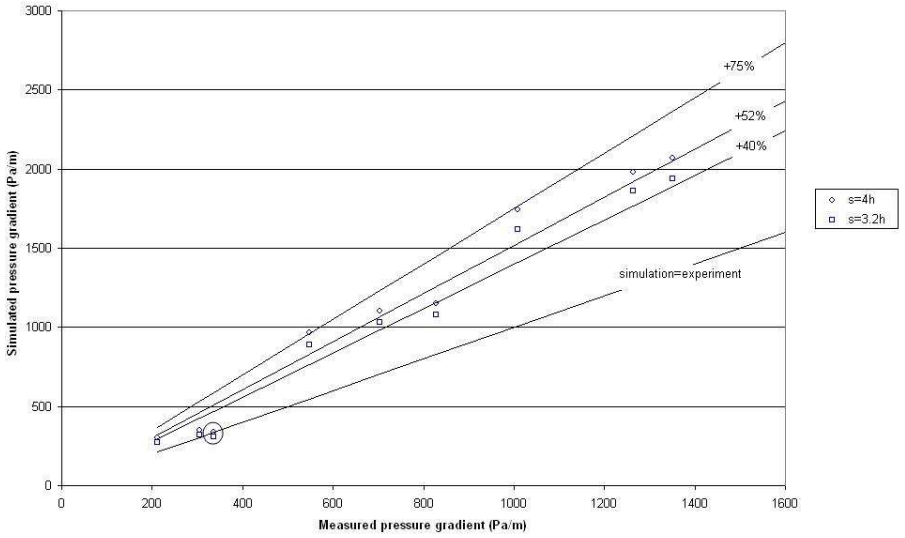

Figure 6.3: Comparison of the pressure drop predictions with $s/h = 4$ and $s/h = 3.2$.

flow rates (3.18, 7.45 and 9.94 g/s). The pressure gradients results are plotted on Figure 6.3. If one excludes the circled points (difficulty of convergence), the average difference with experimental data for $s/h = 4$ was 52%. With a ratio of $s/h = 3.2$ this error drops to 40%. Even if the predicted pressure drop has improved, it seems that the ratio of the sand roughness height to the height of the film is still overestimated.
The heights of the film are reported on Figure 6.4. The height of the film increases when s/h is smaller. It is expected because the decrease of the roughness height implies a decrease of the turbulent kinetic energy of the gas by the wall. Consequently the interfacial shear which is modeled by:

$$\tau_i = \rho_g \sqrt{C_\mu} k_g \tag{6.7}$$

becomes lower. Then the velocity of the film decreases and the height of the film increases. With $s/h = 4$ the mean overestimation of the film height is 3%. With $s/h = 3.2$, it is 7% (excluding the circled data). Since the uncertainty measurements was not given by Asali (1984), it is not possible to tell if these errors are significant. One can notice however that, for $s/h = 3.2$, one point is outside the range of the $\pm 20\%$. The ratio of the sand roughness to the height of the film has less effect on the film height than on the pressure drop. This will be explain later in this chapter.
The additional simulations showed that the ratio s/h is lower than 3.2. It seems that it can be decreased further without increasing the height of the film significantly. If this is verified, the simulation results will be in better agreement

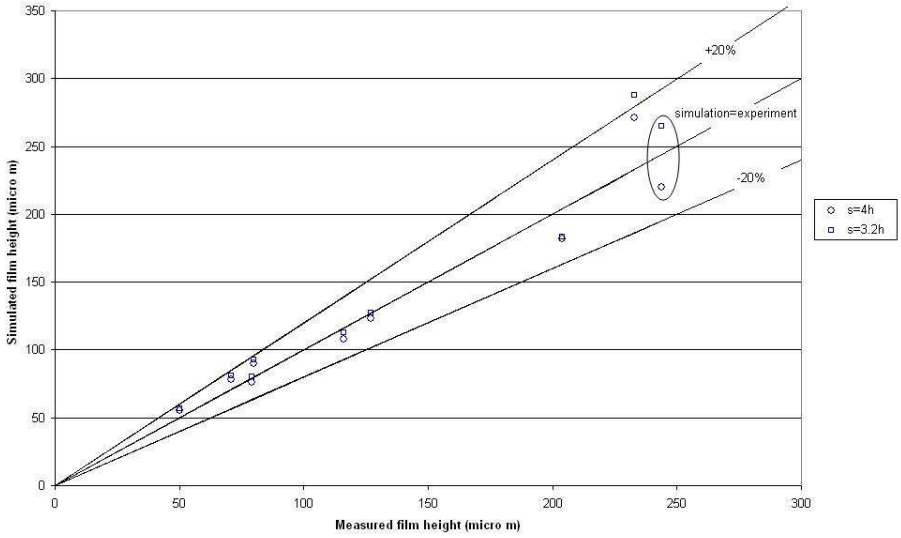

Figure 6.4: Comparison of the heights of the film with $s/h = 4$ and $s/h = 3.2$.

with the pressure drop measurements of Asali (1984) and still be in agreement with his film heights measurements.

c) Additional indications that $s/h < 3.2$

The effect of entrainment and deposition on experimental correlations. Before lowering further the value of s/h one should check if this is not in contradiction with experimental results. The value of s/h came from two equations that are re-written below:

$$C_{fg} \approx 0.005 \left(1 + \Gamma \frac{h}{D}\right) \tag{6.8}$$

and

$$C_{fg} \approx 0.005 \left(1 + 75 \frac{s}{D}\right) \tag{6.9}$$

Equation (6.8) is empirical. Wallis(1969) proposed $\Gamma = 300$ and Dobran (1987) and Nigmatulin (1991) proposed $\Gamma \approx 240$. Equation (6.9) is an approximation of the friction factor for a fully rough regime. Equating (6.8) and (6.9) leads to

$$s/h = \Gamma/75 \tag{6.10}$$

However one should be aware that the measurements made to obtain relation (6.8) are pressure drops measurements. We underlined previously that a significant part of this pressure drop is generated by the deposition/entrainment process and not only from the roughness of the liquid film. Fore and Dukler (1995a) showed that up to 20% of the pressure drop could be due to the

deposition/entrainment process in an annular flow (air-water vertical flow at atmospheric pressure). If then only 80% of the measured friction coefficient is taken into account, the relation between the film height and its equivalent roughness becomes

$$0.8 \cdot 0.005 \left(1 + \Gamma \frac{h}{D}\right) = 0.005 \left(1 + 75 \frac{s}{D}\right) \tag{6.11}$$

Then the ratio s/h is:

$$\frac{s}{h} = \frac{0.8\Gamma}{75} - \frac{0.2}{75} \frac{D}{h} \tag{6.12}$$

Experimental results from the literature show that $240 \leq \Gamma \leq 300$ (see chapter 3). According to the experiments performed by Asali (1984), in the present case, $172 \leq D/h \leq 840$. Then it gives for s/h the following range:

$$0.3 \leq \frac{s}{h} \leq 2.7 \tag{6.13}$$

The maximum of this range is below 3.2. One can then conclude that a lower value of s/h is likely and that this value is not in contradiction with the experimental results of the literature if one takes into account the pressure drop due to the entrainment and the deposition.

The shape of the interface. Another model, based on different principles confirms a low value of s/h. Let us first consider a model for the shape of the interface. The interface is assumed to be a periodic function. On a space period L this interface has two heights values. A high value h_2 corresponding to a wave and a low value h_1 on the rest of the period. The portion of the period occupied by the wave is $\mathscr{I} L$ where $\mathscr{I}$ is the intermittency. We suppose that the roughness of the interface is $s = h_2 - h_1$. This model of the interface is illustrated on Figure 6.5. The mean height h is:

$$h = \frac{\mathscr{I} L\, h_2 + (L - \mathscr{I} L)\, h_1}{L} = \mathscr{I} h_2 - (1 - \mathscr{I})\, h_1 \tag{6.14}$$

Introducing $s/h = (h_2 - h_1)/h$ one obtains:

$$\frac{h}{h_1} = \frac{1}{1 - \mathscr{I} \frac{s}{h}} \tag{6.15}$$

Schadel (1988) and Paras *et al.* (1994) showed that for annular air water flow at atmospheric pressure the intermittency could be approximated by 0.4. This implies that $s/h < 2.5$ because otherwise h/h_1 would be less than 0. Figure 6.6 illustrates the shape of the interface for different values of s/h. This figure shows that the film is highly deformed for $s/h > 1$. If the interface is highly deformed, the liquid layer may be disrupted, leading to entrainment. Since entrainment was not experimentally observe it is likely that s/h is 1 or less.

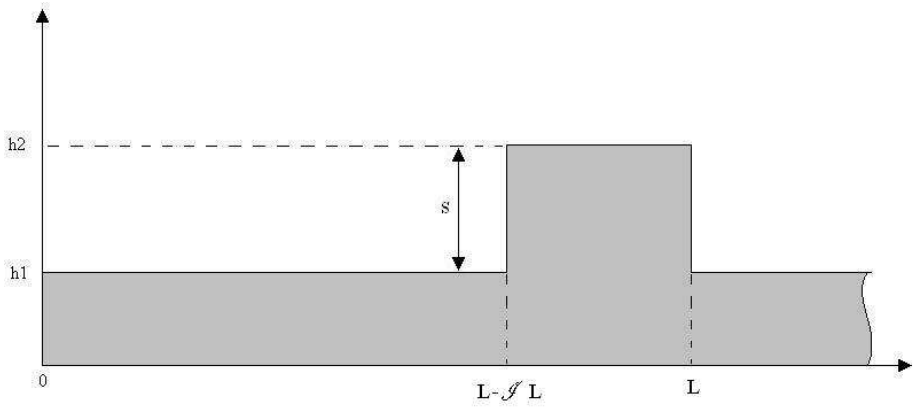

Figure 6.5: Simplified model of the film/gas interface.

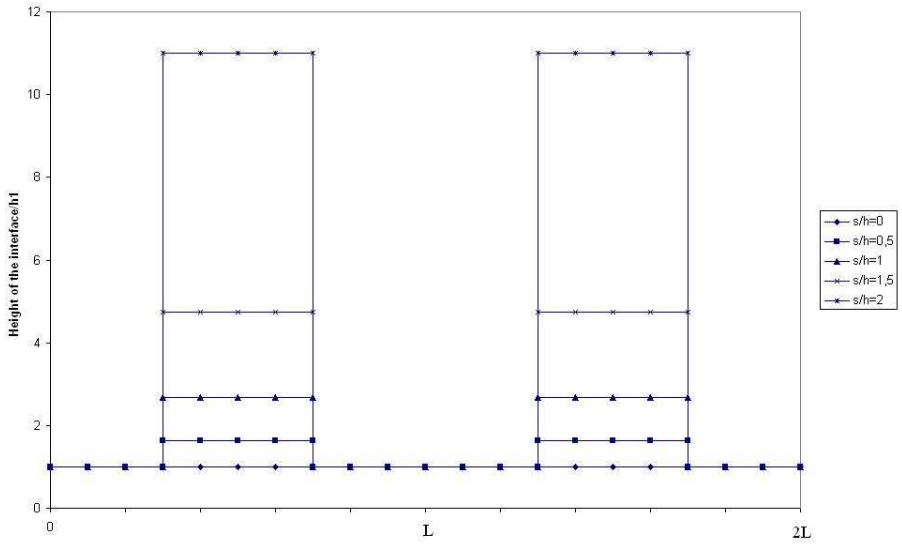

Figure 6.6: Shape of the interface for different values of s/h.

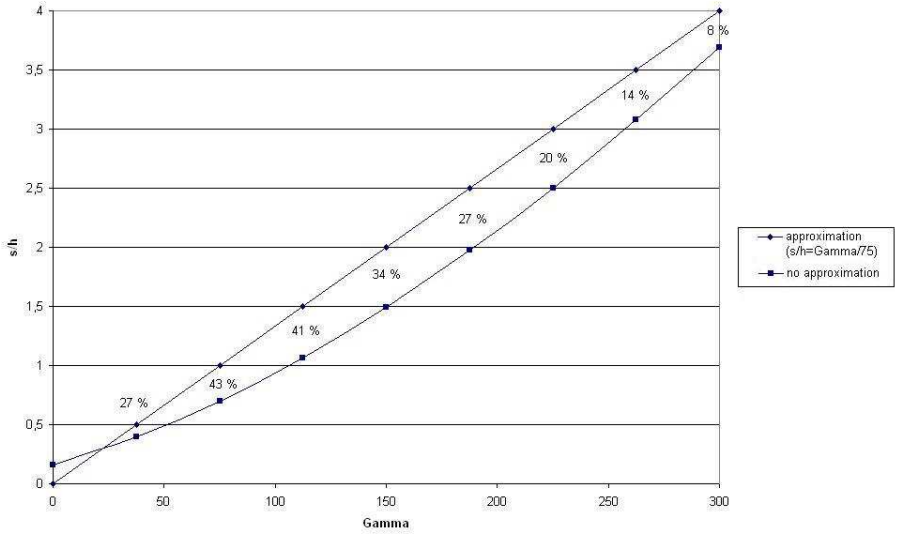

Figure 6.7: Approximated and non-approximated value of s/h.

The approximation of the friction coefficient in the fully rough regime. It must be underlined that relation (6.9) is an approximation. The expression of the friction factor in a fully rough regime (3.71) and equation (3.66) lead to relation (3.72). Equation (6.10), which is an approximation of equation (3.72), was only used to avoid a diameter dependence of the relation between the equivalent sand roughness of the film and the height of the film. Figure 6.7 shows how the ratio s/h is changed by the approximation $s/h = \Gamma/75$ compare to the non-approximated value given by (3.72). Except if $\Gamma < 20$, $s/h = \Gamma/75$ overestimates the value of s/h. This overestimation in % is reported on Figure 6.7. It is shown that this overestimation is important especially for $0.5 \leq s/h \leq 2.5$. Thus in the present case, the rough approximation of the friction coefficient by equation (6.10) overestimates the ratio s/h and consequently the pressure drop. This overestimation is diameter dependant.

The assumption of the fully rough regime. As underlined by Oliemans *et al.* (1986), if the protrusions of the liquid layer are within the gas viscous sublayer, the equivalent roughness of the film must be 0. According to these authors:

$$\frac{s}{h} = Max\left(\frac{\Gamma}{75}\left(1 - \frac{5\nu_g}{u_\tau h}\right); 0\right) = Max\left(\frac{\Gamma}{75}\left(1 - \frac{5}{h^+}\right); 0\right) \tag{6.16}$$

Figure 6.8 shows for $\Gamma = 300$ the value of s/h according to equation (6.16). If a fully rough regime is not assumed and if equation (6.16) is valid, one can see that, for $h^+ < 100$, there is a significant difference between the value of s/h and

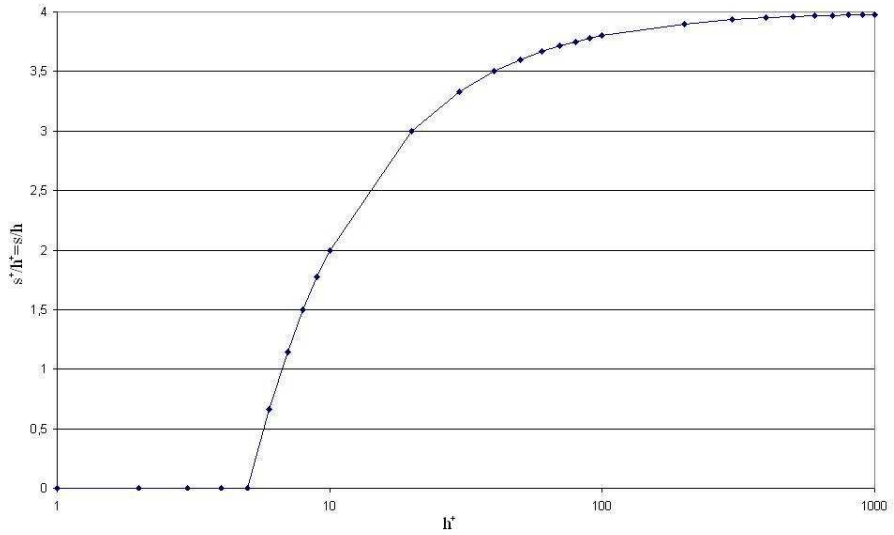

Figure 6.8: Value of s/h according to Oliemans *et al.* (1986).

the asymptotic value $\Gamma/75 = 4$. In the simulations the value of h^+ was between 20 and 100. Thus the roughness height was systematically overestimated.

Sum-up. The discussions above indicated that s/h is overestimated and that this overestimation has several sources. We can say that s/h is probably less than 2.5 and may be close to 1. However such an important change in the ratio of the equivalent roughness height to the mean height of the film implies important changes in the film height and the pressure drop. In the next subsection, we will present a simplified model of the film and study quantitatively the effect of the ratio s/h and of the turbulent viscosity of the film on the interfacial shear stress and on the height of the film.

d) Effects of s/h and of the turbulent viscosity of the film on the height of the film and on the interfacial shear stress

Equations of the model. The interfacial shear stress is by definition:

$$\tau_i \equiv \frac{1}{2} C_{fg}(h) \rho_g U_g^2 \tag{6.17}$$

This latter equation assumes that the velocity of the interface is negligible with respect to the bulk gas velocity U_g. Since there is no entrainment in the experiments of Asali, the film volume flow rate $\dot{Q}_{f0}$ is a constant and the conservation of mass can be written:

$$\dot{Q}_{f0} = U_f \cdot h \tag{6.18}$$

The conservation of momentum is given by equation (3.33). In can be written as follows:

$$U_f = \left(\rho_f g h + \frac{3}{2}\tau_i\right) \frac{h}{3\left(\mu_f + \mu_{Tf}\right)} \tag{6.19}$$

We will also suppose that:

$$C_{fg}(h) = 0.005\left(1 + \Gamma\frac{h}{D}\right) \tag{6.20}$$

where Γ is free to vary between 0 and 300. Finally it is admitted that:

$$\frac{s}{h} = \frac{\Gamma}{75} \tag{6.21}$$

Solution. The set of equations (6.17), (6.18), (6.19), (6.20) and (6.21) leads to a third order algebraic equation in h:

$$3\left(\mu_f + \mu_{Tf}\right) = \left(-G\,h + I\,C_{fg}(h)\right)h^2 \tag{6.22}$$

G is a coefficient related to the gravity:

$$G \equiv -\frac{\rho_f g}{\dot{Q}_{f0}} \tag{6.23}$$

I is a coefficient related to the interfacial shear:

$$I \equiv \frac{3}{4}\rho_g \frac{U_g^2}{\dot{Q}_{f0}} \tag{6.24}$$

Equation (6.22) can be solved exactly but the expression for h is quite cumbersome so it was solved numerically[2]. Two cases were studied:

1. If the film is laminar (μ_{Tf}=0), what is the impact of s/h on the film height and on the interfacial shear stress τ_i ?
2. If Wallis' correlation is valid ($\Gamma = 300$), what is the impact of μ_{Tf}/μ_f on the film height and on the interfacial shear stress τ_i ?

Effect of s/h. We define the index 0 which indicates the value of a quantity when $s/h = 4$ and $\mu_{Tf} = 0$. For the Simple Algebraic Model (SAM):

$$h_0 = h\left(s/h = 4; \mu_{Tf} = 0\right) = 103\ \mu m$$

Similarly

$$\tau_{i0} = \tau_i\left(s/h = 4; \mu_{Tf} = 0\right) = 18.8\ Pa$$

Assuming a laminar film, the effect of s/h on the height of the film and on the interfacial shear is shown on Figure 6.9. Table 6.1 compares the values given by the curves of Figure 6.9 at $s/h = 3.2$ and the values given by the simulations

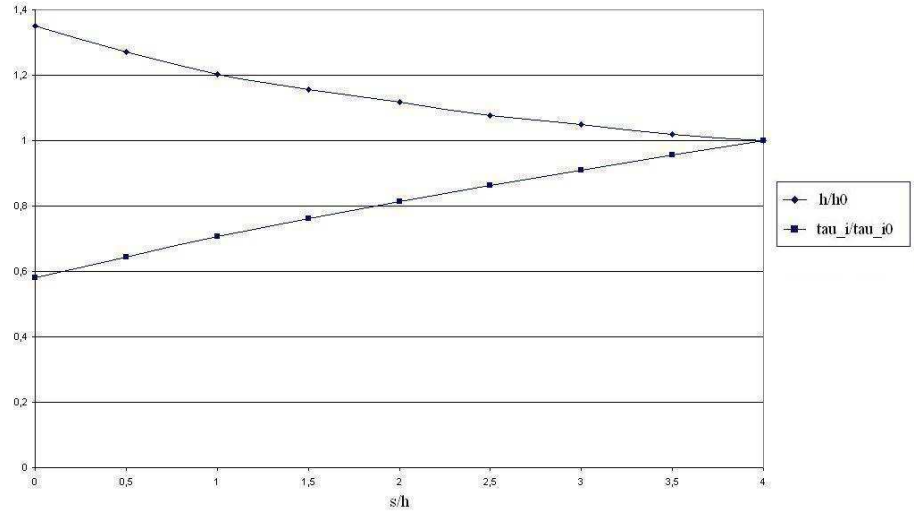

Figure 6.9: Effect of s/h on the height of the film and the interfacial shear stress.

	SAM	Simulation
h_0 (μm)	103	55
$h\left(s/h = 3.2; \mu_{Tf} = 0\right)/h_0$	1.039	1.036
$\tau_i\left(s/h = 3.2; \mu_{Tf} = 0\right)/\tau_{i0}$ (SAM) $\Delta P\left(s/h = 3.2; \mu_{Tf} = 0\right)/\Delta P_0$ (Simulation)	0.931	0.929

Table 6.1: Comparison $s/h = 3.2$ and $s/h = 4$ in the simulation and in the Simple Algebraic Model (SAM).

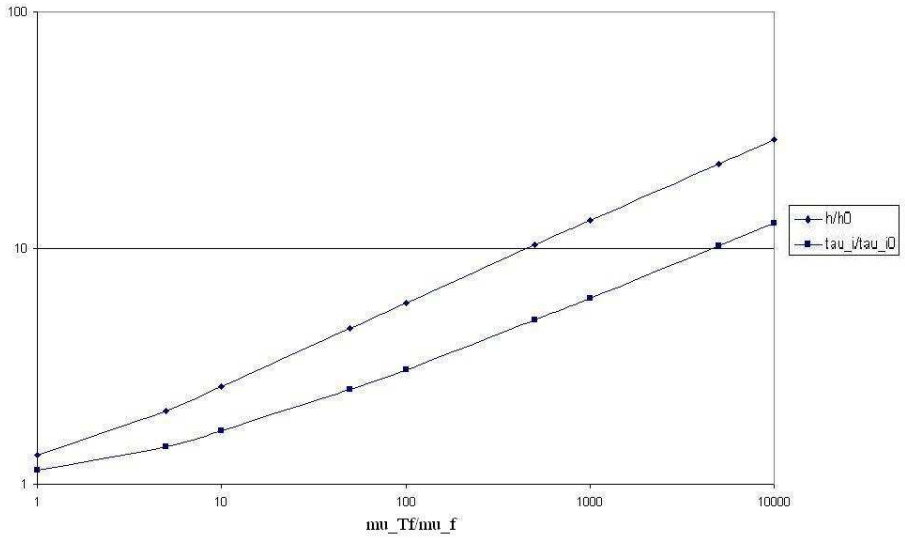

Figure 6.10: Influence of μ_{Tf}/μ_f on the height of the film and the interfacial shear stress.

when $s/h = 3.2$. Despite a difference between the reference heights, in terms of non-dimensional quantities, the algebraic model is in agreement with the simulation data. The algebraic model then seems to give reliable predictions of the influence of the ratio s/h on h and on τ_i. As indicated earlier, the value $s/h = 1$ might be the most appropriate. If $s/h = 1$, the interfacial shear stress decreases by 30% so that the pressure drop would be in a much better agreement with the measured value of Asali. However the height of the film would increase significantly (20%) because the slope of h/h_0 is steeper as s/h tends toward 0. Thus one expect for $s/h = 1$ a certain desagreement with the height measurements of Asali (1984).

Effect of an additional turbulent viscosity. The aim is here to see what is the overall effect of an additional averaged turbulent viscosity of the liquid film which value μ_{Tf} varies between 0 and $10000\mu_f$. Figure 6.10 indicates the influence of the ratio μ_{Tf}/μ_f on the height of the film and on the interfacial shear. The figure shows that both quantities increase with the turbulent viscosity of the liquid layer. However this increase is very slow. The interfacial shear is only multiplied by ten when the turbulent viscosity is multiplied by a factor 10000. As a result, one can consider that the turbulent viscosity of the film is not a crucial factor in the present case, the present case having a low water mass flow rate, a high air mass flow rate and no entrainment. Increasing

[2]The input data from Asali (1984) were taken with the highest air flow rate (104.9 g/s) and the lowest water flow rate (3.18 g/s).

the turbulent viscosity of the film would slightly increase the difference between the simulation data and the experimental measurements.

e) Sum-up of the critical analysis of the model.

The overestimation of the pressure drop comes from:

- an inaccurate wall boundary condition for the gas phase that does not account for the velocity of the interface.
- an overestimation of the equivalent sand roughness of the film which is here modeled by $s/h = 4$.

Considerations on the shape of the interface showed that s/h is probably around 1. A simple algebraic model confirmed that if $s/h = 1$, there is a significant decrease of the pressure drop (-30%). The conterpart is an increase of the film height (+20%). The turbulent viscosity of the film in contrast had no significant influence on the height of the film and on the interfacial shear unless μ_{Tf} was very high (10000 times the molecular viscosity).

6.4 Performance of the model for pure annular flows

In this chapter, the predictions of the model were compared to the experimental results of Asali (1984). He measured the thickness of the liquid film and the pressure drop in vertical annular flows without droplets. The film heights are predicted correctly by the model. However the pressure drops are significantly overpredicted. It seems that, for obtaining the correct pressure drop; first the velocity of the interface should be incorporated in the wall boundary condition of the gas and second the ratio of the sand roughness of the film s to the height of the film h must be decreased significantly, possibly divided by a factor 4.

Chapter 7

Simulation of an annular flow

In this chapter the predictions of the model have been compared with the experimental data obtained by Azzopardi and Teixeira (1994a, 1994b) in an annular flow. They made measurements of droplet fluxes, gas and droplet velocity profiles as well as turbulent intensities.

7.1 Experiments

7.1.1 Experimental arrangement

Azzopardi and Teixeira made measurements in a vertical air/water annular flow. They used a pipe of 32 mm inner diameter. The liquid film was introduced by a porous sinter at the bottom of the test section. Measurements were made 120 diameters above the liquid entry point. The pressure was 1.5 bar (see Azzopardi (1999)).

7.1.2 Measurements

Measurement of the droplet flux

Unfortunately, the authors did not specify how they measured the droplet flux at the outlet of the test section. It is however probable that they used the same technique as Azzopardi *et al.* (1991). The latter determined the film flow rate by withdrawing the liquid layer through a porous wall.

Other measurements

Azzopardi and Teixeira used Laser Doppler Anemometry to measure the gas velocity and the turbulent fluctuations. The light was scattered from 1 μm

polystyrene particles. The droplet velocities and diameters were measured by Phase Doppler Velocimetry.

7.2 Set-up of the numerical case

7.2.1 Grid and inlet condition

The grid was axisymmetric. Each cell had a radial length of a twentieth of a diameter and an axial length of 2.5 diameters ($D/20$ x $2.5D$). This mesh and two finer meshes have been tested on a single phase flow. For the finner meshes we used first cells of ($D/40$ x $D/20$) and second cells of ($D/20$ x $D/20$). The single phase solution was grid-independent.
The inlet condition for the film was similar to that discussed in the previous chapter. The height of the film at the inlet was 400 μm.

7.2.2 Droplet diameter

The model cannot handle several droplet diameters. It needs a mean value as an input parameter. Azzopardi and Teixeira (1994a) made measurements at three radial locations: the centerline, the eighth and the forth of the diameter from the centerline. According to the experiments, for given gas and liquid flow rates, the diameter of the droplets had its highest value at the center line and it decreased with the radial position. It is not obvious that this decrease continued when droplets were close to the film. Thus, it is doubtful to extrapolate the values of the droplet diameters on the whole pipe radius from the experimental data. Since the diameter of the droplets is unknown over half of the radius, an accurate value of the mean diameter cannot be calculated from the data of Azzopardi and Teixeira. In the simulation the droplet diameter has been determined by calculating an arithmetic mean of the measured values. The extremes of the measured values differed by no more than $\pm 8\%$ from the arithmetic mean.

7.2.3 Tested cases

Two series of cases have been simulated. The first series had a constant liquid mass flux of 15.9 $kg/(m^2 s)$ and four gas fluxes were tested: 24.5, 31.8, 43.7, and 55.6 $kg/(m^2 s)$. The second series had a constant gas mass flux of 31.8 $kg/(m^2 s)$ and three liquid fluxes were tested: 15.9, 31.7, and 47.6 $kg/(m^2 s)$.

7.3 Results

7.3.1 Entrained liquid mass flux

a) Simulation data

The predicted entrained liquid fluxes, which are the droplet mass fluxes, are presented in Table 7.1 and Table 7.2. As a rule the predictions are bad. In half

Gas mass flux ($kg/(m^2s)$)	24.5	31.8	43.7	55.6
Experimental value	0.86	0.96	1.43	2.19
Predicted value	downward flow	*0.37*	0.51	1.03

Table 7.1: Entrained liquid mass fluxes. Liquid mass flux: 15.9 $kg/(m^2s)$.

Liquid mass flux ($kg/(m^2s)$)	15.9	31.7	47.6
Experimental value	0.96	2.92	5.20
Predicted value	*0.37*	downward flow	downward flow

Table 7.2: Entrained liquid mass fluxes. Gas mass flux: 31.8 $kg/(m^2s)$.

of the cases, the model predicts a downward flow of the liquid. More precisely, the film comes in because of the imposed inlet condition but reaches a point where its velocity is 0. After, the liquid layer is caught between the inlet and this point and becomes very unstable. Entrainment occurs but the values of the entrained fraction cannot be compared with experiments because the calculated flow is not a clear upward annular flow as observed by Azzopardi and Teixeira. The difference between the predicted and the experimental entrained flux are -64% and -53% for gas fluxes of respectively 43.7 and 55.6 $kg/(m^2s)$. The value in italic is the same case for the two tables (gass mass flux 31.8 $kg/(m^2s)$ and liquid mass flux 15.9 $kg/(m^2s)$). This value is doubtful because the flow was barely upward. In this case, 44 mm after the inlet the liquid film velocity was practicaly 0 (0.7 mm/s).

b) Critical analysis

Two difficulties appeared during the simulation of the experiment performed by Azzopardi and Teixeira (1994a), (1994b). First a downward flow often occurred in the simulation while an upward flow was observed experimentally. Given that at the inlet there is a positive film mass flow rate, it means that the velocity of the film decreases along the tube before becoming 0 and then negative when the downflow starts. There is then an underestimation of the film velocity by the model. The velocity of the film is the result of a balance between forces driving the film upward (interfacial shear, momentum transfers due to deposition) and phenomena driving the film downward or slowing it down (gravity, viscosity, momentum transfers due to entrainment, turbulence of the film).
The second difficulty is that, even when the film flow is upward, the droplet mass flux is too small. It means that the entrainment rate in the simulation is lower than in the experiments. We will attempt with a simplified analytical model to find why the velocity of the film and the entrainment rate are too low. It is worth noticing that the velocity of the film and the entrainment rate are closely related phenomena.

c) Analytical model

In this section we will use the same type of algebraic model as that used in chapter 6 but adapted to take into account entrainment and deposition. We will first give the equations of the model, then study the influence of:

1. s/h, the ratio of the equivalent sand roughness of the film to the mean height of the film
2. $\mu_{Tf,i}/\mu_f$, the ratio of the turbulent viscosity induced by the film flow to the molecular viscosity
3. We_{crit} the critical Weber number
4. the proportionality coefficient 0.023 in equation (3.155) (entrainment rate correlation of Alipchenkov *et al.* (2002b))

Finally a test has been conducted with another type of entrainment rate correlation based on the Reynolds number of the film instead of its Weber number.

Equations of the model. If the velocity of the interface is very small compare to the bulk velocity U_g, the definition of the interfacial shear stress is:

$$\tau_i \equiv \frac{1}{2} C_f(h) \rho_g U_g^2 \tag{7.1}$$

We will suppose that an equilibrium takes place between entrainment and deposition that is to say:

$$J_e = J_d \tag{7.2}$$

Equation (7.2) implies that the mass conservation equation can be written:

$$U_f \, h = \dot{Q}_{f0} \tag{7.3}$$

Assuming that the velocity of the interface is negligible compared to the velocity of the droplet phase, the momentum equation (3.33) for the film leads to:

$$U_f = \left(\rho_f \, g \, h + \frac{3}{2} \tau_i + J_d \, U_d \right) \frac{h}{3 \left(\mu_f + \mu_{Tf,i} + \mu_{Tf,d} \right)} \tag{7.4}$$

where U_d is the droplet velocity, $\mu_{Tf,i}$ the turbulent viscosity induced by the film flow and $\mu_{Tf,d}$ the turbulent viscosity due to droplet deposition. The latter is modeled by:

$$\mu_{Tf,d} = J_d \, h \tag{7.5}$$

Finally, according to Alipchenkov *et al.* (2002b), the entrainment rate can be modeled by an equation which has the following form:

$$J_e = \chi \sqrt{\rho_f \, \tau_i} \left(\frac{\tau_i \, h}{\Sigma} - We_{crit} \right) \tag{7.6}$$

where χ is a proportionality constant. The previous equations (from (7.1) to (7.6)) lead to:

$$J_e = EC_f(h)^{3/2}h - E_{crit}\sqrt{C_f(h)} \tag{7.7}$$

where E is a coefficient representing entrainment. E is defined by:

$$E \equiv \chi\sqrt{\frac{\rho_f}{2}}\rho_g^{3/2}\frac{U_g^3}{\Sigma} \tag{7.8}$$

E_{crit} is a coefficient representing the influence of the entrainment threshold. It is defined by:

$$E_{crit} \equiv \chi\sqrt{\frac{\rho_f\rho_g}{2}}U_g\,We_{crit} \tag{7.9}$$

The above equations lead to an equation for h which is:

$$\begin{aligned}\left(-G + D\,C_f(h)^{3/2}\right)h^3 \\ + \left(I\,C_f(h) - D_{crit}\sqrt{C_f(h)} - T_d\,C_f(h)^{3/2}\right)h^2 \\ +T_{d,crit}\sqrt{C_f(h)}h - 3\mu_f\left(1 + \frac{\mu_{Tf,i}}{\mu_f}\right) \;=\; 0\end{aligned} \tag{7.10}$$

G is a gravity coefficient defined by equation (6.23). I is a coefficient related to the interfacial shear and is defined by equation (6.24). D is a coefficient related to the transfer of momentum due to droplet deposition. It is defined by:

$$D \equiv \frac{E\,U_d}{\dot{Q}_{f0}} \tag{7.11}$$

Similarly D_{crit} is defined by:

$$D_{crit} \equiv \frac{E_{crit}\,U_d}{\dot{Q}_{f0}} \tag{7.12}$$

Finally T_d is a coefficient related to the increase of the turbulent viscosity of the film due to deposition. It is defined by:

$$T_d \equiv 3E \tag{7.13}$$

Similarly $T_{d,crit}$ is defined by:

$$T_{d,crit} \equiv 3E_{crit} \tag{7.14}$$

To solve equation (7.10), we will assume that the friction coefficient takes the form:

$$C_f(h) = 0.005\left(1 + \Gamma\frac{h}{D}\right) \tag{7.15}$$

and that:

$$\frac{s}{h} = \frac{\Gamma}{75} \tag{7.16}$$

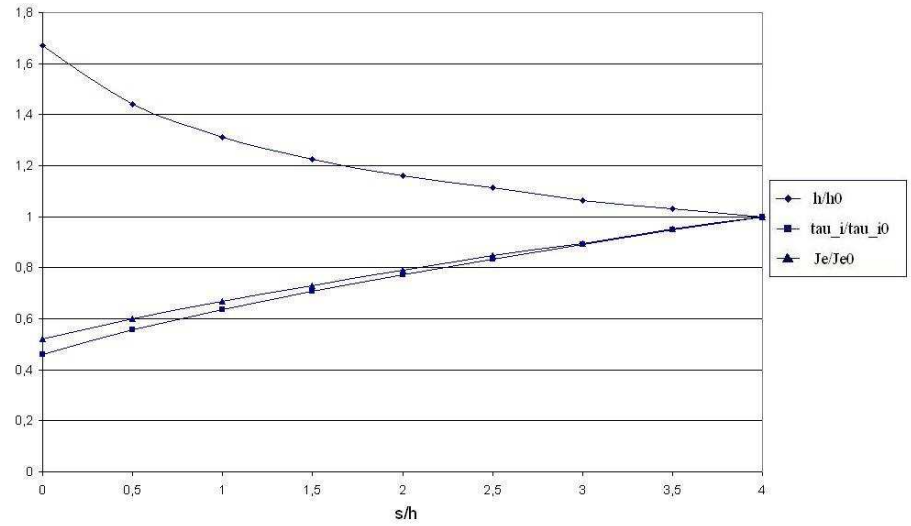

Figure 7.1: Effect of s/h in an annular flow with entrainment.

The height of the film was calculated in the case of the experiment of Azzopardi and Teixeira (1994a),(1994b) for the highest air mass flux 55.6 $kg/(m^2 s)$ and the lowest liquid mass flux 15.9 $kg/(m^2 s)$. It was also assumed that the droplet velocity was 80% of the gas velocity. This has been verified by Azzopardi and Teixeira and in the present simulation. Finally, unless specified otherwise, the critical Weber number was 0.

Influence of s/h. Figure 7.1 shows the effect of the ratio s/h on the height of the film, the interfacial shear stress and the entrainment rate. The normalization values correspond to the values for $s/h = 4$ and $\mu_{Tf,i} = 0$.

$$h_0 = 125\ \mu m\ ; \tau_{i0} = 9.33\ Pa\ ; J_{e0} = 3.55 \cdot 10^{-2}\ kg/(m^2 s^{-1})$$

Figure 7.1 shows a similar feature for the height of the film and for the interfacial shear as Figure 6.9 where entrainment was zero. The entrainment rate decreases when s/h is reduced. Thus reducing the ratio s/h will not provide a better match with experimental results. In addition when s/h is reduced, h increases, that is to say that the velocity of the film decreases. A comparison of the simulation data and of the experimental data showed that the velocity of the film was too low (leading sometimes to a downward flow), and that the entrainment rate was also underestimated. Lowering s/h can only worsen these two effects. So, the source of the underestimation of the film velocity and of the entrainment rate is not an overestimation of s/h.

Influence of $\mu_{Tf,i}/\mu_f$. Figure 7.2 shows the effect of the ratio $\mu_{Tf,i}/\mu_f$ on the height of the film, the interfacial shear stress and the entrainment rate. Figure

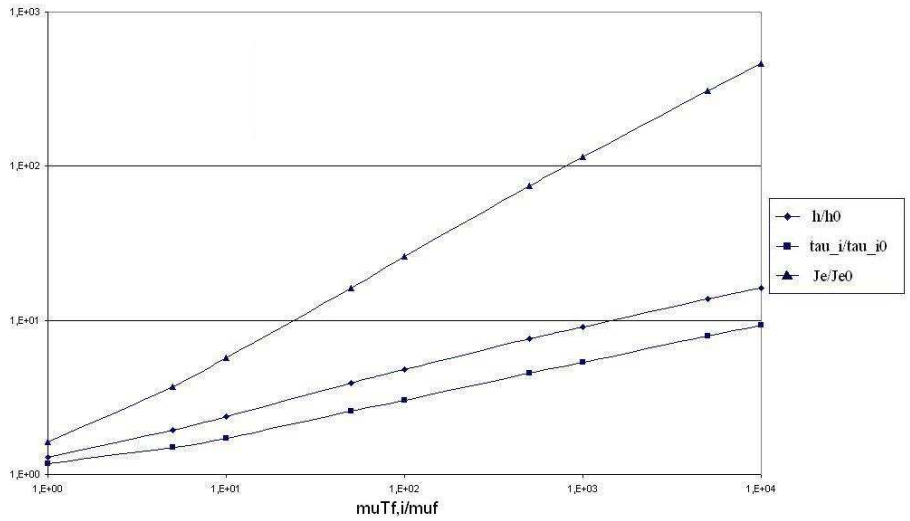

Figure 7.2: Effect of $\mu_{Tf,i}/\mu_f$ in an annular flow with entrainment.

7.2 shows a similar feature for the height of the film and for the interfacial shear as Figure 6.10 where entrainment was zero. The influence of the turbulent viscosity induced by the film flow is small on h and on τ_i. In contrast, if $\mu_{Tf,i} = 5\mu_f$ the entrainment rate is already 3.7 times higher. Then, taking into account the turbulence induced by the film flow and not only the turbulence due to droplet deposition, is likely to improve entrainment predictions. However it is not going to improve the bad estimation of the film velocity.

Influence of We_{crit}. Figure 7.3 shows the influence of the critical Weber number on the height of the film, the interfacial shear stress and the entrainment flux. The striking feature of this graph is that quite unexpectedly an increase of the threshold for the beginning of entrainment leads to an increase of the entrainment flux. Indeed, according to Figure 7.3 as We_{crit} increases, the height of the film increases and so does the interfacial shear stress. This increases both the Weber number of the film $We = \tau_i \, h/\Sigma$ and $\sqrt{\tau_i}$. Since $Je \propto \sqrt{\tau_i}\, We$, the entrainment flux is significantly increased when the critical Weber number is higher.
The effect of a decrease of the critical Weber number on the flow is thus two fold. On the one hand it will reduce the entrainment rate. This reduction is not desirable since the entrainment rate given by the simulation is already too low. However this unwanted effect can be compensated with an increase of the turbulent viscosity of the film. On the other hand a decrease of the critical Weber number leads to a decrease of the liquid film height and thus to an increase of

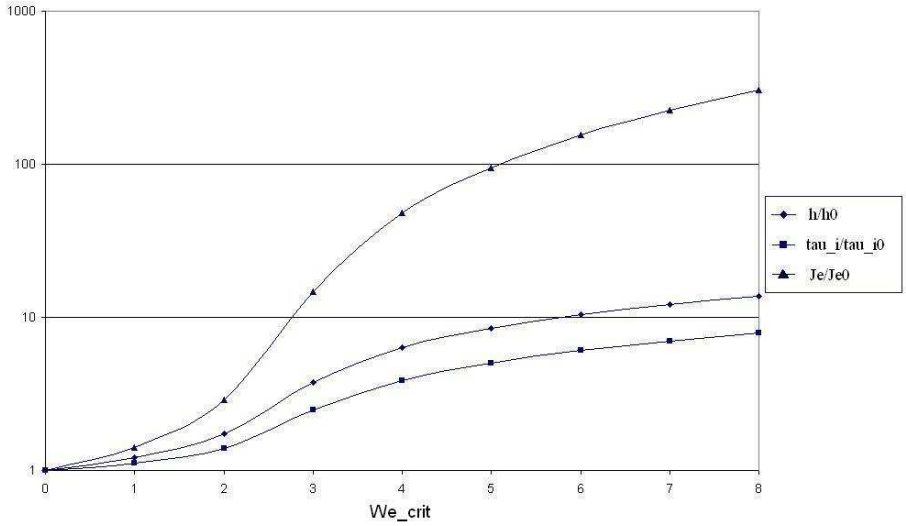

Figure 7.3: Effect of the critical Weber number in an annular flow with entrainment.

the film velocity[1]. It is then possible that the simulation indicated a downward film flow because the critical Weber number was too high, leading to a thicker film and thus to an underprediction of the film velocity.
Figure 3.23 indicated that the equations (3.159) and (3.160) proposed by Nigmatulin *et al.* (1996) for the calculation of the critical Weber number, need to be further validated. It seems that these relations overestimate the value of the critical Weber number. Nevertheless this overestimation should be taken with caution because the accuracy of the experimental points reported on Figure 3.23 is not known.

Influence of χ. Figure 7.4 shows the changes in the height of the film, the interfacial shear stress and the entrainment rate with the proportionality coefficient χ of the entrainment correlation (3.155). In this correlation $\chi = 0.023$. The interfacial shear stress and the height of the film are practically independent of χ. Thus the velocity of the film is unaffected by the proportionality coefficient of the entrainment rate correlation. The entrainment rate increases proportionally with χ and consequently an increase of the value of χ will lead to a better collapse of the droplet flux data collected by Azzopardi and Teixiera (1994b) and of the simulated values. However as detailed in chapter 3, the value $\chi = 0.023$ agrees with the data of Schadel and Hanratty (1989) (Figure 3.20). As a result it seems unlikely that the lack of accuracy of the present model is

[1] Assuming that the there is an equilibrium between the droplet deposition and entrainment fluxes.

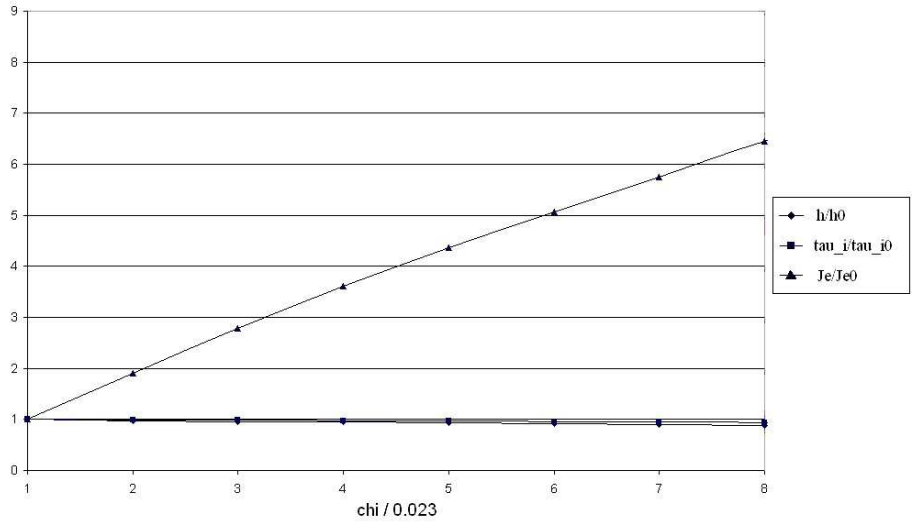

Figure 7.4: Influence of the proportionality coefficient of the entrainment rate correlation for an annular flow.

due to an erroneous value of χ.

Test of a correlation based on the Reynolds number of the film. In this paragraph we will compare the correlation of Pan and Hanratty (2002a), based on the Reynolds number of the film, and the correlation of Alipchenkov *et al.* (2002b). Neglecting the critical Reynolds number, the correlation of Pan and Hanratty is:

$$J_e = \frac{\chi' U_g^2 \sqrt{\rho_g \rho_f} \mu_f}{\Sigma} \left(\frac{\rho_f U_f h}{\mu_f} \right) \tag{7.17}$$

Where $\chi' = 3 \cdot 10^{-6}$ is a non-dimensional constant. If this equation is inserted instead equation (7.6) in our algebraic model one obtains a constant entrainment rate of droplets from the liquid layer:

$$J_e = J'_{e0} = \frac{\chi' U_g^2 \rho_g^{1/2} \rho_f^{3/2} \dot{Q}_{f0}}{\Sigma} \tag{7.18}$$

The equation for the height of the film is then

$$G h^3 + (I C_f(h) + D') h^2 - T'_d h - 3\mu_f \left(1 + \frac{\mu_{Tf,i}}{\mu_f} \right) = 0 \tag{7.19}$$

Where D' is a coefficient linked to the momentum transfer from the droplet phase to the liquid layer.

$$D' \equiv \frac{J'_{e0} U_d}{\dot{Q}_{f0}} \tag{7.20}$$

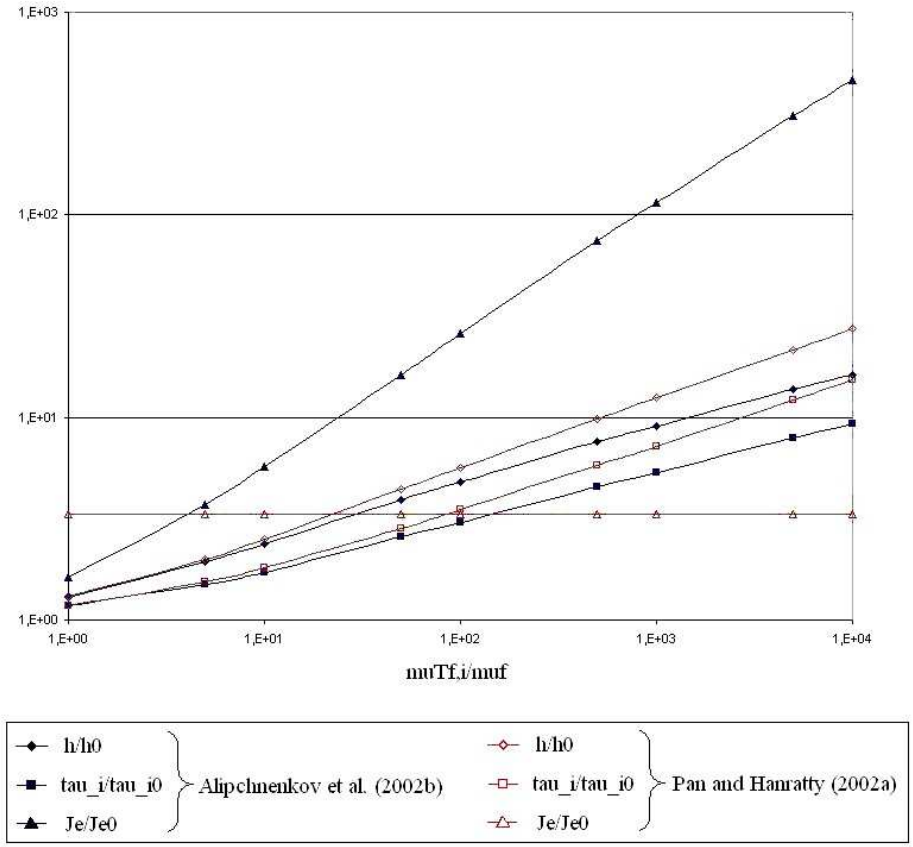

Figure 7.5: Comparison of a Reynolds number based and a Weber number based entrainment rate correlation.

T'_d is a coefficient related to the turbulent viscosity generated in the liquid film by depositing droplets.

$$T'_d \equiv 3\, J'_{e0} \tag{7.21}$$

If the critical Weber number is neglected, the correlation of Alipchenkov *et al.* (2002b) gives:

$$\begin{aligned} \left(-G + D\, C_f(h)^{3/2}\right) h^3 + \left(I\, C_f(h) - T_d\, C_f(h)^{3/2}\right) h^2 & \\ -3\mu_f \left(1 + \frac{\mu_{Tf,i}}{\mu_f}\right) &= 0 \end{aligned} \tag{7.22}$$

Figure 7.5 compares the behavior of the entrainment correlations with respect to an increase of the turbulent viscosity induced by the film flow. On Figure 7.5, the index 0 corresponds to values given by the correlation of Alipchenkov

et al. (2002b) when $s/h = 4$ and $\mu_{Tf,i} = 0$.

$$h_0 = 125\ \mu m\ ; \tau_{i0} = 9.33\ Pa\ ; J_{e0} = 3.55 \cdot 10^{-2}\ kg/(m^2 s)$$

First one can notice that, when $\mu_{Tf,i}/\mu_f$ is small, the two types of correlation give identical results both for the height of the film and for the interfacial shear stress. The value of the entrainment rate with $\mu_{Tf,i} = 0$ is 3.35 times larger with the correlation of Pan and Hanratty (2002a) than with that of Alipchenkov *et al.* (2002b). Thus, when $\mu_{Tf,i}$ is small, using equation (7.18) instead of (3.155) will not have an influence on the velocity of the film (h is the same) but will increase substantially the entrainment rate. However, the fact that the entrainment rate is totally independent of the turbulent viscosity of the film seems surprising. Moreover, when the simulation manage to predict an upward flow, the value of the entrained liquid flux is roughly half of the experimental value. Correcting the entrainment rate by a factor greater than 3, as the relation of Pan and Hanratty indicates, may lead to an overprediction of the entrainment flux. To summarize, it is not believed that an entrainment correlation based on the Reynolds number of the film will lead to a significant improvement of the present model because:

1. It will probably not solve the underprediction of the velocity of the film (h is the same).

2. It implies that the entrainment flux is independent of the turbulent viscosity of the film.

3. It might overpredict the flux of entrained droplets when the film is close to being laminar.

Conclusions of the analytical model. It as been shown that the underprediction of the flux of droplets may be due to the fact that the turbulent viscosity of the film induced by the film flow has been neglected. The inability of the model to predict correctly the direction of the film flow for high liquid flow rates and low gas flow rates, may be explained by a value of the critical Weber number which is too high. The decrease of the parameter s/h worsen the predictions of the model. There is no reason to believe that the proportionality coefficient of relation (3.155) giving the entrainment rate should be modified. Finally, it is not expected that an entrainment rate correlation based on the Reynolds number of the film will give substantially better results.

d) Conclusion for the entrained liquid mass flux

The entrained liquid mass flux is not predicted correctly for high liquid flow rates and low gas flow rates. This may come from an overestimation of the critical Weber number for the onset of entrainment. It is not recommended to use the present model for low gas flow rates and high liquid flow rates which is the exact opposite situation of that encountered in high-pressure gas-liquid separators.

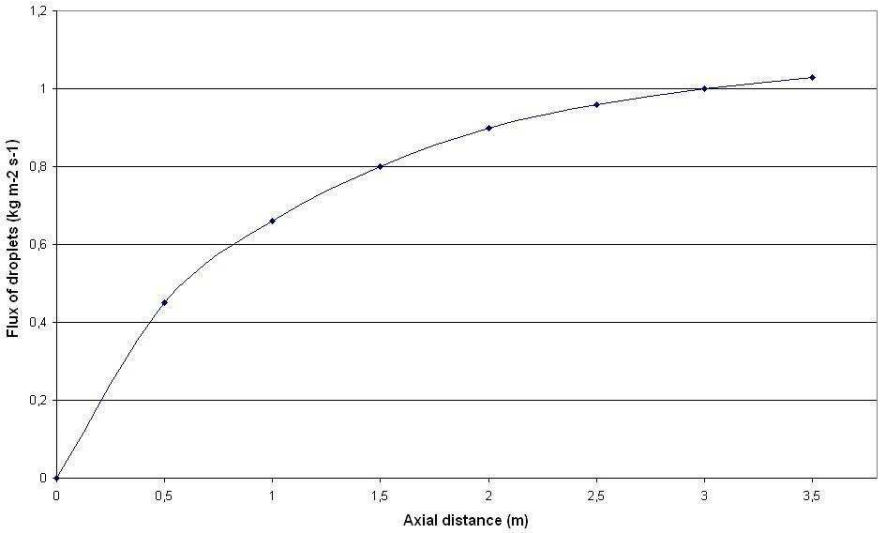

Figure 7.6: Mass flux of droplets along the pipe.

The entrained liquid mass flux is quantitatively inaccurate for high gas flow rates and low liquid flow rates. It seems that taking into account the turbulent viscosity induced by the film flow can correct this inaccuracy. One must however underline, that the liquid layer present in a high pressure scrubber can still be laminar. Nevertheless, because of the lack of high pressure experimental data with real fluids, it seems necessary to introduce the possibility for the film to be in a turbulent regime.

7.3.2 Equilibrium between entrainment and deposition

From now on, the results will be presented only for the case with the highest gas flow rate (55.6 $kg/(m^2s)$) and the lowest liquid flow rate (15.9 $kg/(m^2s)$). Figure 7.6 shows the droplet mass flux as a function of the axial position. The flux increases strongly close to the inlet of the pipe. Then it gradually stabilizes as the entrainment and deposition starts balancing. This balance is studied more closely in the following.
Another simulation was performed to study the equilibrium between entrainment and deposition rates. For this new case the liquid at the inlet was totally dispersed. A comparison of the two simulations can be seen on Figure 7.7. It shows the entrainment flux $\dot{E}$ and the deposition flux $\dot{D}$ as a function of the axial distance. The filled symbols represent the results obtained with the original simulation where the film generates droplets (indicated f->d). The open symbols are the results of the simulation where droplets generate the film (indicated (d->f)). For the (f->d) simulation, the entrainment is slightly larger

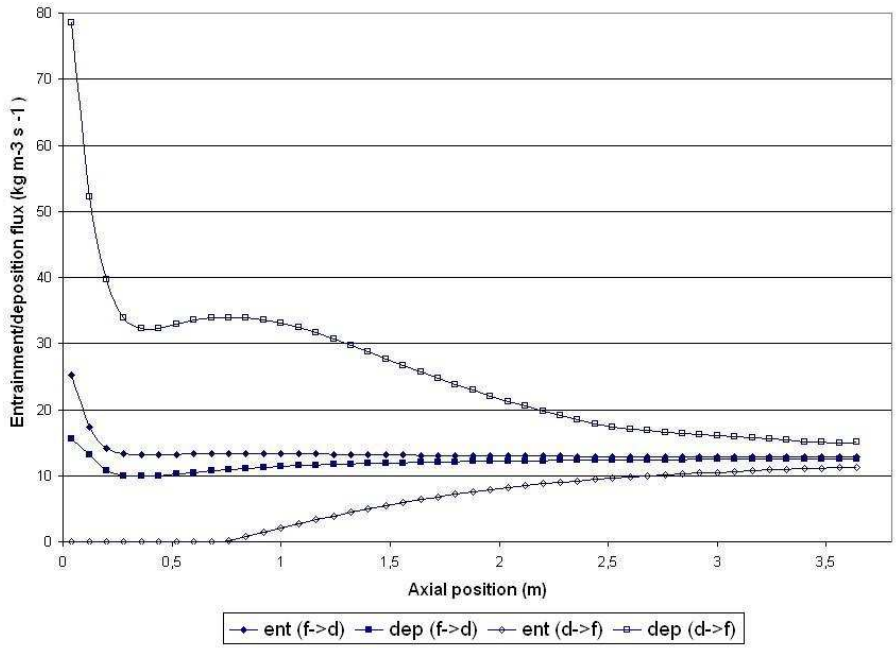

Figure 7.7: Equilibrium of the entrainment rate and of the deposition rate.

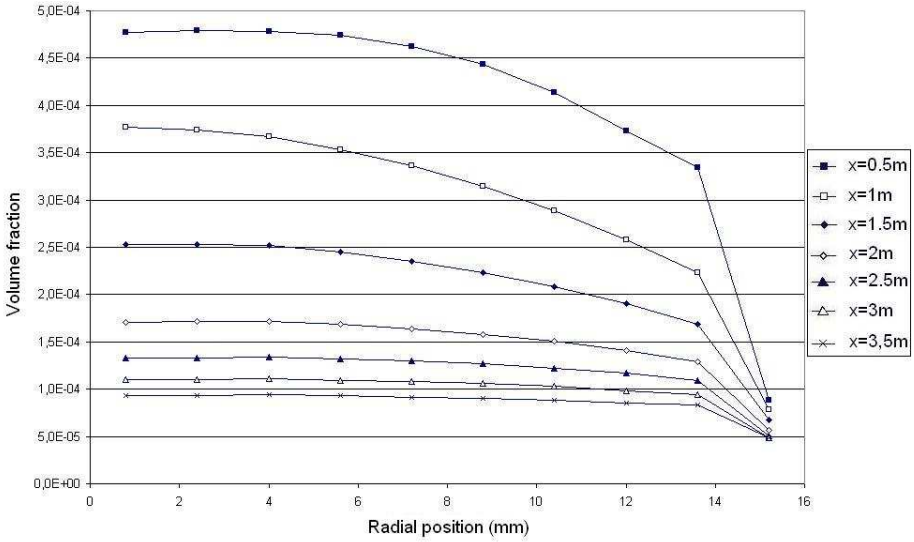

Figure 7.8: Concentration profile for the (d->f) simulation.

than the deposition. The two processes come to equilibrium quite quickly. For the (d->f)) simulation, at the inlet, the deposition is much larger than the entrainment and the deposited droplets form a liquid layer. At the beginning of the pipe, this liquid layer is too thin to atomize because its Weber number is under the critical Weber number. At 0.75 m downstream, this threshold is overcome and entrainment starts. The entrainment rate then tends toward the same value as the deposition rate. It is clear that both simulations indicate a similar equilibrium value of the interchange rate (12.6 $kg/(m^3 s)$). However the equilibrium is reached later in the (d->f) simulation compared to the (f->d) simulation.

The concentration profiles of the simulation (d->f) for several axial distances are given on Figure 7.8. The mean concentration decreases as the axial distance increases. Close to the center line, the concentration profiles are flat. The extent of this flat zone increases with the axial coordinate x. For $x = 3.5\,m$, the droplet concentration profile is flat over most of the pipe cross-section except close to the wall. There is a large concentration difference between the cell at the wall (centroid at $r = 15.2\ mm$) and the last cell of the core (centroid at $r = 13.6\ mm$). The concentration at the wall is low immediately after the inlet because of a high deposition rate. Figure 7.8 shows that for $x > 2\ \ m$, the value of the volume fraction of droplets at the wall is practically constant. However the large drop in concentration between the cell at the wall and its neighbor shows that there is no equilibrium between the wall layer and the core. The flow is vertical, hence the only force driving the dispersed phase toward the wall is the turbulent dispersion. A low volume fraction of droplets at the wall and

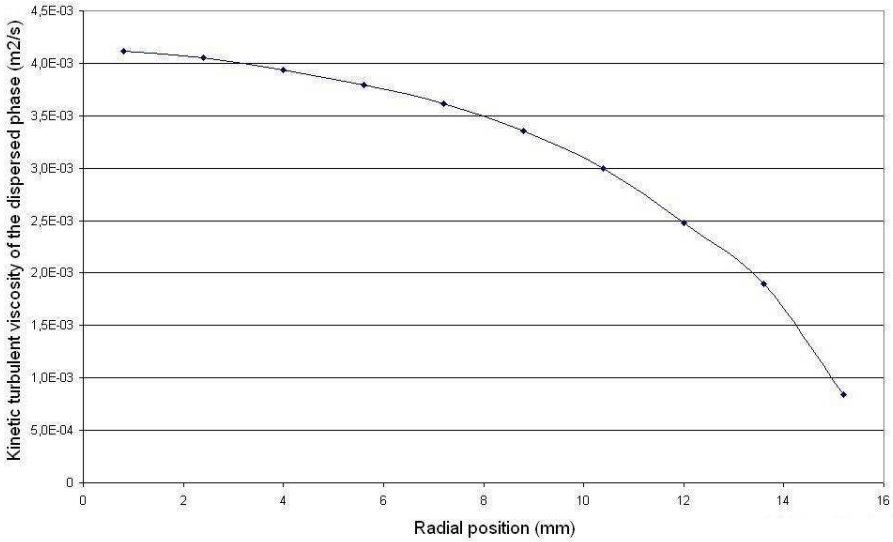

Figure 7.9: Turbulent kinetic viscosity of the dispersed phase.

a high concentration in the core shows that it is the turbulent dispersion that controls the deposition. In the present case, the flux of droplets from the wall boundary cell to the film, governed by the deposition velocity K_D^+, is greater than the flux of droplets from the core to the wall boundary cell (governed by the turbulent dispersion). The turbulent dispersion acts as a bottle neck and slows down the movement of the particles toward the vicinity of the wall. This explanation is confirmed by Figure 7.9. It shows the turbulent kinetic viscosity profile of the dispersed phase 3.5 m after the inlet. One can see that it decreases with the radial position. Consequently, the closer the droplets are from the wall, the less they diffuse radially. That is why the particles do not reach the wall layer easily. Identically, for the (f->d) simulation, the concentrations by the wall rises rapidly toward the equilibrium concentration as seen on Figure 7.10, but droplets do not reach the core easily. Consequently the profiles present a peak by the wall and are rather flat in the core. From the previous analysis, one can see that, in the present simulation, the rate with which the global equilibrium is reached in the flow is governed by the turbulent dispersion.
Figure 7.11 shows the concentration profiles at $x = 3.5\ m$ for the (f->d) and the (d->f) simulations. First, one notices that the concentration by the wall is the same. It is the concentration reached when the deposition and the entrainment rates are in equilibrium. This concentration verifies:

$$\overline{\alpha_d}\,\rho_d\,K_D^+\,u_\tau = 0.023\sqrt{\rho_d \tau_i}\,(We - We_{crit}) \tag{7.23}$$

It gives:

$$\overline{\alpha_d} = \frac{0.023}{K_D^+}\sqrt{\frac{\rho_g}{\rho_d}}\,(We - We_{crit}) \tag{7.24}$$

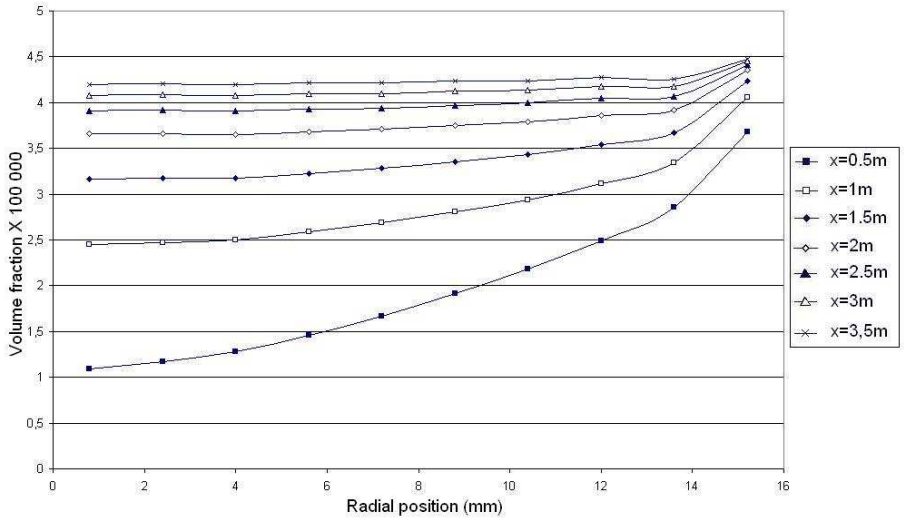

Figure 7.10: Concentration profiles in the (f->d) simulation.

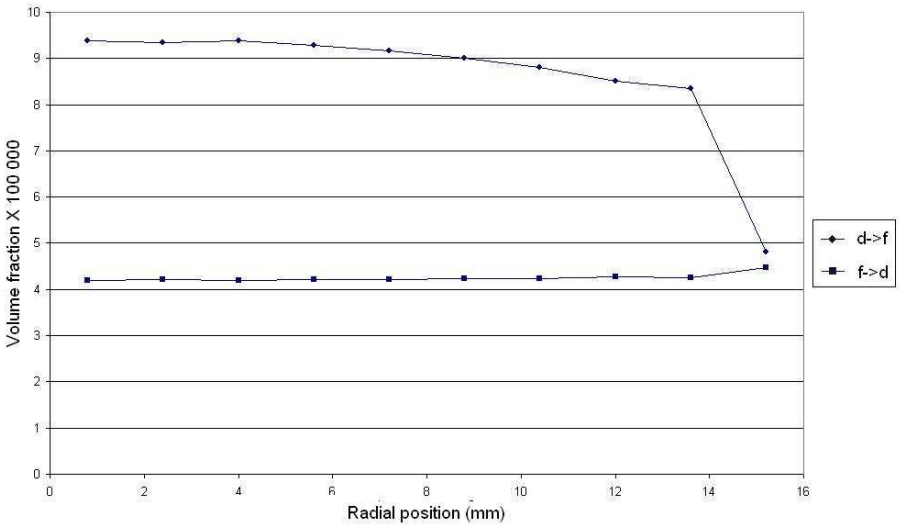

Figure 7.11: Comparison of the concentration profiles of the (d->f) and of the (f->d) simulations at $x = 3.5\ m$.

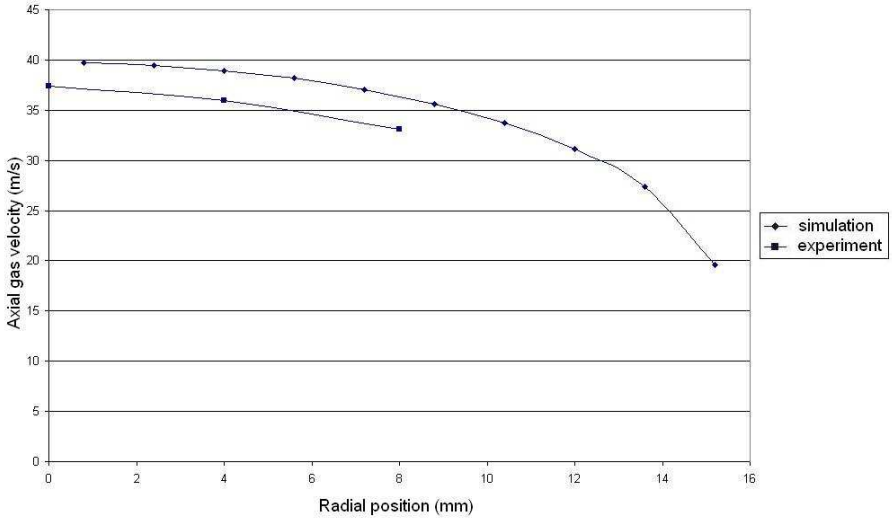

Figure 7.12: Gas velocity profile.

The two simulations tends toward the same equilibrium state. Nevertheless it is clear that the (f->d) simulation is much closer to equilibrium because the value in the core and by the wall are practically equal. The experimental equilibrium state has a much larger part of the liquid flowing as a film (85%) rather than as a dispersed phase. The inlet condition of the (d->f) simulation is then further from the equilibrium and the necessary distance to achieve this equilibrium is larger.

7.3.3 Velocity profiles

Gas velocity profile

Figure 7.12 shows the measured and the predicted gas velocity profiles at $x = 3.5$ m. The curves are in agreement but there is a gap between the two profiles. The mass balance of the gas phase is perfect in the simulation. A polynomial has been fitted through the three experimental points. This polynomial has been extrapolated to the wall by a straight line which slope was the derivative of the polynomial on the left of the experimental point closest to the wall. This function is an overevaluation of the possible velocity profiles, given the experimental points are correct. The integration of this function gave a gas flux which was lower than the measured inlet flux. Therefore either the measurements of the gas velocity were incorrect, or the gas flow rate (measured by an orifice plate) was overestimated.

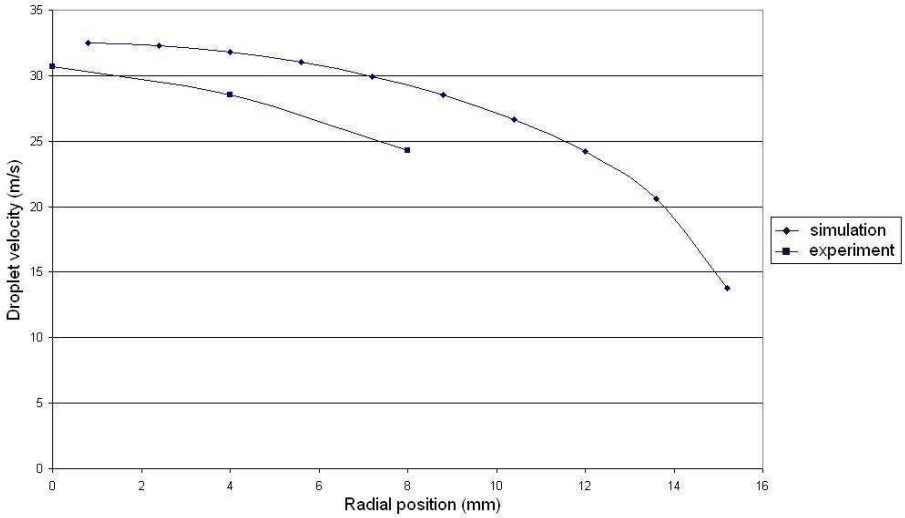

Figure 7.13: Droplet velocity profile.

Droplet velocity profile

Figure 7.13 shows the measured and the predicted droplet velocity profiles at $x = 3.5\ m$. Here as well, the profiles are in agreement but the same type of gap as for the gas velocity profile can be seen. It is interesting to plot the ratio of the droplet velocity to the gas velocity as a function of the radial position. It is shown on Figure 7.14. One can see that there is a very good agreement between the experimental and the calculated values. Both predict that the local droplet velocity is roughly 80% of the local gas velocity. This is also in agreement with the measurements performed by Fore and Dukler (1995b). In annular flows, in contrast with solid particles dispersed flows, the equilibrium state is dynamic. Droplets are continuously created and absorbed by the film phase. The new droplets are accelerated but deposit before they reach their terminal velocity. That is why the droplets lag significantly behind the gas. The agreement of the simulated and experimental values on Figure 7.14 indicates that the model provides accurate predictions for the velocity of the dispersed phase.

7.3.4 Height of the film

Azzopardi and Teixeira (1994 a) did not measure the height of the liquid film. However they estimated that the mean height of the film was between 100 and 400 μm. The simulation indicates a value of 150 μm at the end of the pipe. It is in the correct range.

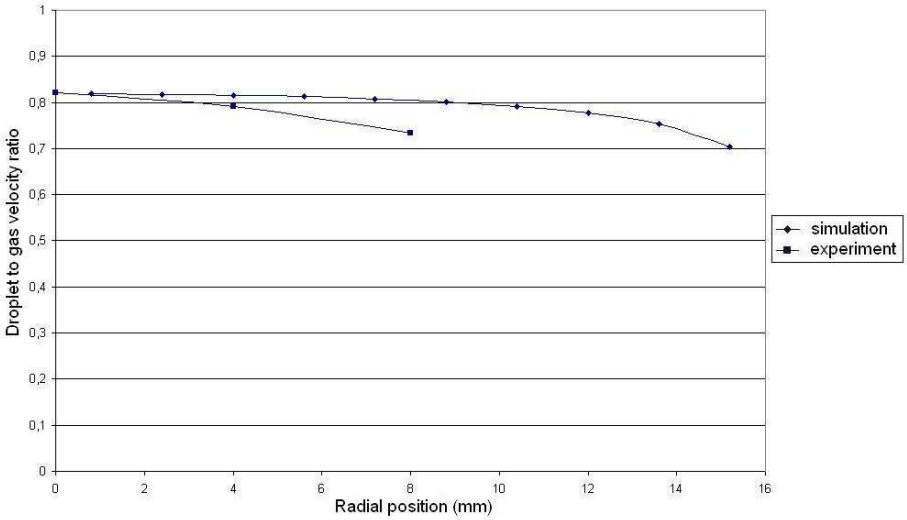

Figure 7.14: Droplet to gas velocity ratio.

7.3.5 Turbulent kinetic energy

Figure 7.15 shows the turbulent kinetic energy of the gas as a function of the radial position. There is just one experimental point in the center of the channel because the authors could not measure the circumferential turbulent intensity at other positions for such a high gas flow rate. The data roughly agrees. One can see that there is again a gap between the simulation and the experimental points. This is probably due to the previously mentioned measurement error. When the TKE is normalized by the square of the axial velocity at the center of the channel one gets a better agreement.

7.4 Conclusion on the performances of the model for an annular flow

The model underestimates the entrained fraction in an annular flow. It has been shown that taking into account the turbulent viscosity induced by the film flow and not only the turbulent viscosity due to droplet deposition, may increase significantly the entrained droplet fraction. The present model also underestimates the velocity of the liquid layer, especially at low gas mass flow rates and high liquid mass flow rates. Lowering the critical Weber number for the onset of entrainment may lead to better results. Whatever the film/droplet proportions at the inlet, the equilibrium state that is reached is the same. Gas and droplet velocity profiles are predicted correctly. The model is able to reproduce the 20% difference between gas and droplet local velocities. The calculated

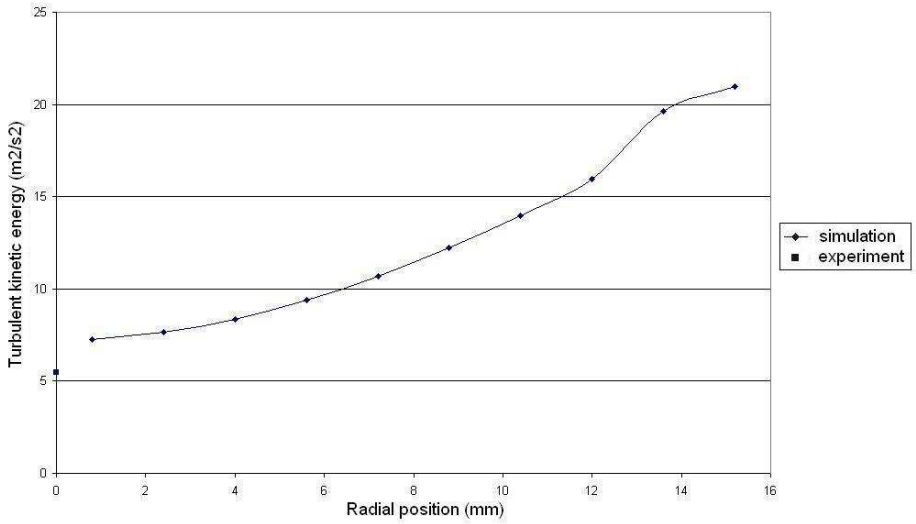

Figure 7.15: Profile of the turbulent kinetic energy of the gas.

turbulent kinetic energy agrees with the measurments made by Azzopardi and Teixeira (1994b).

Chapter 8

High pressure gas/liquid separation

In this chapter, the model is used to study the behavior of a vane-pack demister at high pressure. An identical device has been studied in a simulation performed by James *et al.* (2005). First we will compare the prediction of the model with the predictions of the model of James *et al.* at low pressure with water and air. Then we will study the effect of high pressure. Finally we will analyze an unsuccessful attempt to simulate an axial cyclone.

8.1 Low pressure simulation of a vane-pack demister

In this section we will compare the results of the present model with the calculation performed by James *et al.* (2005) on a vane-pack demister.

8.1.1 Geometry

The geometry of the vane-pack used by James *et al.* (2005) is pictured on Figure 8.1. For the purpose of the analysis, the computational domain has been divided in 6 sections numbered with roman numerals.

8.1.2 The model of James *et al.* (2005)

James *et al.* used a Lagrangian tracking of the droplet phase to calculate the efficiency of the vane-pack demister. They took into account the influence of the gas phase on the motion of the dispersed phase with an eddy interaction model. A film model was also integrated. The film was formed by a postulated deposition rate and flowed under the action of the interfacial shear stress and gravity. The gravity was oriented normal to the plane of Figure 8.1. The authors neglected the influence of gravity on both the gas and the droplet flow. James

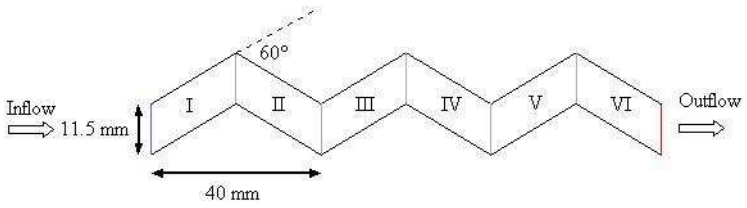

Figure 8.1: Geometry of the vane-pack demister used by James *et al.* (2005).

Zones	I	II	III	IV	V	VI	Out	Efficiency
James *et al.*	50.0	37.3	7.6	1.4	1.5	0.5	1.7	98.3%
Present model	52.9	35.8	6.9	2.8	1.1	0.0	0.4	99.4%

Table 8.1: Percentage of liquid trapped in each zone.

et al. also studied whether or not entrainment occurred from the liquid film. Their criteria was based on the flow of the film around sharp bends. However their model did not incorporate the calculation of the entrainment rate in itself.

8.1.3 Set-up of the numerical case

The grid we used is shown on Figure 8.2, which is a close up of section III. The cells had a constant equiangle skew of 0.33. Their large and short sides were respectively 1 mm and 0.96 mm long.
At the inlet, the gas and the droplets had a velocity of 8 m/s normal to the inlet opening. The volume fraction of droplets was 10^{-4}. The turbulent kinetic energy of the gas phase was 1 m^2/s^2 and its dissipation rate 1 m^2/s^3. The diameter of the droplets was 25 μm. In the simulation, only a 2D flow has been considered because James *et al.* neglected the effect of gravity on the motion of the droplet and gas phases.

8.1.4 Results

Efficiency

James *et al.* (2005) reported the percentage of liquid trapped in each section. They used velocities between 3 and 8 m/s and droplet diameters between 15 and 25 μm. Table 8.1 reports their results for a diameter of 25 μm and 8 m/s and compare them to the prediction of our model. Results are very close to each other despite a completely different modeling of the dispersed phase (Lagrangian for James *et al.* and Eulerian in the present model). The percentage of liquid trapped in each section is dependent on the deposition velocity. K_D^+, the deposition velocity in our model, is based on the local deposition flux at

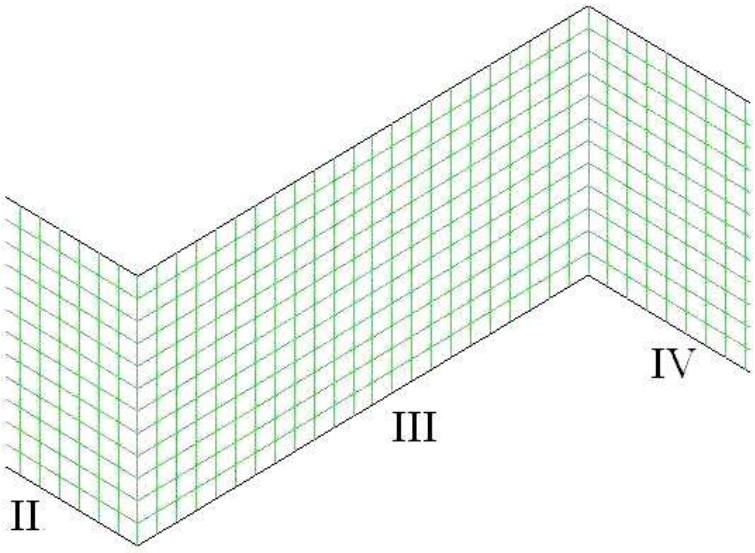

Figure 8.2: Grid for the simulation of the vane-pack demister.

the wall (equation (3.89)). K_D^+ is the sum of a non-diffusive velocity $K^+_{non\ diff}$ and a diffusional velocity K^+_{wall} (equation (3.92)). $K^+_{non\ diff}$ results from the mean convection and the gravity while K^+_{wall} results from near-wall phenomena. The vane-pack is based primarily on "impact deposition" which means that the deposition velocity mainly depends on its non-diffusive part. The good agreement of the two models indicates that our non-diffusive deposition model is promising (although an experimental validation is necessary).

Entrainment and liquid film height

The present model and the model of James *et al.* (2005) did not predict entrainment from the liquid film. However the two models are hardly comparable because their entrainment criteria were based on totally different physical mechanisms.
The top of Figure 8.3 represents the stream lines at the bottom wall between the sections II and III. One can see a recirculation zone. The enlargement shows the velocity vectors of the gas phase. The size of the triangles represents the magnitude of the gas velocity. The projections of the gas velocity on the wall inside and outside the recirculation zone do not have the same sign. This counterflow by the wall induces an accumulation of film just upstream of the recirculation zone. This phenomenon is illustrated on Figure 8.4. The figure shows heights of the liquid film on the bottom wall of zone II as a function of the position. No deposition occurs on this wall. There are 500 μs in time between each curve. The first 2 ms there is practically no film on the wall except at

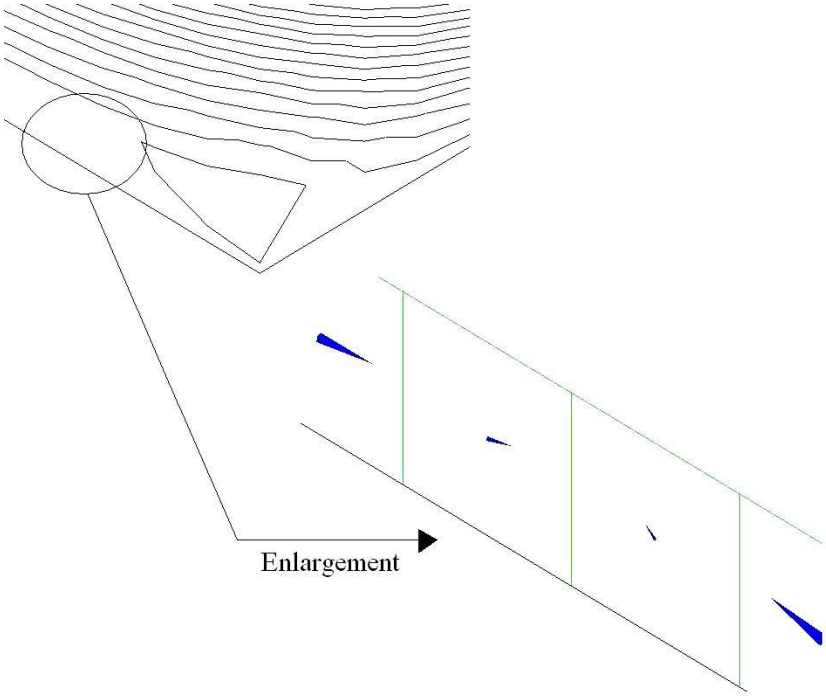

Figure 8.3: Recirculation zone: stream function and gas phase velocity vectors by the wall.

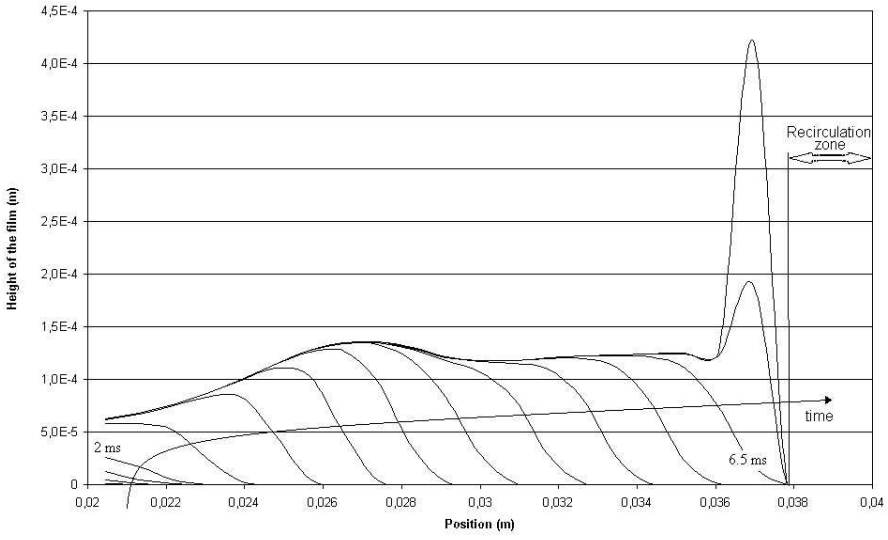

Figure 8.4: Height of the liquid film at the bottom wall of zone II.

the very edge of zone I. From 2 to 6.5 ms the film starts flowing toward the recirculation zone. After 6.5 ms the film cannot pass through the counter flow of gas and starts accumulating at the edge of the recirculation zone. This is not necessarily unphysical. In reality the film becomes quickly unstable and entrainment occurs. The physics of re-entrainment at the edge of a recirculation zone is different from the one considered in the present model. Close to the recirculation zone, the velocity by the wall has a non negligible wall-normal component. This may lead to a shear on the film front (see Figure 8.5 (a)). It is then sensible to suppose that the front of the film forms a ligament normal to the wall (Figure 8.5 (b)). The ligament will then atomize, and this type of atomization might have common points with the break-up of a jet (Figure 8.5 (c)). Equation (3.155) that governs the entrainment rate has not been developed for this type of entrainment situation. This equation did not predict entrainment and consequently lead to very high values of the height of the film. A close look at the different terms involved in correlation (3.155) showed that, at the edge of the recirculation zone, the critical Weber number became extremely large. This was due to the Reynolds number of the film which was very large (see equations (3.159), (3.160) and (3.161)). It is believed that a different entrainment correlation, possibly based on the physics of jet break-up, must be used to get rid of this problem.
Handling recirculation zones is an important issue. Indeed, recirculation zones are very common in industrial geometries. The inability of the model to predict entrainment for this type of situation leads to extremely large values of film heights. In the worst case it can result in a divergence of the calculation[1].

8.2 High pressure gas liquid separation in a vane-pack demister

In this section we will compare three cases:

- An air/water flow at 1 bar. It will be referred as the LP case (Low Pressure).
- A natural gas/condensate flow[2] at 92 bars without entrainment. It will be referred as the HPNE case (High Pressure No Entrainment).
- A natural gas/condensate flow at 92 bars with entrainment. It will be referred as the HPE case (High Pressure Entrainment).

[1] Unfortunately divergence occurred in the present simulation. The calculation was stopped after 9 ms. At this time the maximum height of the film (by the recirculation region between zone II and zone III) was over 1 mm. The results presented in Table 8.1 are given for a time of 5 ms. At this time the droplet concentration was stationary. Between 5 and 9 ms, despite high values of film heights at specific locations, no significant change concerning the droplet phase concentration were noticed. Therefore, it is believed that the results presented in Table 8.1 are trustworthy.

[2] The gas and the liquid were mixtures of methane, ethane and pentane.

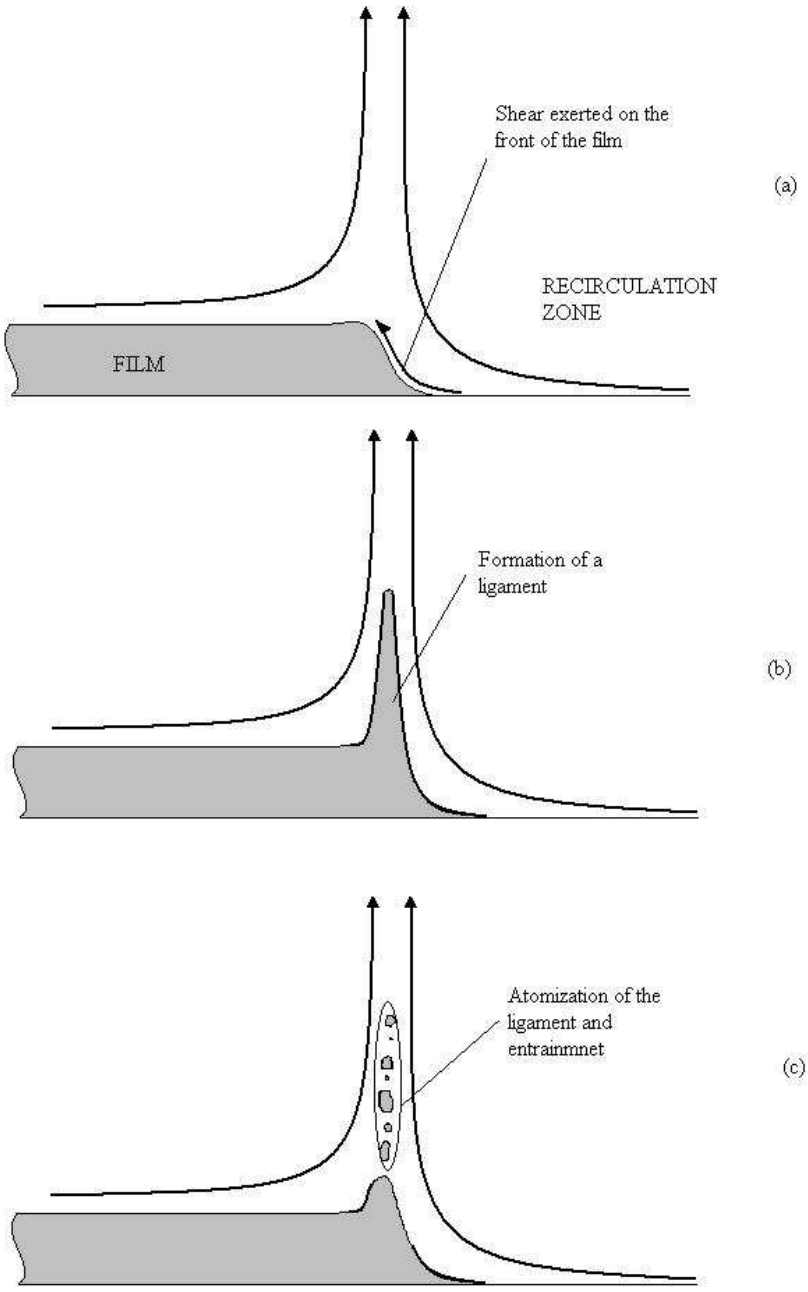

Figure 8.5: Possible mechanism of entrainment at the edge of a recirculation zone.

	Liquid		Gas		Surface tension
	Density (kg/m^3)	Viscosity $(kg/(ms))$	Density (kg/m^3)	Viscosity $(kg/(ms))$	(N/m)
LP	998	0.001	1.225	$1.789\,10^{-5}$	0.073
HPNE	470	$9.6\,10^{-5}$	97.1	$1.5\,10^{-5}$	10^9
HPE	470	$9.6\,10^{-5}$	97.1	$1.5\,10^{-5}$	0.0022

Table 8.2: Liquid and gas properties for air, water, natural gas and condensate.

Case	LP	HPNE	HPE
Efficiency	99.7%	70.5 %	0%

Table 8.3: Separation efficiency of the vane-pack demister for three different cases.

8.2.1 Set-up of the numerical case

The grid was identical to that of Figure 8.2. Inlet velocities were 16 m/s (normal to the inlet opening) both for the gas and the droplet phase. The volume fraction of droplets was 10^{-4}. The turbulent kinetic energy of the gas phase was 1 m^2/s^2 and its dissipation rate 1 m^2/s^3. The diameter of the droplets was 25 μm. The flow was 2D. Table 8.2 lists the physical properties of the used fluids[3]. The surface tension of the HPNE case was set to an arbitrarily large value to avoid entrainment.

8.2.2 Results

a) Efficiency and volume fraction

Table 8.3 shows the predicted efficiency of the separator for the LP, HPNE and HPE simulations. In the case of the LP simulation, no entrainment is predicted, the efficiency is excellent. Practically all the droplets are separated after zone II as shown on Figure 8.6 (a). Note that air/water flows at atmospheric pressure are experiments that are usually performed in the industry to test the efficiency of separation devices.
Table 8.3 shows that the HPNE case presents a much lower efficiency. As the liquid gas density ratio is much lower, droplets follow the gas more closely and are not separated as fast. This can be seen on Figure 8.6 (b). However when entrainment is not accounted for, all the droplets that impinge the wall are separated. This is a usual hypothesis for conventional separation simulations.
Including the possibility of re-entrainment has a tremendous effect. Table 8.3 shows that the efficiency is reduced to zero. Figure 8.6 (c) shows that droplet concentration varies a lot in a cross section but that the mean droplet concentration does not decreases along the stream. The pattern of the concentration

[3]The properties of natural gas and condensate at 92 bars were given by personal communications (Austrheim (2006)).

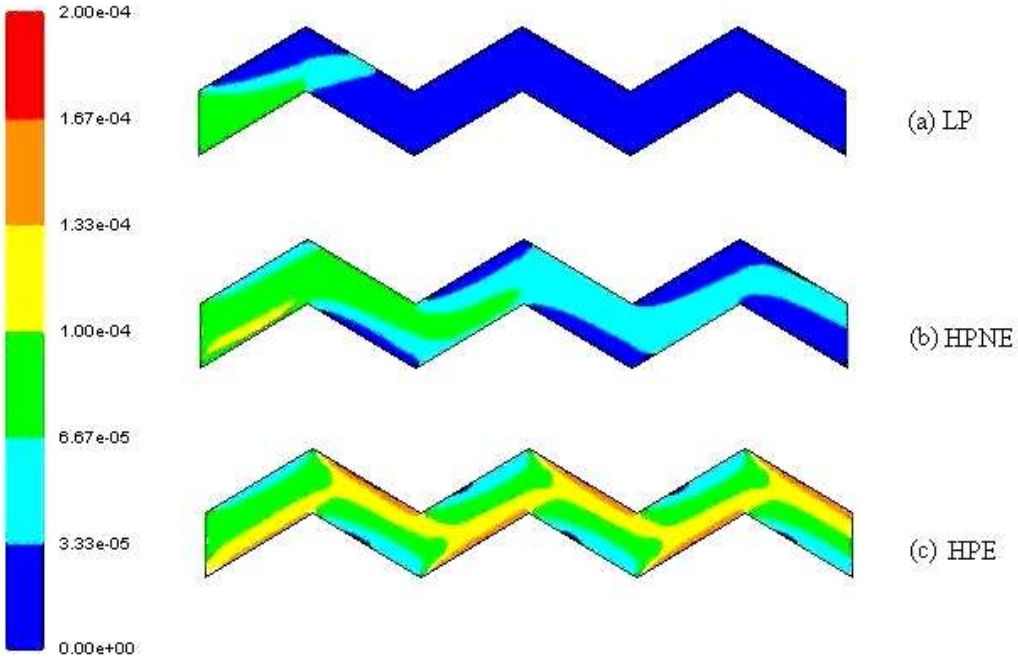

Figure 8.6: Droplet concentration in the vane-pack demister.

	LP	HPNE	HPE
Impact walls	99.6%	95.1%	92.7%
No impact walls	0.4%	4.9%	7.3%

Table 8.4: Proportion of the droplets depositing on impact and no impact walls.

field looks periodic. One must underline that in the present calculation there is no possible drainage of the film. This point will be discussed later.

b) Deposition and entrainment

Deposition. One can divide the deposition walls in two groups:

1. Head on droplet collision walls: There are the bottom walls of sections I, III, and V and the top walls of sections II, IV, and VI.

2. Remaining walls: There are the top walls of sections I, III, and V and the bottom walls of sections II, IV, and VI.

Head on droplet collision walls will be referred in the following as "impact walls". The remaining walls will be referred as "no impact walls" although strictly speaking, droplets are impacting on them as well. James *et al.* (2005) calculated that droplet deposition occurred at 99.9 % on the impact walls for an inlet velocity of 8 m/s. For the same inlet velocity, the present model calculated 99.4 %. Both calculations agrees roughly. At a higher velocty, 16 m/s, the inertia of the droplets is stronger so that it is expected that a larger number of droplets deposit on the impact walls. And indeed when the velocity is doubled from 8 to 16 m/s, the model predicts that the proportion of droplets depositing on impact walls rises from 99.4 to 99.6 %.
Table 8.4 shows the percentage of the overall deposition flux for each group of walls for the LP, HPNE and HPE cases. At higher pressure the proportion of droplets impinging on no impact walls rises. It is expected because the ratio of the droplet density to the gas density is much lower (5 instead of 1000). Consequently the droplets follow more closely the gas stream lines and the diffusive turbulent deposition has a bigger impact compared to the non diffusive inertial deposition. Because the diffusive turbulent deposition rate is the same for impact and no impact walls, the fraction of droplets impinging on no impact wall rises. In the HPE case this fraction is greater than in the HPNE case. This is due to droplets created from the film that redeposit immediately without leaving the vicinity of the liquid layer.
Figure 8.7 shows the deposition rate on the top wall of zone II (first impact wall) as a function of the position on the wall. The deposition is significantly lower in the case of the high pressure simulations. The simulation HPE presents a higher deposition rate because of the droplets created from the film that redeposit immediately. The shape of the curves is the result of complex interactions.
Figure 8.8 shows the deposition rate on the top wall of the vane-pack as a function of the position for the HPNE and for the HPE simulations. As indicated

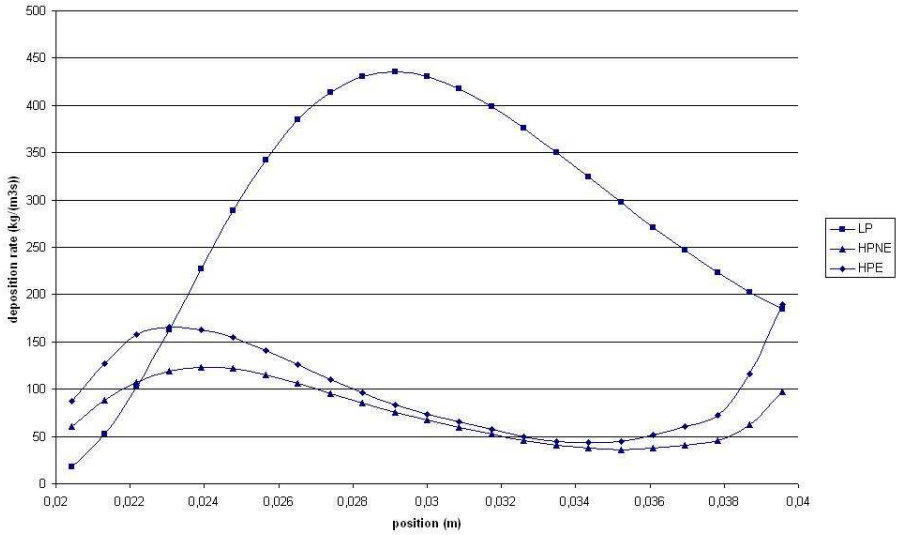

Figure 8.7: Deposition rate as a function of the position on the first impact wall.

by Table 8.4 virtually all the deposition occurs on impact walls. The trends of the two cases are similar. However the HPE simulation exhibits a periodic behavior (except for the inlet zone I and the outlet zone VI) while the HPNE simulation shows a damped periodic behavior. This periodic or periodic-damped behavior is also shown by the concentration fields of Figures 8.6 (b) and (c). The damping in the HPNE simulation is due to the transfer of the liquid from the droplet to the film phase. The lack of damping for the HPE case is a sign of the very poor separation efficiency when entrainment is accounted for.

Entrainment. No entrainment was predicted for the LP case. This paragraph focuses only on the HPE calculation. Figure 8.9 shows the entrainment and deposition rates in the zones I and II. One can notice that a local equilibrium between entrainment and deposition takes place very quickly approximately after the middle of zone I. Figure 8.6 (c) shows that concentrations are high by the wall where a liquid film is present but the droplets are not dispersed in the core and remain close to the wall. The rapid equilibrium between entrainment and deposition shows that the droplet distribution is not controlled by boundary layer transfers between the film and the dispersed phase. Droplet concentration profiles are therefore controlled by other phenomena (such as the turbulent dispersion or the centrifugal force).

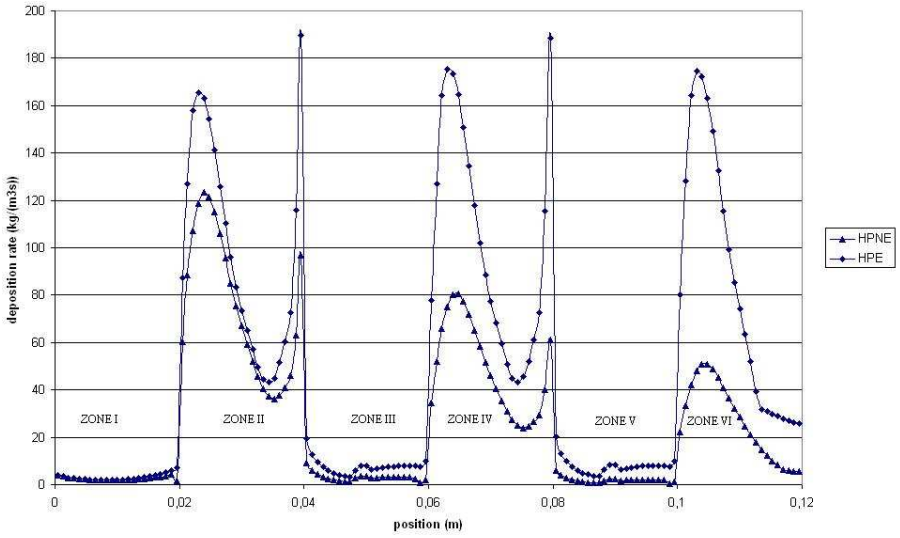

Figure 8.8: Deposition rate on the top wall of the vane-pack. Comparison between the calculations with and without entrainment.

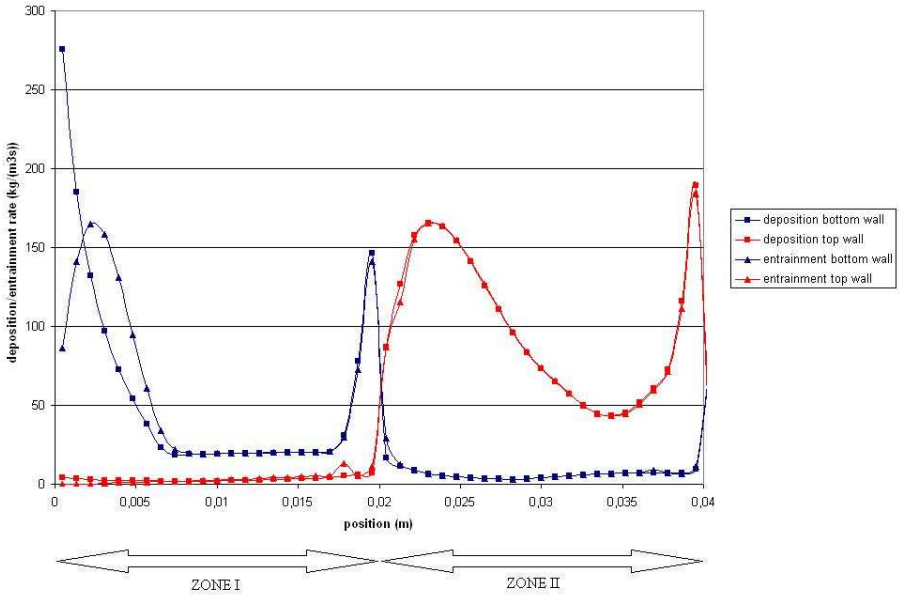

Figure 8.9: Entrainment and deposition rate in the two first sections of the vane-pack for the HPE calculation.

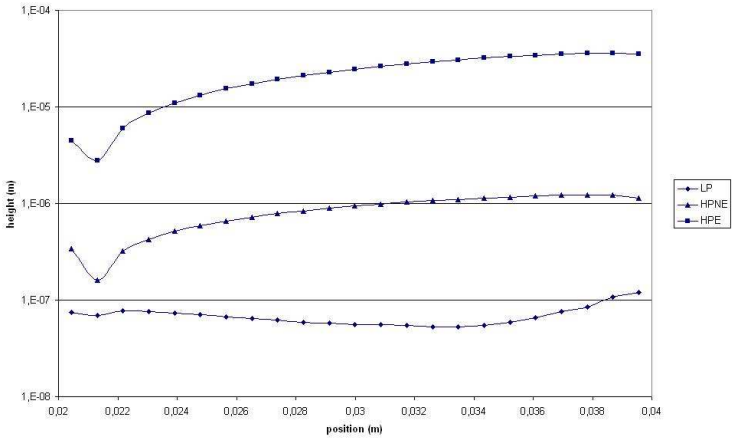

Figure 8.10: Height of the liquid film.

	LP	HPNE	HPE
Mean height (nm)	22 700	855	69
Minimum height (nm)	2 780	162	52
Maximum height (nm)	35 500	1230	120

Table 8.5: Height of the liquid film.

c) Liquid film

Height. Figure 8.10 shows the height of the film as a function of the position on the top wall of zone II at t=5 ms. Table 8.5 shows the mean height, minimum height and maximum height of the film for the curves of Figure 8.10. The order of magnitude of the thickness of the film for the low pressure simulation is typical of air/water annular flow at atmospheric pressure, i.e. between 1 and 1000 μm. A striking feature of Table 8.5 is that the height of the liquid film is 2 orders of magnitude smaller when the pressure is increased to 92 bars and natural gas and condensate are used. The major difference between the low and the high pressure calculations is the magnitude of the interfacial shear. This shear is directly proportional to the gas density and thus an increase of the density of the gas from 1 to 100 kg/m^3 induces an increase of two orders of magnitude of the interfacial shear stress. The velocity of the film is then increased and the height of the liquid layer drops to a much lower value. One can also see that allowing entrainment has an important impact on the film and that its height is reduced even further. There is more than a factor 300 between the mean height of the film for the LP case and for the HPE case.
A question arising when one predicts a film height of a few nanometers, is whether or not the film is actually wetting the surface. Dewetting depends on parameters that have not been tackled in this work. During dewetting, randomly

initiated dry patches grow and the liquid accumulates in rims around these dry spots. The rims may gather into liquid trickles. Finally these trickles may break into droplets by a Rayleigh break-up process. Hartley and Murgatroyd (1964) studied the stability of a dry patch. They proposed a simplified criteria for dry zones stability surrounded by laminar film under the influence of a shear. Given h_{crit}, the critical height of the film under which the dry patch is stable, according to Hartley and Murgatroyd we have:

$$h_{crit} = 1.59 \left(\frac{\Sigma}{\rho_f}\right)^{\frac{1}{3}} \left(\frac{\mu_f}{\tau_i}\right)^{\frac{2}{3}} \tag{8.1}$$

This relation is based on a minimization of the total energy of the film (kinetic and surface energy). As an average on the top wall of zone II, $h_{crit} \approx 1\mu m$ for the HPE and HPNE cases. $h_{crit} \approx 65\mu m$ for the LP case. It is not expected that these values of h_{crit} are very accurate because equation (8.1) does not take into account the effects of surface chemistry. However relation (8.1) can give an order of magnitude of the critical wetting height. As shown in Table 8.5, the mean heights for the LP and HPNE cases are of the same order of magnitude as the critical height. No conclusion can be drawn except that the films are probably close to the dewetting/wetting boundary. In contrast, there is a strong probability of dewetting for the HPE case. This may change the entrainment process. Although it is expected that the Kelvin-Helmholtz instability remains the key mechanism initiating entrainment, it is doubtful to apply the correlation (3.155) of Alipchenkov *et al.* (2004) and the expressions of the critical Weber number (3.159) and (3.160) (Nigamtulin *et al.* (1996)) when dewetting occurs. Though these equations have been tested against high pressure steam-water data, Alipchenkov *et al.* (2004) and Nigamtulin *et al.* (1996) did not mention dewetting. In the following, the possible disruption of the film due to dewetting has been disregarded.

For a film height of about 60 nm the roughness of the wall has a large impact on the film flow. A negligible roughness of the wall with respect to such a thin film requires a wall which roughness is less than a nanometer. A vane-pack demister is typically made of steel (for example carbon steel [102]). At best, the arithmetic average roughness of these type of material is 6 nm [169]. In addition, the arithmetic average roughness is the absolute deviation from the mean surface level, therefore the peak-to-valley roughness is bigger than the arithmetic average roughness. As a result it is probable that at the scale of a a 60 nm thick film, the flow occurs on top of or in between randomly placed large buffer bodies that create very large disturbances of the film flow. The flow of the gas in between randomly spaced roughness elements is also very complex and has an impact on the interfacial shear. The impact of the protrusions of the wall on a submicrometer liquid layer is a complex topic that can not be examined in detail within the frame of this work. In the following, the analysis will be done as if the wall was smooth even at a nanoscale.

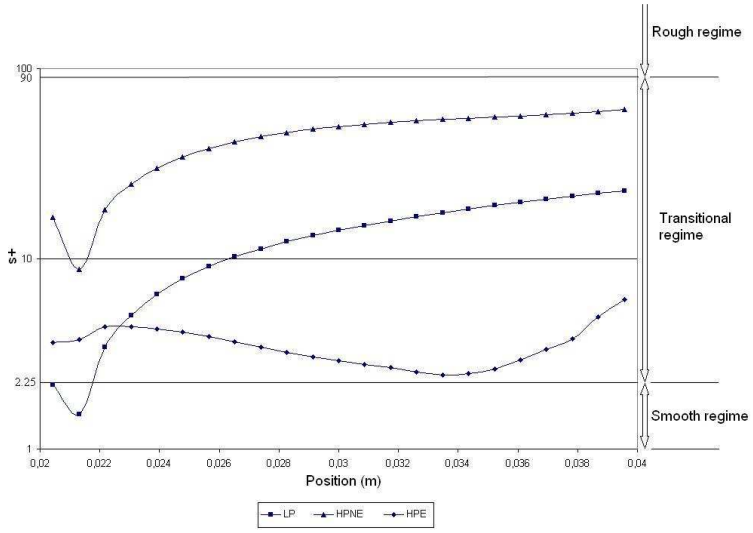

Figure 8.11: Non-dimensional equivalent roughness height of the film.

Equivalent roughness height. The analysis contained in this paragraph is not relevant if the roughness height of the wall is comparable to or larger than the equivalent roughness height of the film.
Figure 8.11 shows the values of the non-dimensional roughness $s^+ = s\ u_\tau/\nu_g$ on the top wall of zone II as a function of the position. The frictional velocity was calculated by:

$$u_\tau = \sqrt{\sqrt{C_\mu} k_g}$$

One can see on Figure 8.11 that whatever the case, the roughness regime is transitional. The little change of the non-dimensional roughness height, despite the large decrease in the roughness height can be explained by a large decrease of the kinematic viscosity of the gas $\nu_g = \mu_g/\rho_g$. Indeed, the gas density is increased by a factor hundred in the high pressure cases with respect to the LP case, while the dynamic viscosity does not change (see Table 8.2).
We will admit that $s/h = 4$ is approximately valid for a fully rough regime. In the smooth regime $s/h = 0$. Therefore in the transitional regime we expect $0 < s/h < 4$. Since according to Figure 8.11 the regime is transitional, $s/h = 4$ is too high and there is an overestimation of the turbulent kinetic energy by the wall. Consequently the interfacial shear stress and of the mean film velocity are overestimated. As a result, the height of the film is probably slightly underpredicted in this simulation. However the order of magnitude of the height of the film (due to the influence of the density of the gas on the interfacial shear stress) is most likely to be correct.

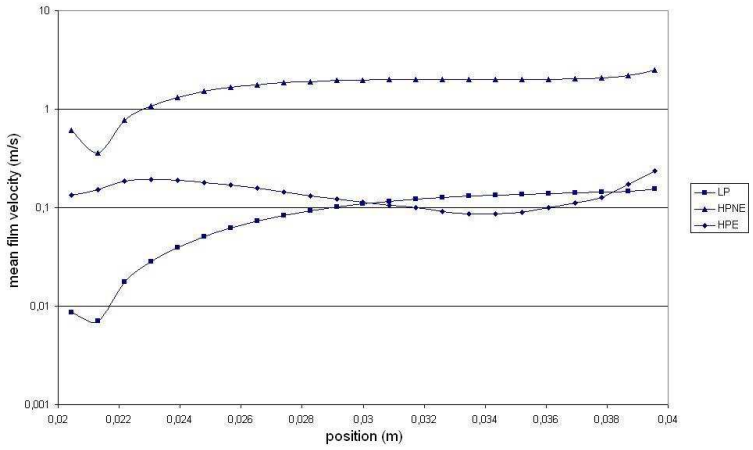

Figure 8.12: Velocity of the film.

Velocity of the liquid layer. The analysis of this paragraph should be significantly changed if the film is disrupted or if the roughness of the wall is large with respect to the thickness of the film.
Figure 8.12 shows the mean velocity of the liquid film on the top wall of section II at t=5 ms. The averaged values are 0.09, 1.72, and 0.14 m/s respectively for the LP, HPNE and HPE simulations. There is a 20 fold increase in the mean velocity of the film in the HPNE case with respect to the LP case. This is due to the increase of the interfacial shear stress caused by an increased gas density. When entrainment is allowed the velocity of the liquid film drops down because of the strong reduction of the film height.
The model assumes that the gas flows over a rough motionless surface. It requires that in the wall-boundary cells the velocity of the interface c is small with respect to the velocity of the gas U_g. For the values on the top wall of zone II, for the LP case c/U_g is always between 0.5 and 2% so that the assumption $c << U_g$ is indeed valid. For the HPNE simulation, because of the increase of the interfacial shear, this assumption breaks down. $c/U_g \approx 20\%$ as a rule and reaches up to 98.6 % by the recirculation zone at the edge of zone I. The non negligible velocity of the gas/film interface modifies the boundary condition for the gas phase. This condition becomes:

$$u^+ = \frac{1}{\kappa} ln\left(y^+\right) + B + f\left(s^+\right) + \frac{c}{u_\tau} \tag{8.2}$$

where the function $f\left(s^+\right)$ is given by the equations (3.68), (3.69) an (3.70) and c/u_τ is an additional term to take into account the movement of the liquid layer. Then the boundary condition becomes:

$$\tau_i = \rho_g u_\tau \frac{U_g}{\frac{1}{\kappa} ln\left(y^+\right) + B + f\left(s^+\right) + \frac{c}{u_\tau}} \tag{8.3}$$

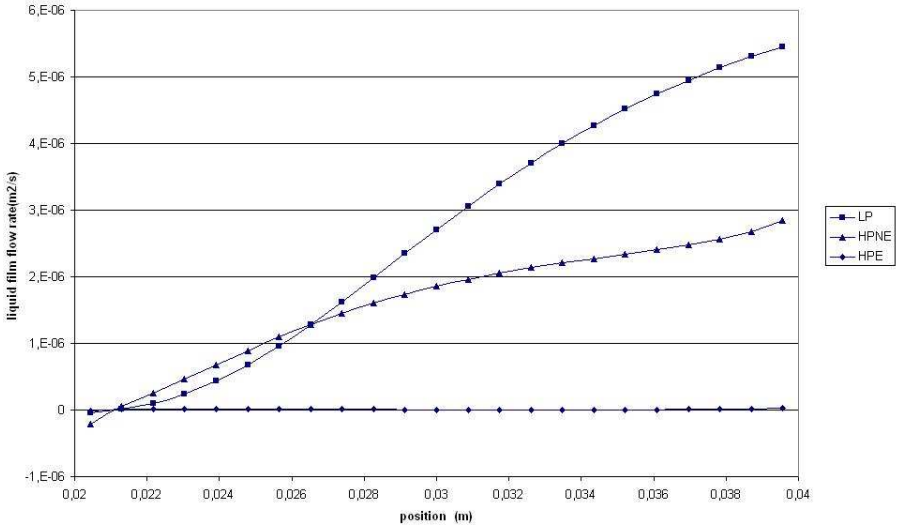

Figure 8.13: Flux of film along the top wall of zone II.

Therefore, the additional term c/u_τ reduces the interfacial shear and the pressure drop.
One can also notice that if the velocity of the film is significant, the loss of momentum of the droplet phase is smaller during the deposition/entrainment process. Indeed this loss of momentum is proportional to the velocity difference between the interface and the droplet phase (equation (3.7)). As a result the pressure drop due to deposition and entrainment is smaller when the velocity of the interface is significant.
If the entrainment is taken into account, the ratio of the interface velocity to the wall cell gas velocity is much smaller and the assumption $c << U_g$ is generally valid. However, locally, this assumption may break down. For the present case, c/U_g reaches up to 32.2% in the vicinity of the recirculation zone at the edge of zone I. In the zones were $c << U_g$ is not verified, simulation results must be taken with caution.

Film flow rate. The film flow rate is a key parameter for the drainage of the film. Figure 8.13 shows the value of the film flow rate as a function of the position along the top wall of zone II. The low pressure case combines a high liquid film height and a low film velocity. The liquid film flow rate increases along the wall as droplets deposit. A drainage opening at the end of the wall will result in an effective way of removing the film. For the high pressure case without entrainment, the height of the film is low but its velocity is high. The liquid flux has the same order of magnitude as in the low pressure case. Since the deposition rate is lower for the HPNE than for the LP case, the film flow

rate is slightly lower at high pressure. As emphasized earlier, the results of the HPNE case are to be taken with caution because in this case the interfacial velocity is not negligible with respect to the gas velocity in the wall-boundary cells. The negative value of the film flow rate is due to a recirculation zone at the beginning of the wall. The striking feature of Figure 8.13 is that the film flow rate is practically zero for the high pressure case when entrainment is considered. It is actually 250 time lower than if entrainment is not considered. The HPE case combines indeed a very small height with a low velocity of the liquid layer. Consequently the film flow rate is almost zero. There is practically no film at all. It means that a drainage hole, whatever its position on the wall, is inefficient because there is no film to collect. As a result, even if the simulation had integrated a drainage system, the efficiency of the vane-pack demister would not have improved significantly.

Concluding remarks on the liquid film. According to the simulation, at high pressure with entrainment, the liquid layer practically vanishes. The film may be disrupted, and is likely to be affected by the roughness of the wall. If the wall is perfectly smooth, it is shown that the equivalent sand roughness of the film is overestimated. The equivalent sand roughness height of the film may however not be such a critical issue if the physical roughness of the wall is larger than the height of the film. For the velocity of the liquid layer, both a disruption of the film and the roughness of the wall may have a significant impact. Supposing that the wall is perfectly smooth and that dewetting does not occur, the results showed that at high pressure the velocity of the film is not necessarily very small with respect to the gas velocity. The boundary condition of the gas phase must then be modified to take into account the velocity of the gas/film interface. It is very likely that the film flux is practically zero at high pressure if entrainment is accounted for. Then, collecting the film through slits is inefficient.

d) Droplet diameter

The droplet diameter is considered to be a constant (25 μm) in the present work. However, there are indications that the actual mean droplet diameter is smaller than the value used in the computation:

- First, the maximum stable diameter of a droplet in a turbulent flow increases with the surface tension (Hinze (1955)). In high pressure turbulent gas/liquid flows, the surface tension is lower than for low pressure flows. As a result, the maximum stable droplet diameter is smaller in high pressure flows than in low pressure flows.

- Second, the diameter of the droplets used in the model is much larger than the height of the liquid film. It is unlikely that a 70 nm thick film generates droplets with a diameter of 25 μm. With an extremely thin film, a large 25 μm droplet impinging against the wall will probably be

atomized in a fine mist of particles. These small droplets will then be entrained.

This second diameter-reducing effect may be compensated by coalescence in areas where the droplet concentration is high. This is relevant near the walls where entrainment occurs (see Figure 8.6 (c)). It is then important to integrate a population balance to calculate the probability of coalescence of the droplets near the walls. The initiation of the re-entrained droplets should also be studied closely. If the film is only 70 nanometers thick, it seems important to have a further understanding of what happens in details when a large 25 μm droplet deposits.
It is important to note that small droplets have a small relaxation time. The 25 μm droplets were far in the inertia-moderated regime of deposition with $t^+ \approx 22000$ by the wall. In contrast if droplets have the size of the liquid film (50 nm), they deposit because of Brownian diffusion ($t^+ \approx 0.09$ by the wall). Consequently the basic idea of the vane-pack demister, the "inertial separation", may be totally inefficient.

e) Velocities

The velocities of the gas and of the dispersed phase are similar. There are recirculation zones in concave corners. Convex corners tend to compress the stream lines and generate an acceleration. The recirculating and high velocity zones are shown on Figure 8.14.
The separation efficiency of the vane-pack is related to the possibility for the dispersed phase to deviate from the gas trajectory. To quantify this deviation one can for example associate to each couple $(U_{ig}; U_{id})$ in a computational cell, a complex number z such as:

$$z = \frac{||U_{id}||}{||U_{ig}||} e^{i\theta} \tag{8.4}$$

where θ is the angle between the droplet velocity vector and the gas velocity vector. If $U_{id} = U_{ig}$ then $z = 1$, the droplet phase follows perfectly the gas and the separation efficiency is 0. Figure 8.15 shows the distribution of z for the LP and the HPE cases in the complex plane. In the case of the high pressure simulation the points are much closer to 1 and therefore follow closely the gas resulting in a poor separation. In contrast for the LPE simulation, the points show a clear deviation of the droplet velocity vectors with respect to the gas velocity vectors. Quantitatively the median of the absolute value of the argument of the z points is 19.5^o for the LPE case and 3.6^o for the HPE case. This shows that the particle phase is not significantly deviated from the gas trajectory in the high pressure case. The median of the modulus of the z points is 0.98 for the HPE case and 0.76 for the LP case. For an annular flow calculations by Fore and Dukler (1995b), Azzopardi and Teixeira (1994a), and the simulation of chapter 7, showed that the value of local droplet velocity is roughly 80% of the local gas velocity for air/water flow at atmospehric pressure.

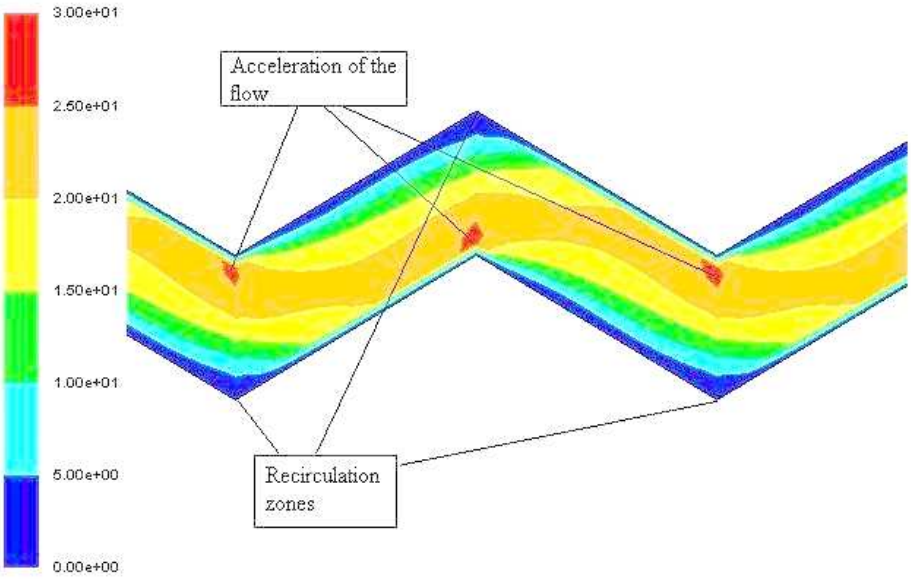

Figure 8.14: Horizontal gas velocity in m/s for the HPE simulation. Zones II, III, IV and V.

It is then interesting that for the same fluids and same pressure condition the flow in a vane-pack indicates also a ratio of the local velocity magnitudes of roughly 80%. Neglecting gravity, this ratio is the direct consequence of the momentum loss during the entrainment/deposition process. At high pressure the median modulus is much closer to 1. It indicates, as previously detailed, that the loss of momentum by the dispersed phase during deposition and entrainment is not important.

8.2.3 Conclusion on the simulation of a vane-pack mist eliminator at high pressure

The simulation of a vane-pack demister with real fluids at high pressure with entrainment shows a radically different behavior compared to an air/water flow at atmospheric pressure. The separation efficiency is dramatically reduced because:

1. Comparable densities of the two phases leads to a smaller inertia of the dispersed phase and thereby to a smaller deposition rate.

2. The entrainment is so large that no film remains on the walls.

3. The reduction of the droplet diameter, that have not been quantified here, leads to a smaller deposition rate.

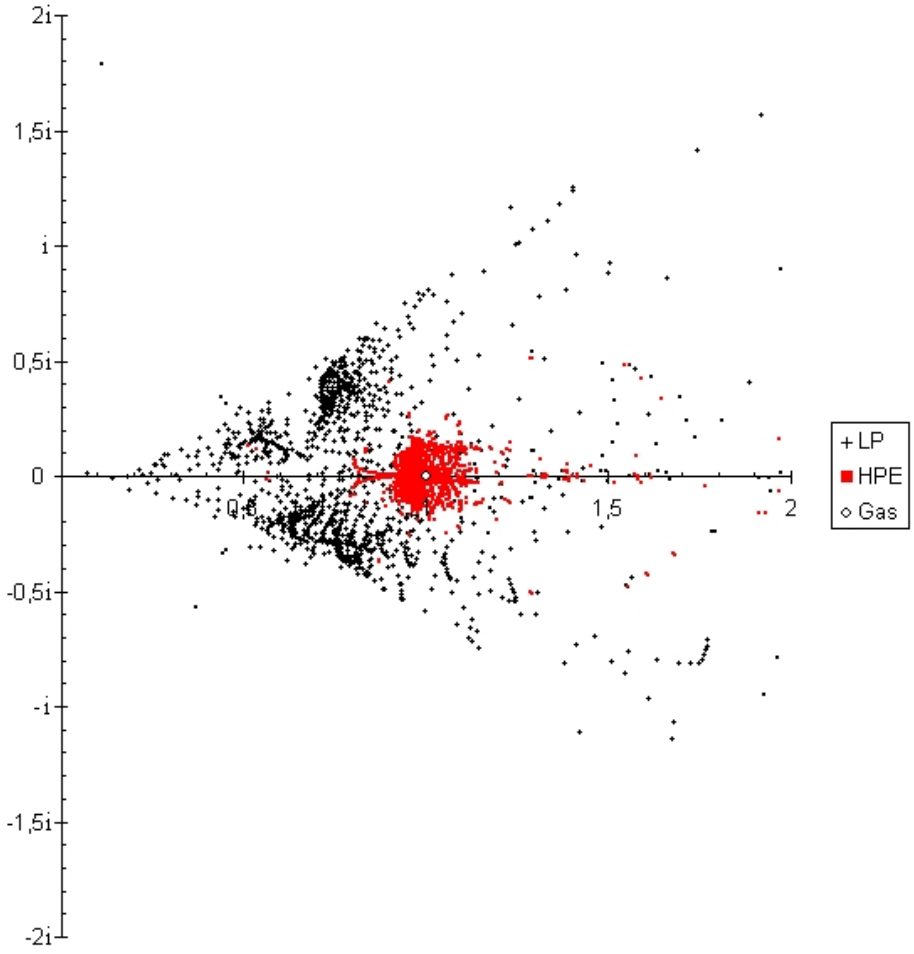

Figure 8.15: Distribution of z in the complex plane showing the separation efficiency of the vane-pack demister.

The key result of this simulation is that at high pressure the liquid film vanishes. The common design of simple slits in the wall to collect a liquid film is then inefficient. Moreover droplets cannot be efficiently separated because their inertia is too small.

8.3 Attempt of a high pressure simulation of an axial cyclone

An attempt has been made to calculate the separation efficiency of an axial cyclone. This cyclone has been described in Verlaan (1991). The calculation revealed a deficiency of the model not only in unstructured grids but also in any grid having a convex corner cell (as pictured on Figure 4.10). The model is not able to conserve the liquid mass if such a configuration occurs. The mass balance of both phases was always fulfilled in the the test cases described previously (annular or vane-pack simulations).
The problem came from equation (3.8), the mass conservation equation of the film, which is re-written below:

$$\frac{\partial h}{\partial t} + \frac{\partial}{\partial X_i} h\, U_{if} = \frac{V}{\rho_f A}\left(\widetilde{\dot{D}} - \widetilde{\dot{E}}\right) \tag{8.5}$$

If the liquid phase is assumed incompressible, the "true" mass-conservation equation for the film is:

$$\frac{\partial \overline{\alpha_f}}{\partial t} + \frac{\partial}{\partial X_i} \overline{\alpha_f}\, U_{if} = \frac{\left(\widetilde{\dot{D}} - \widetilde{\dot{E}}\right)}{\rho_f} \tag{8.6}$$

Equation (8.5) is based on the implicit definition:

$$h \equiv \frac{\overline{\alpha_f} V}{A} \tag{8.7}$$

and assumes that V/A is a constant. As currently implemented, our model is able to tackle cells which area is zero by techniques explained previously in chapter 4. However, if these techniques were satisfactory computationally they appeared to be unsatisfactory physically. The finite volume method is based on an integration of the mass conservation equation on the cell volume and in time. The integration of equation (8.6) is leading to the conservation of the volume of film which is the same as the mass conservation for an incompressible fluid. In contrast, the integration of equation (8.5) leads to the conservation of the quantity hV which has the unit of m^4. This quantity is however not conserved except if V/A is a constant. In certain area of the computational domain, conserving hV instead of the mass leads to a break-down of the mass balance. The present model, used in a grid with convex corners or unstructured grids, might however give a qualitative idea of the critical spots for liquid accumulation and entrainment.

It is suggested, to solve this issue, to come back to a mass conservation equation for the liquid layer which is based on the film volume fraction (equation (8.6)). The closure relations (such as the equivalent sand roughness of the film or the entrainment rate equation) must then be expressed in terms of $\overline{\alpha_f}$.

8.4 Conclusion on high pressure gas/liquid separation

The model was used to predict the separation efficiency of a vane-pack demister. The present model and the model developed by James *et al.* (2005) based on a Lagrangian tracking of the dispersed phase gave similar results. Then a simulation of the same vane-pack has been performed for typical industrial conditions with high-pressure liquid and gas properties, together with entrainment. The change of the density ratio decreased the efficiency of the demister. Including re-entrainment led to dramatic changes since the liquid film vanishes. It was also underlined that the droplet diameter is smaller for high pressure flows than for low presure flows. This diameter change reduces as well the efficiency of the demister but this was not accounted for in the computation.
These specifically high pressure phenomena result in an ineffective drainage and makes it very difficult for the droplets to separate from the gas phase because of their very small inertia. The predicted efficiency of the vane-pack demister at high pressure with entrainment is 0% while at low-pressure with air and water the model predicts an efficiency of 99.7%.

Chapter 9

Conclusion

9.1 Summary

The present work developed a new model for predicting the efficiency of gas-liquid separators especially at high pressure conditions. The model is based on a fully Eulerian description of the flow. 11 transport equations are solved: 3 mass conservation equations (gas, dispersed liquid phase and liquid film), 6 momentum equations (gas and droplet phase), 1 equation for the turbulent kinetic energy of the gas and 1 for the dissipation rate of the turbulent kinetic energy of the gas. The turbulent kinetic energy of the droplet phase and the turbulent dispersion are calculated by algebraic relations. The velocity of the film is calculated by an algebraic relation as well. The influence of the film on the gas is modeled by a steady rough wall boundary condition. The interfacial shear stress is estimated from the turbulent kinetic energy of the gas phase. The total deposition rate is determined by the turbulent dispersion and by a near-wall deposition rate. The near-wall deposition rate is the sum of two terms. The first term represents non diffusive phenomena (gravity, mean convection of the flow) and is calculated by means of an ordinary differential equation. The second term models near-wall diffusive phenomena. This second term takes into account two deposition regimes: the diffusion-impaction regime and the inertia moderated regime. The entrainment correlation is experimental and has been chosen because:

1. It has been tested on a large number of data including high-pressure steam-water flows.
2. It is entirely based on local parameters.
3. It is consistent with the theory developed by Taylor (1963) since it is based on a Weber number criteria.

The model has been implemented in Fluent 6.2 which is a finite volume code.

The model was tested against the experimental data of Liu and Agarwal (1974) for a case of pure deposition. A correct order of magnitude of the deposition rate was predicted. However the deposited fraction seemed underestimated by 20-25%. This underestimation probably comes from an innacurate modelling of the near-wall diffusive deposition velocity when the nondimensional relaxation time of the droplets is larger than 20. This inaccurate modelling is not important for relaxation times much larger than 20, since the the deposition rate is then controlled by the turbulent dispersion. Simulations have been performed and compared with experimental data of a pure annular flow without dispersed phase. The height of the film was correctly predicted but the pressure drop was overestimated. This overestimation comes, first, from an innacurate modeling of the equivalent sand roughness of the film and second, from the gas phase wall boundary condition that does not take into account the velocity of the interface. The model was then tested against the data gathered by Azzopardi and Teixeira (1994a, 1994b) in an annular dispersed flow. For low gas flow rates and high liquid flow rates, the computed flow was not qualitatively correct. It came from an underestimation of the velocity of the liquid film. The source of this error may be an innaccurate evaluation of the critical Weber number. In the case of high gas flow rates and low liquid flow rates, which is relevant for natural gas processing, the entrainment rate was significantly underestimated (about -50%). A better estimation of the entrainment flux will probably be obtained if one accounts for the turbulence in the film induced by the film flow and not only for the turbulence in the film due to the deposition of droplets. In agreement with former experimental observations, the model predicted a 20% lag of the droplet velocity with respect to the gas velocity. Finally, the model was tested on a vane-pack demister. At low pressure for air and water, the results were similar to these of the model of James *et al.* (2005). At high pressure, dramatic changes were observed. The liquid film disappeared and the deposition rate was much smaller than in the low pressure case. The predicted efficiency of the vane-pack demister drops from 99.7 % for an air/water flow at atmospheric pressure to 0% for a natural gas/condensate flow at 92 bars.

9.2 Further works

9.2.1 Deposition

The model underpredicts the deposition rate when the particle relaxation time is at the edge of the diffusion-impaction regime and of the the inertia moderated regime. To correct this, it would be interesting to conduct a study to determine precisely what is the value of the near-wall diffusive deposition velocity, especially for non-dimensional relaxation times between 10 and 50. Such a study will allow to distinguish clearly what fraction of the deposition rate is controlled by turbulent dispersion and what fraction is controlled by the near wall diffusive deposition velocity.

9.2.2 Film model

To be able to use the model in complex geometries, it is important to adapt the film model so it fulfills the conservation equations whatever the type of grid. The inability of the model to tackle correctly convex corners and unstructured grids is probably its strongest limitation for a real industrial use. It was also shown that a better modeling of the equivalent sand-roughness of the liquid layer must be found to correctly predict pressure drops. It is also necessary to modify the boundary condition of the gas so that the non-zero velocity of the interface is accounted for. To get better predictions of the entrainment rate for annular air-water flow at atmospheric pressure, a turbulent model for the film flow should be developed.

9.2.3 Entrainment

The correlation for the entrainment seemed to model satisfactorily entrainment phenomena but further experimental studies are needed to obtain a greater accuracy of the correlation providing the critical Weber number. The model had difficulties to calculate the entrainment rate at the edge of recirculation zones. This issue has never been studied before. A deeper understanding of entrainment in this particular case should be achieved to improve the quantitative predictions of the model in complex geometries.

9.2.4 Droplet size

The present work assumed a flow with monodispersed droplets. However, it was underlined that the diameter of the droplets is influenced by several phenomena: coalescence, break-up and splashes that can generate numerous small secondary droplets. It was also emphasized that the droplet size have a direct influence on the efficiency of gas-liquid separators, especially at high pressures. Hence, further works should include a model to correctly estimate droplet size.

Bibliography

[1] Abou-Arab, T. W. (1986). Turbulence models for two-phase flows. In *Encyclopedia of fluid mechanics, Vol 3: gas-liquid flows*. Houston: Gulf Publishing Company.

[2] Adechy, D. and R. I. Issa (2004). Modelling of annular flow through pipes and T-junctions. *Computers & Fluids 33,* 289-313.

[3] Ahrabi, F., S. J. Ashcroft and R. B. Shearn (1987). High-pressure volumetric, phase-composition and viscosity data for north-sea crude-oil and NGL. *Chem. Eng. Res. Des., 65(1)*, 63-73.

[4] Ahrabi, F., S. J. Ashcroft and R. B. Shearn (1989). High-pressure PVT and viscosity measurements on north-sea crude oil-NGL mixtures. *Chem. Eng. Res. Des. 67(3)*, 329-335.

[5] Alexander, L. G. and C. L. Coldren (1951). Droplet transfer from suspending air to duct walls. *Industrial and Eng. Chem. 43,* 1325-1331.

[6] Alipchenkov, V. M., L. I. Zaichik, Y. A. Zeigarnik, S. L. Solov'ev and O. G. Stonik (2002a). The development of a three-fluid model of two-phase flow for a dispersed-annular mode of flow in channels: Size of droplets. *High Temp. 40(4),* 594-603.

[7] Alipchenkov, V. M., L. I. Zaichik, Y. A. Zeigarnik, S. L. Solov'ev and O. G. Stonik (2002b). The development of a three-fluid model of two-phase flow for a dispersed-annular mode of flow in channels: Deposition and entrainment of droplets. *High Temp. 40(5),* 716-722.

[8] Alipchenkov, V. M., R. I. Nigmatulin, S. L. Soloviev, O. G. Stonik, L. I. Zaichik and Y. A. Zeigarnik (2004). A three-fluid model of two-phase dispersed-annular flow. *Int. J. of Heat and Mass Transf. 47,* 5323-5338.

[9] Ambrosini, W., P. Andreussi and B. J. Azzopardi (1991). A physically based correlation for drop size in annular flow. *Int J. of Multiphase Flow 17,* 497-507.

[10] Andreussi, P. (1983). Droplet transfer in two-phase annular flow. *Int. J. of Multiphase Flow 9,* 697-713.

[11] Andreussi, P., J. C. Asali and T. J Hanratty (1985). Initiation of roll waves in gas-liquid flows. *A.I.Ch.E J. 31,* 119-126.

[12] Antal, S. P., D. P. Edwards and T. D. Strayer (1998). Predicting multidimensional annular flows with a locally based two-fluid model. In *Third Int. Conf. on Multiphase Flow, ICFM'98,* Lyon.

[13] Antipin, V. A., L. I. Zaichik, Y. A. Zeigarnik, D. M. Markovich, S. L. Solov'ev, O. G. Stonik, S. M. Kharlamov and A. V. Cherdantsev (2003). The development of a three-fluid model of two-phase flow for a dispersed-annular mode of flow in channels: Film thickness and pressure drop. *High Temp. 41(3),* 399-403.

[14] Asali, J. C. (1984). *Entrainment in vertical gas-liquid annular flows.* Ph.D. thesis. University of Illinois, Urbana.

[15] Asali, J. C. and T. J. Hanratty (1985). Interfacial drag and film height for vertical annular flow. *A.I.Ch.E J. 31,* 895-902.

[16] Ashrafian, A. (2004). *Numerical investigation of turbulent flow in a channel flow with rough walls.* Ph.D. thesis. NTNU, Trondheim.

[17] Ashrafian, A., H. I. Andersson and M. Manhart (2004). DNS of turbulent flow in a rod-roughened channel. *Int. J. Heat Fluid Flow 25,* 373-383.

[18] Assad, A., C. Jan, M. Lopez de Bertodano and S. Beus (1998). Scaled entrainment measurements in ripple-annular flow in a small tube. *Nucl. Eng. and Des. 184,* 437-447.

[19] Austrheim, T. (2005). Experimental investigation of high-pressure gas scrubbers. *Hipgas meeting presentation at Statoil,* Trondheim.

[20] Austrheim, T. (2006). Personal communications. 02/09/06 (e-mail) and 04/19/06 (phone).

[21] Azzopardi, B. J. and D. B. Gibbons (1983). Annular two phase flow in a large diameter tube. *Chem. Eng. 398,* 19-31.

[22] Azzopardi, B. J., A. Piearcey and D. M. Jepson (1991). Drop size measurements for annular two-phase flow in a 20 mm diameter vertical tube. *Experiments in Fluids 11,* 191-197.

[23] Azzopardi, B. J. and J. C. F. Teixeira (1994a). Detailed measurements of vertical annular two-phase flow-Part I: Drop velocities and sizes. *Trans. of the ASME 116,* 792-795.

[24] Azzopardi, B. J. and J. C. F. Teixeira (1994b). Detailed measurements of vertical annular two-phase flow-Part II: Gas core turbulence. *Trans. of the ASME 116,* 796-800.

[25] Azzopardi, B. J. (1997). Drops in annular two-phase flow. *Int. J. of Multiphase Flow 23 Suppl.,* 1-53.

[26] Azzopardi, B. J. (1999). Turbulence modification in annular gas/liquid flow. *Int J. of Multiphase Flow 25,* 945-955.

[27] Binder, J. L. and T. J. Hanratty (1991). A diffusion model for droplet deposition in gas/liquid annular flow. *Int. J. of Multiphase Flow 17,* 1-11.

[28] Binder, J. L. and T. J. Hanratty (1992). Use of Lagrangian methods to describe drop deposition and distribution in horizontal gas-liquid annular flows. *Int. J. of Multiphase Flow 18,* 803-820.

[29] Brandt, A. (1977). Multi-level adaptive solutions for boundary-value problems. *Mathematics of computation 31,* 333-390.

[30] Briggs, W. L. (1987). *A multigrid tutorial*. Philadelphia: SIAM.

[31] Bürkholz, A. (1989). *Droplet separation.* Weinheim : VCH.

[32] CDS engineering. Miscellaneous Internals [online: web], updated unknown, cited 23 Feb. 2005. URL: http://www.cds-separation.com/

[33] Chung, M. K., H. J. Sung and K. B. Lee (1986). Computational study of turbulent gas-particle flow in a venturi. *Trans. of the ASME 108,* 248-253.

[34] Cleaver, J. W. and B. Yates (1975). A sub layer model for the deposition of particles from a turbulent flow. *Chem. Engineering Sci 30,* 983-992.

[35] Clift, R., J. R. Grace, and M. E. Weber (1978). *Bubbles, drops and particles*. New York: Academic Press.

[36] Crowe, C. T., T. R. Troutt and J. N. Chung (1996). Numerical models for two-phase turbulent flows. *Annu. Rev. Fluid. Mech. 28*, 11-43.

[37] Crowe , C. T., M. Sommerfeld and Y. Tsuji (1998). *Multiphase flows with droplets and particles*. Boca Raton: CRC Press.

[38] Crowe, C. T. (2000). On models for turbulence modulation in fluid-particle flows. *Int J. of Multiphase Flow 26,* 719-727

[39] Csanady, G. T. (1963). Turbulent diffusion of heavy particles in the atmosphere. *J. of the Atmospheric Sci. 20,* 201-208.

[40] Dahlquist, G. and Å. Björck (1974). *Numerical methods*. Englewood Cliffs: Prentice-Hall Incorporated.

[41] Dallman, J. C., B. G. Jones and T. J. Hanratty (1979). Interpretation of entrainment measurements in annular gas-liquid flows. In *Two-phase momentum, heat and mass transfer, Vol 2*. Whashington D.C: Hemisphere.

[42] Davis, C. N. (1966). *Aerosol Science*. London: Academic Press.

[43] Delhaye, J. M. (1974). Jump conditions and entropy sources in two-phase systems. Local instant formulation. *Int. J. of Multiphase flow 1,* 395-409.

[44] Derevich, I. V. and L. I. Zaichik (1988). Particle deposition from a turbulent flow. *Fluid Dyn. 23,* 722-729.

[45] Derevich, I. V. (2000a). Statistical modelling of mass transfer in turbulent two-phase dispersed flows - 1. Model development. *Int. J. Heat and Mass transf. 43,* 3709-3723.

[46] Derevich, I. V. (2000b). Statistical modelling of mass transfer in turbulent two-phase dispersed flows - 2. Calculation results. *Int. J. Heat and Mass transf. 43,* 3725-3734.

[47] Dobran, F. (1987). Nonequilibrium modeling of two-phase critical flows in tubes. *J. of Heat Transf. 109,* 731-738.

[48] Drew, D. A. and S. L. Passman (1998). *Theory of multicompoment fluids.* Applied Mathematical Sciences, Vol 135. New York: Springer.

[49] Dykhno, L. A. and T. J Hanratty (1996). Use of the interchange model to predict entrainment in vertical annular flow. *Chem. Eng. Comm. 141-142,* 207-235.

[50] Elghobashi, S. E. and T. W. Abou-Arab (1983). A two-equation turbulence model for two-phase flows. *Phys. Fluids 26,* 931-938.

[51] Favre, A. (1969). Statistical equations of turbulent gases. In *Problems of hydrodynamics and continuum mechanics*. 231-266. Philadelphia: Society for industrial and applied mechanics.

[52] Fichman, M., C. Gutfinger and D. Pnueli (1988). A model for turbulent deposition of aerosols. *J. of Aerosol. Sci. 19,* 123-136.

[53] Fluent Inc. (2004a). *Gambit 2.2 user's guide*. Lebanon NH: Fluent Incorporated.

[54] Fluent Inc. (2004b). *Gambit 2.2 modeling guide. Vol. 2*. Lebanon NH: Fluent Incorporated.

[55] Fluent Inc. (2005). *Fluent 6.2 user's guide. Vol. 3*. Lebanon NH: Fluent Incorporated.

[56] Fore, L. B. and A. E. Dukler (1995a). Droplet deposition and momentum transfer in annular flow. *A.I.Ch.E J. 41(9)*, 2040-2046.

[57] Fore, L. B. and A. E. Dukler (1995b). The distribution of drop size and velocity in gas-liquid annular flow. *Int. J. of Mutliphase Flow 21,* 137-149.

[58] Fore, L. B., S. G. Beus and R. C. Bauer (2000). Interfacial friction in gas-liquid annular flow: analogies to full and transition roughness. *Int. J. of Multiphase Flow 26,* 1755-1769.

[59] Fossa, M. (1995). A simple model to evaluate direct contact heat transfer and flow characteristics in annular two-phase flow. *Int. J. Heat and Fluid Flow 16,* 272-279.

[60] Fossa, M., C. Pisoni and L. A. Tagliafico (1998). Experimental and theoritical results on upward annular flow in thermal non-equilibrium. *Experimental Thermal and Fluid Sci. 16,* 220-229.

[61] Friedlander, S. K. and H. F. Johnstone (1957). Deposition of suspended particles from turbulent gas streams. *Ind. and Engineering Chem. 49,* 1151-1156.

[62] Frohn, A. and N. Roth (2000). *Dynamics of droplets.* Berlin: Springer-Verlag.

[63] Fukano, T. and A. Ousaka (1989). Prediction of the circumferential distribution of film thickness in horizontal and near-horizontal gas-liquid annular flows. *Int. J. of Multiphase Flow 15,* 403-419.

[64] Fukano, T. and T. Furukawa (1998). Prediction of the effects of liquid viscosity on interfacial shear stress and frictional pressure drop in vertical upward gas-liquid annular flow. *Int. J. of Multiphase Flow 24,* 587-603.

[65] Ganesan, S. and D. R. Poirier (1990). Conservation of mass and momentum for the flow of interdentritic liquid during solidification. *Metallurgical Trans. 21B,* 173-181.

[66] Ganić, E. N. and K. Mastanaiah (1981). Investigation of droplet deposition from a turbulent gas stream. *Int. J. of Multiphase Flow 7,* 401-422.

[67] Gillandt, I. and C. T. Crowe (1998). Turbulent modulation of fluid-particle flows _ a basic approach. In *Third Int. Conf. on Multiphase Flow, ICFM'98,* Lyon.

[68] Gouesbet, G., A. Berlemont and A. Picart (1984). Dispersion of discrete particles by continuous turbulent motions. Extensive discusion of the Tchen's theory, using a two-parameter family of Lagrangian correlation functions. *Phys. Fluids 27*, 827-837.

[69] Gouesbet, G. and A. Berlemont (1999). Eulerian and Lagrangian approaches for predicting the behaviour of discrete particles in turbulent flows. *Progress in Energy and Combustion Sci. 25*, 133-159.

[70] Guha, A. (1997). A unified Eulerian theory of turbulent deposition to smooth and rough surfaces. *J. of Aerosol Sci. 28,* 1517-1537.

[71] Hanratty, T. J. and J. M. Engen (1957). Interaction between a turbulent air stream and a moving water surface. *A.I.Ch.E 3,* 299-304.

[72] Hartley, D. E. and W. Murgatroyd (1964). Criteria for the break-up of thin liquid layers flowing isothermally over solid surfaces. *Int. J. Heat Mass Transf. 7,* 1003-1015.

[73] Havelka, P., C. Gotaas, H. A. Jakobsen and H. F. Svendsen (2004). Droplet formation and interaction under normal and high pressure. In *Fifth Int. Conf. on Multiphase Flow.* Paper No. 123. Yokohama.

[74] H.A.S.T (Haver standard india pvt. ltd.). Misterscreen / Demister Pad / Mist Eliminator [online: web], updated unknown, cited 23 Feb. 2005. URL: http://www.haverstandard.com/demi.htm

[75] Hay, K. J., Z.-C. Liu and T. J. Hanratty (1996). Relation of deposition to drop size when the rate law is nonlinear. *Int. J. of Multiphase Flow 22,* 829-848.

[76] Henstock, W. H., and T. J. Hanratty (1976). The interfacial drag and the height of the wall layer in annular flows. *A.I.Ch.E J. 22,* 990-1000.

[77] Hewitt, G. F. and N. S. Hall Taylor (1970). *Annular two-phase flow.* Oxford: Pergamon Press.

[78] Hewitt, G. F. and A. H. Govan (1990). Phenomenological modelling of non-equilibrium flows with phase change. *Int. J. Heat. Mass Transf. 33,* 229-242.

[79] Himmelsbach, J., B. Noll and S. Wittig (1994). Experimental and numerical studies of evaporating wavy fuel films in turbulent air flow. *Int. J. Heat Mass Transf. 37,* 1217-1226.

[80] Hinze, J. O. (1955). Fundamentals of the hydrodynamic mechanism of splitting in dispersion processes. *A.I.Ch.E 1,* 289-295.

[81] Hinze, J. O. (1959). *Turbulence.* New York: Mc Graw-Hill.

[82] Ho Kee King, S. and G. Piar (1999). Effects of entrainment and deposition mechanisms on annular dispersed two-phase flow in a converging nozzle. *Int. J. of Multiphase Flow 25,* 321-347.

[83] Hurlburt, E. T. and T. A. Newell (2000). Prediction of the circumferential film thickness distribution in horizontal annular gas-liquid flow. *Trans. of the ASME 122,* 396-402.

[84] Hutchinson, P., G. F. Hewitt and A. E. Dukler (1971). Deposition of liquid or solid dispersions from turbulent gas streams: a stochastic model. *Chem. Engineering Sci. 26,* 419-439.

[85] Hutchinson, P. and P. B. Whalley (1973). A possible characterisation of entrainment in annular flow. *Chem. Engineering Sci. 28,* 974-975.

[86] Hwang, G.-J. and H. H. Shen (1993). Fluctuation energy equations for turbulent fluid-solid flows. *Int. J. of Multiphase Flow 19,* 887-895.

[87] Ishii, M. (1975). *Thermo-fluid dynamic theory of two-phase flow.* Paris: Eyrolles

[88] Ishii, M. and M. A. Grolmes (1975). Inception criteria for droplet entrainment in two-phase cocurrent film flow. *A.I.Ch.E 21,* 308-318.

[89] Ishii, M. and K. Mishima (1989). Droplet entrainment correlation in annular two-phase flow. *Int. J. Heat Mass Transf. 32,* 1835-1846.

[90] Jagota, A. K., E. Rhodes and D. S. Scott (1973). Tracer measurements in two phase annular flow to obtain interchange and entrainment. *Can. J. Chem. Eng. 51,* 139-147.

[91] Jakobsen, H. A. (1993). *On the modelling and simulation of bubble column reactors using a two-fluid model.* Ph.D. thesis, Norges Tekniske Høgskole, Trondheim.

[92] James, P. W., B. J. Azzopardi, Y. Wang and J. P. Hughes (2005). A model for liquid film flow and separation in a wave-plate mist eliminator. *Chem. Eng. Res. and Design 83(A5),* 469-477.

[93] Jayanti, S. and M. Valette (2004). Prediction of dryout and post-dryout heat transfer at high pressures using a one-dimensional three-fluid model. *Int. J. of Heat and Mass Transf. 47,* 4895-4910.

[94] Jepson, D. M., B. J. Azzopardi and P. B. Whalley (1989). The effect of gas properties on drops in annular flow. *Int. J. of Multiphase Flow 15,* 327-339.

[95] Johansen, S. T. (1990). *On the modelling of disperse two-phase flows.* Ph.D. thesis. Norges Tekniske Høgskole, Trondheim.

[96] Johansen, S. T. (1991). The deposition of particles on vertical walls. *Int. J. of Multiphase Flow 17,* 355-376.

[97] Jones, W. P. and B. E. Launder (1972). The prediction of laminarization with a two-equation model of turbulence. *Int. J. Heat Mass Transfer 15,* 301-314.

[98] Kallio, G. A. and M. W. Reeks (1989). A numerical simulation of particle deposition in turbulent boundary layers. *Int. J. of Multiphase Flow 15,* 433-446.

[99] Kataoka, I. (1986). Local instant formulation of two-phase flow. *Int. J. of Multiphase Flow 12,* 745-758.

[100] Kataoka, I. and A. Serizawa (1989). Bacic equations of turbulence in gas-liquid two-phase flow. *Int. J. of Multiphase Flow 15,* 843-855.

[101] Kataoka, I., M. Ishii and A. Nakayama (2000). Entrainment and deposition rates of droplets in annular two-phase flow. *Int. J. of Heat and Mass Transf. 43,* 1573-1589.

[102] Koch-Otto York. Mist elimination [online: web], updated 2003, cited 19 Apr. 2006. URL: http://kochottoyork.com/downloads/ProductCatalog.pdf

[103] Kocamustafaogullari, G. and M. Ishii (1995). Foundation of the interfacial area transport equation and its closure relations. *Int. J. Heat Mass Transfer 38,* 481-493.

[104] Kumar, R. and T. A. Trabold (2000). High pressure annular two-phase flow in a narrow duct: Part II-Three-field modeling. *J. of Fluids Eng. 122,* 375-384.

[105] Larsson, J. CFD Resources Online - Software [online: web], updated 2004, cited 24 Feb. 2005. URL: http://www.cfd-online.com/Resources/soft.html#com

[106] Launder, B. E. and B. I. Sharma (1974). Application of the energy-dissipation model of turbulence to the calculation of flow near a spinning disc. *Lett. Heat Mass Transf. 1*, 131-138.

[107] Laux, H. (2006). Personal communications. 01/20/06 (e-mail).

[108] Lee, M. M. (1987). *Droplet motion and deposition in vertical turbulent pipe flow.* Ph.D. thesis. University of Illinois, Urbana.

[109] Lee, M. M., T. J. Hanratty and R. J. Adrian (1989). The interpretation of drop deposition measurements with a diffusion model. *Int. J. of Multiphase Flow 15,* 459-469.

[110] Leman, G. W., M. Agostini and P. Andreussi (1985). Tracer analysis of developing two-phase annular flow. *Physico-Chemical Hydrodynamics 6,* 223-237.

[111] Ligrani, P. M. and R. J. Moffat (1986). Structure of transitionally rough and fully rough turbulent boundary layers. *J. of Fluid Mech. 162,* 69-98.

[112] Liu, B. Y. H. and J. K. Agarwal (1974). Experimental observation of aerosol deposition in turbulent flow. *Aerosol Sci. 5,* 145-155.

[113] Lopes, J. C. B. and A. E. Dukler (1986). Droplet entrainment in vertical annular flow and its contribution to momentum transfer. *A.I.Ch.E J. 32(9)*, 1500-1515.

[114] Lopez de Bertodano, M. A., C. S. Jan and S. G. Beus (1997). Annular flow entrainment rate experiment in a small vertical pipe. *Nucl. Eng. and Design 178,* 61-70.

[115] Lopez de Bertodano, M. A., A. Assad and S. G. Beus (2001). Experiments for entrainment rate of droplets in the annular regime. *Int. J. of Multiphase Flow 27,* 685-699.

[116] Marchioli, C., A. Giusti, M. V. Salvetti and A. Soldati (2003). Direct numerical simulation of particule wall transfer and deposition in upward turbulent pipe flow. *Int. J. of Multiphase Flow 29,* 1017-1038.

[117] Marchisio, D. L. and R. O. Fox (2005). Solution of population balance equations using the direct quadrature method of moments. *Aerosol Sci. 36,* 43-73.

[118] Maroteaux, F., D. Llory, J. F. Le Coz and C. Habchi (2002). Liquid film atomization on wall edges-Separation criterion and droplets formation model. *J. Fluids Engineering 124,* 565-575.

[119] Mashayek, F. and R. V. R. Pandya (2003). Analytical description of particle/droplet-laden turbulent flows. *Progress in Energy and Combustion Sci. 29*, 329-378.

[120] Mathur, S. R. and J. Y. Murthy (1997). A pressure-based method for unstructured meshes. *Num. Heat Transf. Part B 31,* 195-215.

[121] McCoy, D. D. and T. J. Hanratty (1977). Rate of deposition of droplets in annular two-phase flow. *Int. J. of Multiphase Flow 3,* 319-331.

[122] Meland R. and S. T. Johansen (2002). *Dispersed multiphase flow.* Lecture Notes: Departemnet of Energy and Process Engineering. Norges Tekniske-Naturvitenskapelige Universitet, Trondheim.

[123] Meng, W., X. T. Chen, G. E. Kouba, C. Sarica and J. P. Brill (2001). Experimental study of low-liquid-loading gas-liquid flow in near-horizontal pipes. *SPE Production and Facilities november,* 240-249.

[124] Mito, Y. and T. J. Hanratty (2004). A stochastic description of wall sources in a turbulent field: part2. Calculation for a simplified model of horizontal annular flows. *Int. J. of Multiphase Flow 30,* 803-825

[125] Moeck, E. O. and J. W. Stachiewicz (1972). A droplet interchange model for annular-dispersed, two-phase flow. *Int. J. Heat Mass Transf. 15,* 637-653.

[126] Mols, B., and R. V. A. Oliemans (1998). A turbulent diffusion model for particle dispersion and deposition in horizontal tube flow. *Int. J. of Multiphase Flow 24,* 55-75.

[127] Mols, B., I. Mittendorff and R. V. A. Oliemans (2000). Results from a two-dimensional turbulent diffusion-model for dispersion and deposition of droplets in horizontal annular dispersed gas/liquid flow. *Int. J. of Multiphase Flow 26,* 949-975.

[128] Morsi, S. A. and A. J. Alexander (1972). An investigation of particle trajectories in two-phase flow systems. *J. Fluid. Mech 55, part 2*, 193-208.

[129] Moukalled, F. and M. Darwish (2002). A comparative assessment of the performance of mass conserveation-based algorithms for incompressible multiphase flows. *Numerical Heat Transf. Part B 42,* 259-283.

[130] Namie, S. and T. Ueda (1972). Droplet transfer in two-phase annular mist flow. *Bull. JSME 15,* 1568-1580.

[131] Narasimha, R. and K. R. Sreenivasan (1979). Relaminarisation of fluid flows. *Advances in Applied Mech. 19,* 221-303.

[132] Narayanan, C., D. Lakehal, L. Botto and A. Soldati (2003). Mechanisms of particle deposition in a fully developed turbulent open channel. *Phys. Fluids 15,* 763-775.

[133] N.G.S.A (Natural Gas Supply Association). Processing natural gas [online: web], updated 2004, cited 23 Feb. 2005. URL: http://www.naturalgas.org/naturalgas/processing_ng.asp

[134] Nigmatulin, R. I. (1991). *Dynamics of multiphase media. Vol. 2.* New York: Hemisphere Publishing Corporation.

[135] Nigmatulin, R. I., B. I. Nigmatulin, YA. D. Khodzaev and V. E. Kroshilin (1996). Entrainment and deposition rates in a dispersed-film flow. *Int. J. of Multiphase Flow 22,* 19-30.

[136] Nusselt, W. (1916). Die Oberflächenkondensation des Wasserdampfes. *Zeitschrift des Vereines Deutscher Ingenieure 60,* 541-546 and 569-575. (in German)

[137] Oliemans, R. V. A., B. F. M. Pots and N. Trompé (1986). Modelling of annular dispersed two-phase flow in vertical pipes. *Int. J. of Multiphase Flow 12,* 711-732.

[138] OpenCFD Ltd. OpenFOAM launched 10th December 2004 [online: web], updated 2005, cited 24 Feb. 2005. URL: http://www.opencfd.co.uk/ openfoam/launch.html#launch

[139] Owen, D. G., G. F. Hewitt, and T. R. Bott (1985). Equilibrium annular flows at high mass fluxes; data and interpretation. *PhysicoChemical Hydrodynamics 6,* 115-131.

[140] Owen, P. R. (1969). Pneumatic transport. *J. Fluid Mech. 39,* 407-432.

[141] Pan, L. and T. J. Hanratty (2002a). Correlation of entrainment for annular flow in vertical pipes. *Int. J. of Multiphase Flow 28,* 363-384.

[142] Pan, L. and T. J. Hanratty (2002b). Correlation of entrainment for annular flow in horizontal pipes. *Int. J. of Multiphase Flow 28,* 385-408.

[143] Papavergos, P. G. and A. B. Hedley (1984). Particle deposition behaviour from turbulent flows. *Chem. Eng. Res. Des. 62,* 275-295.

[144] Paras, S. V. and A. J. Karabelas (1991). Properties of the liquid layer in horizontal annular flow. *Int. J. of Multiphase Flow 17,* 439-454.

[145] Paras, S. V., N. A Vlachos and A. J. Karabelas (1994). Liquid layer characteristics in stratified-atomization flow. *Int. J. of Multiphase Flow 20,* 939-956.

[146] Patankar S. V. (1980). *Numerical heat transfer and fluid flow.* New York: Hemisphere Publishing Corporation.

[147] Picart, A., A. Berlemont and G. Gouesbet (1986). Modelling and predicting turbulence fields and the dispersion of discrete particles transported by turbulent flows. *Int. J. of Multiphase Flow 12,* 237-261.

[148] Pope, S. B. (2000). *Turbulent flows.* Cambridge: Cambridge University Press.

[149] Pourahmadi, F. (1982). *Turbulence modeling of single and two phase curved channel flow.* Ph. D. thesis. University of California, Berkeley.

[150] Pourahmadi, F. and J. A. C. Humphrey (1983). Modeling solid-fluid turbulent flows with application to predicting erosive wear. *PhysicoChemical Hydrodynamics 4,* 191-219.

[151] Prosperetti, A. and A. V. Jones (1984). Pressure forces in disperse two-phase flow. *Int. J. of Multiphase Flow 10*, 425-440.

[152] Quandt, E. R. (1965). Measurements of some basic parameters in two-phase annular flow. *A.I.Ch.E J. 11,* 311-318.

[153] Reeks, M. W. and G. Skyrme (1976) The dependence of particle deposition velocity on the particle inertia in turbulent pipe flow. *J. Aerosol Sci. 7,* 485-495.

[154] Reeks, M. W. (1977). On the dispersion of small particles suspended in an isotropic turbulent fluid. *J. of Fluid Mech., 83* 529-546.

[155] Reeks, M. W. (1983). The transport of discrete particles in inhomogeneous turbulence. *J. Aerosol Sci. 14,* 729-739.

[156] Reeks, M. W. (1991). On a kinetic equation for the transport of particles in turbulent flows. *Phys. Fluids A 3,* 446-456.

[157] Rhie, C. M. and W. L. Chow (1983). Numerical study of the turbulent flow past an airfoil with trailing edge sparation. *A.I.A.A. J. 21,* 1525-1532.

[158] Rhine Ruhr. Separation equipment [online: web], updated unknown, cited 23 Feb. 2005. URL: http://www.rhineruhr.com.au/separation.asp

[159] Rizk, M. A. and S. E. Elghobashi (1989). A two-equation model for dispersed dilute confined two-phase flows. *Int. J. of Multiphase Flow 15*, 119-133.

[160] Ruyer-Quil, C. and P. Manneville (1998). Modeling film flows down inclined planes. *Eur. Phys. J. B 6,* 277-292.

[161] Saito, T., E. D. Hughes and M. W. Carbon (1978). Multi-fluid modeling of annular two-phase flow. *Nucl. Eng. and Des. 50,* 225-271.

[162] Scarborough, J. B. (1962). *Numerical mathematical analysis. Fifth ed.* Baltimore: The Johns Hopkins Press.

[163] Schadel, S. A. (1988). *Atomization and deposition rates in vertical annular two-phase flow.* Ph.D. thesis. University of Illinois, Urbana.

[164] Schadel, S. and T. J. Hanratty (1989). Interpretation of atomization rates of the liquid film in gas-liquid annular flow. *Int. J. of Multiphase Flow 15,* 893-900.

[165] Schadel, S. A., G. W. Leman, J. L. Binder and T. J. Hanratty (1990). Rates of atomization and deposition in vertical annular flow. *Int J. of Multiphase Flow 16,* 363-374.

[166] Schlichting, H. (1958). *Grenzschicht-Theorie.* Karlsruhe: Verlag G. Braun. (in German)

[167] Schmehl, R., H. Rosskamp, M. Willmann and S. Wittig (1999). CFD analysis of spray propagation and evaporation including wall film formation and spray/film interactions. *Int. J. of Heat and Fluid Flow 20,* 520-529.

[168] Schmidt, K. A. G., S. E. Quiñones-Cisneros, B. Kvamme and E. H. Stenby (2004). Density and viscosity behaviour of a north sea crude oil, natural gas liquid and their mixtures. In *Fifth International Conference on Petroleum Phase Behaviour and Fouling,* Banff.

[169] Schoeller-Bleckmann Edelstahlrohr. Seamless stainless steel pipes and tubes [online: web], updated: unknown, cited 19 Apr. 2006. URL: http://www.sber.at/download/services/pipestubes.pdf

[170] Sehmel, G. A. (1970). Particle deposition from turbulent air flow. *J. of Geophys. Res. 75,* 1766-1781.

[171] Simonin, O., (1990). Eulerian formulation for particle dispersion in turbulent two-phase flows. In *Proceedings of the Fifth Workshop on Two-Phase Flow Predictions.* Erlangen: M. Sommerfeld and D. Wennerberg eds.

[172] Simonin, O. and P. L. Viollet (1990). Predictions of an oxygen droplet pulverization in a compressible subsonic coflowing hydrogen flow. In *Numerical methods for multiphase flows, FED 91,* 65-82.

[173] Simonin, O., E. Deutsch and J. P. Minier (1993). Eulerian prediction of the fluid/particle correlated motion in turbulent two-phase flows. *Appl. Scientific Res. 51,* 275-283.

[174] Slater, S. A., A. D. Leeming and J. B. Young (2003). Particle deposition from two-dimensional turbulent gas flows. *Int. J. of Multiphase Flow 29,* 721-750.

[175] Sleicher, C. A. (1962). Maximum stable drop size in turbulent flow. *A.I.Ch.E 8,* 471-477.

[176] Soldati, A. and P. Andreussi (1996). The influence of coalescence on droplet transfer in vertical annular flow. *Chem. Engng. Sci. 51,* 353-363.

[177] Son, G. (2003). Efficient implementation of a coupled level-set and volume-of-fluid method for three-dimensional incompressible two-phase flows. *Num. Heat Transf. Part B 43,* 549-565.

[178] Soo, S. L. (1967). *Fluid dynamics of multiphase systems.* Waltham: Blaisdell Publishing.

[179] Soo, S. L. (1989). *Particulates and continuum - Multiphase fluid dynamics.* New York: Hemisphere Publishing.

[180] Stevanovic, V. and M. Studovic (1995). A simple model for vertical annular and horizontal stratified two-phase flows with liquid entrainment and phase transitions: one-dimensional steady state conditions. *Nucl. Eng. and Des. 154,* 357-379.

[181] Stüben, K. (1999). Algebraic multigrid (AMG): An introduction with applications. *GMD Report 70.*

[182] Su, G., J. Gou, S. Qiu, X. Yang and D. Jia (2003). Theoretical calculation of annular upward flow in a narrow annuli with bilateral heating. *Nucl. Eng. and Design 225,* 219-247.

[183] Sugawara, S. (1990). Droplet deposition and entrainment modeling based on the three-fluid model. *Nucl. Eng. and Des. 122,* 67-84.

[184] Sugawara, S. and Y. Miyamoto (1990). FIDAS: Detailed subchannel analysis code based on the three-fluid and three-field model. *Nucl. Eng. and Des. 120,* 147-161.

[185] Svendsen, H. High pressure gas separation, Introduction [online: web], updated 14 June 2004, cited 23 Feb. 2005. URL: http://www.hipgas.ntnu.no/

[186] Tatterson, D. F. (1975). *Rates of atomization and drop size in annular two-phase flow.* Ph.D. thesis. University of Illinois, Urbana.

[187] Taylor, G. I. (1963). Generation of ripples by wind blowing over a viscous fluid. In *The scientific papers of Sir Geoffrey Ingram Taylor. Vol. III.* Cambridge: Cambridge University Press.

[188] Tennekes, H. and J. L. Lumley (1972). *A first course in turbulence.* Cambridge: MIT Press.

[189] Tomiyama, A. and N. Shimada (2001). A numerical method for bubbly flow simulation based on a multi-fluid model. *Journal of pressure vessel technology-Transactions of the ASME 123,* 510-516.

[190] Trabold, T. A., R. Kumar and P. F. Vassallo (1999). Experimental study of dispersed droplets in high-pressure annular flows. *J. of Heat Transf. 121,* 924-933.

[191] Trabold, T. A. and R. Kumar (2000a). High pressure annular two-phase flow in a narrow duct: Part I-Local measurments in the droplet field. *Trans. of the ASME 122* 364-374.

[192] Trabold, T. A. and R. Kumar (2000b). Vapor core turbulence in annular two-phase flow. *Exp. in Fluids 28,* 187-194.

[193] Trela, M. (1982). Deposition of droplets from turbulent stream. *Wärme und Stoffübertragung 16,* 161-168.

[194] Trela, M., Zembik, J. and B. Durkiewicz (1982). Droplet deposition on a flat plate from an air/water turbulent mist flow. *Int. J. of Multiphase Flow 8,* 227-238.

[195] Tso, C. P. and S. Sugawara (1990). Film thickness prediction in a horizontal annular flow. *Int. J. of Multiphase Flow 16,* 867-884.

[196] Tsuji Y., Y. Morikawa and H. Shiomi (1984). LDV measurements of an air-solid two-phase flow in a vertical pipe. *J. Fluid Mech. 139,* 417-434.

[197] Ueda, T. (1979). Entrainment rate and size of entrained droplets. *Bull. of the JSME 22,* 1258-1265.

[198] Uijttewall, W. S. and R. V. A. Oliemans (1996). Particle dispersion and deposition in direct numerical and large eddy simulations of vertical pipe flows. *Phys. Fluids 8,* 2590-2604.

[199] U.N.T.C.A.D (United Nations Conference On Trade and Development). Information on natural gas [online: web], updated 26 July 2004, cited 23 Feb. 2005. URL: http://r0.unctad.org/infocomm/anglais/gas/sitemap.htm

[200] Van Rossum, J. J. (1959). Experimental investigation of horizontal liquid films. *Chem. Eng. Sci. 11,* 35-52.

[201] Von Schiller, L. und A. Naumann (1933). Über die grundlegenden Berechnungen bei der Schwerkraftaufbereitung. *Zeit. des Ver. deutscher Ing. 77,* 318-320. (in German)

[202] Vasquez, S. A. and V. A. Ivanov (2000). A phase coupled method for solving multiphase problems on unstructured meshes. In *Proc. of ASME FEDSM'00: ASME 2000 Fluids Engineering Division Summer Meeting.* Boston.

[203] Vassalo, P. (1999). Near wall structure in vertical air-water annular flows. *Int. J. of Multiphase Flow 25,* 459-476.

[204] Verberk, J. Q. J. C. Air-water cleaning for micro and ultrafiltration - ir [online: web], updated 27 Aug. 2003, cited 8 Mar. 2005. URL: http://www.gezondheidstechniek.tudelft.nl/verberk.htm

[205] Verlaan, C. (1991). *Performance of novel mist eliminators.* Ph.D. thesis. Delft University of Technology, Delf.

[206] Wallis, G. B. (1968). Phenomena of liquid transfer in two-phase dispersed annular flow. *Int. J. of Heat Mass Transf. 11,* 783-785.

[207] Wallis, G. B. (1969). *One-dimensional two-phase flow.* New York: McGraw-Hill Book.

[208] Wang, Q., K. D. Squires and O. Simonin (1998). Large eddy simulation of turbulent gas-solid flows in a vertical channel and evaluation of second-order models. *Int. J. of Heat and Fluid Flow 19,* 505-511.

[209] Wehrli, M., S. Hirschberg and R. Schweizer(2003). Influence of vapour feed design on the flow distribution below packings. *Trans. IChemE 81, part A*, 116-121.

[210] Whitaker, S. (1969). Advances in theory of fluid motion in porous media. *Ind. and Eng. Chem. 61 (12),* 14-28.

[211] White, F. M. (1991). *Viscous fluid flow (second edition).* New York: McGraw-Hill.

[212] Williams, L. R., L. A. Dykhno and T. J Hanratty (1996). Dropet flux distributions and entrainment in horizontal gas-liquid flows. *Int. J. of Multiphase Flow 22,* 1-18.

[213] Wongwises, S. and W. Kongkiatwanitch (2001). Interfacial friction factor in vertical upward gas-liquid annular two-phase flow. *Int. Comm. Heat and Mass Transf. 28,* 323-336.

[214] Woodmansee, D. E. and T. J. Hanratty (1969). Mechanism for the removal of droplets from a liquid surface by a parallel air flow. *Chem. Eng. Sci. 24,* 299-307.

[215] Yan, J. Energy density of natural gas [online: web], updated 2004, cited 23 Feb. 2005. URL: http://hypertextbook.com/facts/2004/JessicaYan.shtml

[216] Yano, T., M. Aritomi, H. Kikura and H. Obata (2001). Mechanistic modeling for ring-type boiling water reactor fuel spacer design (3) run-off effect and model formulation. *Nucl. Eng. and Des. 210,* 21-36.

[217] Young, J. and A. Leeming (1997). A theory of particle deposition in turbulent pipe flow. *J. of Fluid Mech. 340,* 129-159.

[218] Yu, Y., L. X. Zhou, C. G. Zheng and Z. H. Liu (2003). Simulation of swirling gas-particle flows using different time scales for the closure of two-phase velocity correlation in the second-order moment two-phase turbulence model. *J. of Fluids Engineering, 125,* 247-250.

[219] Zaichik, L. I., V. A. Pershokov, M. V. Kozelev and A. A. Vinberg (1997). Modeling of dynamics, heat transfer, and combustion in two-phase turbulent flows: 1. Isothermal flows. *Exp. Thermal and Fluid Sci. 15,* 291-310.

[220] Zaichik, L. I. and V. M. Alipchenkov (2001). A statistical model for transport and deposition of high-inertia colliding particles in turbulent flow. *Int. J. of Heat and Fluid Flow 22,* 365-371.